Measurement of Triple Gauge Boson Couplings using $\mathrm{W}^+\mathrm{W}^- \rightarrow l\nu q\bar{q}$ Events with OPAL

Kay Roscoe

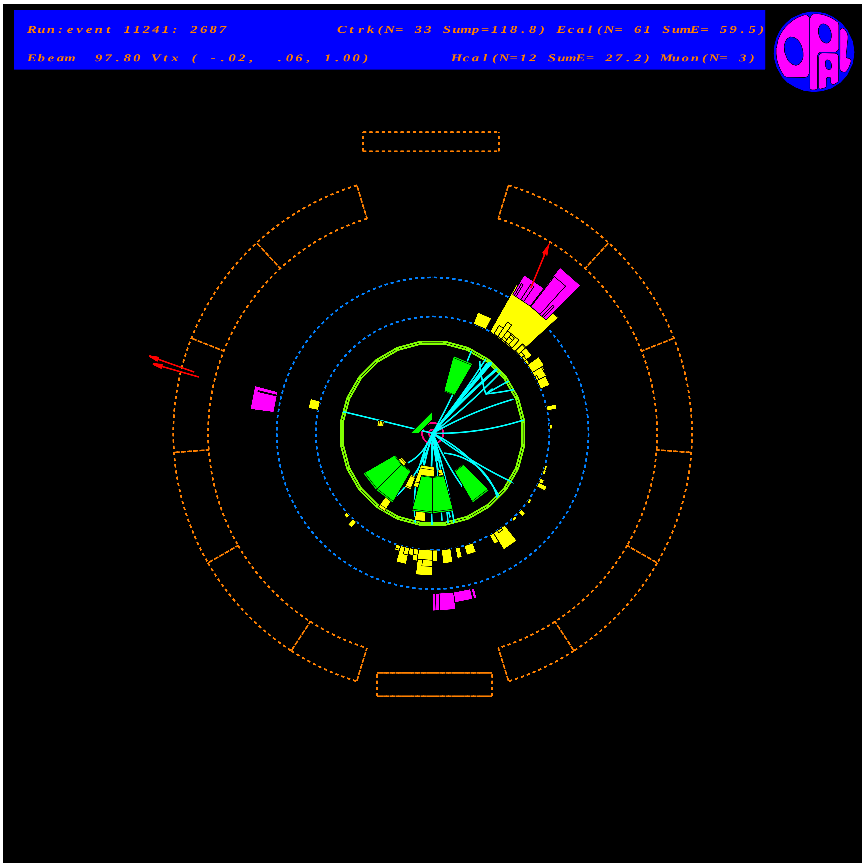

Particle Physics Group
Department of Physics and Astronomy

2001

A thesis submitted to The University of Manchester for the degree of
Doctor of Philosophy in the Faculty of Science and Engineering

Contents

List of Figures

List of Tables

Abstract

Three analyses are presented in this thesis. They were performed on data collected by the OPAL experiment on the LEP collider at CERN between 1997 and 1999.

Measurements of the triple gauge boson coupling parameters are presented from $e^+e^- \rightarrow \mathrm{W^+W^-} \rightarrow l\nu q\bar{q}$ interactions recorded during the 1999 LEP run with a total integrated luminosity of 212 pb^{-1}, and centre-of-mass collision energies between 192 and 202 GeV. The optimal observable technique was used to extract the coupling values. The combined results for the single parameter fits (when one coupling was allowed to vary and the other two were set to their Standard Model values) are: $\kappa_\gamma = 0.722\,^{+\,0.191}_{-\,0.160}$, $g_1^{\mathrm{Z}} = 0.962\,^{+\,0.066}_{-\,0.063}$ and $\lambda = -0.070^{+\,0.064}_{-\,0.062}$, where errors include both statistical and systematic uncertainties. These results are consistent with Standard Model predictions at 95% confidence.

Acollinearity dependent momentum cuts were introduced to improve the classification of $\mathrm{W^+W^-} \rightarrow l^+\nu l^-\bar{\nu}$ events. The study describes how the cut values were determined using 183 pb^{-1} of data collected at $\sqrt{s} = 189$ GeV, and why they improve the classification. The resultant improvements to the W leptonic branching fractions were found to be of order 5-12%.

For the start of data taking in 1997, 4 layers of scintillator tiles (MIP plugs) were installed in both endcaps of the OPAL detector. The main purpose of these tiles was to detect the presence of minimum ionizing particles at low angles to the beam axis. These tiles were found to have certain readout problems. The adjustments to be applied to the MIP plug data to obtain the correct ϕ sector for individual MIP hits are discussed. The MIP plug response to muons was investigated using $e^+e^- \rightarrow e^+e^-\mu^+\mu^-$ events and a set of criteria to define "good" MIP plug coincident hits for use as a veto in search analyses is described. Noise rates have been measured using events that have been randomly triggered.

Declaration

No portion of the work referred to in this thesis has been submitted in support of an application for another degree or qualification of this or any other university or other institute of learning.

Copyright

Copyright in text of this thesis rests with the Author. Copies (by any process) either in full, or of extracts, may be made **only** in accordance with instructions given by the Author and lodged in the John Rylands University Library of Manchester. Details may be obtained from the Librarian. This page must form part of any such copies made. Further copies (by any process) of copies made in accordance with such instructions may not be made without the permission (in writing) of the Author.

The ownership of any intellectual property rights which may be described in this thesis is vested in the University of Manchester, subject to any prior agreement to the contrary, and may not be made available for use by third parties without the written permission of the University, which will prescribe the terms and conditions of any such agreement.

Further information on the conditions under which disclosures and exploitation may take place is available from the Head of the Department of Physics and Astronomy.

The Author

The author was educated at Filton College, Bristol before joining the School of Physics and Chemistry, Lancaster University for an MPhysics degree. In 1997 she joined the Department of Physics & Astronomy at the University of Manchester.

The work presented here was undertaken at Manchester and CERN, Geneva.

> *Cherish your visions; cherish your ideals; cherish the music that stirs in your heart; the beauty that forms in your mind, the loveliness that drapes your purest thoughts, for . . . if you remain true to them, your world will at last be built.*
>
> JAMES ALLEN

Acknowledgements

There are many people I would like to thank for their help, advice, support (both moral and technical) throughout the past few years. Apologies to all those who are inadvertently not mentioned here. Firstly I would like to thank my supervisor, Roger Barlow, who came riding into my life to rescue my PhD from certain death. I would like to thank him for his optimism, patience, technical help (especially in all things statistical) and for proof reading this thesis. Many thanks Roger, for taking this on in spite of your many other commitments.

The other person who I would especially like to thank is Helge Voss (formerly at Bonn University now at CERN) for not only handing over the reigns of the TGC $\mathcal{OO}$ analysis code, but there on afterwards for explaining so many of its intricacies plus many, many invaluable discussions, help etc. Thank you Helge - its been a great pleasure working with you.

I would very much like to thank other members of the OPAL TGC working group, especially Gideon Bella, and also Carla Sbarra, Dave Charlton, Alun Lloyd, Paul Dervan, Ian Bailey and Jon Couchman (plus others) for many useful discussions and advice etc. For help with the WW $\rightarrow l\nu l\bar{\nu}$ classification projects, plus many other useful comments and suggestions etc I would like to thank Graham Wilson. For the original idea of having acollinearity dependent momentum cuts I would like to thank Bob Jacabson from the ALEPH collaboration. Also thanks to Mark Thomson, Eric Torrence and Richard Hawkings plus other members of OPAL WW working group for their help. For the MIP plug project I am indebted to Alick McPherson, Stan Bentvelson and Austin Ball.

At Manchester, I would very much like to thank past and present members of the HEP group for their hospitality, general help and support. Particularly thanks to George, Fred, Vato, John, Richard, the system administrators Stuart and Andrew, plus many of my fellow PhD students. I acknowledge the technical advice and help from my first supervisor, Terry Wyatt, for the MIP plug and WW$\rightarrow l\nu l\bar{\nu}$ classification projects.

There are many, many other people at CERN who I would like to thank. So many people its impossible to mention everyone by name (apologies for that), but in particular Pauline Gagnon, Tom Junk, Chris Rembser and Tara Shears readily spring to mind. Thanks also to the shift and SnOPAL system admin. people Ann Williamson, Thomas Kress and Olivier Cesar for coming to the rescue in many a dire moment. Mention also Matthias Schroeder for help with ROPE, ODFIX and putting up with my poor attempts at German. Thanks to everyone who helped translate odd bits of Helge's thesis. Thank you Jo Pater (and Ian Duerdoth) for teaching me about MB (gas system). Thanks also to the OPAL secretariat - Mette, Dawn and Dominique for helping to make OPAL the friendly place it is.

Many thanks also to my many friends at CERN - my time out there would have been much the poorer without your friendship. Thanks particularly for your encouragement and moral support during the 'black days' of supervisor problems and latterly whilst writing this thesis. Thanks to PPARC for the financial support, and mum 'n' dad and other friends for moral support. Thank you Gareth for allowing me to use two of your quotations.

The effort to understand the universe is one of the very few things that lifts human life a little above the level of farce, and gives it some of the grace of tragedy.

STEVEN WEINBERG, *The first three minutes, Flamingo, Harper Collins (1977)*

Chapter 1

Introduction

The Large Electron Positron collider (LEP), at CERN (La Centre Européenne pour la Recherche Nucléaire) near Geneva in Switzerland, began operation in 1989 with centre of mass energies around the Z^0 resonance peak (the so called LEP I phase of operation). LEP was a truly remarkable machine, the largest scientific instrument ever built. Since 1995, the beam energy was steadily increased and in 1996 LEP entered its second phase of operation, LEP 2, when the first W pair events were produced with $E_{\text{beam}} \gtrsim 80.5$ GeV. The main topics of the LEP 2 physics program have included studies of the W boson and searches for new particles, in particular searches for the elusive Standard Model Higgs boson. In November 2000 despite tantalizing hints at a possible 115 GeV Higgs, wild protests from the LEP physics community and behind the scenes political intrigues, LEP was finally shut down to make way for the LHC (Large Hadron Collider) project. But analyses of LEP data continue . . .

LEP could be described as a boson factory; it enables precise measurements to be made of the Z^0 and $W^{\pm}$ boson properties including their production cross sections, masses, decay branching fractions and widths to form important tests of electroweak theory. One such measurement, that of the triple gauge boson coupling between two charged W bosons and either a neutral photon or Z^0 boson is the main topic of this thesis. The analysis was performed using the optimal observable ($\mathcal{OO}$) technique to extract the coupling values from a selection of $WW \rightarrow l\nu q\bar{q}$ events. Measurement of triple gauge coupling (TGC) values is important, not only as a test of the underlying $SU(2)_L \times U(1)_Y$ gauge symmetry, but also by providing a possible insight into new physics (if the new particles are too massive to be produced with the current energies available).

In order to select signal events for analyses, it is often necessary to identify and then reject sources of background processes. Before the start of data taking in 1997 a new subdetector, the Minimum Ionizing Particle (MIP) plugs, were installed in the OPAL detector to detect the yes/no presence of minimum ionizing particles (i.e. muons) close to the beam axis. It is particularly important to reject two photon processes which might otherwise masquerade as candidate events (for example in searches for di-lepton events plus missing energy or leptonically decaying W pair events). An investigation was made of MIP plug detector performance during its first two years of operation and is described in this thesis.

A number of analyses (for example measurements of W→leptons branching ratios and TGCs in the fully leptonic channel) rely on the correct identification and classification of $W^+W^- \rightarrow l^+\nu l^-\bar{\nu}$ events. Although experimentally it is relatively easy to classify events in which (at least) one W boson decays to tau (plus neutrino) and then the tau subsequently decays hadronically, it is quite challenging to separate events in which the tau decays leptonically to either electron or muon (plus neutrinos) from events where the W decays promptly to electron or muon (plus neutrino). Until 1998, the standard OPAL algorithms relied solely on simple momentum cuts to separate these processes. However, it has been found that momentum cuts dependent on the angle between the two leptons have better separating power. This study, and the resulting improvements to the leptonic branching ratio measurements, is outlined in this thesis.

All three analyses were made using data collected by the OPAL detector during the years 1997 to 1999. Table 1.1 shows how much integrated luminosity was collected at each centre of mass energy[1] and the year. The analyses performed on which data sets are also indicated.

The layout of the thesis is as follows: after a brief introduction to some theoretical ideas of the Standard Model and W boson physics at LEP 2, chapter 3 describes the LEP collider and the OPAL detector which collected the data. Chapter 4 describes an investigation of the MIP plug detector performance. Chapter 5 provides a general introduction to W pair events (including certain background processes) and a short description of the $WW \rightarrow l\nu l\bar{\nu}$ and $WW \rightarrow l\nu q\bar{q}$ event selections and kinematic fitting. Chapter 6 discusses some improvements made to the classification of $WW \rightarrow l\nu l\bar{\nu}$ events. The remaining chapters describe the

---

[1] Throughout this thesis, the datasets are normally referred to by the nearest integer value of the centre of mass energy.

Year	Average Energy (GeV)	Luminosity (pb^{-1})	Analysis Project
1997	182.7	57.2 ± 0.3	MIP plugs
1998	188.6	183.1 ± 0.4	MIP plugs & WW $\rightarrow l\nu l\bar{\nu}$ classification
1999	191.6	29.3 ± 0.1	TGCs
”	195.5	69.0 ± 0.2	”
”	199.5	76.5 ± 0.2	”
”	201.6	37.6 ± 0.1	”

Table 1.1: *List of data collected around each centre of mass energy and the analysis performed for each data set.*

theory and an experimental measurement of the triple gauge boson couplings using optimal observables. Chapter 8 includes a description of the systematic uncertainties investigated, bias tests and the subsampling tests (used to determine the statistical uncertainties). Finally chapters 9 and 10 conclude with an overall discussion of the TGC results and their relevance to other measurements. Details of OPAL track parameters, a list of Monte Carlo samples used in the analyses and a list of abbreviations used throughout this thesis may be found in the appendices.

Apparently there is colour, apparently sweetness, apparently bitterness; actually there are only atoms and the void.

DEMOCRITUS, 420 B.C.

Chapter 2

Theoretical Ideas

The quest to understand the origins of the universe and the constituents of matter began with the early civilizations. The ancient Greeks based their understanding on Aristotle's "earth, air, fire and water" model of the elements. Today, we have the so-called "Standard Model" of Particle Physics to describe subnuclear matter at very small distance scales in the presence of the fundamental forces. But we know that this model is incomplete - a low energy approximation of the "real" universe that agrees with experimental observations at the energy scales currently accessible.

This chapter begins with a brief introduction to the Standard Model (SM), concentrating on the areas relevant to the analyses in this thesis. The SM has been described extensively in the literature and further details can be found in, for example [1]. One of the main goals of LEP 2 physics was the study of the W boson: including measurements of its mass, width, production and decay properties as well as couplings to other particles. The second part of this chapter discusses some of the theoretical issues behind the study of W boson physics. The coupling of the W boson to other gauge bosons (the so-called 'triple gauge boson couplings') are discussed in chapter 7. Some experimental aspects of W boson physics are addressed in chapter 5.

2.1 The Standard Model

The SM describes our current knowledge of all known elementary particles and their interactions under three (electromagnetic, weak and strong) of the four fundamental forces.

(Gravity has yet to be incorporated in the SM but its effects are negligible at the energies and scales involved in particle physics). In the SM there are two main types of ‘matter’ particle: quarks and leptons which are spin 1/2 fermions and can be arranged in doublets into three generations or families:

$$\begin{array}{lcccc}
 & \text{I} & \text{II} & \text{III} & \text{CHARGE} \\
\text{QUARKS} & \binom{u}{d} & \binom{c}{s} & \binom{t}{b} & \begin{matrix} +\frac{2}{3} \\ -\frac{1}{3} \end{matrix} \\
\text{LEPTONS} & \binom{e}{\nu_e} & \binom{\mu}{\nu_\mu} & \binom{\tau}{\nu_\tau} & \begin{matrix} -1 \\ 0 \end{matrix}
\end{array}$$

Table 2.1: *The fundamental fermions, arranged in generations of increasing mass for the charged particles.*

Each matter particle has a corresponding anti-matter partner which has the same properties and quantum numbers but opposite charge. The interactions between the fermions are mediated by the exchange of virtual gauge vector bosons (with integral spin):

Force	Vector Boson	Range	Theory
Electromagnetic	photon (γ)	∞	Quantum Electrodynamics
Weak Nuclear	$W^{\pm}$, Z^0	10^{-18}m	Electroweak
Strong Nuclear	gluons ($g_{1...8}$)	∞	Quantum Chromodynamics
Gravitation	graviton[1] ?	∞	Gravity

Table 2.2: *The four fundamental forces of Nature and their mediators.*

All fermions experience the weak force but only the charged particles can interact electromagnetically. Quarks also interact via the strong force. The photon and Z^0 are chargeless and cannot self-interact, unlike the $W^{\pm}$ bosons which carry electric charge and the gluons which carry colour charge.

Cabibbo-Kobayashi-Maskawa Matrix

The quark mass eigenstates are not the same as the quark weak eigenstates. The down type quarks (d,s,b) are said to ‘mix’ to give the weak eigenstates (d’,s’,b’). A 3×3 unitary

---

[1] So far there has been no direct experimental evidence for the graviton which is postulated to be a spin 2 particle, unlike the other vector bosons which are all spin 1.

transformation matrix called the Cabibbo-Kobayashi-Maskawa (CKM) matrix relates the mass and weak eigenstates:

$$\begin{pmatrix} d' \\ s' \\ b' \end{pmatrix} = \begin{pmatrix} V_{ud} & V_{us} & V_{ub} \\ V_{cd} & V_{cs} & V_{cb} \\ V_{td} & V_{ts} & V_{tb} \end{pmatrix} \begin{pmatrix} d \\ s \\ b \end{pmatrix} \tag{2.1}$$

2.1.1 Gauge Field Theories and Lagrangians

Symmetries are important in nature because they give rise to conservation laws, and similarly conservation laws reveal underlying symmetries (Noether's theorem). For example, if a system is invariant under space translation then momentum will be conserved. This is a type of *'global'* symmetry, which means that it is independent of space-time. In particle physics we are concerned with invariance under a special type of transformation: phase or 'gauge' transformations. For example, a wave function $\psi(x)$ that describes a state can undergo a phase transformation:

$$\psi(x) \rightarrow \psi'(x) = e^{i\phi(x)}\psi(x) \tag{2.2}$$

If $\phi(x)$ is space-time dependent, then this is a *'local'* gauge transformation. We believe that gauge symmetry is one of the most fundamental symmetries in nature.

Any physical system can be fully described by its Lagrangian or Lagrangian density: $\mathcal{L} = T - V$ where T and V represent the kinetic and potential energies respectively. The Lagrangian is a function of the fields and their derivatives. The equations of motion can be derived from the principle of least action using the Lagrangian. The Lagrangian may also possess "hidden" symmetries, and it is the breaking of such a symmetry that is responsible for the masses of the gauge bosons.

Quantum field theory (QFT) is the formalism that describes the relationships between the fundamental particles and forces, and hence enables the calculation of physical observables through the underlying symmetry in the Lagrangian. A gauge theory is a relativistic QFT that obeys local gauge invariance (ie it is invariant under local transformations of a characteristic symmetry group). For example, the SM is a quantum field gauge theory based on the symmetry group SU(3)⊗SU(2)⊗U(1), where the SU(3) term corresponds to the strong interactions of quantum chromodynamics (QCD) and the SU(2)$\otimes$U(1) term corresponds to electroweak interactions.

Under phase transformations, gauge invariance can only be preserved if extra fields are introduced. Importantly, these new fields correspond to the gauge bosons. An example of this can be found in quantum electrodynamics (QED), the theory that describes electromagnetic interactions. Here, the set of local phase transformations $e^{i\psi(x)}$ form a mathematical set called the U(1) group. A new vector field A_μ is introduced by replacing the normal derivative ∂_μ in the Lagrangian by: $D_\mu = \partial_\mu - ieA_\mu$. This new field corresponds to the massless photon and the conserved quantity is electric charge.

2.1.2 Electroweak Theory

Glashow, Salam and Weinberg proposed the unification of the electromagnetic and weak forces into a single gauge field theory, known as electroweak (EW) theory [2]. This theory is based on the SU(2)$_\mathrm{L}\otimes$U(1)$_\mathrm{Y}$ gauge symmetric field theory, where the SU(2)$_\mathrm{L}$ term corresponds to the weak *isospin* group which acts only on left-handed fermions, and the U(1)$_\mathrm{Y}$ term is the weak *hypercharge* group. The SU(2)$_\mathrm{L}\otimes$U(1)$_\mathrm{Y}$ group has four generators with a corresponding number of gauge bosons. Three of these bosons W^i_μ (where $i = 1, 2, 3$) are associated with the SU(2)$_\mathrm{L}$ group, and the fourth B_μ couples to the weak hypercharge U(1)$_\mathrm{Y}$ group. These fields must be introduced to the Lagrangian to preserve gauge invariance.

The electroweak Lagrangian is comprised of three parts:

$$\mathcal{L}_\mathrm{EW} = \mathcal{L}_f + \mathcal{L}_\mathrm{YM} + \mathcal{L}_\mathrm{Higgs} \tag{2.3}$$

The first term, $\mathcal{L}_f$ represents the lepton and quark kinetic energies and interactions with the W_μ and B_μ fields. The second term represents the kinetic energies and self-interactions of the W_μ and B_μ fields:

$$\mathcal{L}_\mathrm{YM} = -\frac{1}{4}W^i_{\mu\nu}W^{\mu\nu}_i - \frac{1}{4}B_{\mu\nu}B^{\mu\nu} \tag{2.4}$$

where:

$$B^{\mu\nu} = \partial^\mu B^\nu - \partial^\nu B^\mu \tag{2.5}$$

and

$$W_i^{\mu\nu} = \partial^\mu W_i^\nu - \partial^\nu W_i^\mu + g\epsilon_{ijk} W_j^\mu W_k^\mu \tag{2.6}$$

The 'YM' subscript indicates that this is a pure Yang Mills term [3]. One of the most important differences between QED and EW/QCD interactions is that the former is Abelian whereas the latter are non-Abelian (mathematically this means the elements do not commute). In EW theory this is evident by the $W_{\mu\nu}^i W_i^{\mu\nu}$ term in the Lagrangian which gives rise to the trilinear and quadrilinear self boson couplings - a characteristic of non-Abelian gauge theories. (In QCD the self interactions occur between the eight gluon fields).

The first two terms in equation 2.3 describe the interactions of the fermions with the electroweak fields, and the self interactions of these fields, but no mass terms are present. Mass terms for the gauge fields of the form $mW_\mu^i W_\mu^i$ are forbidden if gauge invariance is to be maintained under SU(2)$_\mathrm{L}\otimes$U(1)$_\mathrm{Y}$ gauge transformations. Furthermore, since left and right handed fermions transform differently, their masses cannot be included either. This problem is solved by the scalar sector of the SM in the so-called *'Higgs mechanism'* [4] which *"spontaneously breaks the symmetry"* through a non-zero vacuum expectation value (vev) of the Higgs field. This gives rise to the gauge boson masses whilst preserving local gauge invariance of the electroweak Lagrangian.

The observable fields corresponding to the vector bosons of the electroweak interaction are a linear combination of the massless W_μ^3 and B_μ fields which mix to form two new fields Z_μ and A_μ. These can be identified as the Z^0 and γ bosons respectively:

$$\begin{aligned} A_\mu &= B\cos\theta_W + W^3\sin\theta_W \\ Z_\mu &= -B\sin\theta_W + W^3\cos\theta_W \end{aligned} \tag{2.7}$$

The degree of mixing between the neutral gauge fields depends on the weak mixing angle θ_W which relates the coupling constants of the SU(2)$_\mathrm{L}$ and U(1)$_\mathrm{Y}$ groups (denoted by g and g' respectively) to the electric charge e by:

$$e = g\sin\theta_W = g'\cos\theta_W \tag{2.8}$$

The W_μ^1 and W_μ^2 fields are related to the W$^+$ and W$^-$ bosons which mediate the charged current interactions by:

$$W^{\pm} = (W^1 \mp W^2)/\sqrt{2} \tag{2.9}$$

The masses which the W^+, W^- and Z^0 bosons acquire from the vacuum expection value via the Higgs mechanism are related by:

$$M_{\mathrm{W}} = M_{\mathrm{Z}} \cos\theta_W \tag{2.10}$$

Conversely, the residual photon field remains massless as a direct consequence of the U(1) gauge invariance of the vacuum. The interaction terms in equations 2.4 and 2.6 persist after the symmetry breaking. The interaction of a W^+, W^- and W^3 is re-expressed as the interactions between $W^+W^-Z^0$ and $W^+W^-\gamma$. This forms the basis of the SM prediction of the triple gauge boson couplings described in chapter 7.

2.2 W Boson Physics

This section discusses some of the basic theoretical ideas behind the study of W bosons at LEP 2. After a brief résumé of some W boson properties, the W pair production cross section is discussed together with some correction factors which need to be considered in the calculations. Other four fermion processes at LEP 2 are reviewed and finally the W branching fractions and W decay properties are discussed.

The W boson is a massive particle (M_W = 80.450 ± 0.039 GeV/c^2) with a Breit-Wigner mass sprectrum and width of Γ = 2.150 ± 0.091 GeV [5]. This implies that $W^{\pm}$ bosons have finite lifetime and limited range (of order 10^{-18}m). $W^{\pm}$ bosons cannot be observed directly but instead their existence is inferred from their decay products. Unlike its neutral weak boson partner the Z^0, the $W^{\pm}$ bosons are charged and have non-zero weak isospin. They can couple to both the photon and Z^0 gauge bosons (the triple gauge boson vertex), as well as to charged and neutral fermions. Neutral current interactions, ie those involving either the Z^0 or γ propagators, cannot change the flavour of fermions or anti-fermions, whereas the charged current processes must do so. The W boson is a spin-1 particle which can have three helicity states: -1, 0 or +1. The positive and negative helicity states correspond to transverse polarizations and the zero helicity state corresponds to longitudinal polarization.

2.2.1 $\mathrm{W}^+\mathrm{W}^-$ Production

In e^+e^- collisions with centre of mass (E_{cm}) energies above the threshold value of twice the W mass ($\sqrt{s} \approx 161$ GeV), $\mathrm{W}^+\mathrm{W}^-$ production proceeds at tree level via one of the three processes shown in figure 2.1[2]. These three diagrams are referred to as the 'CC03' (charged current 3) diagram family. The non-Abelian diagrams on the left and centre arise from e^+e^- annihilation and are called 's-channel' processes. They involve the interaction of the triple gauge boson vertex. The neutrino exchange diagram on the right is a 't-channel' process which contributes only left handed electrons, but experimentally cannot be separated from the s-channel diagrams with unpolarized beams. The s and t parameters refer to the Mandelstam variables which are defined as:

$$\begin{aligned} s &\equiv (p+q)^2 = (k+l)^2 = 4E_{\text{beam}}^2 \\ t &\equiv (p-k)^2 = (q-l)^2 = -E_{\text{beam}}^2\left(1+\beta^2-2\beta\cos\theta\right) \\ u &\equiv (p-l)^2 = (q-k)^2 = -E_{\text{beam}}^2\left(1+\beta^2+2\beta\cos\theta\right) \end{aligned} \tag{2.11}$$

where p (q) is the momenta of the incoming electron (positron), k (l) is the momenta of the outgoing W^+ (W^-), $\mathrm{E}_{\mathrm{beam}}$ is the beam energy, θ is the scattering angle between the W^- and e^- and $\beta = \sqrt{1 - M_{\mathrm{W}}^2/E_{\text{beam}}^2}$.

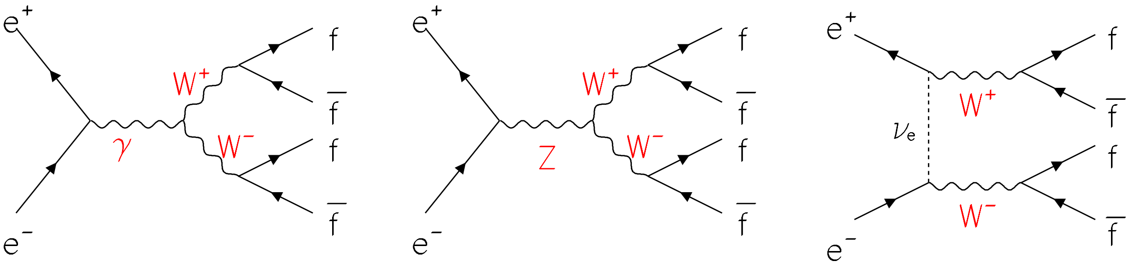

Figure 2.1: *Lowest order Feynman diagrams illustrating the 3 lowest order processes (known as CC03) at LEP which produce W pairs. The matrix element for these are given in [8].*

The W pair production cross section increases with E_{cm} above its threshold value. At threshold, the t-channel process is dominant and hence the cross section is not very sensitive to

---

[2] In principle there is an additional diagram via SM Higgs decay ($e^+e^- \rightarrow \mathrm{H}^0 \rightarrow \mathrm{W}^+\mathrm{W}^-$) but since the coupling between the Higgs and the light electrons is very small, the cross section is negligible at LEP 2 energies and ignored throughout the following discussions.

triple gauge boson couplings. Above threshold the s-channel processes become more important and destructively interfere with the t-channel process, so reducing the overall cross section. The total cross section for WW production as a function of E_{cm} as measured by the OPAL experiment is shown in figure 2.2 [6]. The SM theoretical prediction, calculated by the analytical GENTLE [7] package, is also shown together with predictions for the scenarios when there are no WWZ, WWγ vertices or only ν_e exchange diagrams. Comparing the OPAL measured values with the predictions, this plot clearly shows the existence of triple gauge boson couplings and confirms their Yang Mills character. Anomalous boson couplings, ie coupling values that differ from their SM predictions, would in general lead to an increase in the cross section and thus violate unitarity[3] at high energies [8]. With the available energies at LEP 2, the angular distribution methods of measuring the TGCs are more sensitive in the study of anomalous couplings, because they are suppressed by a factor β^2 in the total cross section. This is discussed further in chapter 7.

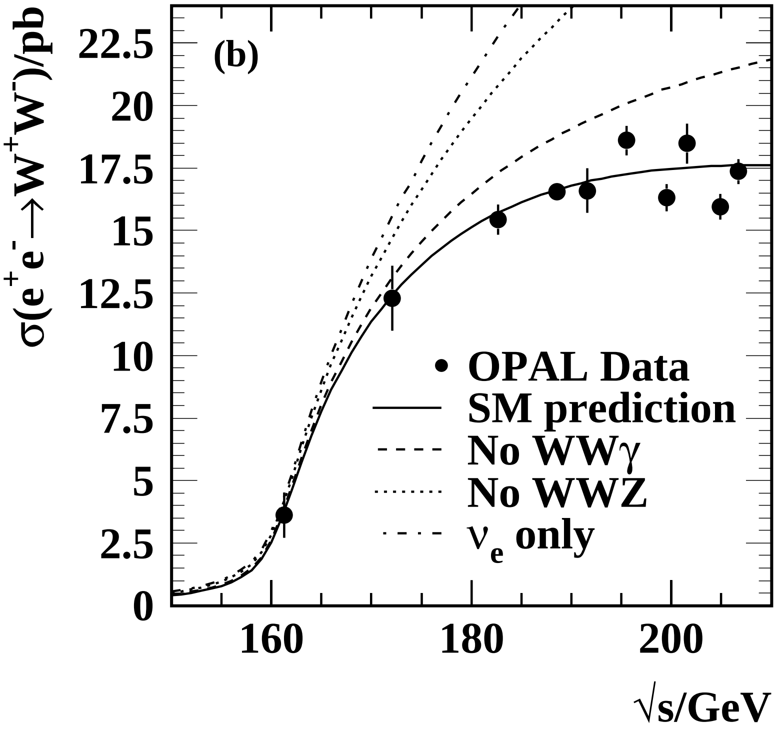

Figure 2.2: *The WW cross section (σ_{WW}) measured by the OPAL experiment at LEP 2. The theoretical predictions were obtained with the* GENTLE *[7] package and are shown for the SM prediction and the cases when some of the CC03 diagrams are removed.*

---

[3] Unitarity is the requirement that a probability cannot exceed one.

On-shell Production

To facilitate analytical calculations of the total $\mathrm{W^+W^-}$ production cross section in the Born approximation (lowest order), the $\mathrm{W^\pm}$ bosons may be treated as stable particles (ie on-shell[4] and with zero width). This approach acts as a foundation for the off-shell case.

In this scenario, the total production cross section near threshold may be written as [9]:

$$\sigma_{\mathrm{WW}} \approx \frac{\pi\alpha^2}{s}\,\frac{1}{4\sin^4\theta_W}\,4\beta + \mathcal{O}(\beta^3) \tag{2.12}$$

where α is the electromagnetic coupling and θ_W is the weak mixing angle. In this region ($\beta \ll 1$) the W bosons are produced virtually at rest and the t-channel neutrino exchange diagram is dominant ($\sim \beta$). The s-channel and s-t interference contributions are proportional to β^3 and hence the shape of the total cross section is completely governed by the linear rise in β, ie from kinematics alone. This is important for W mass determination.

Off-shell Production

The above description with stable on-shell W bosons provides a reasonable approximation. However, in a proper treatment the W bosons need to be considered as Breit Wigner resonances with finite width to avoid singularities in the phase space. This means that W pair production cannot be separated from the subsequent decays of the $\mathrm{W^\pm}$ and hence the whole process:

$$e^+e^- \to \mathrm{W^+W^-} \to f_1\bar{f}_2f_3\bar{f}_4 \tag{2.13}$$

needs to be taken into account (see figure 2.1 for lowest order CC03 diagrams). The leading order cross section for off-shell $\mathrm{W^+W^-}$ production can be written as [10]:

$$\sigma(s) = \int_0^s \mathrm{d}s_1 \int_0^{\left(\sqrt{s}-\sqrt{s_1}\right)^2} \mathrm{d}s_2\,\rho(s_1)\,\rho(s_2)\,\sigma_0(s,s_1,s_2) \tag{2.14}$$

where $\sigma_0(s,s_1,s_2)$ is the total cross section for e^+e^- annihilations into two virtual W bosons with invariant masses squared s_1 and s_2, s is the total energy squared of the initial e^+e^- and the weight factor $\rho(s)$ comes from the W propagator:

$$\rho(s) = \frac{1}{\pi}\,\frac{\Gamma_{\mathrm{W}}}{\mathrm{M_W}}\,\frac{s}{(s-\mathrm{M_W^2}) + s^2\,\Gamma_{\mathrm{W}}^2/\mathrm{M_W^2}} \tag{2.15}$$

---

[4] On-shell particles obey the relativistic energy equation: $m^2 = E^2 - p^2$. Particles which do not obey this equality are known as virtual and cannot propagate in free space.

The W width depends on the centre of mass energy:

$$\Gamma_{\mathrm{W}}(s) = \frac{s}{M_{\mathrm{W}}^2}\,\Gamma_{\mathrm{W}}(M_{\mathrm{W}}^2) \tag{2.16}$$

The finite W width destroys the gauge invariance of the CC03 diagrams. Experimentally, the finite W width has the largest effect on the cross section at threshold where the initial steep rise at $\sqrt{s} \approx 2M_{\mathrm{W}}$ is smeared out. Finite width effects also influence the angular distributions (see section 7.3) and so could fake non-standard TGCs if not taken into consideration.

Radiative Corrections

In addition to finite W width, the main corrections to the W pair production cross section arise from radiative effects. These radiative corrections cannot be separated into electromagnetic and weak contributions in a gauge invariant way since W pair production involves the charged current at lowest order. Radiative corrections to $\mathcal{O}(\alpha)$ can be divided into virtual, soft-photonic and hard-photonic contributions. The virtual corrections contain infrared divergences from the virtual photons exchanged between the charged particles but are cancelled when the external photon contributions are added.

The most important correction for both the W classification and TGC analyses, arises from QED initial state radiation (ISR), whereby one of the incoming electrons emits a (hard) photon before interaction. This reduces the available centre of mass energy and consequently affects the s-dependent forward peak of the W pair production cross section. At threshold, the initial steep rise of the cross section is smeared out, but the effects are more pronounced at higher energies where the total cross section is decreased. Furthermore, the recoil of the WW system against the emitted photon affects the W angular distribution [9], which results in more negative TGC values. In the WW classification analysis, the position of the acollinearity dependent momentum cuts (described in chapter 6) will be changed.

In addition to hard photon radiation, sizeable logarithmically divergent corrections $\sim \ln(s/m_e^2)$ due to collinear emission of external photons must also be included. It is important that all ISR effects are well modelled in the Monte Carlo. This is rather a complicated procedure, but suffice to say that for the main EXCALIBUR generator (used for the TGC analysis and discussed in section 5.3), only ISR photons collinear with the z axis are generated with at most one photon in either direction.

The final state radiation (FSR) occurs when one of the particles in the final state emits a photon which can often be observed directly in the detector. From an experimental point of view, high transverse momentum photons from ISR can be extremely difficult to separate from FSR photons when close to other particles. Theoretically, FSR cannot be treated as independent in a completely gauge-invariant description from ISR although this is a reasonable approximation in the soft or collinear limit.

Loop corrections also need to be considered for the calculations but are suppressed by the additional vertices.

Other Corrections

At threshold one of the most important corrections is the Coulomb singularity which arises because of the long range electromagnetic interaction between the almost stationary W bosons. However, at the centre of mass energies considered for the two analysis described in this thesis, the effects are negligible.

QCD corrections (for the semi-leptonic channel) can lead to additional jets in the final state from hard gluon emission, which may bias the results (for example if the wrong jet angle is measured and also the kinematic fits could be affected). To account for the QCD corrections to the W hadronic decay width, a so-called ‘naive’ correction factor is added to the appropriate vertices:

$$\Gamma(W \to q\bar{q}) \to \Gamma(W \to q\bar{q}) \left(1 + \frac{\alpha_s}{\pi}\right) \tag{2.17}$$

which modifies the cross section and branching ratios. It is called a ‘naive’ correction factor because strictly it only applies to the ideal case of W pair production diagrams when no cuts have been applied and its effect cannot be rigorously assessed. However, it is expected that QCD effects will enter at the level of $\mathcal{O}(\alpha_s)$.

Final state interactions (FSI), for example colour reconnection and Bose Einstein effects, are important for the fully hadronic final state (WW $\to q\bar{q}q\bar{q}$) but not for either the semi-leptonic (WW $\to l\nu q\bar{q}$) or fully leptonic (WW $\to l\nu l\bar{\nu}$) events used in the analyses described in this thesis.

2.2.2 Four Fermion Processes

In addition to the W pair production processes in figure 2.1, there are contributions from other processes which have the same initial and final states but proceed through different intermediate states.

The number of Feynman diagrams for the process $e^+e^- \to 4f$ depends on the final state but in general all possible four fermion processes can be classified as either neutral current (NC) or charged current (CC). As the name suggests, CC processes involve the propagation of at least one (singly resonant) or two (doubly resonant) virtual $W^\pm$ bosons with final states consisting of up (anti-up) and anti-down (down) fermion pairs. Table 2.3 summarizes the number of CC processes for a given final state.

	$\bar{d}u$	$\bar{s}c$	$e^+\nu_e$	$\mu^+\nu_\mu$	$\tau^+\nu_\tau$
$d\bar{u}$	43	11	20	10	10
$e^-\bar{\nu}_e$	20	20	56	18	18
$\mu^-\bar{\nu}_\mu$	10	10	18	19	9

Table 2.3: *Number of Feynman diagrams contributing to the charged current (CC) production of four fermion states [8].*

NC processes are mediated with the exchange of two neutral vector bosons (see for example the Zee and Z pair production diagrams in figures 5.2j-l). These background processes have final states of the form:

$$(f_i\ \bar{f}_i) + (f_j\ \bar{f}_j) \tag{2.18}$$

where f may be up or down type and i,j are the generation indices. Clearly there is some overlap with the CC processes for certain final states (eg $e^+e^-\nu_e\bar{\nu}_e$). In total there are 452 diagrams that make up the full four fermion set and the largest number of diagrams occurs for the process $e^+e^-e^+e^-$ which has 144 diagrams.

In general it is necessary to include all the Feynman diagrams with a given final state in order to maintain gauge invariance. The doubly resonant CC03 process (figure 2.1) are based on a subset of diagrams which are gauge dependent and usually defined in the 't Hooft-Feynman gauge. In order to maintain gauge invariance it is sufficient to add only the singly resonant Z^0/γ exchange diagrams (for example figure 2.3) [9].

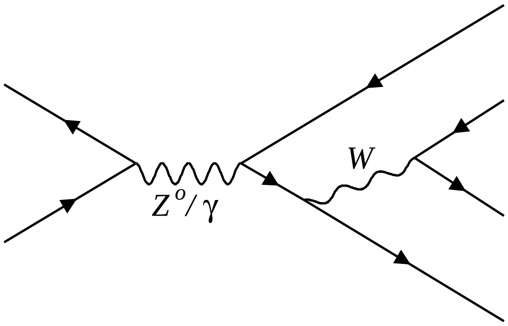

Figure 2.3: *Example of singly resonant diagram.*

All possible classes of four fermion diagrams are shown in figure 2.4. The relevant diagrams for W pair production are shown by the Abelian *conversion* and non-Abelian *annihilation* diagrams. *Multiperipheral* diagrams have the largest cross section but generally have final states that can be separated from the CC03 processes.

2.2.3 Total Cross Section

Experimentally it is extremely difficult to distinguish different processes with the same final state. Hence to extract W pair production cross section (σ_{WW}), it is usual to measure the total four fermion cross section (σ_{Tot}) and subtract the expected contribution from four fermion background processes. The cross section for $e^+e^- \to 4f$ (+γ, g, $\ldots$) may be written schematically as [8]:

$$\begin{aligned} \sigma_{\mathrm{Tot}} &= \sigma_{\mathrm{WW}} + \sigma_{\mathrm{bkg}} \\ \sigma_{\mathrm{WW}} &= \sigma_0^{\mathrm{WW}}\ (1 + \delta_{\mathrm{EW}} + \delta_{\mathrm{QCD}}) \end{aligned} \qquad (2.19)$$

where:

$\boldsymbol{\sigma_0^{\mathrm{WW}}}$ is the Born level contribution from the three CC03 leading order diagrams for W pair production involving t-channel ν exchange and s-channel Z^0/γ exchange, (figure 2.1) calculated using off shell W propagators.

Abelian Classes

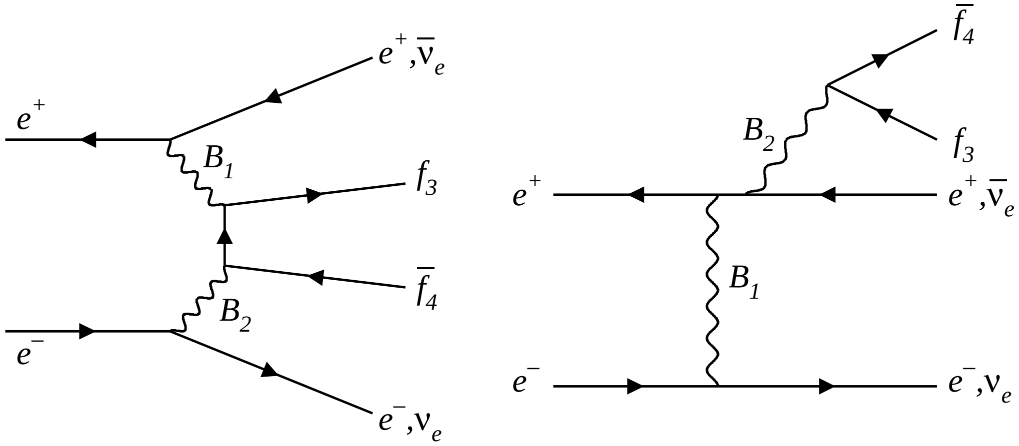

Multiperipheral *Bremsstrahlung*

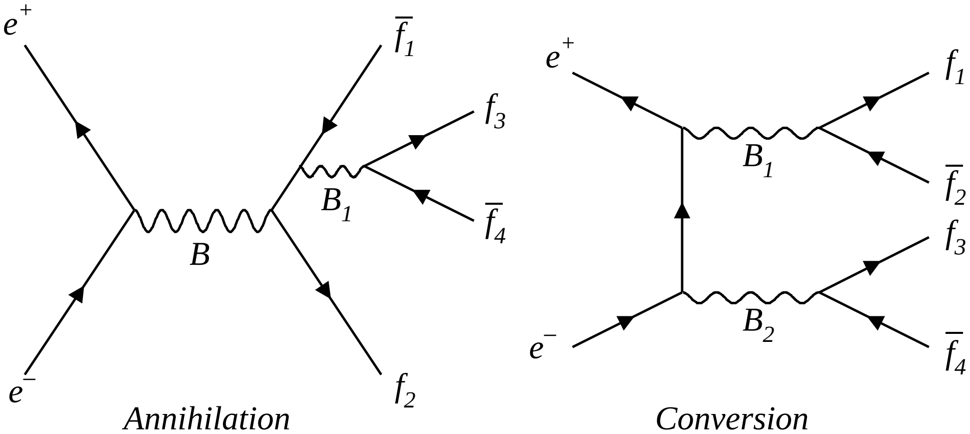

Annihilation *Conversion*

Nonabelian Classes

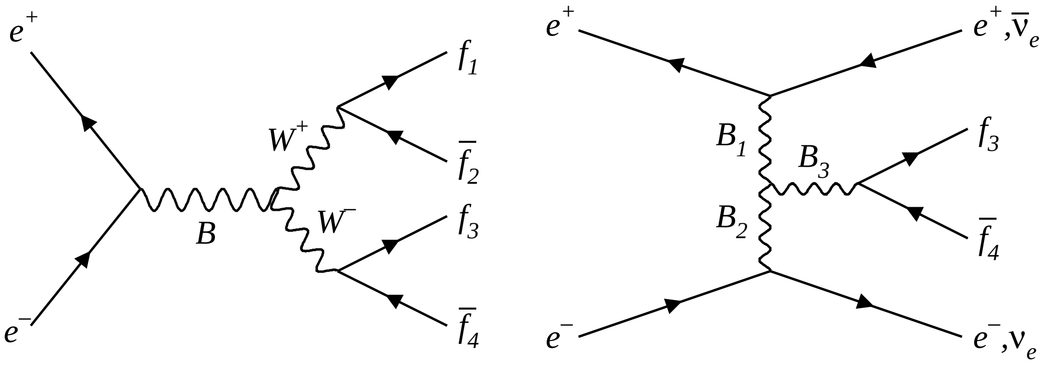

Annihilation *Fusion*

Figure 2.4: *Feynman diagrams of the CC03 and background four fermion processes [8]. Only the non-Abelian classes involve couplings between three gauge bosons.* $B = Z^0\ \gamma$; B_1,B_2,B_3 = Z^0,γ, W^+W^-.

δ_{EW} represents the higher order electroweak corrections, including loop corrections, real photon emission etc. described above.

δ_{QCD} are the higher order QCD corrections to W^+W^- final states containing $q\bar{q}$ pairs described above.

σ_{bkg} represents the four fermion background contributions.

2.2.4 W decays

W bosons can decay either hadronically or leptonically with branching fractions that can be calculated from electroweak theory. The branching ratio (BR) of a given state is defined as the partial decay width divided by the total width. In the SM, the W boson couples universally to fermion pairs (figure 2.5) and so measurement of the leptonic branching ratios provide a test of lepton universality (ie equal coupling of the W^+W^- to $e\nu$, $\mu\nu$, and $\tau\nu$ final states). For the quarks, since the mass eigenstates are not the same as the weak eigenstates, the W could have non-diagonal couplings. However, since the CKM matrix is unitary ($V^\dagger_{CKM}V_{CKM} = 1$), the overall coupling of the W bosons to leptons and quarks (of each colour) is the same. The partial decay rates of the W into quark pairs measure the elements of the CKM matrix directly. The total rate will be independent of V_{CKM} provided quark masses are neglected.

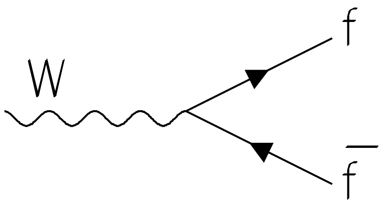

Figure 2.5: *Basic vertex for W decay to two fermions. f≡ e, μ, τ, ν_e, ν_μ, ν_τ or q.*

The partial decay width of the W boson into (massless) leptons and quarks can be expressed in terms of the W mass (M_W) and Fermi coupling constant (G_F):

$$\begin{aligned}\Gamma(W \to l\nu) &= \frac{G_F M_W^3}{6\sqrt{2}\pi} \\ \Gamma(W \to q\bar{q}) &= \frac{G_F M_W^3}{6\sqrt{2}\pi}\, 3 \,|V_{ij}|^2 \left[1 + \frac{\alpha_s}{\pi} + \mathcal{O}\left(\frac{\alpha_s^2}{\pi^2}\right)\right]\end{aligned} \tag{2.20}$$

The factor 3 in the lower equation corresponds to the number of quark colours and $| V_{ij} |$ is the CKM matrix which describes the flavour mixing between quarks. The total width is sum of the partial widths:

$$\Gamma_{\mathrm{W}} = \frac{G_F M_{\mathrm{W}}^3}{2\sqrt{2}\pi} \left[3 + 2\,\frac{\alpha_s}{\pi} + \mathcal{O}\left(\frac{\alpha_s^2}{\pi^2}\right)\right] \tag{2.21}$$

The decay rate of the W boson is related to the transition probability and therefore proportional to the matrix element squared ($|\mathcal{M}|^2$), where $\mathcal{M}$ is the transition amplitude for one in-going particle (W) and two out going particles ($f\bar{f}$). The theoretically predicted branching fractions are listed in table 2.4 [8].

Process	Branching Ratio
Γ(W → $e\nu_e$)	10.83
Γ(W → $\mu\nu_\mu$)	10.83
Γ(W → $\tau\nu_\tau$)	10.82
Γ(W → leptons)	32.49
Γ(W → hadrons)	67.51

Table 2.4: *Theoretically predicted W→ $f\bar{f}$ branching fractions [8].*

It broke my heart
when they took LEP apart

ULOSEHIGGS (Played by Patrick Janot),
Christmas Play of CERN Theory Division by John Ellis, (Dec. 2000)

Chapter 3

The OPAL detector and the LEP collider

The OPAL (Omni-Purpose Apparatus at LEP) detector was one of four large particle detectors situated on the LEP (Large Electron Positron) collider for the study of elementary particle physics. The experiment began operation in 1989, initially studying e^+e^- interactions at the Z^0 resonance peak. After a short period of data taking in 1995 with beam energies of around 68 GeV (the so-called LEP 1.5 phase of operation), LEP entered its second phase of operation (LEP 2) in 1996, with centre of mass energies above the W^+W^- threshold ($E_{cm} > 161$ GeV). Since then further upgrades to the LEP accelerator have allowed the beam energy to increase year by year, up to a maximum of 104.40 GeV which was achieved during LEP's final year of operation in 2000. During the LEP 2 phase it was desirable to run at the highest possible energy, not only to increase the possibility of discovering 'new' particles, but also because the W pair cross section increases with energy. This chapter presents an over-view of the LEP collider and OPAL detector. More details can be found in [11] and [12] respectively.

3.1 The LEP Collider

The LEP collider was a 26.7 km circular e^+e^- storage ring, straddling the Swiss-Franco border at the foot of the Jura mountains, approximately 100m underground. It was designed to accelerate, store and then collide electron and positron bunches[1] in opposite directions. The beam pipe consisted of a highly evacuated beryllium tube ($< 3 \times 10^{-9}$ torr)

---

[1] A typical bunch contains $\sim 10^{11}$ particles. For most of LEP operation 4 bunches of electrons and 4 bunches of positrons were used. These circulated 11 250 times per second in opposite directions in the LEP ring.

to reduce beam gas interactions. It was arranged in eight long straight sections (to reduce synchrotron radiation losses) which were joined together in roughly circular shape. The accelerating sections consisted of a mixture of copper and superconducting radio-frequency (RF) cavities (the latter were installed during the LEP 2 upgrades). Over 3300 dipole bending magnets were used to steer the beams around the ring and nearly 2000 focusing magnets (quadruple, sextupole and octupole) were used to bring the beams to a tight focus in the straight sections just before collision in each of the four LEP detectors: ALEPH [13], DELPHI [14], L3 [15] and OPAL [12]. For geological reasons the plane of the LEP ring was inclined at a 1.42% slope.

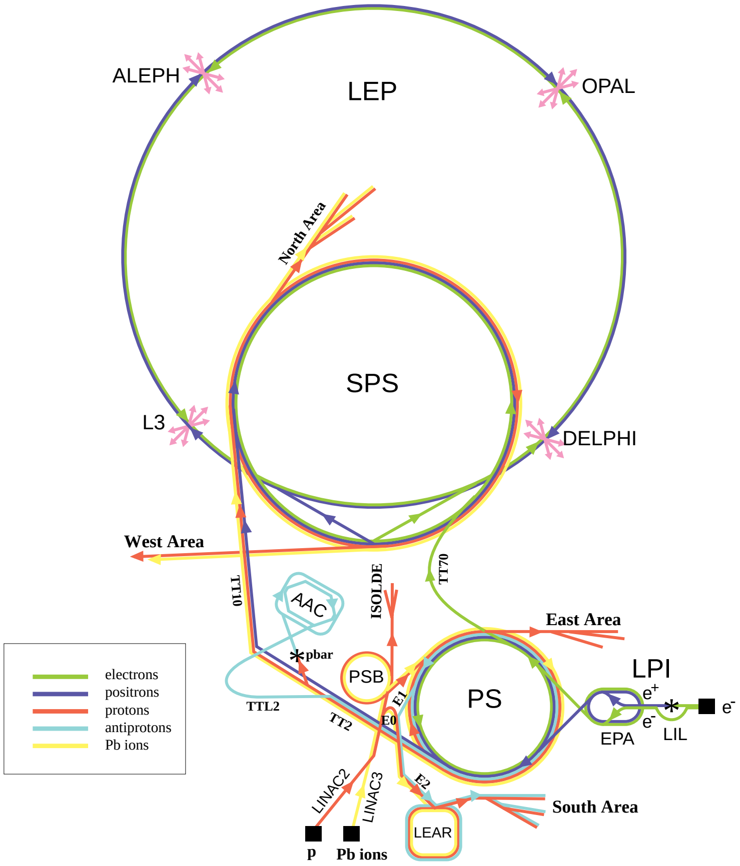

LEP: Large Electron Positron collider
SPS: Super Proton Synchrotron
AAC: Antiproton Accumulator Complex
ISOLDE: Isotope Separator OnLine DEvice
PSB: Proton Synchrotron Booster
PS: Proton Synchrotron
LPI: Lep Pre-Injector
EPA: Electron Positron Accumulator
LIL: Lep Injector Linac
LINAC: LINear ACcelerator
LEAR: Low Energy Antiproton Ring

Figure 3.1: *The CERN accelerator complex illustrating the various stages through which particles were accelerated until eventual injection into the LEP ring.*

Injection of particles into LEP made use of the previously existing proton accelerator complex (figure 3.1). Electrons were produced by thermionic emission and accelerated in the LEP Injector Linac (LIL) to 200 MeV. Positrons were made from bremsstrahlung photons emitted when some of these electrons were rapidly decelerated in a tungsten target. The positrons were separated by a magnetic field, and then both the electrons and positrons were accelerated to 600 MeV before being stored in the Electron Positron Accumulator (EPA). When sufficient particles had been accumulated, they were transfered to the 200m diameter Proton Synchrotron (PS) and accelerated to 3.5 GeV before being injected into the 2.2 km circumference Super Proton Synchrotron (SPS) and accelerated further to 22 GeV. Finally they were injected into the LEP ring and accelerated to maximum energy. Beams could circulate in LEP for up to 12 hours owing to the high vacuum.

3.2 The OPAL Detector

The OPAL detector was a general multipurpose purpose detector, situated in a large underground chamber ($\sim$100m underground) on the LEP ring. It was designed to efficiently reconstruct and identify all types of particle processes arising from e^+e^- interactions and provide accurate measurements of charged tracks and electromagnetic energy. It was approximately 12m in length, 10m in diameter and weighed $\sim$3000 tons. Figure 3.2 illustrates the general layout of the detector and figure 3.3 shows a quadrant of the detector in cross section, parallel and perpendicular to the beam axis.

The detector consisted of a series of cylindrical, concentric subdetectors or ‘components’ arranged around the beam-pipe with the interaction point at the centre and a set of endcap subdetectors covering the ends of the cylinders. This provided nearly 4π of solid angle coverage. Each of the subdetector components were known within OPAL by a two letter acronym (for example: EE for the electromagnetic calorimeter endcap). The principal detector components were:

- a large volume *central tracking detector* (to measure the positions and momenta of charged particles)
- an *electromagnetic calorimeter* (to identify and measure energy deposited by electrons and photons)

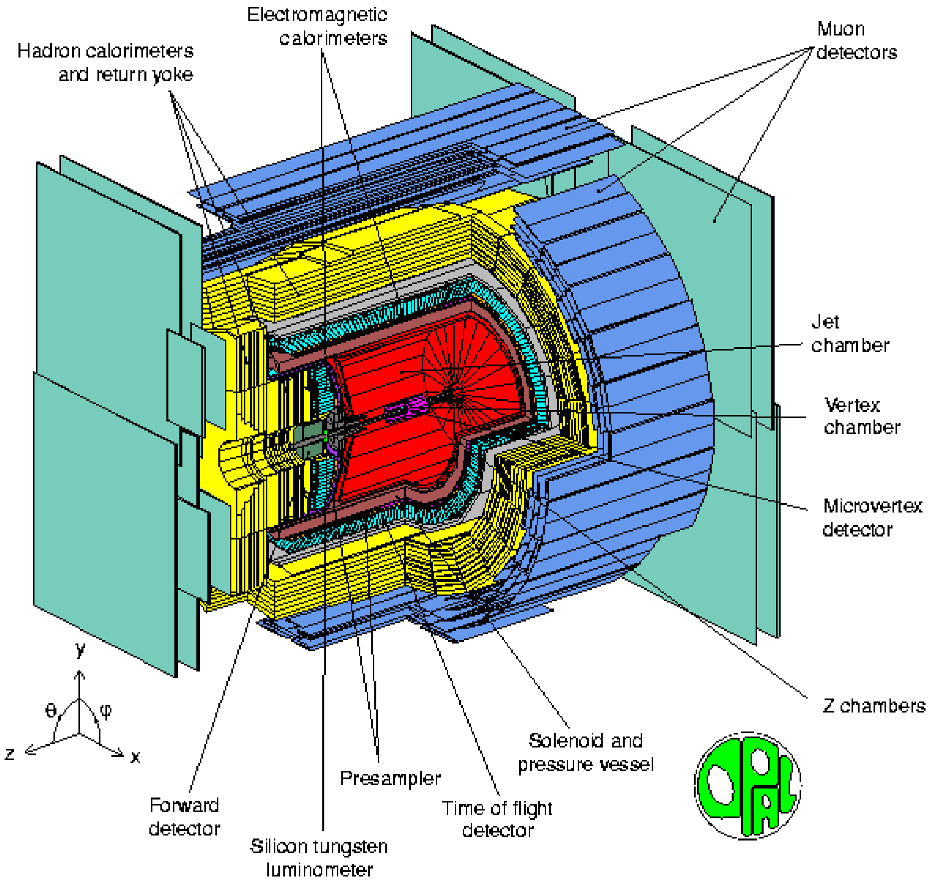

Figure 3.2: *Schematic diagram of the OPAL detector at LEP.*

- a *hadron calorimeter* (for measuring the energy deposited by neutral hadronic particles and muon identification)
- outer *muon chambers* (for penetrating muon identification)
- *forward detectors* (to detect particles close to the beam axis and measure the luminosity)
- a *solenoid coil* surrounding the tracking detectors (to provide a uniform 0.435 T magnetic field)

The central detector and electromagnetic calorimeters were the most important parts of the detector for the TGC and WW $\rightarrow l\nu l\bar{\nu}$ classification projects, since they enabled accurate measurements of lepton track position, momenta and energy. The muon chambers provided information about muon decays and the hadronic calorimeters provided additional information about quark jets from W decays. The endcap detectors (particularly those in the forward region), were crucial to the investigation of MIP plug performance.

3.2.1 OPAL co-ordinate system

The OPAL co-ordinate system is indicated in figure 3.2. It is a right-handed Cartesian system with its origin at the nominal interaction point. The x axis points towards the centre of LEP and the y axis is slightly away from the vertical (since the LEP beam at the OPAL interaction region was inclined at 13.9 mrad to the horizontal). The z axis points along the electron beam direction in LEP (ie anti-clockwise when viewed from above). The polar angle θ is measured from the positive z axis and the azimuthal angle ϕ is measured clockwise from the x axis looking along the positive z axis.

3.2.2 The Central Tracking Detectors

OPAL's central tracking system consisted of four subdetectors. In order of increasing radius these were a silicon microvertex detector and three drift chamber devices: a vertex detector, a jet chamber and the Z-chambers. The drift chambers were enclosed inside a pressure vessel (as shown in figure 3.3). The drift chambers all operated with the same gas mixture of 88.2% argon, 9.8% methane and 2.0% isobutane at 4 bar. The drift chambers measured the direction and curvature of charged particles in the magnetic field from which the particles' momenta and charge could be determined. All three drift chambers gave 3 dimensional readout, but the vertex and jet chambers gave accurate measurements of the track co-ordinates in the plane perpendicular to the beam axis (the r-ϕ plane) whilst the Z-chambers gave accurate measurements of the perpendicular z co-ordinates of the tracks.

Silicon Microvertex Detector (SI)

The silicon microvertex detector (SI) was the innermost subdetector. It was originally installed in 1991 [16], and upgraded in 1993 [17] and 1995 [18] to increase its geometrical acceptance and permit 3-d track reconstruction. The detector provided high precision measurements of charged particle trajectories close to the interaction point. This enabled the

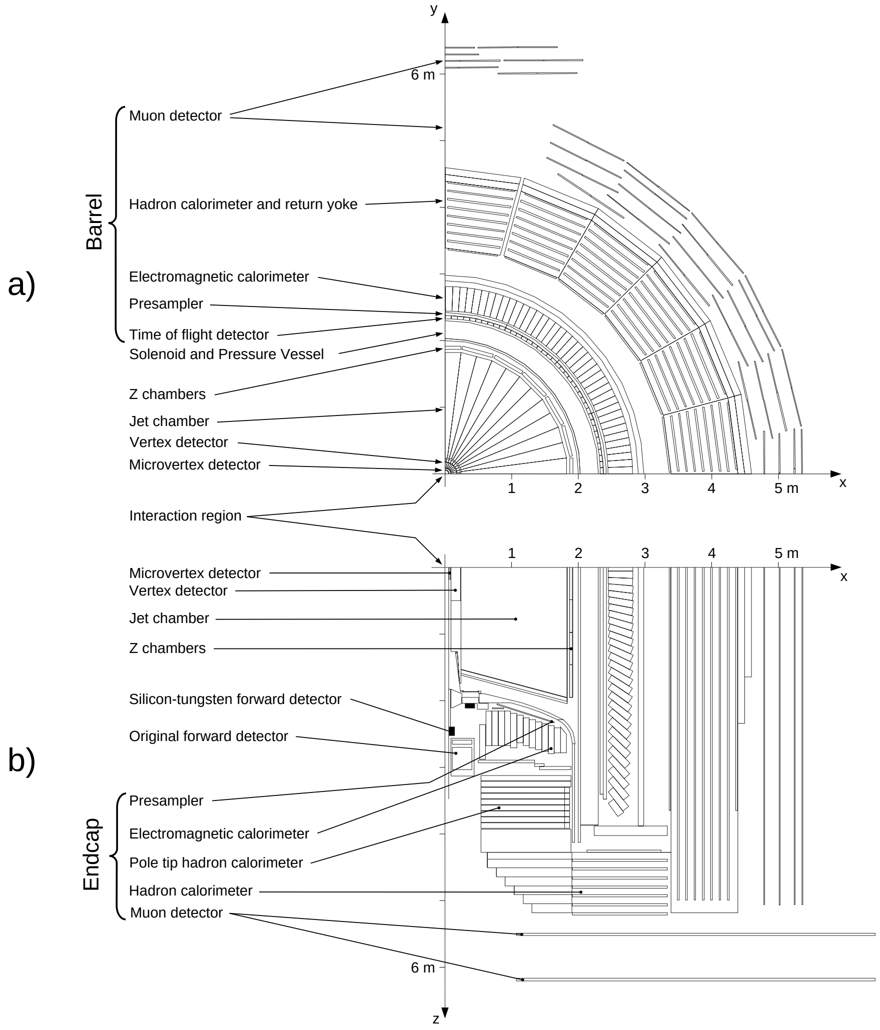

Figure 3.3: *Cross section of a quadrant of the detector a) parallel and b) perpendicular to the LEP beam axis.*

identification of short-lived particles (for example B hadrons and τ leptons) with typical decay lengths down to a few tenths of a millimetre.

Silicon detectors are essentially reversed-biased diodes which behave like solid ionization chambers. A charged particle traversing the detector created ionization, and the charges thus produced drifted towards the electrodes in the presence of the strong electric field. Following amplification, the signals were grouped together and read out. SI consisted of two concentric layers of single-sided silicon microstrips with radii 61 mm and 75 mm, sandwiched between the beam pipe (outer radius 56.5 mm) and the wire chamber pressure vessel (with an inner radius of 80 mm). The outer and inner layers had 15 and 12 ladders respectively and were tilted to avoid gaps in ϕ. Each ladder was made up of 5 pairs of silicon wafers which were 6 cm long and 3 cm wide. A pair of wafers consisted of a one single-sided wafer with readout strips every 50 μm running parallel to the beam axis and a one single-sided wafer with readout every 100 μm perpendicular to the beam axis. It had azimuthal angular coverage of 97% and a polar angle acceptance for tracks with $|\cos\theta| < 0.89$.

Central Vertex Chamber (CV)

The vertex detector [19] was a 1m long, high resolution cylindrical drift chamber surrounding SI with an inner radius of 80 mm and outer radius of 235 mm. It was similar in design to a small jet chamber and provided precise measurements of track positions with good multi-hit detection to resolve individual particles within jets. When a charged particle traversed through the chamber, it caused ionization in the gas. The liberated electrons drifted towards the positively charged anodes. Near the wires, the strong electric field accelerated the electrons thus caused further ionization of the gas atoms. This ‘avalanche’ effect induced a measurable pulse on the sense wires.

CV was radially segmented into two layers of 36 sectors each. The inner layer consisted of 36 axial cells each containing 12 wires running parallel to the beam direction and spaced 5.3 mm apart. From drift time measurements these yielded a precise r-ϕ resolution of 55 μm. A fast but coarse z position measurement could be obtained by measuring the time difference between the signals from the two ends of the anode wire. This was used by the OPAL track trigger and offline in pattern recognition. The outer layer consisted of 36 stereo cells each containing 6 wires spaced 5 mm apart and inclined at 4^0 to the beam axis. By combining the axial and stereo drift time information, the z co-ordinate could be measured to around 700 μm. The angular coverage of this detector corresponded to $\mid \cos\theta \mid < 0.92$ for both the axial and stereo wires.

Central Jet Chamber (CJ)

The jet chamber [20] was the largest tracking detector in OPAL. It measured approximately 4m in length and surrounded CV with inner and outer radii of 25 cm and 185 cm respectively. It provided nearly 4π solid angle coverage. Its main function was to accurately measure the track positions of charged particles as they traversed the detector in the magnetic field. The radius of track curvature was used to calculate a particle's momentum perpendicular to the field:

$$p_{\perp} = 0.3\mathrm{B}r \tag{3.1}$$

where B is the magnetic field in Tesla and r is the radius of curvature in metres. The direction of curvature determines a particle's charge (see equation A.2). Particle identification [21] was made by multiple sampling of the energy loss from ionization in the gas. The rate of energy loss (dE/dx) was determined from the sum of the measured charge on each sense wire and depended on the particle's mass, velocity and angle of trajectory.

The sensitive volume of the detector was divided into 24 sectors, each containing a plane with 159 anode wires running parallel to the z axis. The cathode wire planes formed boundaries between adjacent sectors. The anode wires were spaced 10 mm apart, interleaved with potential wires held at -2.38 kV. To resolve left-right ambiguities, the anode wires were alternately staggered by $\pm$100 μm either side of the plane defined by the potential wires. Measurement of drift time provided a r-ϕ spatial resolution of 100-350 μm depending on the drift distance from the wire. The z co-ordinate was determined from the the ratio of integrated charge measured at each end of a sense wire and had a resolution of $\sim$6 cm. Angular coverage extended up to $|\cos\theta| < 0.98$, although track reconstruction was optimal for the range $|\cos\theta| < 0.73$ when the full 159 hits per track could be measured.

The Z-Chambers (CZ)

As the name suggests, the Z-chambers [22] were designed to make precise measurements of particles' z co-ordinates as they left the jet chamber in the barrel region. The detector consisted of 24 drift chambers: 4m long, 50 cm wide and 59 mm thick. Each chamber was divided into eight 50×50 cm^2 cells. Each cell contained 6 sense wires which were spaced 4 mm apart. The wires ran perpendicular to the beam axis and were staggered to resolve left-right ambiguity. Depending on the drift distance to the wire, the spatial resolution in z was $\sim$100-300 μm. The chambers covered 94% of the azimuthal angle and had polar range from 44^o to 136^o.

3.2.3 The Magnet

The magnet consisted of a water-cooled aluminium solenoid coil and an iron yoke constructed from soft steel plates. It produced a uniform magnetic field of 0.435 T in the central volume from a current of $\sim$ 7000 A. The solenoid surrounded the central tracking chambers but unfortunately was positioned inside the electromagnetic calorimeter. It was wound from a single long unit (to reduce field distortions to within ±0.5%). The return yoke formed part of the hadronic calorimetry system.

3.2.4 Time-Of-Flight System (TE & TB)

Surrounding the solenoid were the barrel time-of-flight (T.O.F.) counters which were designed to measure particle flight times from the interaction point. The system consisted of 160 scintillation counters, 6.84m in length, forming a barrel with average radius 2.36m and covered the angular range $|\cos\theta| < 0.82$. For charged particles and photons with energies 0.6-2.5 GeV, the time resolution varied between 280 ps (at the centre of the detector) to 350 ps (at the detector ends). This fast response time meant that it was used to supply trigger information and helped reject certain background processes (for example cosmic rays). The time-of-flight endcap (TE), which were also known as the tile endcap detectors, are described in section 3.2.8.

3.2.5 The Electromagnetic Calorimeters

The electromagnetic calorimeter system was designed to measure the energies and positions of electrons, positrons and photons. It was a total absorption calorimeter which consisted of three large overlapping assemblies of lead glass blocks (the barrel and two endcap regions). It was mounted between the coil and return yoke of the magnet and covered 98% of the solid angle. Since the pressure vessel and magnetic coil constituted approximately 2 radiation lengths of material, particles used to start showering before they reached the lead glass. Presampling devices were therefore installed immediately in front of the lead glass in both the barrel and endcap regions, to measure particle position, improve the energy resolution of these showers and provide additional γ/π^o and electron/hadron discrimination.

The electromagnetic calorimeter system was complemented by the gamma catcher and the forward detector calorimeter (described in section 3.2.8).

The Electromagnetic Presamplers (PE & PB)

The barrel electromagnetic presampler (PB) [23] consisted of 16 chambers, situated between the T.O.F. system and the barrel lead glass calorimeter. Each chamber was 3 cm thick and contained two layers of streamer mode drift tubes with the anode wires running parallel to the z axis. The chambers were arranged in a cylinder of length 662.3 cm and radius 238.8 cm, and provided polar angle coverage $|\cos\theta| < 0.81$. The signals were readout from 1 cm cathode strips orientated at $\pm 45^o$ to the anode wires. These provided spatial resolution in r-ϕ of $\sim$5 mm.

The endcap presampler (PE) [24] consisted of 32 thin high gain multiwire chambers arranged in 16 sectors in the shape of an umbrella. It was located between the pressure vessel and the endcap calorimeter and covered the azimuthal angular range $0.83 < |\cos\theta| < 0.95$.

Barrel Electromagnetic Calorimeter (EB)

The barrel electromagnetic calorimeter [25] consisted of a cylindrical array of 9440 lead glass blocks. It was situated outside the magnetic coil at a radius of 245.5 cm and provided full azimuthal angular coverage and $|\cos\theta| < 0.82$. Each $\sim 10 \times 10$ cm^2 block was made from SF57 heavy glass with a depth of 24.6 radiation lengths (37 cm) to minimize shower leakage. The blocks were angled to point towards the interaction region (to minimize the probability of a particle traversing more than one block), but with a slight offset (to reduce the number of neutral particles escaping detection in the gaps between the blocks).

High energy ($>$100 MeV) electrons and positrons traversing the lead glass would predominantly lose energy by bremsstrahlung. High energy photons lost energy by pair creation. From these processes, cascade showers would develop. The number of secondary particles produced in these showers was proportional to the incident energy (typically several thousand particles at shower maximum for a 50 GeV incident electron [26]). Since these secondary particles were produced with velocities greater than the speed of light, they emitted Čerenkov radiation which was detected by 3 inch diameter, magnetic field tolerant photo-tubes mounted at the base of each block.

The overall intrinsic energy resolution of the calorimeter system in the barrel region was found to be: $\sigma_E/E = 0.2\% + 6.3\%/\sqrt{E}$, where E is the energy of the incoming particle measured in GeV. This figure was significantly degraded by the presence of material in front of the calorimeter, but 50% of the degradation could be recovered by using the presampler information.

Electromagnetic Endcap Calorimeter (EE)

The electromagnetic endcap calorimeter [27] consisted of 1132 lead glass blocks arranged in a dome-shaped array at each end of the detector. It was situated between the pressure vessel and the pole tip hadron calorimeter and covered the angular range: $0.81 <\mid \cos\theta \mid< 0.98$ and the full angle in azimuth. Unlike the barrel detector, the blocks were made from CEREN-25 lead glass (with typical depths of 22 radiation lengths) and aligned parallel to the beam axis (because of geometrical constraints), following the contours of the pressure vessel. Vacuum photo triodes (VPT's) replaced the photo-multiplier tubes because of the high magnetic field ($\sim$0.4 T) in the endcaps. For low energy ($<$10 GeV) particles, the energy and spatial resolutions were $\sigma_E/E = 5\%/\sqrt{E}$ and $\sim$8-14 mm respectively.

3.2.6 The Hadron Calorimeters

The hadron calorimeter [28] surrounded the electromagnetic calorimeter and was comprised of three parts: the barrel, two endcaps and two pole-tip detectors. It provided full solid angle coverage. Most hadronic showers were initiated in the lead glass of the electromagnetic calorimeter, and hence it was necessary to combine the signals from both detectors in order to determine the energy of hadronic particles.

Hadronic showers proceed in a similar manner to electromagnetic ones, but are more complex since they involve both electromagnetic and strong interactions. In general hadronic showers have lower multiplicity, are less compact and less precisely measured than electromagnetic ones (typical resolution $\sim$120%/$\sqrt{E}$ for a 10 GeV particle in OPAL). Since shower depth increases logarithmically with energy of the incident particle, hadronic calorimeters need to have greater depth than electromagnetic ones (of the same type) to contain the shower. In OPAL at least four additional interaction lengths of absorber were obtained from the iron return yoke of the magnet, which was positioned between the detector layers.

Hadron Barrel and Endcap Calorimeters (HB & HE)

The barrel hadron calorimeter consisted of 9 layers of PVC chambers, segmented with 8 layers of 10 cm thick iron slabs and covered the angular range $0.81 > |\cos\theta|$. The chambers were operated in limited streamer mode and filled with 75% isobutane and 25% argon gas mixture. The anode wires ran parallel to the beam direction, spaced 1 cm apart, and provided signals for monitoring purposes. Particle energy was measured by summing the induced charge collected on $\sim 500 \times 500$ mm^2 pads located on the outer surface of each chamber. The pads were grouped together to form towers pointing to the interaction region so that the signal sum over all pads in the same tower was proportional to the energy of the incident hadron producing the shower. On the inner surface, 0.4 cm wide aluminium strips positioned above the anode wires and running parallel to them, provided muon tracking information.

A doughnut-shaped endcap hadron calorimeter closed the barrel at each end. It was similar in design to the barrel and consisted of 8 layers of streamer tubes alternated with 7 plates of iron. It extended the angular coverage to $0.81 < |\cos\theta| < 0.91$.

Hadron Poletip Calorimeter (HP)

The poletip hadron calorimeter [29] complemented the barrel and endcaps by extending the angular coverage in the forward region to $|\cos\theta| < 0.99$. The detector consisted of 10 layers of high gain multiwire proportional chambers sandwiched between 10 layers of 8 cm thick iron absorber. Similar in configuration to the barrel and endcap calorimeters, the chambers were read out by means of strips (aligned radially) and cathode pads (arranged so that corresponding pads from each layer formed a tower pointing to the interaction region). The strips and pads were etched onto opposite inner edges of the chambers which were operated with a gas mixture of 55% CO_2 and 45% n-pentane.

3.2.7 The Muon Chambers

The muon chambers formed the outermost layer of the detector and extended over 93% of the solid angle with a detection efficiency for muons (with energies greater than 3 GeV) close to 100%. The detector was divided into barrel [30] and endcap [31] components, with gaps for support legs, the beam pipe and cable feedthrough to the inner subdetectors. The muon chambers were important in separating muons from the hadronic background. Most hadronic particles were absorbed in the 1.3m of iron equivalent material before the muon chambers, resulting in a μ/π mis-identification probability of less than 1% for an isolated 5 GeV pion.

Muon Barrel detector (MB)

The muon barrel detector consisted of 110 large area drift chambers filled with a 90% argon and 10% ethane gas mixture. As shown in figures 3.2 and 3.3, the chambers were arranged in layers with 44 chambers mounted either side of the barrel, 10 in the top and 12 in the bottom modules. Angular range for at least one layer was $|\cos\theta| < 0.72$, and $|\cos\theta| < 0.69$ for four layer coverage. The chambers were 1.2m wide, 9 cm deep and varied in length between 6.0m and 10.4m to allow room for the magnet supports. Each chamber was split into two adjacent drift cells, each containing an anode sense wire running the full length of the chamber, parallel to the z axis. A rough estimate of the z position was made by comparing the difference in time and pulse height of signals arriving at both ends of the anode wire. A more accurate determination of the z co-ordinate ($\sim$2mm) was obtained from induced signals on “diamond shaped” cathode pads located opposite the anode wire. The r-ϕ co-ordinate was measured from the drift time with a resolution of $\sim$1.5 mm. The maximum drift time was 8 μs and the drift velocity was around 38 mm/μs.

Muon Endcap detector (ME)

The muon endcap detector consisted of eight 6×6 m^2 quadrant chambers and four 3×2.5 m^2 patch chambers located either end of the detector in a plane perpendicular to the beam direction. The patch chambers were situated above and below the beam pipe, slightly overlapping the quadrant chambers, but with gaps for the magnet supplies, shielding and inner subdetector cables. Each chamber consisted of two layers of limited streamer tubes: one layer with sense wires running vertically and the other horizontally. Aluminium cathode strips were positioned each side of the plane of tubes, running parallel and perpendicular to the wires. Spatial resolutions of ~1mm and ~3mm were obtained from the perpendicular and parallel strips respectively. The chambers were operated with a gas mixture of 25% argon and 75% isobutane. Angular acceptance covered the range $\sim 0.67 <\mid \cos\theta \mid <\sim 0.985$.

3.2.8 Low Angle Subdetectors

The low angle subdetectors were situated close the beampipe and further out from the interaction region than the tracking chambers. The main purpose of these detectors was to determine the beam luminosity by measuring the rate of forward “Bhabha” scattering events. The integrated luminosity $\mathcal{L}$ for a particular process $ab \to cd$ with cross section $\sigma_{ab\to cd}$ is given by:

$$\mathcal{L} = N_{ab\to cd}/\sigma_{ab\to cd} \tag{3.2}$$

where $N_{ab\to cd}$ is the number of observed events. At small angles the t-channel QED Bhabha scattering process dominates the $e^+e^- \to e^+e^-$ cross-section and is proportional to $1/\theta^3$, where θ is the scattering angle. By counting the number of Bhabha events in the known acceptance of the forward region of the detector and precisely measuring the polar angles of the scattered particles, the luminosity could be determined.

These detectors were also used to tag $\gamma\gamma$ events (and thus act as a veto for background events in some search analyses) and to supply trigger information. The forward subdetectors were used extensively in the selection of events for the MIP plug analysis (described in chapter 4). Figure 4.5 illustrates the relative position of some of these low angle detectors and their polar angle coverage.

The Forward Detector (FD)

The forward detector [32] consisted of four separate subdetectors:

- The *forward calorimeter* consisted of 35 layers of lead-scintillator sandwich providing a total depth of 24 radiation lengths. The first 4 X_0 acted as a presampler. The main calorimeter had an energy resolution of $\sigma_{\mathrm{E}}/\mathrm{E} = 17\%/\sqrt{\mathrm{E}}$ (where E is in GeV) and position resolutions of 2 mm radially and 1.5^o (or less) azimuthally.

- The *tube chambers* consisted of three layers of proportional tubes located between the presampler and main forward calorimeter. They could measure shower positions to within ± 3mm.

- The *far forward monitor* counters were small lead-scintillator calorimeters of thickness 20 radiation lengths. They were mounted either side of the beampipe, approximately 7.85m from the interaction region. Their primary purpose was to detect scattered electrons that were deflected outwards by the LEP quadrupole focusing magnets in the range 5 to 10 mrad.

- The *gamma catcher (GC)* was a small non-containing electromagnetic calorimeter. It consisted of a ring of eight lead-scintillator sandwich modules with a radiation length of $7X_o$. It was designed to complement the lead-glass calorimeter and filled the acceptance gap between the inner edge of the endcaps and the outer edge of the forward detectors ($143 < \theta < 193$ mrads). Electrons or photons with energy > 2 GeV were detected with coarse ϕ resolution from each of the eight segments.

  During 1998 data taking, a number of GC sectors went bad, particularly in the right endcap. Rather than risk damage to other subdetector components by opening up the detector and repairing the GC during the annual shutdown, it was decided to use MIP plug information as a replacement for the GC.

The forward detectors covered the angular range $47 < \theta < 120$ mrad. This region had very clean acceptance since the only obstructions came from the beam pipe and 2mm of aluminium in the central detector pressure vessel.

The Silicon Tungsten Luminosity Monitor (SW)

The silicon tungsten detectors [33] were installed in OPAL in 1993 to improve the beam luminosity measurement by detecting low angle Bhabha scattering events. There were two sampling calorimeters situated approximately 2.4m from the interaction point at each end of the detector, covering the angular range between 25 and 59 mrad. Each calorimeter was segmented into 19 layers of silicon interleaved with 18 tungsten slabs providing spatial resolution of 220μm and energy resolution of $\sim \sigma_{\mathrm{E}}/\mathrm{E} = 24\%/\sqrt{\mathrm{E}}$ (where E is in GeV).

The Tile Endcap (TE)

The first part of the tile endcap (or time-of-flight endcap) detector [34] was installed in 1996 to precisely determine the time of a collision and improve trigger information in the forward region. The first part of the TE system consisted of a single layer of 120 10mm thick scintillator tiles arranged in the form of a truncated cone. They were located at each end of the detector, between the presampler and EE and covered the angular range $82 < |\cos\theta| < 0.95$.

The second part of the TE system, the "MIP Plugs" were installed in 1997. They were made from the organic scintillator BC408 (refractive index n=1.58) with embedded wavelength shifting optical fibres (WLS). The signals were read out by coupling the emerging light to clear fibres via precision optical connectors. The fibres conducted the light away from the high magnetic field environment of the detector to the photomultipliers (PMTs). The MIP plugs are discussed in more detail in chapter 4.

3.2.9 The OPAL Trigger System

When LEP was operating in 4 $\times$ 4 bunch mode, the electron and positron beams crossed every 22 μs at a rate of 45 kHz. With a detector readout time of 20 ms, it clearly would have been impossible to fully read out all the detector subcomponents following each beam crossing. Instead the trigger system [35] was designed to reduce the rate down to a level manageable by the data acquisition system ($\sim$10 Hz at LEP II). Its purpose was to reject recording of background processes (for example cosmic rays, beam gas interactions) and detector noise signals whilst maintaining a high efficiency for 'interesting' physics processes.

Following each beam crossing, independent trigger signals from the various subdetectors were sent to the "central trigger logic" processor. This combined the digital signals and formed the overall trigger decision. There were two complementary categories of trigger signals: 'stand-alone' signals (for example, track multiplicity counts and total energy) which had relatively high thresholds from a single subdetector, and lower threshold signals which permitted θ-ϕ spatial coincidences between subdetectors. In 1998, the MIP plug detector became part of the OPAL trigger system. It provided trigger signals for two photon physics processes and missing energy channel Higgs searches, based on coincidence hits in the same ϕ sector between layers 4A and 4B or 5A and 5B.

3.2.10 The Data Acquisition System (DAQ)

Following a positive decision by the trigger, the data from each subdetector were read out and sent to individual local system crates (LSC). The information was then reformatted to reduce its size and sent to the event builder (EVB) for assembly. This had to be done as quickly as possible, since no further events could be selected during this 'deadtime'. The EVB was a VME based multiprocessor system, connected to the LSC's via high-speed 'VIC' links. From there, the complete events were passed to the filter [36] via another high-speed 'VIC' link. The filter was a high performance HP UNIX workstation acting as a second stage software trigger to analyse and check the events. It removed obvious 'junk' events and classified the remainder into different categories of physics event (for example multi-hadron or low-multiplicity). Approximately 15-35% of all events were rejected at this stage. Surviving events were further compressed and buffered onto the filter disk in 20 Mbyte long partitions. A permanent back-up onto tape was also made. Figure 3.4 is a schematic diagram illustrating the various stages of the OPAL online DAQ [37] system.

3.2.11 Event Reconstruction

Events were reconstructed from the raw data for later physics analysis using the OPAL software package ROPE (Reconstruction of OPal Events) [38]. The large filter buffer meant that the reconstruction system could operate asynchronously from the data acquisition. This was necessary because the subdetector calibration constants stored in the OPCAL (OPal CALibration) [39] database did not become available until about an hour after the data had been collected. From the filter disk, the files were copied to a bank of HP UNIX workstations known as the ROPE farm. ROPE processed the raw data to reconstruct physical quantities (for example particle momenta, track trajectory, decay vertices and particle identification)

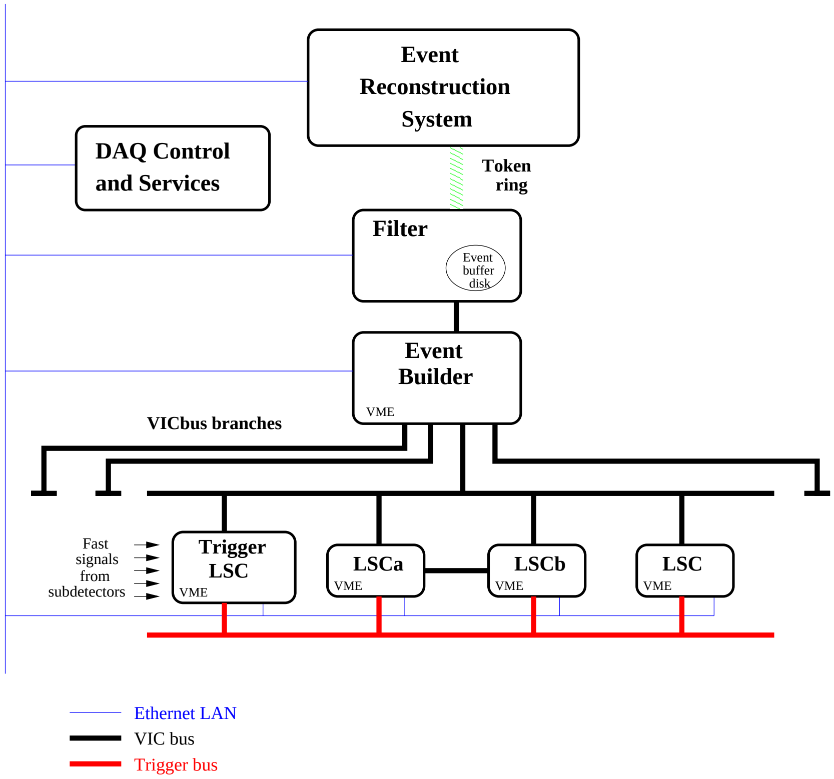

Figure 3.4: *Schematic diagram of the main components of the OPAL DAQ system and their principal connections. (Updated figure from [37].)*

by linking hits observed in the subdetectors and energy deposited in the calorimeters using information supplied by OPCAL. After reconstruction, the information was written out to optical disks known as the data summary tapes (DST) for offline analysis. ROPE also processes Monte Carlo events (discussed in section 5.3).

Reconstructed events may be viewed graphically using the OPAL graphics display package GROPE (Graphical Reconstruction of OPal Events) [40]. An example of a reconstructed event (tilted z-y view) is shown figure 3.5. This same event (in the x-y plane) is shown on the title page of this thesis.

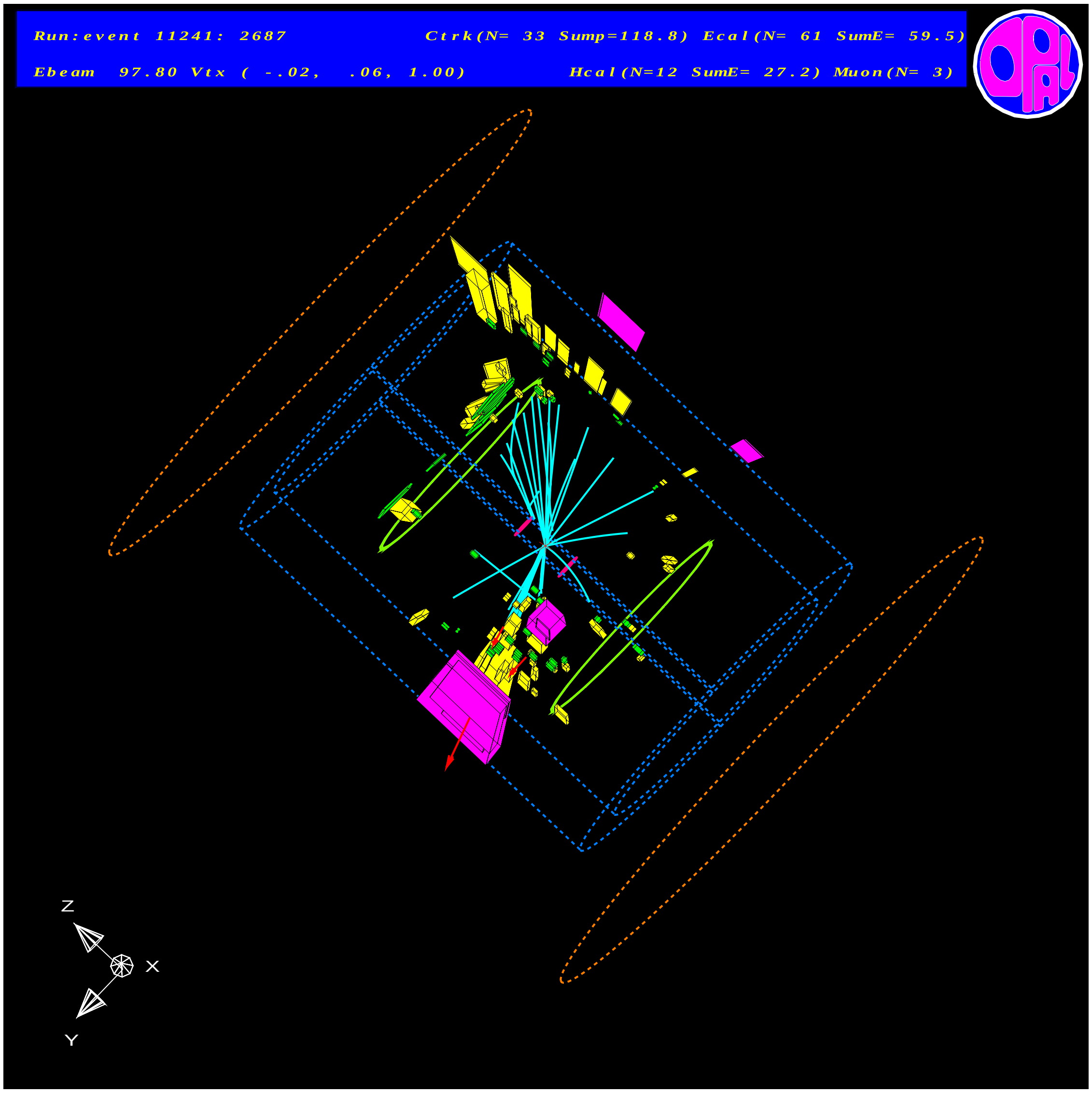

Figure 3.5: *Reconstructed* $W^+W^- \rightarrow l\nu q\bar{q}$ *event selected for the TGC analysis using GROPE [40](tilted* z-y *view). The electromagnetic and hadronic calorimeter energy clusters are represented by the size of the yellow and magenta blocks respectively. The light blue lines represent reconstructed charged particle tracks detected by the central tracking chambers. The outer red arrows show the direction of hits in the outer muon chambers - indicating that this was a* $\mu\nu q\bar{q}$ *event.*

Things in the real universe don't all fit together like the pieces of a child's puzzle.

JOHN TAINE (Eric Temple Bell), *The Time Stream, Three Science Fiction Novels,*
(N.Y.: Dover Publications, Inc., 1964)

Chapter 4

Investigation of MIP Plug Detector Performance

Four layers of scintillator tiles (MIP plugs) were installed in both endcaps of the OPAL detector, before the start of data taking in 1997. The main purpose of these tiles was to detect the presence of minimum ionizing particles at low angles to the beam axis. A full description of the design criteria and geometry for both the MIP plugs and tile encap may be found in [34].

This chapter describes a study of MIP plug performance undertaken as part of the search for acoplanar lepton pair events [41–43] at 183 and 189 GeV. An acoplanar di-lepton event is a low multiplicity event which contains a pair of isolated charged leptons and significant missing momentum in the plane transverse to the beam direction. These events are used in the $W^+W^- \rightarrow l^+\nu l^-\bar{\nu}$ event selection and in the search for new physics (see section 4.2). Two data samples were used in the analysis: randomly triggered events (random triggers) and a selected data sample of $e^+e^- \rightarrow e^+e^-\mu^+\mu^-$ events. These event samples are discussed in section 4.4.1.

A number of MIP plug readout problems were discovered in the 1997 data. For example, there were problems with the charge and time readouts, and also (due to incorrect cabling) problems with the MIP plug ϕ sector readouts. A set of DTE[1] bank corrections for the ϕ sector readouts were therefore determined using the muon events and are discussed in section 4.4.2. Section 4.4.3 describes the MIP plug charge and timing cuts used in [42] and

---

[1] Data for tile endcap and MIP plug. As discussed in section 3.2.11, following an event trigger, data is readout, processed and stored on data summary tapes (DST). The DSTs are arranged in blocks (called banks), of which the DTE is one of them. MIP plug information is stored with the TE detector readout in the DTE banks for later event reconstruction.

updates for the 189 GeV analysis [43]. MIP plug detection efficiencies and background rates are discussed in section 4.4.4. The results of these studies have been used in the acoplanar lepton analysis to veto events which have low angle charged leptons.

4.1 Motivation for installing the MIP Plugs

The MIP plugs were designed primarily to detect the yes/no presence of low angle minimum ionizing particles, the detection of which is a requirement in many physics analyses. Until the installation of the MIP plugs, there were no other detectors providing efficient, low angle coverage (between $\sim$60 to $\sim$160 mrad) for muons. Electrons could be detected, with high efficiency using a combination of EE, FD, SW and GC detectors (angular range $\geq$ 25 mrad), but there was not an equivalent detector for muons (the SW provided some coverage between 25 to 60 mrad, but was not highly efficient).

The MIP plugs were also used to act as a replacement for the gamma catcher (GC) which had non-repairable readout problems (approximately 25% of the readout channels were dead). For the last three years of data taking, the MIP plugs became part of the trigger system for two photon events.

4.2 Event Topologies

In the acoplanar lepton analysis [41,42], the candidate signature is a pair of charged leptons and missing momentum (P_t^{miss}) in a plane transverse to the beam direction (figure 4.1). Since the transverse momentum of the initial state electron pair is zero, then P_t^{miss} will be equal in magnitude but opposite in direction to the vector sum of the two observed leptons.

It is important to select only events with genuine 'prompt' missing particles. (For example, we wish to exclude $\gamma\gamma \to \tau^+\tau^-$ and $\mathrm{Z}^0 \to \tau^+\tau^-$ events since these will contain only secondary neutrinos from the tau decay.) Examples of Standard Model processes containing 'prompt' missing particles include $\mathrm{W}^+\mathrm{W}^- \to l^+\nu l^-\bar{\nu}$ events. This event topology could also indicate the existence of new physics (for example, chargino, higgsino or slepton pair production) if the observed number of such events is in excess of the number predicted by

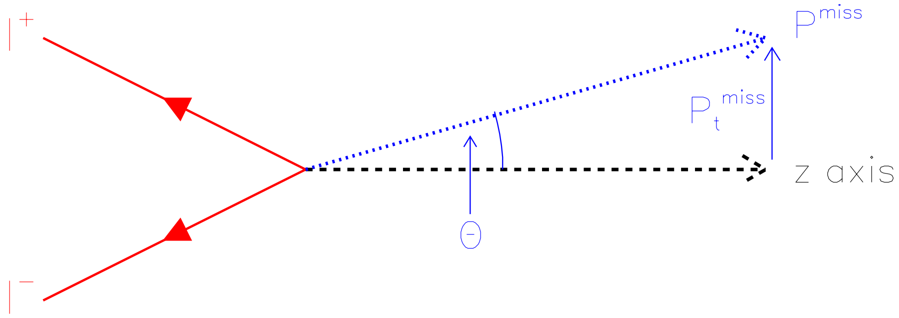

Figure 4.1: *Di-lepton event with missing momentum vector ($r - z$ view). There are several background processes which can mimic this signature. The detection of low angle leptons is crucial to many analyses, especially SUSY searches. MIP plug information is used to veto events which have low angle charged leptons.*

known standard model processes.

However, there are a variety of background processes that can fake the candidate signature including, for example, those illustrated in (figure 4.2). Standard two photon processes do not present a problem when the two electrons go straight down the beam pipe as they have no transverse component of momentum and the other two leptons (in this case the muons) will be back-to-back in ϕ. Problems arise, however, when one of the electrons is deflected and subsequently observed in the detector. One of the muons can escape undetected down the beam pipe (the other electron will also not be observed). The event may then be misidentified as the missing momentum signature as the two identified leptons will no longer be back-to-back in ϕ.

The MIP plug veto is generally applied to events with low P_t^{miss} (typically $P_t^{\text{miss}} < 0.2$ E$_{\text{beam}}$) depending on the acoplanarity[2] since it is only these that can be produced by two photon processes.

4.2.1 Candidate Events Vetoed by the MIP Plugs

Figure 4.3 illustrates an event from the 183 GeV acoplanar lepton analysis [42] which satisfied all the other selection criteria for a candidate event, but was vetoed by the MIP plugs. The charged lepton pair is shown in the diagram by the magenta tracks traversing

---

[2] The acoplanarity angle is defined as the supplement of the angle between the two leptons in the plane transverse to the beam axis.

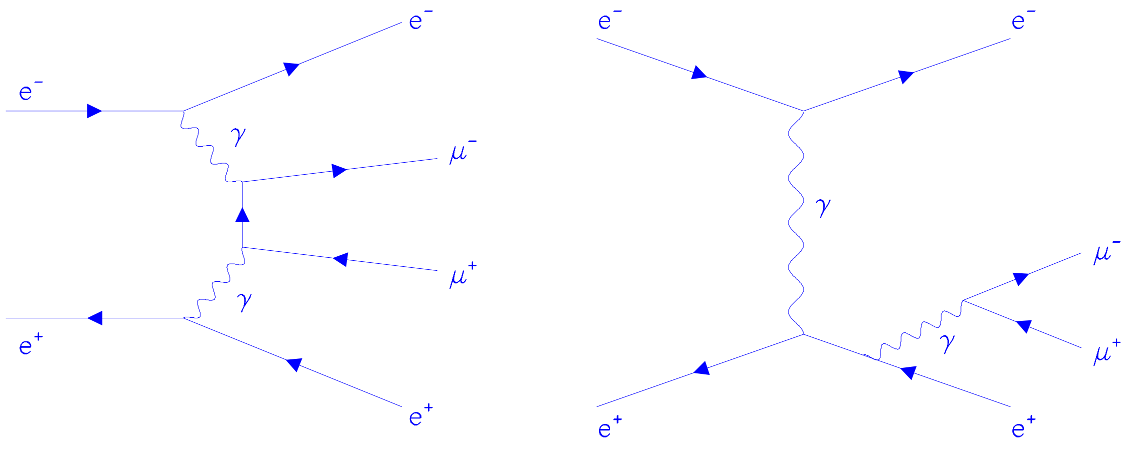

Two Photon

Radiative Bhabha Scattering

Figure 4.2: *Example of background processes (resulting in 4-fermion final states) which can fake the signal signature (of two charged leptons plus missing momentum) if two of the leptons are unobserved at low angles to the beam pipe.*

the central detectors. The lower right track was identified as an electron with momentum 7.61 GeV which deposited energy of 7.76 GeV in EB (shown by the magenta block). The upper left track was a muon of momentum 6.84 GeV which deposited only a small amount of energy (0.68 GeV) in EB but 2.97 GeV in HB. This event therefore has small P_t^{miss}. The green crosses represent hits in the muon chambers.

The event picture was produced from DST information using the OPAL event display package GROPE. Unfortunately GROPE was not updated to include the MIP plug hits for the 183 GeV data. What is not seen in this event picture is the presence of a hit in ϕ sector 2 of MIP layer 4B (see figure 4.6 for MIP plug ϕ segmentation) in coincidence with layer 4A. This event is most likely to be a two photon $e^+e^- \rightarrow e^+e^-\mu^+\mu^-$ event in which the MIP plug hit was produced by the second muon. The second electron escaped undetected down the beam pipe. Hence this event will be vetoed in the acoplanar lepton analysis on the basis of the MIP plug hits.

Figure 4.4 illustrates an example of the MIP plugs acting as a replacement for the GC. The GC should have detected the existence of a low angle electron but did not because of its dead readout channels. However, the particle recorded coincidence hits in MIP layers 4A and 4B in ϕ octants 6, 7 and 8 and these allowed the event to be vetoed. Note the significant amount of energy ($\sim$12 GeV) deposited in EE by this low angle electron (and also the HE clusters).

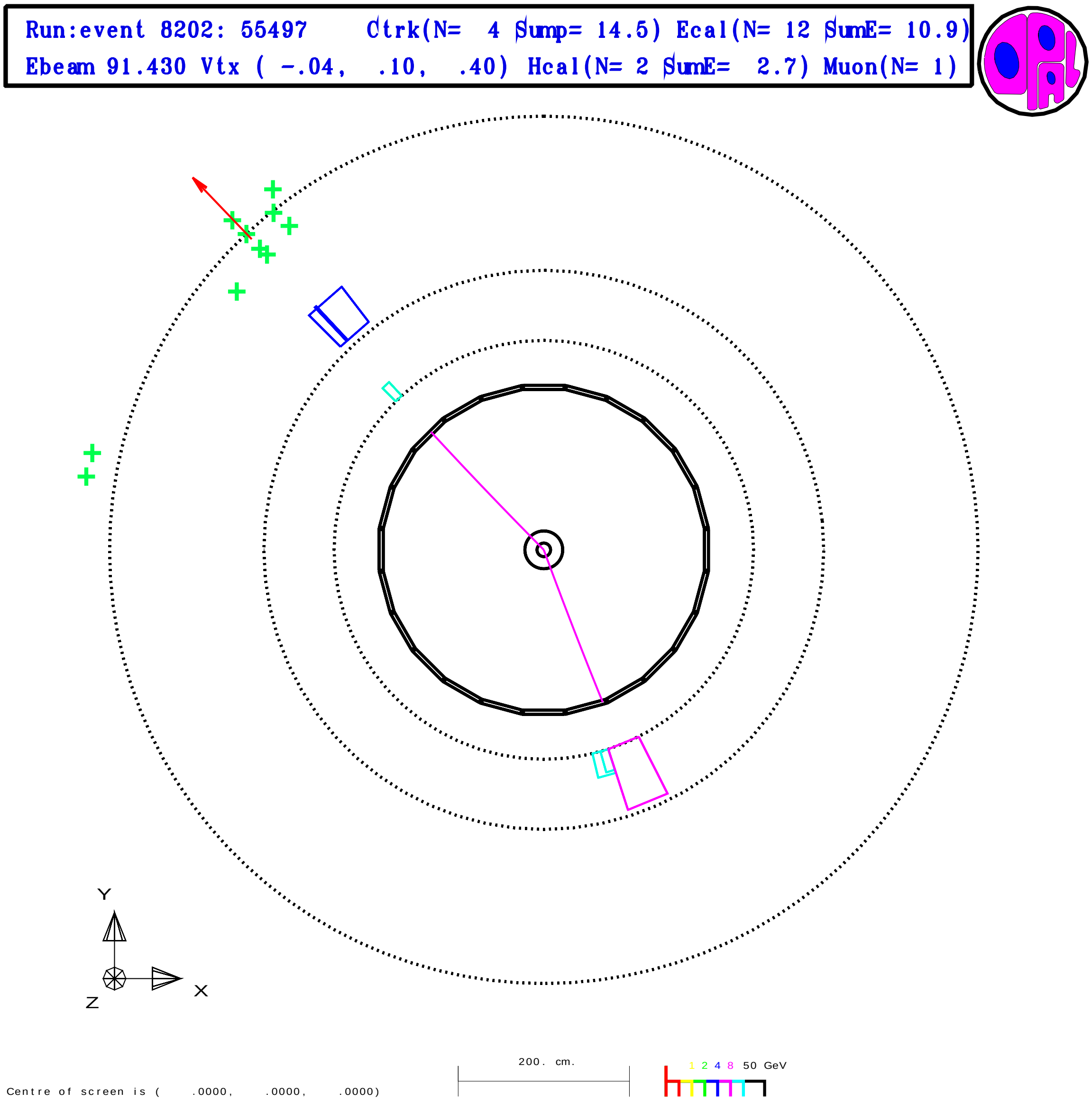

Figure 4.3: *This is a candidate event (event number 55197 run 8202) in the acoplanar lepton pair analysis [42] which was vetoed by the MIP plugs. A MIP coincidence was recorded between layers 4A and 4B in ϕ octant 2 (not shown in this figure).*

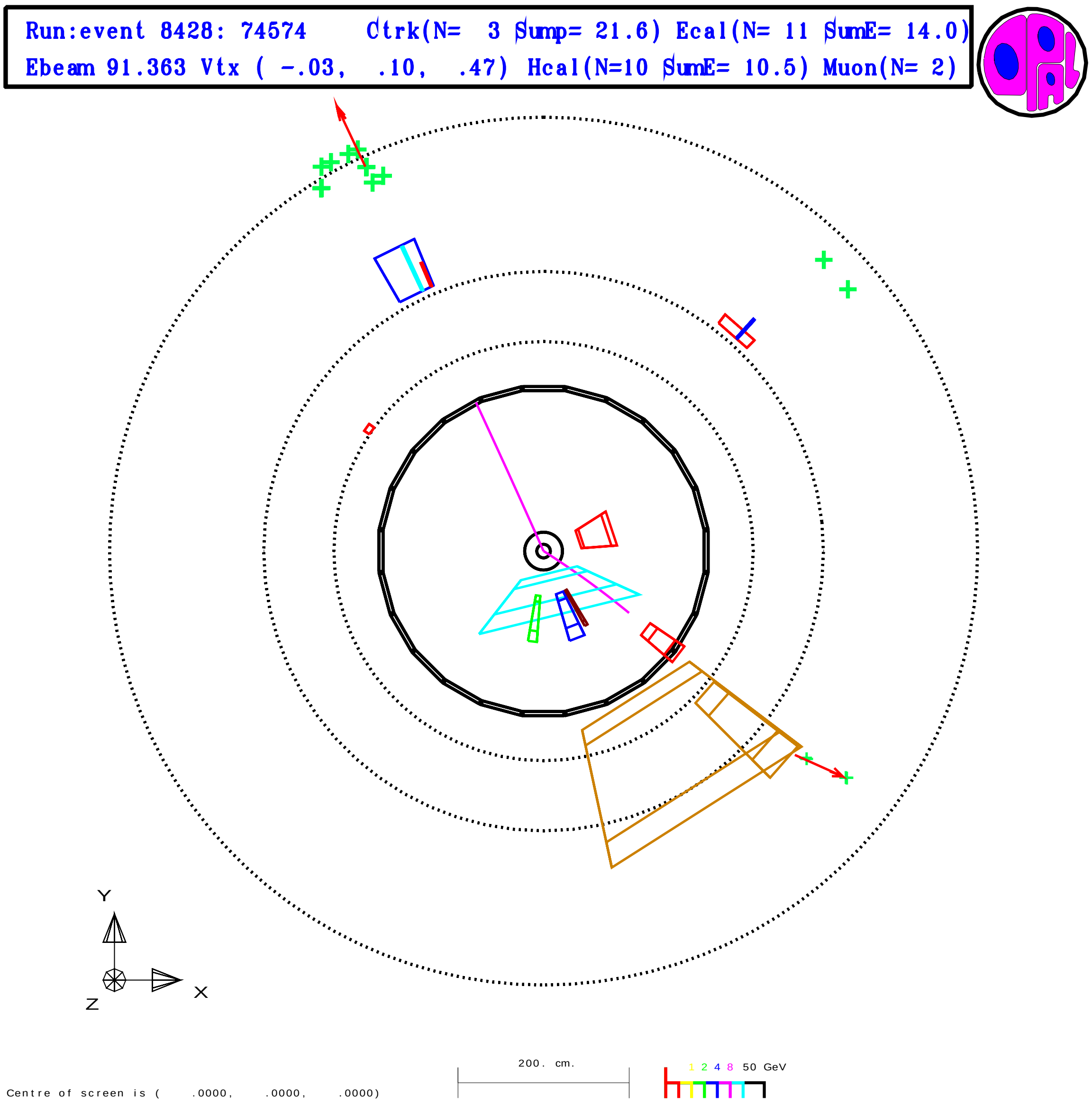

Figure 4.4: *Event 74574 in run 8428 was vetoed by the MIP plugs acting as a replacement for the GC. The energy deposited in the two EE clusters corresponds to a low angle electron which escaped detection in the GC. The MIP plugs recorded hits in ϕ octants 6, 7 and 8 (not shown in the figure).*

4.3 MIP Plug Design and Layout

The MIP plugs consist of 4 layers of 1 cm scintillator (labelled 4A, 4B, 5A and 5B) at each end of the detector, $\sim$2.5 m from the interaction point. The outermost layers 5A and 5B, are situated just behind the GC and separated by 5 mm of lead to reduce background from synchrotron photons. Layer 4A is located just behind layer 5B. Layer 4B sits behind the SW. Figure 4.5 is a schematic diagram illustrating the position of the MIP plug tiles with respect to the FD, SW and GC detectors. The polar angular coverage afforded by each of the layers is as follows:

Layer	θ range (mrad)
5A, 5B	$\sim$ 126 to 220
4A	$\sim$ 45 to 160
4B	$\sim$ 43 to 130

Table 4.1: *Polar angle range (θ) of the MIP plug layers*

This means that there is good overlap between layers 4A, 5A and 5B and between layers 4A and 4B.

The MIP plugs were designed to provide good time resolution and efficiency of detection for single minimum ionizing particles despite severe space constraints which limit their angular resolution in ϕ. Detectors 4A, 5A and 5B are segmented into four ϕ quadrants, whereas detector 4B is segmented into eight octants as shown in figure 4.6.

4.4 Investigation of MIP Plug performance

This section describes the work undertaken to incorporate MIP plug information into the acoplanar lepton analysis [42, 43] including the necessary DTE Bank corrections for MIP plug ϕ sector readout.

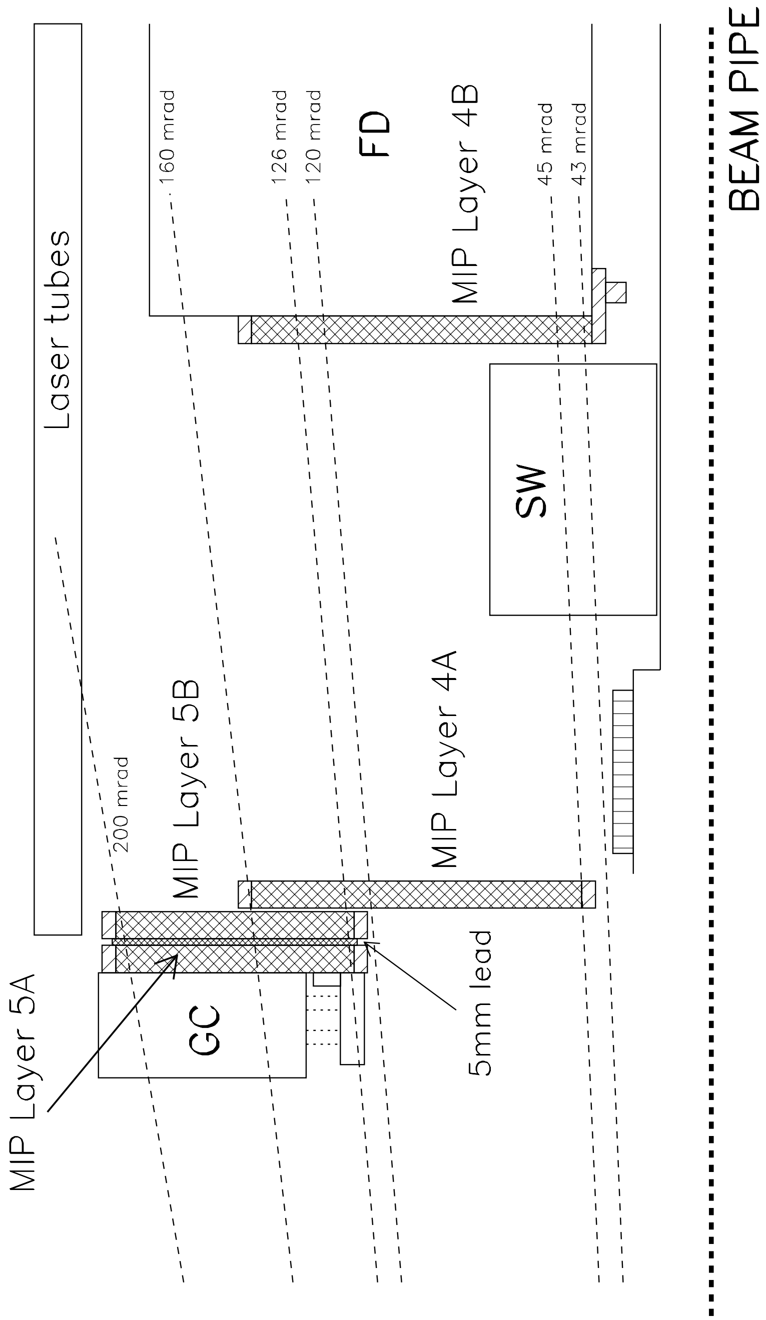

Figure 4.5: *Schematic diagram illustrating MIP plug position [44]. (Not to scale).*

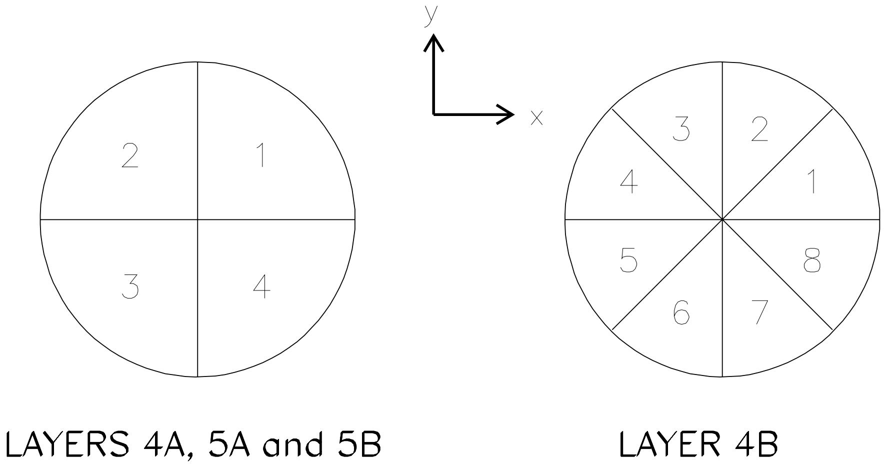

Figure 4.6: *MIP plug ϕ angle segmentation in $x - y$ plane [44].*

4.4.1 Event Samples

There were two data samples used in this analysis:

"Single Muon" Events

Events were required to contain exactly one track in the central detector. The track was required to be identified as a muon. Additional selection criteria for these events are listed in table 4.2.

SELECTION CRITERIA	CUTS
Momentum	$>$ 2.5 GeV
Angular Range	$\mid \cos\theta \mid < 0.95$
Distance of closest approach to beam axis (D_0)	$<$ 0.2 cm
z co-ordinate of the track point where D_0 measured	$<$ 15 cm
Number of FD, EE, SW or GC hits	0 hits or 1 hit and E $<$ 1 GeV

Table 4.2: *Selection criteria for single muon events. 7079 events were selected as single muon in the 183 GeV data and 19297 events in the 189 GeV data.*

Events which satisfy the selection criteria were predominantly from the process $e^+e^- \rightarrow e^+e^-\mu^+\mu^-$. The second muon (which was not observed in the central detector) would be expected to be back-to-back in ϕ with the single muon observed in the central detector. MIP plug activity in the corresponding ϕ sector would then provide evidence for this muon's existence.

Details of DTE bank corrections and MIP plug efficiencies determined using the single muon events may be found in sections 4.4.2 and 4.4.4 respectively.

Random Trigger Events

To estimate spurious MIP plug activity caused by, for example, off-momentum electrons[3] or random noise, random trigger events were analysed. Spurious MIP plug activity will result in an inefficiency in the acoplanar lepton pair analysis. In this respect, it is particularly interesting to study events where there have been no hits in either the FD, SW, EE or GC detectors (since events with hits in any of these detectors are likely to be already vetoed in the acoplanar lepton analysis). Details of background event rates and cuts designed to reduce them are discussed in sections 4.4.4 and 4.4.3 respectively.

4.4.2 DTE Bank Corrections

The single muon events were used to determine two sets of DTE Bank corrections for the MIP plug ϕ sector readout and are described separately in this section. Both sets of DTE bank corrections have been incorporated into a subroutine (TEMADJ) for use in physics analysis at the DST level. The routine may be found in the OPAL software.

First Set of Corrections

Figure 4.7 is a plot of the expected muon ϕ angle (for the second, low angle muon) versus MIP plug ϕ sector which recorded a hit. For layers 4A, 5A & 5B left and 5A & 5B right, there was a clear correspondence between the MIP plug ϕ angle and expected muon ϕ angle.

For the remaining layers (ie 4B left and right, and 4A right) there appeared to be a readout problem, in that the MIP plug hit was observed in a different ϕ sector to the one expected. This was verified by considering coincidences[4] between detector layers, and by using a

---

[3] Electrons which have lost energy in collisions with gas molecules in the beam pipe are said to be 'off-momentum'. Off-momentum electrons can undergo interactions with the detector, resulting in a shower and a spray of noise hits at low angles to the beam pipe.

[4] A coincidence is defined to be a MIP plug hit in a particular ϕ quadrant/octant and another hit in at least one of the other MIP plug layers in the same ϕ sector. The geometrical overlap of the tiles (see figure 4.5) permits coincidences between layers 4A and 4B, and layers 4A, 5A and 5B, but not 4B with 5A or 5B. The reason why it is necessary to consider MIP plug coincidences, as opposed to individual MIP plug hits, will be justified in section 4.4.4.

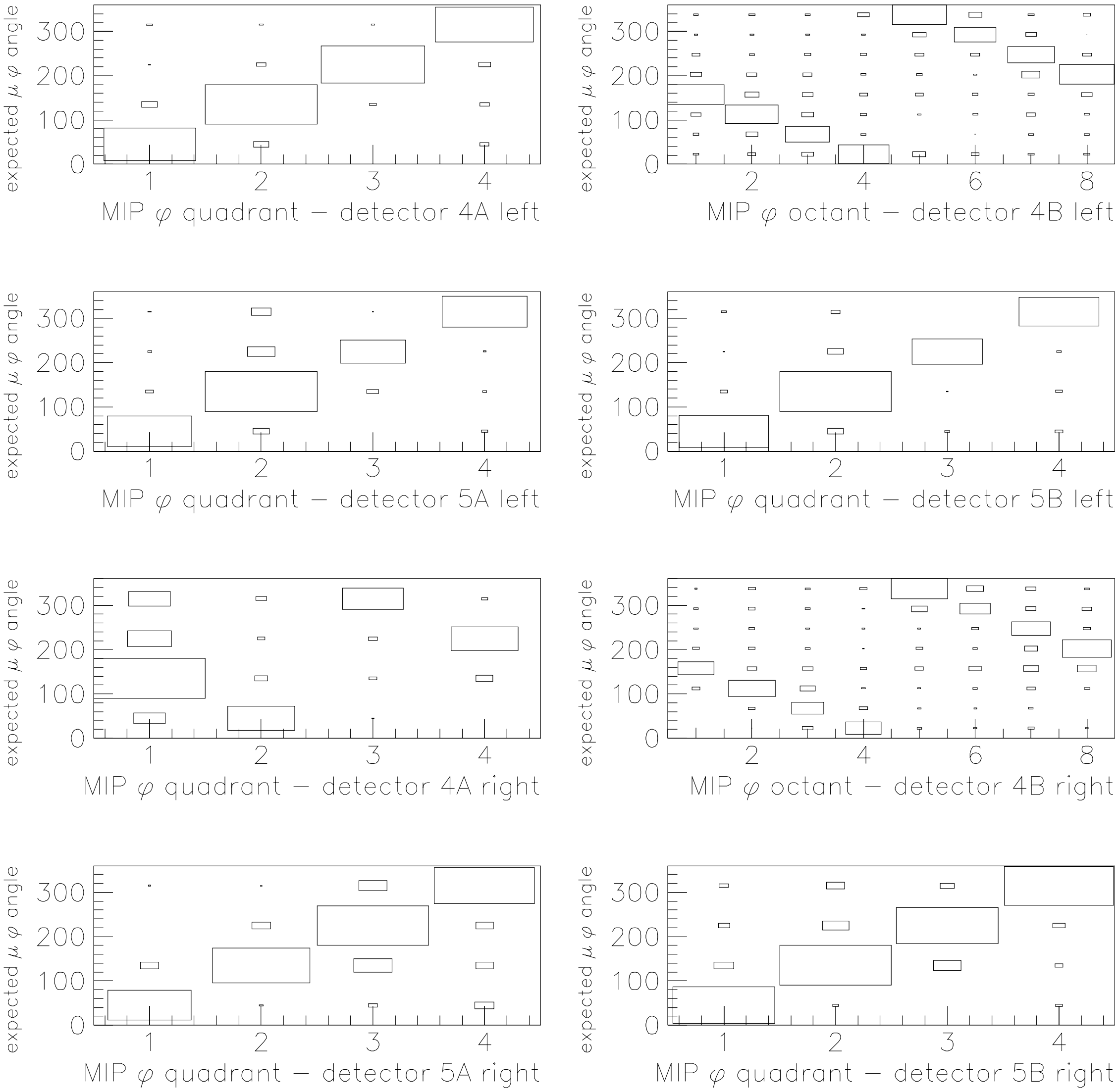

Figure 4.7: *Expected muon ϕ angle versus MIP plug ϕ quadrant (for layers 4A, 5A and 5B) or octant (layer 4B) which detected the hit. Runs $>$ 8600 before any correction made to the DTE banks.*

sub-sample of the single muon events in which the muon was observed as a track in SW.

From the plots in figure 4.7, a set of DTE bank corrections were determined and are listed in table 4.3. After these corrections had been made, the plots in figure 4.8 were obtained from the same data sample. A clear correspondence between the expected muon ϕ angle and MIP plug hit ϕ sector for layers 4A (right) and 4B (left and right) was then evident, in agreement with the other layers.

Second Set of Corrections

One of the MIP plug readout modules was replaced approximately half way through the

angular range (degrees)	MIP plug ϕ octant from DTE bank layer 4B (left & right)	DTE bank correction	angular range (degrees)	MIP plug ϕ quadrant from DTE bank layer 4A (right)	DTE bank correction
0-45	1	4	0-90	1	3
45-90	2	3			
90-135	3	2	90-180	3	1
135-180	4	1			
180-225	5	8	180-270	5	7
225-270	6	7			
270-315	7	6	270-360	7	5
315-360	8	5			

Table 4.3: *First set of DTE bank corrections for MIP plug layers 4A (right) and 4B (left and right).*

year. Further investigation of the single muon events revealed another discrepancy in the correlation between expected muon ϕ angle versus MIP plug octant hit for layer 4B, at both ends of the detector for early runs. This is illustrated in figure 4.9 which shows the expected muon ϕ angle (in terms of MIP plug ϕ octant) against MIP segment for runs < 8600.

For certain muon ϕ angles (for example, muon ϕ angles corresponding to MIP plug ϕ octant 3 in 4B left) there appeared to be no corresponding MIP activity. For other muon ϕ angle ranges (for example those corresponding to MIP plug ϕ octant 1 in 4B left), it appeared that the muons were detected in a different ϕ sector to the one expected. None of these discrepancies were apparent for the later runs which is indicative of another cabling fault. A second set of DTE bank MIP plug ϕ octant corrections have been determined using these results and are listed in table 4.4.

4.4.3 Charge and Timing Distribution Cuts

This section describes the MIP plug cuts applied to the charge and timing distributions in the acoplanar lepton analysis. These cuts were determined using the random trigger events and a selected sub sample of the single muon events in which the muon was observed as a track in the SW in the same θ range as layers 4A and 4B. (There is no geometrical overlap

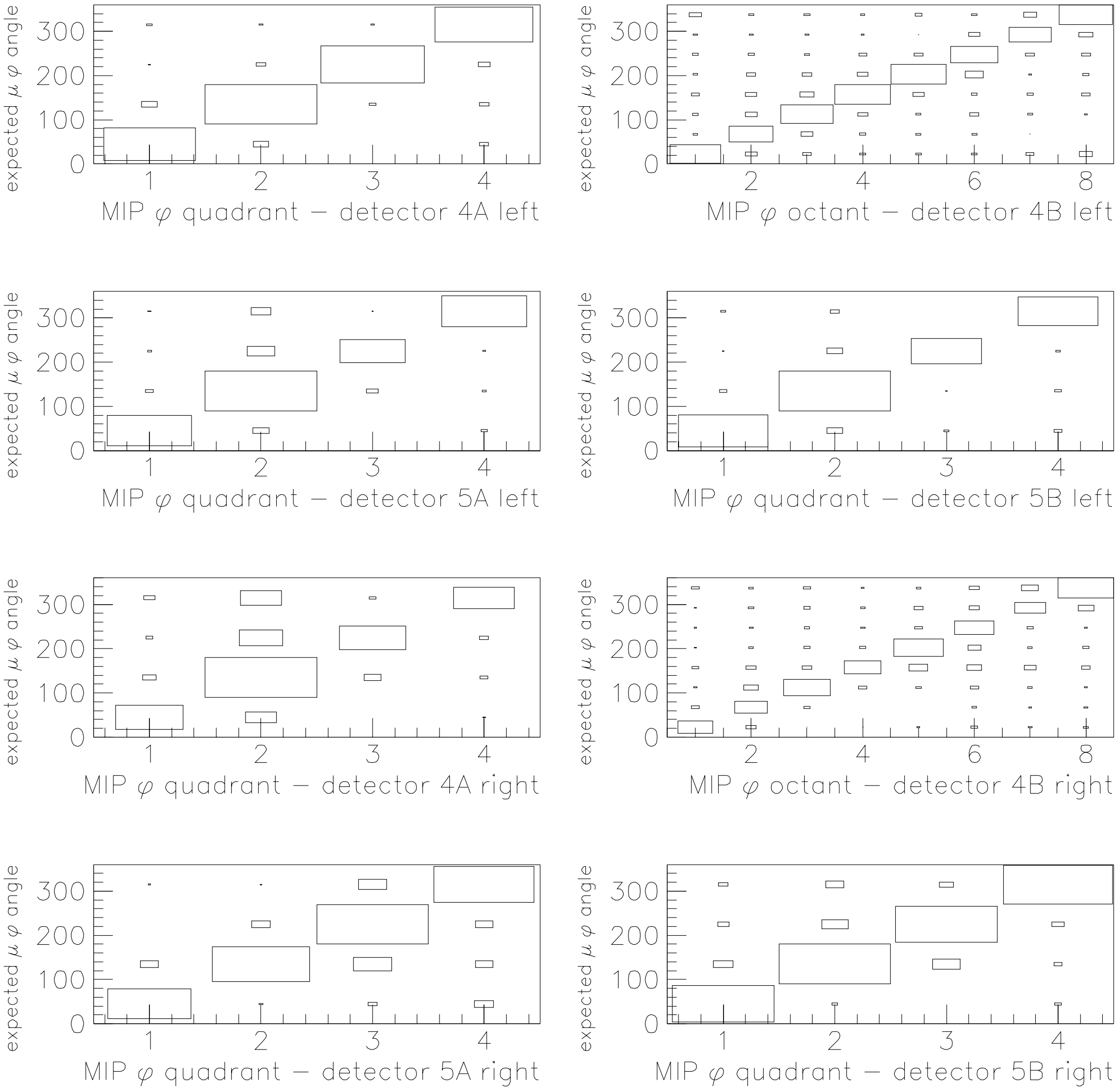

Figure 4.8: *Expected muon ϕ angle versus MIP plug ϕ quadrant (for layers 4A, 5A and 5B) or octant (layer 4B) which detected the hit. Runs $>$ 8600 after first set of DTE bank corrections had been applied.*

MIP plug ϕ octant (after 1^{st} DTE correction)	2^{nd} DTE bank correction
1 (left)	7 (left)
3 (left)	1 (left)
7 (left)	7 (right)
7 (right)	3 (left)

Table 4.4: *Second set of DTE bank corrections for MIP plug layer 4B (left and right).*

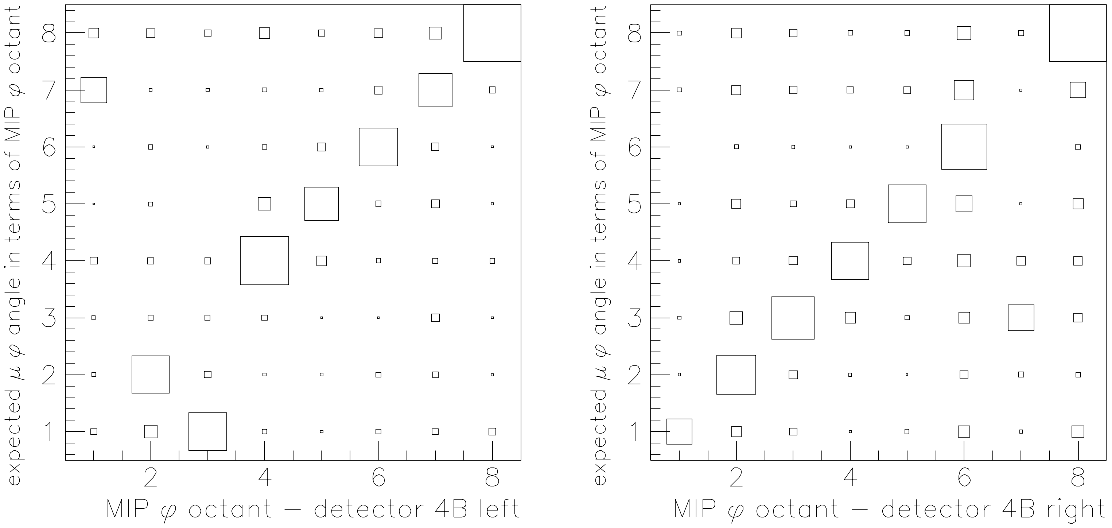

Figure 4.9: *Expected muon ϕ angle versus MIP plug ϕ octant in layer 4B (left and right) for runs $<$ 8600 after first set of DTE bank corrections have been applied.*

between the SW and MIP layers 5A and 5B).

Timing Distributions

The time distribution[5] for layer 4A quadrants in coincidence is shown in figure 4.10 for the random trigger event sample. (The other MIP plug layers exhibit similar distributions). There are two peaks in the distribution: the first one corresponds to the time of the main bunch crossing and the second one corresponds to the next bunch crossing when the TDC gates have failed to close. It was necessary to eliminate coincidences with time readouts corresponding to noise hits in the second peak. However, it was found that in the selected muon events the time readout for layer 4B sometimes fell within this second peak, even though there were genuine hits in the SW in the same ϕ sector. Therefore, it was not possible to simply apply an upper cut on the individual MIP plug layer times to remove this second peak.

The second problem associated with MIP plug layer timing was the existence of a time 'jitter' occurring approximately 18ns (or multiples thereof) after the main bunch crossing in some readout channels. The 'jitter' was entirely random and consequently it was not possible to correct any particular run periods. Furthermore, the time jitter (indicated in fig-

---

[5] The time distributions for the 183 GeV data were obtained using calibration software written by Stan Bentvelsen. Time calibration was undertaken using events collected at the Z^0 peak (with $\sqrt{s}$ = 91 GeV) at the beginning of 1997 data taking and was checked for later run periods. A special correction factor was applied to events following MIP plug recabling.

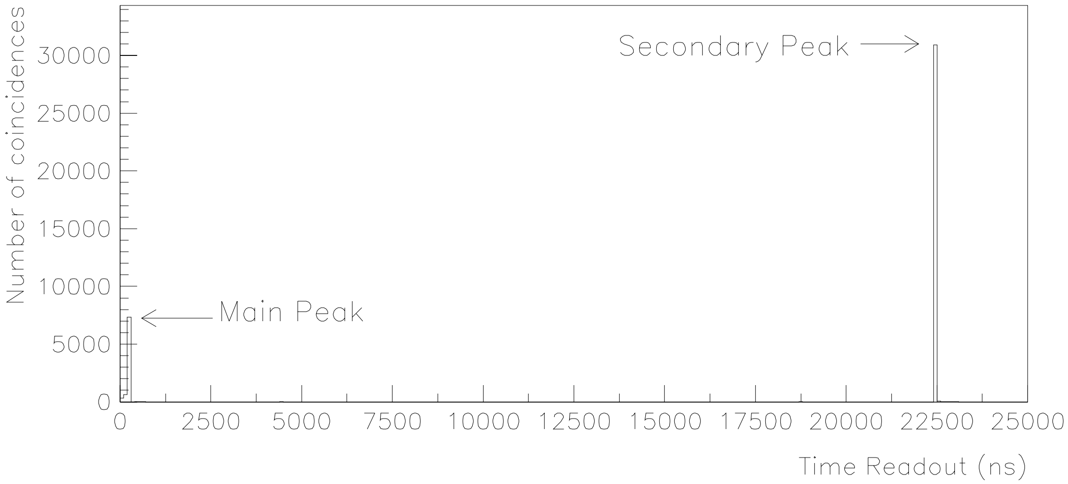

Figure 4.10: *Corrected time readout for layer 4A (all ϕ quadrants in coincidence with another layer) in the random trigger events where there were no hits in either the SW, FD, EE or GC detectors. The second peak corresponds to the next bunch crossing.*

ure 4.11 for the selected muon sample), was too close to the main peak to correct individual events. Since the time distribution was spread around the main peak (events to the left of the peak correspond to events collected with the special timing correction applied after MIP plug recabling) it was not possible to impose tight cuts on individual MIP plug layer time readouts around the peak.

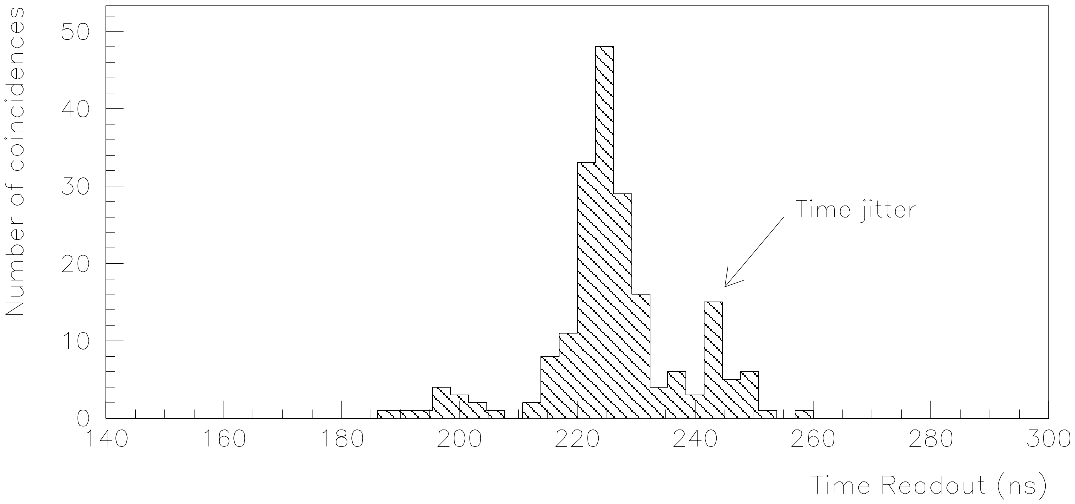

Figure 4.11: *Corrected time readout for layer 4A (selected muon events) where there was an SW hit in the same ϕ sector as the MIP coincidence. The distribution is spread around the main peak position (at ∼225 ns) and the existence of a small (double peak) time jitter is indicated.*

Instead cuts were applied to the time distribution of the MIP hit (in each coincidence) which had time readout closest to the main peak position at 225 ns. This is hereafter referred to as the ‘best time’. Figure 4.12 illustrates this distribution for the selected muon events and figure 4.13 for the combined random triggers. The selected muon peak is much sharper than in figure 4.11 and most of the time ‘jitter’ peak has been removed. However, there were still a few events either side of the main peak and hence tight cuts could not be applied. All selected muon events had best times within the main peak region, whereas noise hits in the random trigger events frequently had much higher best times[6]. Consequently, loose cuts at 150 and 300 ns were applied to the best time distribution to reduce background noise levels.

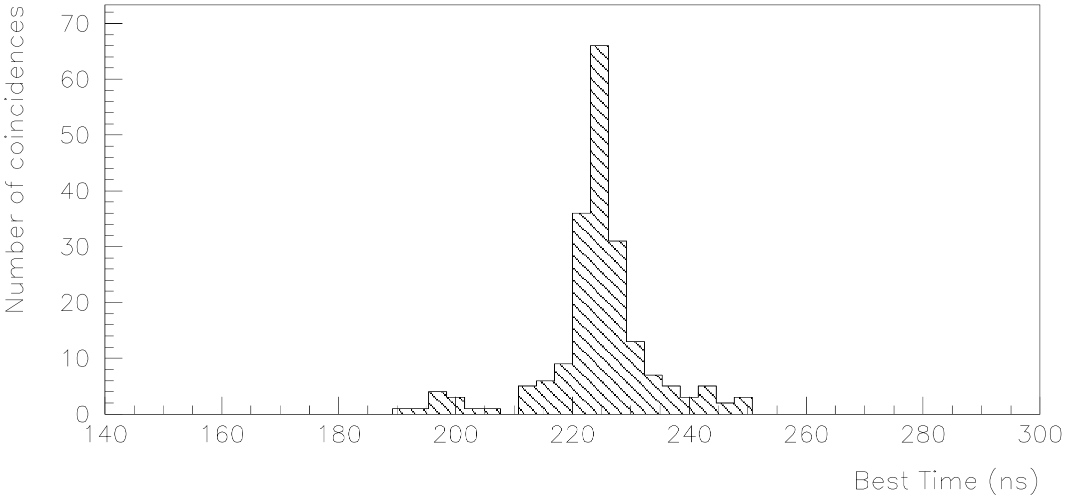

Figure 4.12: *Time distribution of the MIP plug layer with time readout closest to the main peak position at 225 ns for selected muon events. Upper and lower cuts at 300 and 150 ns respectively are used in the acoplanar lepton analysis to veto MIP coincidence events with ‘best times’ lying within the main peak region.*

Off momentum electrons striking the rear face of the FD and SW detectors would be expected to arrive about 15 ns before particles coming from the main interaction since they will have travelled a shorter distance ($\sim 2 \times 2.5$ m less). In the best time distribution for random trigger events (figure 4.13) a small, minor peak is observed to the left of the main peak which corresponds to these electrons. The width of the best time distribution for the selected muon sample (figure 4.12) did not allow this out-of-time background to be removed in the 1997 data.

For the 1998 run season, BX[7] signals were used to correct MIP plug timing, and new cut

---

[6] The histogram plot for the random triggers (figure 4.13) only illustrates the distribution for events with best times around the main peak region. There were in fact many events with best times in the secondary peak at 22500 ns.

[7] Beam crossing

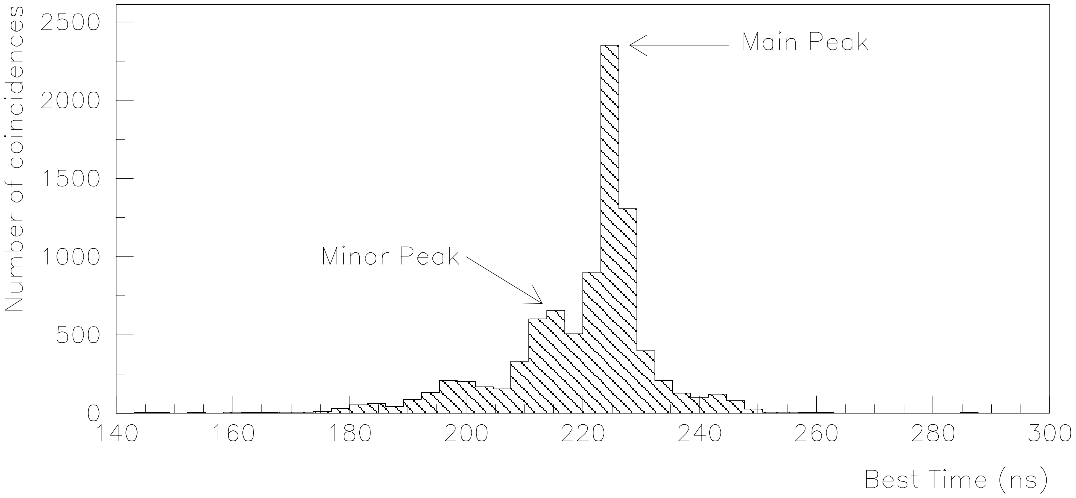

Figure 4.13: *Best time distribution for random trigger coincidences. (Coincidences which have 'best times' greater than 300 ns are not shown). Note the existence of a minor peak approximately 15 ns ahead of the main peak corresponding to off momentum electrons striking the FD/SW detectors.*

positions were investigated based on the individual distributions. Unfortunately, these cuts were not incorporated into the 189 GeV analysis [43].

Charge Distribution

The collected charge was proportional to the light detected. In order to suppress noise hits, each MIP coincidence was required to contain at least two hits with charge greater than 50 pC.

For the 183 GeV data, an exception was made for coincidences containing hits in the odd-numbered ϕ sectors of detector 4B, for which the charge readout always gave zero in 1997. In this case the hit in layer 4A (in coincidence with the hit in 4B) was required to have charge greater than 50 pC. The possibility of changing the cut position, was investigated for the 1998 data.

Figures 4.14 and 4.15 illustrate the charge distributions on which the cut was applied for both the selected muon and random trigger events (after timing cuts had been applied). It can be seen that a significant fraction of the coincidences in the random trigger events have zero charge readout. The charge cut substantially reduced the number of coincidences due to noise hits (figure 4.15) but did not effect the selected muon events (figure 4.14).

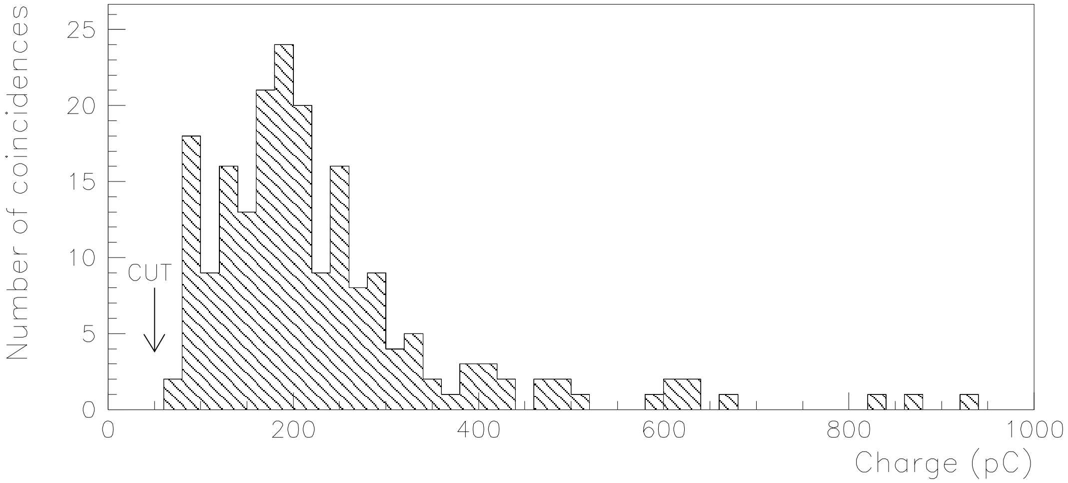

Figure 4.14: *Charge distribution of selected muon coincidence events which have an SW hit in the same ϕ segment as a MIP plug coincidence between layers 4A and 4B, within the geometrical acceptance of 4A. The position of the charge cut at 50 pC is indicated.*

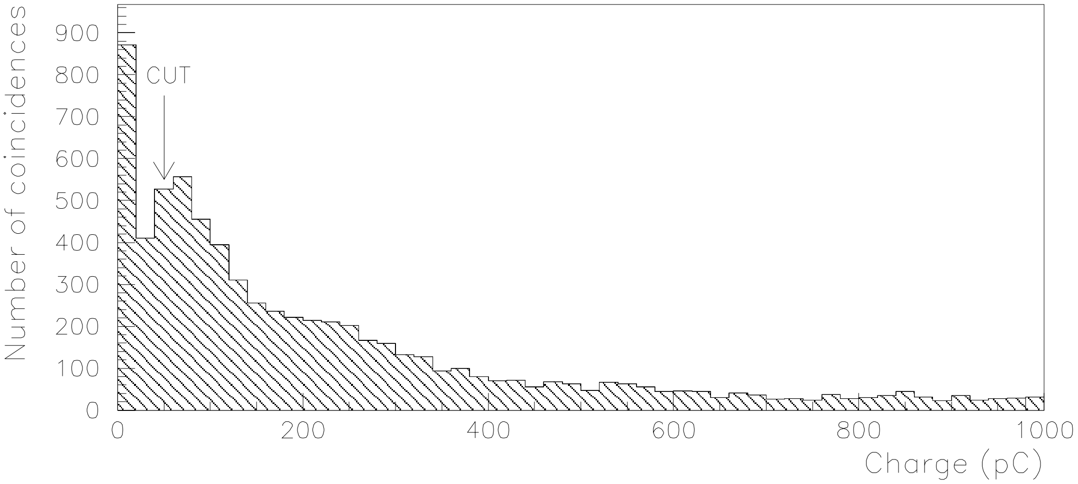

Figure 4.15: *The charge distribution (as in figure 4.14) for coincidences in the combined random trigger sample (periods 84, 85, 86, 88 and 89) before the charge cut at 50 pC had been applied (but after the best time cuts had been applied). Events in this distribution were required to have no hits in either the FD, SW, EE or GC detectors. Note that there are a large number of entries with zero charge readout.*

4.4.4 MIP Plug Efficiency and Background Event Rates

In order to incorporate MIP plug information into physics analyses it was necessary to determine both the detection efficiency for genuine hits and estimate background noise levels.

MIP Plug Efficiency using Single Muon Events

This study was undertaken using the selected muon sample of events described in section 4.4.3. The detection efficiencies for single MIP hits and coincidences (between layers 4A and 4B only) are listed in table 4.5. The figures in the first column were determined using the complete sample of events and do not include MIP plug detector status cuts. These figures show a detection efficiency of minimum ionizing particles of about 80% for the 183 GeV data and 98% for the 189 GeV data. It should be noted that the figures for the 183 GeV data include periods when the MIP plugs were not working perfectly. The last entry in the table has the requirement that there was a MIP coincidence between layers 4A and 4B in the same (or adjacent) phi octant as the muon observed in the SW. This figure provides a good measure of detection efficiency for MIP coincidences, since there was a genuine hit in the SW at a particular ϕ angle. This is the number required for the acoplanar lepton pair physics analysis.

	183 GeV	189 GeV
No. of events in geometrical acceptance of 4A	303	832
No. of events in geometrical acceptance of 4B	366	964
Efficiency of hit detection in 4A	91 %	99 %
Efficiency of hit detection in 4B	86 %	99 %
Efficiency of detecting a MIP coincidence (between 4A and 4B)	82 %	98 %
Require same (or adjacent) ϕ octant as SW hit		
Efficiency of hit detection in 4A	90 %	99 %
Efficiency of hit detection in 4B	83 %	99 %
Efficiency of detecting a MIP coincidence (between 4A and 4B)	80 %	98 %

Table 4.5: *Efficiencies for selected muon events*

To provide a rough check of the detection efficiency for layers 5A and 5B, a similar analysis was performed using events in which hits in the muon chambers and hadron calorimeter indicated that a muon was likely to have entered these layers. No obvious problems were found.

Measuring Background Rates using Random Trigger Events

The combined random trigger event sample was used to investigate background event rates.

(Period 86 in the 183 GeV sample was particularly noisy due to off-momentum electrons caused by a break in the rf cavity close to the OPAL detector (on the right hand side)).

	183 GeV	189 GeV
No. of Events	269649	493146
% Events with MIP hit ≥ 1	31.2 %	58.2 %
% Events with MIP hit ≥ 1 but no FD, SW, EE or GC hits	20.8 %	42.6 %
% Events with MIP coincidence ≥ 1	10.3 % ?	8.7 %
% Events with MIP coincidence ≥ 1 but no FD, SW, EE or GC hits	5.7 %	4.6 %
% Events with MIP coincidence ≥ 1, no FD, SW, EE or GC hits and $150<\mathrm{T_{best}}<300$ ns	1.2 %	3.6 %
% Events with MIP coincidence ≥ 1, no FD/SW/EE/GC hits, $150<\mathrm{T_{best}}<300$ ns and with charge cut > 50 pC	0.9 %	2.1 %

Table 4.6: *Statistics for the combined random trigger events*

Table 4.6 lists some of the results from this analysis. In order to reduce MIP hits caused by random noise, it was required that the MIP plug hits be in coincidence (as defined in section 4.4.2). This reduced the fraction of events with MIP plug activity but no hits in the other forward detectors to $\sim$5.0%. Imposing the additional requirements that at least one layer in the coincidence had time readout between 150 and 300 ns and the charge cut at 50 pC (described in section 4.4.3) further reduced the number of MIP plug coincidences by a factor of five for the 183 GeV data, and by more than half for the 189 GeV data (when the MIP plugs were noisier).

4.5 Conclusion

The MIP plugs provide a reasonably efficient means of detecting the yes/no presence of a low angle minimum ionizing particle. By requiring that the MIP hits between at least two layers (either 4A/4B or any two of 4A/5A/5B) are in coincidence, at least one MIP layer in the coincidence has time readout between 150 and 300 ns, and that the charge stored on at least two layers be greater than 50 pC, many of the problems associated with random noise hits and readout can be avoided.

Before using the DTE bank ϕ information for MIP plug layers 4A (right) and 4B (left and right), the corrections outlined in section 4.4.2 should be applied to correct for the hardware readout problems in 1997 data. Subroutine (TEMADJ) has been written for use in physics analysis at the DST level and may be found with the OPAL software.

MIP plug information has been used in the acoplanar lepton analysis [42,43][8] to veto events which have low angle charged leptons. For the data collected at $\sqrt{s}$ = 183 GeV, 4 out of 83 candidate events were rejected exclusively by the MIP plug cuts and 13 out of 315 events at $\sqrt{s}$ = 189 GeV were rejected by these MIP plug cuts.

---

[8] There are two independent selections used in the acoplanar di-lepton analysis and these are referred to as event selection I and II. The principal differences are discussed in [41]. The MIP plug cuts described in this chapter were applied only to selection I. Selection II has slightly different MIP plug cuts (in particular it uses a different definition for MIP plug coincidences). Selection II is used within OPAL to select WW$\rightarrow l\nu l\bar{\nu}$ events and is discussed further in chapter 5.

> *It seemed to me that in one of my innumerable essays, here and elsewhere, I had expressed a certain gladness at living in a century in which we finally got the basis of the Universe straight.*
>
> ISAAC ASIMOV, *The Relativity of Wrong*

Chapter 5

W^+W^- Framework

Study of W boson properties, for example its production, decay characteristics, measurement of its mass and coupling to other gauge bosons, is one of the main aims of the LEP 2 physics program. This chapter introduces some of the experimental ideas behind W^+W^- production and decay at LEP 2, relevant to the two physics analyses presented in later chapters. Following a general overview of W boson physics including its production and decay topologies, this chapter discusses some of the background processes at LEP 2 (including other four fermion processes). For most particle physics analyses, it is important to have good theoretical models with which to compare the data. This is normally achieved using Monte Carlo (MC) simulated data and a summary of MC event simulation and some of the event generators used in these analyses are also given. The event selection depends principally on the standard OPAL selection routines which are only briefly reviewed here since they form no part of the author's work. Finally the kinematic fits applied to events used in the TGC analysis are described.

5.1 Introduction to W Physics

The W boson was first observed (singly) in 1983 by the UA1 [45] and UA2 [46] experiments on the Sp$\bar{\text{p}}$S collider at CERN in the reactions:

$$u + \bar{d} \rightarrow W^+ \rightarrow l^+ + \nu_l \tag{5.1}$$

$$d + \bar{u} \rightarrow W^- \rightarrow l^- + \bar{\nu}_l \tag{5.2}$$

where $l \equiv$ e or μ. Further measurements of W boson production have been made by the CDF [47] and D0 [48] collaborations at the Tevatron collider. Both the Tevatron and Sp$\bar{\text{p}}$S colliders are p$\bar{\text{p}}$ machines, and the W bosons are produced from interactions between the proton quark constituents either in pairs or singly.

At LEP 2, W bosons can either be produced singly (figure 5.2a, c and f) via the process: $e^+e^- \rightarrow$ W$e\nu$, or in pairs via the process: $e^+e^- \rightarrow$ W$^+$W$^-$. Although some of the single W processes are TGC dependent (for example figure 5.2a) and contribute to the overall LEP TGC combination [49], in this thesis we are only interested in W pair events and hence single W events are treated as part of the four fermion background[1]. The CC03 production cross section was discussed in section 2.2.1. Experimentally the actual number of W pair events observed at a given centre of mass energy (E$_{\text{cm}}$) depends not only on the cross section (σ), but also on the luminosity ($L = \int \mathcal{L}\,\text{d}t$) and selection efficiency (ϵ):

$$N_W = L\epsilon\sigma \tag{5.3}$$

As discussed in section 2.2.4, each W boson in a W pair event decays independently to either leptons or quarks with SM branching ratios of 1/3 and 2/3 respectively. QCD corrections enhance the quark decay width by a factor of approximately (1 + α_s/π), resulting in a W branching fraction to quarks of 67.5% [50]. Consequently there are three possible final state combinations for W pair events. These are shown in figure 5.1 together with their respective branching fractions. Leptons may be classified as either electron, muon or tau, which means that in total there are 10 possible final states for W pair events: $6 \times l\nu l\bar{\nu}$, $3 \times l\nu q\bar{q}$ and $1 \times q\bar{q}q\bar{q}$ (if quark flavour is ignored). At the end of LEP 2 data taking, OPAL has collected nearly 12,000 W pair events, of which $\sim$1000 are $l\nu l\bar{\nu}$ events and $\sim$5000 are $l\nu q\bar{q}$ events.

Fully leptonic events (W$^+$W$^-$ $\rightarrow$ $l^+\nu l^-\bar{\nu}$) are characterized by a clean signature of two (high momentum) leptons with missing energy (from the undetected neutrinos). Electrons and muons appear as single tracks whereas taus decay either leptonically or hadronically within the detector. Although low in statistics, the fully leptonic channel has low background contributions from other processes. Because the two (or more) neutrinos escape detection, these events cannot be fully reconstructed and consequently, for the TGC analy-

---

[1] TGCs in single W events and other processes are discussed further in chapter 7.

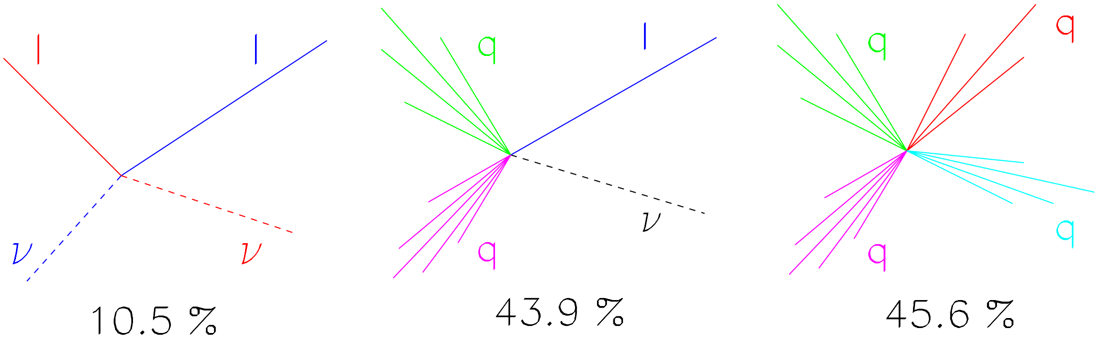

Figure 5.1: *Fully leptonic, semi-leptonic and fully hadronic WW decay modes at LEP2 and their branching fractions.*

sis, there is always some ambiguity in the angular distributions (described in section 7.3).

The fully hadronic, or four quark channel (W$^+$W$^-$ $\longrightarrow q\bar{q}q\bar{q}$) not only has the highest statistics, but also the largest background (mainly from Z$^0/\gamma \longrightarrow q\bar{q}$ events). These events are characterized by at least four hadronic jets with no missing energy. The individual quarks from the W decays are never observed directly, but instead the quarks hadronize into highly collimated jets of particles. Gluons may also be radiated by one (or more) of the quarks in the jets giving rise, for example, to 5 or even 6 jet events. Although it can sometimes be difficult to separate the tracks from overlapping jets, the main problems with this channel concern correct di-jet pairing and jet charge assignment [51]. Furthermore, since it is impossible to establish which of the two jets (in any pair) contain the fermion or anti-fermion quark from the W decay, there is some ambiguity when the angles are reconstructed. Gluons exchanged between quarks from different W bosons before fragmentation (colour recombination) and Bose-Einstein effects between pions in jets originating from different W's after quark fragmentation, give rise to additional systematic effects.

The semi-leptonic W$^+$W$^-$ $\longrightarrow l\nu q\bar{q}$ channel is often described as the "golden" channel for LEP 2 WW physics analyses. Not only is it possible to fully reconstruct these events and determine both the charge and direction of each W boson, but also this channel has high statistics, clean signature and low background (since there are no other significant background processes which produce the same combination of final state particles). Unlike the fully hadronic events, there is no known "cross talk" between decay products of different W bosons. This channel is characterized by two quark jets[2] (which are back-to-back in the W rest frame) and a single (high momentum) charged lepton. Again, since the fermion/anti-fermion in the quark jets cannot be distinguished, there is an ambiguity in the angles from the hadronically decaying W (see section 7.3), but the charged lepton uniquely defines the other set.

The three W pair decay channels are analysed separately (and then the results are combined) because of their different experimental signatures. In this thesis, WW $\rightarrow l\nu l\bar{\nu}$ events were used for the WW lepton classification analysis (discussed in chapter 6) and WW $\rightarrow l\nu q\bar{q}$ events were used in the TGC analysis (described in chapter 8). Fully hadronic events were not used in either of these analyses, except a few ($\sim$1%) fully hadronic events were mistakingly classified as $\tau\nu q\bar{q}$ events.

5.1.1 W Branching Fractions

The latest measured branching fractions from OPAL for the combined LEP 2 data set of W pair events are [6]:

BR($W \rightarrow e\bar{\nu}_e$)	10.40 ± 0.25 (stat.) ± 0.25 (syst.) %
BR($W \rightarrow \mu\bar{\nu}_\mu$)	10.61 ± 0.25 (stat.) ± 0.24 (syst.) %
BR($W \rightarrow \tau\bar{\nu}_\tau$)	11.18 ± 0.31 (stat.) ± 0.37 (syst.) %
BR($W \rightarrow q\bar{q}$)	67.91 ± 0.37 (stat.) ± 0.49 (syst.) %

The lepton branching fractions include the classification cuts described in chapter 6 for the fully leptonic channel. The fits for the leptonic branching fractions were made under the assumption that the quark and three leptonic branching fractions sum to unity. The fit for the branching fraction to hadrons was determined assuming lepton universality. The fit results compare (within errors) to their predicted values in table 2.4.

---

[2] Sometimes three (or more) jets may be observed, for example from gluon radiation or hadronically decaying τ's in $\tau\nu q\bar{q}$ events.

5.2 Background Processes

There are three main types of background associated with the selection of W pair events. Firstly there are backgrounds arising from other physics processes (for example two photon or muon pair events) which have different final states than the signal but are mistakenly selected. The event selections (described in section 5.4) are tuned to reduce these types of background as much as possible whilst maintaining high efficiency. Secondly there are irreducible backgrounds arising from other four fermion processes which have the same final state as the process under investigation. Expected contributions from these sources are evaluated using MC. Finally there are other four fermion processes which have final states that can be distinguished from the CC03 signal, but which cause interference effects. Examples of some Feynman diagrams for background processes are illustrated in figure 5.2.

In OPAL, the contribution from four fermion processes was estimated from MC simulated events and subtracted from the data before measurements of the W cross section and branching fractions were made [52]. The contribution from four fermion non-CC03 processes is most pronounced for the $\mathrm{W}^+\mathrm{W}^- \rightarrow l^+\nu l^-\bar{\nu}$ channel. A detailed breakdown of the background processes considered for the improvements to the leptonic branching ratio measurements (section 6.3) is given in table B.2, appendix B. The background contributions for each channel are listed in table 5.1. As shown by table 5.1, the channels with at least one τ in the final state (particularly the $\tau\tau$ and $e\tau$ channels) have larger background contamination than the others. The main sources of background arise from tau pairs ($e^+e^- \rightarrow \tau^+\tau^-$) and $e^+e^- \rightarrow e^+e^-\tau^+\tau^-$ events for this channel. Lepton pair contamination is characterized

Channel	No. expected non $l\nu l\bar{\nu}$ events	non $l\nu l\bar{\nu}$ contribution to x-section (fb)	No. expected $l\nu l\bar{\nu}$ background events	$l\nu l\bar{\nu}$ contribution to x-section (fb)
ee	0.59 ± 0.26	3.24 ± 1.43	1.49 ± 0.23	8.11 ± 1.27
$e\mu$	0.47 ± 0.20	2.59 ± 1.10	0.77 ± 0.17	4.20 ± 0.92
$e\tau$	2.13 ± 0.21	11.63 ± 1.15	1.96 ± 0.27	10.69 ± 1.46
$\mu\mu$	0.20 ± 0.06	1.08 ± 0.33	1.75 ± 0.25	9.53 ± 1.38
$\mu\tau$	0.99 ± 0.16	5.38 ± 0.87	1.31 ± 0.22	7.14 ± 1.20
$\tau\tau$	4.46 ± 0.65	24.33 ± 3.56	1.58 ± 0.24	8.60 ± 1.31

Table 5.1: *Predicted background contributions from Monte Carlo for each of the 6 classified lepton channels described in chapter 6.*

by two back-to-back leptons with energy $E_l = \sqrt{s}/2$ where $l \equiv e$ or μ. Electron and muon pair events are comparatively easier to remove than tau pair events, since their energy is shared by the undetected neutrinos. The main four fermion background arises from Z^0 pair events, when one Z^0 decays to a pair of charged leptons and the other to neutrinos (which means missing energy).

For the $W^+W^- \rightarrow l\nu q\bar{q}$ events used in the TGC analysis, the background contributions were assessed at each E_{cm} from five independent samples of MC (listed in appendix B). Table 5.2 lists the predicted background contribution from each source after all the appropriate selection cuts have been applied. As can clearly be seen, the dominant background arises from di-jet $Z^0/\gamma \rightarrow q\bar{q}(\gamma)$ events. Single W ($e^+e^- \rightarrow We\nu$) and non-TGC dependent four fermion backgrounds (for example $ZZ \rightarrow q\bar{q}\nu\bar{\nu}$ and $ZZ \rightarrow q\bar{q}ll$) are also important backgrounds, particularly for the $\tau\nu q\bar{q}$ channel.

Source	192 GeV	196 GeV	200 GeV	202 GeV
non-tgc	1.98 ± 0.11	5.74 ± 0.21	5.54 ± 0.20	2.80 ± 0.10
$Z^0/\gamma \rightarrow q\bar{q}(\gamma)$	3.63 ± 0.20	9.13 ± 0.51	7.82 ± 0.41	3.36 ± 0.20
$e^+e^- \rightarrow e^+e^-q\bar{q}$	1.32 ± 0.09	4.26 ± 0.26	3.57 ± 0.23	1.82 ± 0.12
$e^+e^- \rightarrow e^+e^-\tau^+\tau^-$	0.03 ± 0.01	0.03 ± 0.02	0.00 ± 0.00	0.01 ± 0.01
2γ	0.36 ± 0.15	0.77 ± 0.25	0.30 ± 0.15	0.15 ± 0.07
Total	7.31 ± 0.28	19.93 ± 0.65	17.23 ± 0.54	8.13 ± 0.27

Table 5.2: *Predicted background number of events (normalized to the data) at each E_{cm} for the TGC analysis described in chapter 8. The 'non-tgc' source refers to TGC independent four fermion final states. These figures do not include cross migration between the three WW$\rightarrow l\nu q\bar{q}$ channels.*

Four fermion processes

As discussed in section 2.2.2 and above, the four fermion diagrams cannot be separated from the CC03 signal processes when they have the same final states (and often similar event kinematics). Moreover, they interfere with the signal diagrams making it impossible to measure the CC03 cross section independently. Including the W pair production diagrams, there are 20 leading order diagrams that give rise to a $e\nu q\bar{q}$ final state and 10 each for the $\mu\nu q\bar{q}$ and $\tau\nu q\bar{q}$ final states[3]. It is important that these diagrams are accurately modelled in the MC.

---

[3] These are referred to as CC20 and CC10 respectively (see section 2.2.2). The extra 10 diagrams for the $e\nu q\bar{q}$ channel arise through quasi t-channel processes.

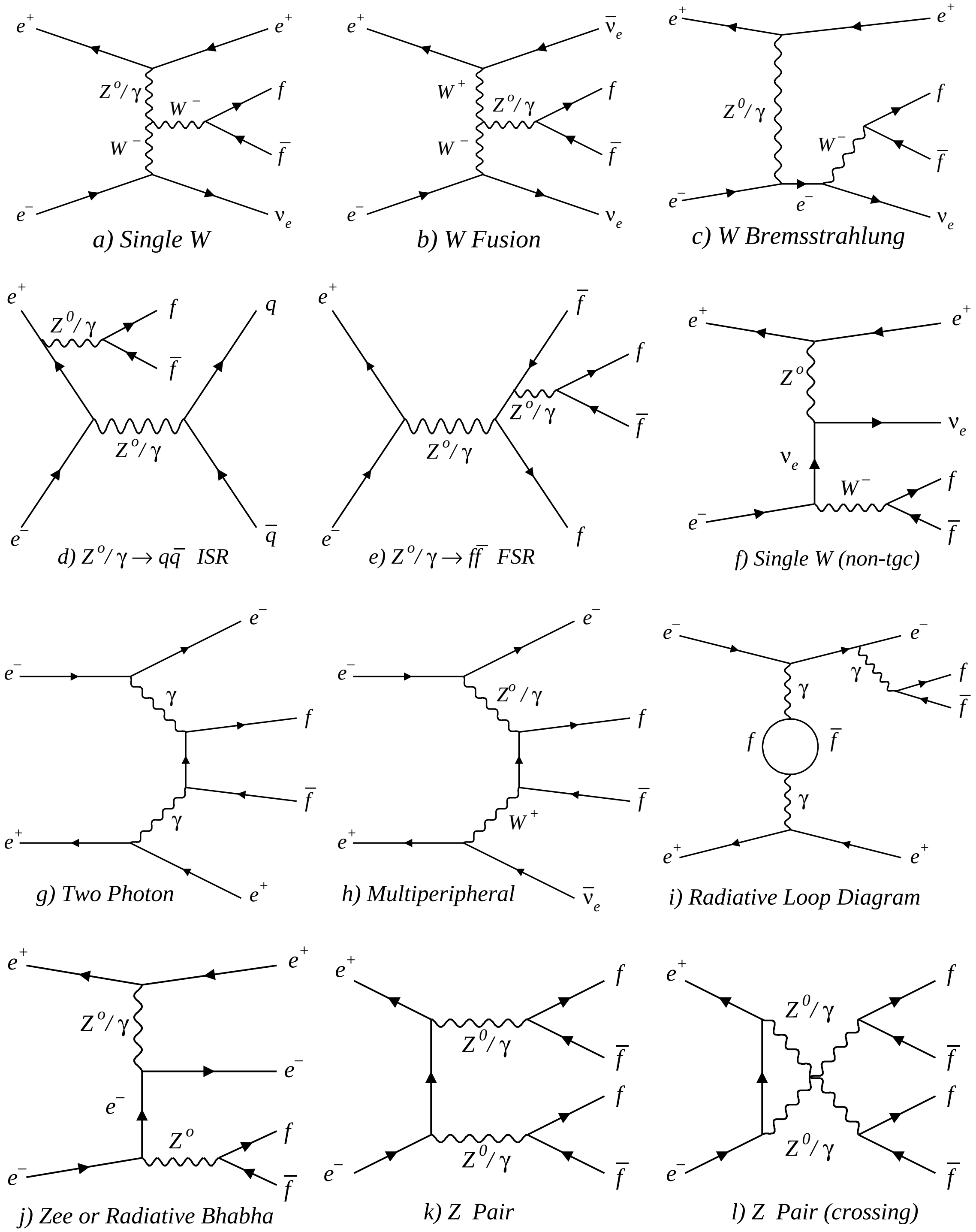

a) Single W

b) W Fusion

c) W Bremsstrahlung

d) $Z^o/\gamma \rightarrow q\bar{q}$ ISR

e) $Z^o/\gamma \rightarrow f\bar{f}$ FSR

f) Single W (non-tgc)

g) Two Photon

h) Multiperipheral

i) Radiative Loop Diagram

j) Zee or Radiative Bhabha

k) Z Pair

l) Z Pair (crossing)

Figure 5.2: *Example Feynman diagrams for some of the many background processes.*

Some of the non-WW four fermion processes are TGC dependent (for example figure 5.2a and b). In both these diagrams, the γ can be replaced by a Z^0 but these diagrams are heavily suppressed by the mass of the gauge boson. (The W fusion process will only contribute to the background if either the photon converts or the Z^0 decays to fermion/anti-fermion pair). In the single W diagram, the scattered electron normally escapes down the beam pipe, but when it is observed the event can masquerade as signal. These processes are discussed further in section 7.2.

As well as the charged current processes, there are 48 neutral current diagrams giving $e^-e^+q\bar{q}$ final states, and 24 for both $\mu^-\mu^+q\bar{q}$ and $\tau^-\tau^+q\bar{q}$ final states. Examples of some of these are shown in diagrams 5.2 d, e, g, j, k and l. (Figure 5.2i is also a neutral current process, but it is not leading order). The Z^0 pair production diagrams are important backgrounds when one of the Z^0s decays hadronically, and the other decays to two charged leptons (with one lepton escaping detection down the beam pipe) or else decaying to two neutrinos (and one of the jet tracks is mis-identified as a lepton). The Compton scattering Zee process differs from Z^0 pair production in that the final state electron or positron travels along the beam direction which means that there is missing energy, but not missing transverse energy. Special cuts are applied in the selection to remove these processes.

Other background processes

In general non-four fermion processes do not cause interference effects with the signal, but as some of them have very large cross sections at LEP 2 energies, they can contribute significantly to the background if they are mis-identified as signal.

Two photon events (figure 5.2g) form an important background in the WW $\rightarrow l\nu l\bar{\nu}$ selection. There are two types of two photon event: *'untagged'*, where both beam electrons are lost down the beam pipe and *'tagged'* where one of the beam electrons is observed in the detector. (Only rarely are both the scattered electron and positron observed in *'double tagged'* events). The MIP plug cuts, described in the previous chapter, were designed to remove this type of background in the $l\nu l\bar{\nu}$ selection. In the WW$\rightarrow l\nu q\bar{q}$ selection, the two photon background is less important since the invariant mass of the hadronic system is low compared to $e^+e^- \rightarrow \mathrm{W}^+\mathrm{W}^-$ events and these events can only be confused with signal if one of the electrons is tagged.

Di-lepton processes (illustrated in figure 5.3) are the main background to the WW $\rightarrow l\nu l\bar{\nu}$ selection. In the absence of ISR, the s-channel processes will occur at full centre of mass energy and the lepton pairs will be produced colinearly. If either the incident electron or positron radiates an ISR photon, the four momenta of the incident particles will be asymmetric so that the event will be boosted in the laboratory frame, and the leptons produced will be acollinear. Appropriate cuts (described in section 5.4) can reduce this background substantially, and in particular the requirement that the final state leptons are acoplanar ensures that the missing momentum is transverse to the beam axis.

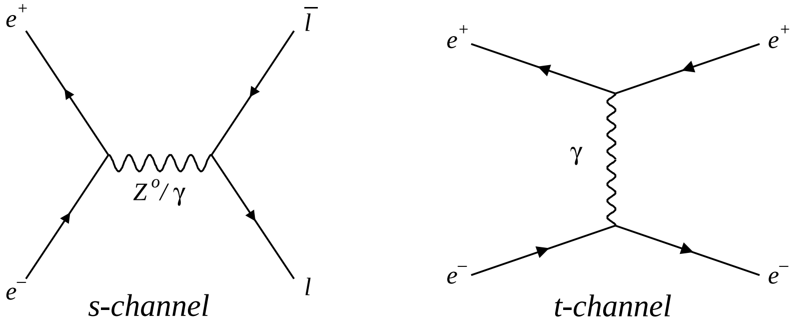

Figure 5.3: *Di-lepton background processes in the s and t-channels.*

As shown in table 5.2, the $Z^0/\gamma \rightarrow q\bar{q}(\gamma)$ background is the dominant background in the WW $\rightarrow l\nu q\bar{q}$ selection and has a cross section $\sim$ 13 times higher than the signal [50]. Although dissimilar to the signal process, $Z^0/\gamma \rightarrow q\bar{q}(\gamma)$ events can contribute to the accepted background either when one of the tracks in the quark jets is mis-identified as a lepton from W decay, or when one of the incident or final state fermions radiates a photon which then converts into a lepton pair and only one of the leptons is detected. This is illustrated in figures 5.2 d and e). (The radiative photon can be replaced by a Z^0, but this process is suppressed due to the mass of the gauge boson.) If the ISR photon is radiated with an energy such that the Z^0 is on shell, the quark jets will be boosted and have similar invariant mass to jets produced from W-decay.

5.3 Monte Carlo Simulation

In high energy physics experiments, Monte Carlo (MC) methods are used extensively to simulate data from theoretical models, which can then be compared with real experimental data. MC has many uses in particle physics, including testing and refining analyses programs, simulating new or rare physics processes, and calculating the efficiency and purity of event selections. One of the main advantages of MC is that the *'truth'* (or tree level) information is available for each simulated event as well as the *'observed'* (or measured) physical parameters. In this thesis, MC simulated events were used in the WW→lepton classification analysis (chapter 6) to determine cut positions and estimate the background contributions in the improvements to the leptonic branching ratio measurements. In the TGC analysis (chapter 8) MC samples were used as reference samples (to determine calibration curves by reweighting), estimate backgrounds and also in the systematic checks and tests of the method. The same event selections were applied to the MC samples as the data. A list of all the MC samples used in these analyses may be found in appendix B.

Events are generated in a three stage process. The first stage concerns primary parton generation where particles' 4-vectors are simulated by one of the event generator packages. Events containing quarks and gluons are then fragmented in a hadronization routine. Hadronization is the process which combines the initial partons (ie quarks and gluons) to form hadronic jets (in the non-perturbative region of QCD) which may subsequently decay. There are two separate phenomenological models widely used in OPAL to describe this process. The first, and most developed is based on the *"Lund string"* fragmentation model [53] and is implemented in the JETSET [54] program. The second uses a *"cluster"* fragmentation model and is incorporated in the HERWIG [55] event generator.

Finally, events are passed through the OPAL detector simulation program GOPAL [56]. GOPAL simulates the precise geometrical configuration of the OPAL detector using the GEANT [57] detector modelling package to simulate detector response and the effect of particles passing through matter. It models both the interactions of particles with detector material and the possible decays of particles with lifetimes such that they are likely to decay within the detector volume. The output from GOPAL is intended to match real data as closely as possible. Events are then processed (in the same way as the data) by the reconstruction program ROPE [38] for later physics analysis.

5.3.1 Event Generators

Different event generators have different specifications and generate different processes. For example, some are dedicated two photon generators, whereas others can be used to generate the full range of four fermion diagrams. Some can be used to simulate processes beyond the SM, whereas others have different treatments of, for example, Coulomb corrections, fermion masses, or particle polarization. Hence it is advisable to use a range of samples generated with different generators as systematic checks and background estimates. A brief description of the main generators used in the two WW analyses is given below. Further details of the MC generators used at LEP 2 may be found in [8] Vol II, [58] and the individual references.

- **EXCALIBUR** [59] was the main four fermion event generator used in the TGC analysis. It was used to generate all the reference signal samples with both SM and anomalous couplings. It also generated separate non-TGC background samples for the TGC analysis, and $l\nu l\bar{\nu}$ background processes for the improved branching ratio measurements. To speed computation, EXCALIBUR treats the fermions as massless particles and so cuts have to be applied during generation to avoid singularities in the phase space. It includes the widths of the $\mathrm{W}^{\pm}$ and Z^0 bosons but not diagrams where a Higgs boson couples to fermions since interference effects are small in the limit of massless fermions. It employs a simplified treatment of ISR without the transverse momentum of the photon. However, previous systematic studies [60] comparing EXCALIBUR with the KORALW generator (which has a better treatment of ISR), have indicated that the overall effects are small. It is interfaced to the JETSET hadronization package.

- **KORALW** [61] generated all the CC03 samples used to determine the cut positions in the WW classification analysis. KORALW CC03 samples generated with different values of M_{W} were used in the TGC analysis for the W mass systematic (described in section 8.3). Four fermion KORALW samples were used for the MC generator systematic. Tau and muon pair MC samples produced with the related generator, KORALZ [62], were used as backgrounds in the improvements to the leptonic branching ratio measurements.

KORALW is similar to EXCALIBUR but is a CC03 generator which takes account of all the diagrams by using GRACE [63] matrix elements to calculate the four fermion cross sections. KORALW has a better treatment of ISR using the Yennie-Frautschi-Suura exponentiation (YFS) [64]. FSR is implemented via PHOTOS [65] and the effect of the Coulomb correction [66] between the W bosons is modelled. It is interfaced to the TAUOLA [67] package which correctly models τ polarization (this effects the momentum distribution of τ decay products). It links to the JETSET hadronization package.

- **GRC4F** [68] is a full four fermion event generator. It was used to generate the background processes: $e^+e^- \rightarrow ee\tau\tau$ and $e^+e^- \rightarrow eeqq$ in the TGC analysis and $e^+e^- \rightarrow eell$, $e^+e^- \rightarrow eeqq$ and $e^+e^- \rightarrow llqq$ in the improvements to leptonic branching ratio measurements. GRC4F uses the GRACE system to generate the matrix elements. Fermion masses are non-zero and $\mathrm{W}^{\pm}$ and Z^0 widths are incorporated as well as Coulomb corrections between the W bosons. In the TGC fragmentation systematic study, two GRC4F samples were generated with the same four-vectors but interfaced separately with HERWIG or JETSET (see section 8.3). Problems for some types of events in certain regions of phase space have recently been noticed, and these are discussed further in section 9.2.

- **HERWIG** is general purpose event generator which uses parton showering to simulate higher order QCD effects. In addition to the fragmentation and $\mathrm{Z}^0/\gamma \rightarrow q\bar{q}$ background systematic studies, HERWIG generated samples were used to simulate the two photon backgrounds in the TGC analysis. (In the improvements to the leptonic branching ratio measurements, VERMASEREN [69] was used to simulate this process).

- **KK2F** [70] was used to generate the $e^+e^- \rightarrow \mathrm{Z}^o/\gamma \rightarrow q\bar{q}$ backgrounds for the TGC analysis. It covers the complete region of phase space with order α treatment of ISR and FSR. It links to the PYTHIA/JETSET [71] fragmentation package. (Pythia is a multi-purpose generator which was also used to generate a separate sample of $\mathrm{Z}^0/\gamma \rightarrow q\bar{q}$ events for the TGC systematic checks.)

The $e^+e^- \to e^+e^-$ and $e^+e^- \to e^+e^-\gamma(\gamma)$ background processes in the improvements to the leptonic branching ratio measurements, were simulated by the BHWIDE [72] and TEEGG [73] generators respectively.

5.4 Selection of W Pair Events

Selection of W pair events is a necessary prerequisite for many analyses including measurements of W^+W^- production cross section, $W^\pm$ mass and triple gauge coupling parameters and also as a starting point in certain other analyses (for example ZZ production) which need to reject W^+W^- background. The $WW \to l\nu l\bar{\nu}$ and $WW \to l\nu q\bar{q}$ events used for the WW classification and TGC analyses described in this thesis, were selected using the standard OPAL W^+W^- set of routines explained in [74]. In OPAL W pair selection proceeds in three distinct stages, each part corresponding to one of the three final state topologies. The three event selections are mutually exclusive. Events which pass the initial preselection criteria [75] for reconstructed events are first considered for the $WW \to l\nu l\bar{\nu}$ event selection. If an event passes the selection criteria for a $WW \to l\nu l\bar{\nu}$ event it is not considered further. Failing events are next considered as possible $WW \to l\nu q\bar{q}$ candidates. Only events failing both the $WW \to l\nu l\bar{\nu}$ and $WW \to l\nu q\bar{q}$ selections are considered as possible $WW \to q\bar{q}q\bar{q}$ candidates. The $WW \to l\nu l\bar{\nu}$ selection is completely cut based, whereas the $WW \to l\nu q\bar{q}$ and $WW \to q\bar{q}q\bar{q}$ selections rely on multivariate likelihood selections after the preselection cuts.

General Preselection cuts

For each of the three selections, it is required that the main subdetectors providing information to reconstruct the events are fully operational at the time the events were recorded. For example the central tracking chambers, electromagnetic calorimeters (and hadronic calorimeters for $WW \to l\nu q\bar{q}$ and $WW \to q\bar{q}q\bar{q}$ events) and muon chambers are all required to have good status. Depending on the class of event under study, certain other criteria are imposed; for example to reject cosmic rays or beam gas events, and ensure that the selected events are well reconstructed. Examples of these cuts include constraints on the distance of closest approach to the interaction region ($|d_0|$ and $|z_0|$), minimum requirements for track momenta and the number of hits in the tracking chambers. Details of all the standard OPAL preselection criteria for each event class may be found in [75].

5.4.1 Selection of $W^+W^- \rightarrow l^+\nu l^-\bar{\nu}$ Events

The WW $\rightarrow l\nu l\bar{\nu}$ event selection is optimized to identify events with a pair of charged leptons and significant missing transverse momentum (p_t^{miss}). Candidate WW$\rightarrow l\nu l\bar{\nu}$ events must pass a series of cuts (preselection, track quality and kinematic) which are designed to isolate the signal whilst rejecting the dominant backgrounds. The selection does not attempt to remove non-CC03 SM processes which share the same final state $l\nu l\bar{\nu}$ topology. Initially events are selected from a low multiplicity preselection which requires there to be at least one and no more than eight charged tracks, and the total number of charged tracks and clusters must not exceed 15. The number of jets[4] must be between one and three. Additional preselection track and cluster energy quality cuts ensure that only well reconstructed tracks are used for physics analysis. Full details of these are given in [41, 77, 78].

Different sets of cuts are then applied to surviving events, depending on the number of observed jets. The majority (89%) of preselected events are two jet, with only 6% and 5% of events classed respectively as one or three jet events. In most one jet events, the decay products of one of the W's are either not reconstructed or only partially reconstructed in the forward direction. Sometimes the decay particles from both W's are reconstructed within the same cone. Three jet events correspond to events where there is significant photon radiation observed in the detector (in general the two highest energy jets are taken to be the lepton candidates).

For the most common di-jet events, the number of additional cuts applied depends upon the ratio of the net transverse momentum of the two jet system divided by the beam energy (x_t). The most important cuts require that the acollinearity[5] angle between the two leptons exceed 5^o (to reduce back-to-back fermion pair and ZZ $\rightarrow l^+l^-\nu\bar{\nu}$ events) and $x_t > 5$% (so that the total missing momentum vector points away from the beam axis, thereby eliminating events in which ISR photons escape down the beam pipe). Other cuts are placed on the x_t significance, $|\cos\theta|$ distribution, number of track and cluster hits in various subdetectors,

---

[4] In each event the reconstructed tracks and energy clusters are grouped into jets using a cone jet finding algorithm [76] with a cone half-opening angle of 20^o and a jet energy threshold of 2.5 GeV.

[5] The acollinearity angle is defined as the supplement of the angle between the two charged leptons.

track association, the scaled missing transverse momentum with respect to the transverse thrust axis (a_t^{miss}/E$_{\text{Beam}}$) and dedicated cuts to remove specific background processes (for example MIP plug cuts to remove $\gamma\gamma \rightarrow \mu^+\mu^-$ background). A full listing of all these cuts, and the criteria under which they are applied may be found in [78]. It should be noted that the MIP plug cuts and the definition of a MIP plug coincidence for the WW $\rightarrow l\nu l\bar{\nu}$ selection are not the same as those described in chapter 4.

Analogous cuts are applied to single and tri-jet events. Single jet events will only be accepted if they pass any one of three separate selections (which include additional timing cuts to reject cosmics and tighter cuts on x_t to suppress two photon backgrounds). The tri-jet event selection is designed to accept $l\nu l\bar{\nu}\gamma$ events but reject two-fermion $\tau\tau\gamma$ background. The inclusive WW$\rightarrow l\nu l\bar{\nu}$ selection efficiency for 189 GeV events was (82.1 ± 1.2)% with purity 90.3% [52]. Figure 5.4 is an example of a selected di-jet event used in the leptonic branching ratio measurements at 189 GeV.

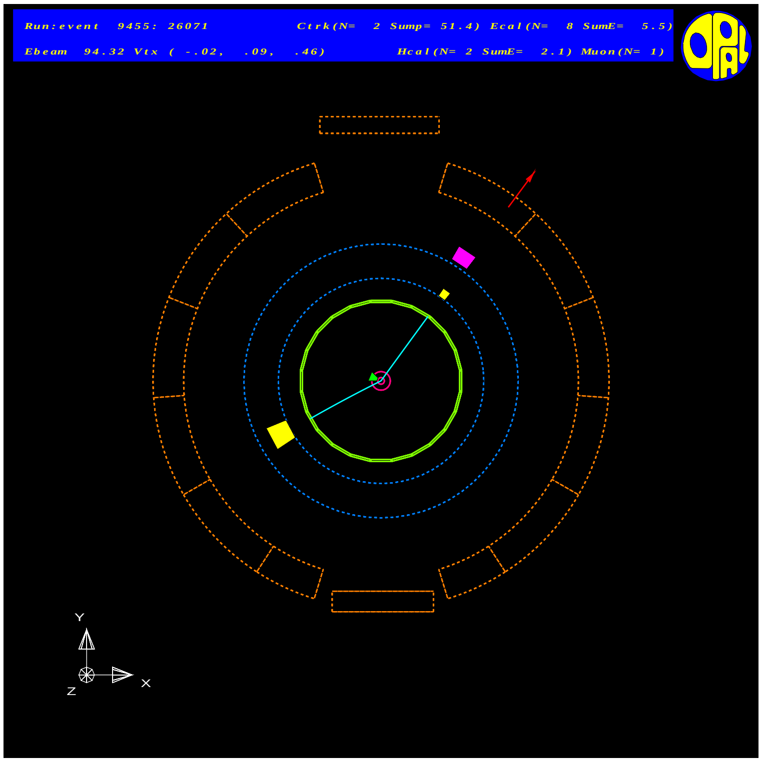

Figure 5.4: *Transverse view of a reconstructed* $W^+W^- \rightarrow \mu^+\nu_\mu\tau^-\bar{\nu}_\tau$ *event, where the* τ^- *decays promptly to an electron. The muon is identified by hits in the muon chambers (red arrow) and also a small amount of energy deposited in the hadron calorimeters (magenta block). The electron is identified by energy deposited in the electromagnetic calorimeter (yellow block). The small turquoise triangle near the inner detectors indicates a noise hit in one MIP plug layer.*

Selected events are then classified according to lepton flavour. Electrons are initially identified using dE/dx and the ratio of energy deposited in the electromagnetic calorimeters to track momentum (E/p). Tracks which are consistent with originating from photon conversions are removed. Muons are initially identified as tracks in the central detector with associated hits in the hadron calorimeters or muon chambers (and only a small amount of energy deposited in the electromagnetic calorimeters). Hadronically decaying taus are identified using hadron identification and from track multiplicity. Second stage lepton classification algorithms [79] based on acollinearity dependent momentum cuts are then applied to separate leptonically decaying taus. This is the subject of the next chapter.

A total of 278 $W^+W^- \to l^+\nu l^-\bar{\nu}$ events were selected from 183.14 ± 0.55 pb^{-1} of data collected at $\sqrt{s}$ =188.64 GeV, which compares to the SM expectation of 290.0 ± 8.9 events [80] (assuming SM cross sections). The breakdown of the number of events selected for each of the six lepton classification channels is given in table 5.3.

Channel	Data	Expected
ee	39	34.4 ± 1.4
$e\mu$	70	69.8 ± 2.2
$e\tau$	45	62.5 ± 3.6
$\mu\mu$	33	37.8 ± 1.6
$\mu\tau$	57	56.5 ± 2.6
$\tau\tau$	34	29.0 ± 2.5

Table 5.3: *Number of data events selected in each WW$\to l\nu l\bar{\nu}$ channel compared with Monte Carlo predictions (SM signal + background) after the acollinearity dependent momentum cuts (described in the next chapter) have been applied.*

5.4.2 Selection of $W^+W^- \to l\nu q\bar{q}$ Events

The selection of WW $\to l\nu q\bar{q}$ events is more complicated than for WW $\to l\nu l\bar{\nu}$ events and is based on a series of relative likelihood selections after initial preselection cuts and identification of the 'best' lepton candidate track in the event. Events are then categorized according to lepton type. Full details of the event selection may be found in [50] and only a brief summary of the salient features is given here.

WW $\to$ e$\nu q\bar{q}$ and WW $\to \mu\nu q\bar{q}$ events are characterized by two well separated hadronic jets and a high momentum charged lepton, plus missing energy from the unobserved neutrino. In WW $\rightarrow \tau\nu q\bar{q}$ events, the visible τ decay products will tend to have lower energies than the prompt leptons in the other channels, due to the extra neutrino(s). Both one and three prong decays of the τ are considered, which results in six possible decay chains for the leptonically decaying W boson: W $\rightarrow e\nu_e$, W $\rightarrow \mu\nu_\mu$, W $\rightarrow \tau\nu_\tau \rightarrow e\nu_e\nu_\tau\bar{\nu}_\tau$, W $\rightarrow \tau\nu_\tau \rightarrow \mu\nu_\mu\nu_\tau\bar{\nu}_\tau$, W $\rightarrow \tau\nu_\tau \rightarrow h(n\pi^0)\nu_\tau\bar{\nu}_\tau$ and W $\rightarrow \tau\nu_\tau \rightarrow 3h(n\pi^0)\nu_\tau\bar{\nu}_\tau$. The WW$\rightarrow l\nu q\bar{q}$ event selection in fact consists of three separate selections, one for each of the semi-leptonic decay channels, although the selections for $e\nu q\bar{q}$ and $\mu\nu q\bar{q}$ events are very similar.

Analogous to the initial low multiplicity preselection cuts for WW$\rightarrow l\nu l\bar{\nu}$ events, candidate WW $\rightarrow l\nu q\bar{q}$ events are only considered if they pass initial high multiplicity preselection criteria [75] carried out by the filter. (Events passing the WW$\rightarrow l\nu l\bar{\nu}$ selection are not considered as $l\nu q\bar{q}$ candidates.) To remove events without quarks in them, the high multiplicity selection requires each event to have at least five charged tracks or six energy clusters in the electromagnetic calorimeters. Additional track quality cuts are placed on $|d_0|$ and $|z_0|$, the minimum number of track hits in the central detectors (or the minimum energy deposited in each cluster), track momentum and angles. A loose cut is also placed on the visible energy (scaled by the E_{cm}) to remove two photon background.

Charged Lepton Identification

The first stage in the main WW $\rightarrow l\nu q\bar{q}$ selection is to identify the track in each event (surviving the initial track quality cuts) with the highest probability of being a lepton in each of the six possible semi-leptonic decay chains. Even events that do not have a lepton will still have a lepton track assigned to them, however improbable this may be, in order to retain maximum efficiency at this stage. A loop is made over all the charged tracks and each track (or tracks in the case of three prong τ decays) is assigned six probabilities corresponding to the six decay chains. There are two aspects in determining these probabilities in each event: identifying which track is a lepton and whether it came directly from the W decay. To estimate these probabilities, energy or momentum loss in the tracking chambers/deposited in the electromagnetic calorimeters, number of hits in the muon chambers and hadron calorimeters, lepton momentum and isolation from other tracks are considered. This information is then combined in a relative likelihood, and the best lepton candidate is taken to be the one with the highest absolute likelihood value. No events are rejected during this stage.

These best lepton candidates are used to determine the event kinematic properties. The tracks and clusters not associated with the track(s) identified as the best lepton candidate are forced into a two or three jet topology using the Durham algorithm [81]. Energy corrections are then applied with the Globally Corrected Energy (GCE) [82] algorithm. This algorithm sums the energy of all the tracks and clusters in each event and corrects for any double counting of the jet energy.

Loose Preselection

The main purpose of the preselection cuts is to remove as much of the $\mathrm{Z}^0/\gamma \rightarrow q\bar{q}(\gamma)$ background as possible. This also improves the performance of the likelihood in the next stage of the selection. For each of the three selections ($e\nu q\bar{q}$, $\mu\nu q\bar{q}$ and $\tau\nu q\bar{q}$), a series of loose cuts are applied using the best lepton candidates to determine the kinematic event properties. Exact details of these cuts and their values are given in [50], but the cut variables include the invariant mass of the system, the lepton and visible energies, track and cluster multiplicities, lepton identification probabilities, the angle between the charged lepton and missing momentum vector, the track polar angle and energy of the highest energy isolated photon. Additional cuts are applied to the WW → $\mathrm{e}\nu q\bar{q}$ channel to remove radiative $\mathrm{Z}^0/\gamma \rightarrow q\bar{q}(\gamma)$ events where the ISR photon converts into an e^+e^- pair and one of the electrons is mis-identified as an electron from W decay. This preselection is over 97% efficient for WW → $\mathrm{e}\nu q\bar{q}$ and WW → $\mu\nu q\bar{q}$ events but reduces the $\mathrm{Z}^0/\gamma \rightarrow q\bar{q}(\gamma)$ background by an order of magnitude.

Relative Likelihood Selection

In order to further improve the signal/background separation, and in particular to reduce the $\mathrm{Z}^0/\gamma \rightarrow q\bar{q}$ background, a relative likelihood method is used for all events passing the pre-selection cuts. There are six likelihood selections corresponding to each of the six decay chains. Each selection has a different set x_i of kinematic variables used to construct its likelihood. Each likelihood is determined by comparing the observed x_i values with the expected signal MC distributions for that decay chain, in order to calculate the probabilities $P_i(x_i)$. The likelihood $L_{l\nu q\bar{q}}$ is evaluated as the product of the individual probabilities (for each decay chain). Similarly, the background likelihood for $\mathrm{Z}^0/\gamma \rightarrow q\bar{q}(\gamma)$ events ($L_{q\bar{q}}$) is obtained using the MC distributions of $\mathrm{Z}^0/\gamma \rightarrow q\bar{q}(\gamma)$ events. The relative likelihood $\mathcal{L}_{l\nu q\bar{q}}$ is then simply:

$$\mathcal{L}_{l\nu q\bar{q}} = \frac{L_{l\nu q\bar{q}}}{L_{l\nu q\bar{q}} + f \times L_{q\bar{q}}} \tag{5.4}$$

where the normalization factor f, is the estimated ratio of preselected MC background and MC signal cross sections. Full details of the kinematic variables used to construct these likelihoods and their distributions are given in [50]. Essentially there are five main types of variables: those that relate to the isolation of the lepton candidate, the lepton identification probability, the energy or momentum of the lepton candidate, the event topology (eg angles between the lepton and the nearest jet or missing momentum vector) and the global event properties (for example visible energy, y-cut value - where the event changes from two to three jets). To select events for the TGC analysis, two different sets of MC reference distributions were used: one for the 192 GeV data and the other for the 196, 200 and 202 GeV data.

Events are selected if they have a likelihood value greater than 0.5. Only events that fail the WW $\rightarrow$ e$\nu q\bar{q}$ and WW $\rightarrow$ $\mu\nu q\bar{q}$ likelihood selections are passed to the WW $\rightarrow$ $\tau\nu q\bar{q}$ likelihood selection. Approximately 33% of WW $\rightarrow$ $\tau\nu q\bar{q}$ events pass either the WW $\rightarrow$ e$\nu q\bar{q}$ or WW $\rightarrow$ $\mu\nu q\bar{q}$ selections and the cross migration between the channels is resolved during the next stage of the selection procedure. Events passing any of the likelihood selections are considered to be WW$\rightarrow$$l\nu q\bar{q}$ candidates.

The relative likelihood selections are optimized to reduce the dominant $\mathrm{Z}^0/\gamma \rightarrow q\bar{q}(\gamma)$ background by a further factor of 100. However, there are several sources of four-fermion background still present at this stage. These include $e^-e^+q\bar{q}$ events from ZZ and Zee processes which contaminate the WW $\rightarrow$ e$\nu q\bar{q}$ sample, and $\mu^-\mu^+q\bar{q}$ and $\tau^-\tau^+q\bar{q}$ events selected as either WW $\rightarrow$ $\mu\nu q\bar{q}$ or WW $\rightarrow$ $\tau\nu q\bar{q}$ events. Single W (W$e\nu$) and Z^0 pair $\nu\nu q\bar{q}$ events are also contribute to the WW $\rightarrow$ $\tau\nu q\bar{q}$ selection. Special cuts (for example further likelihood discriminants, kinematic fits and exploiting the different event topologies) are imposed to reduce these backgrounds. Details of these cuts may be found in [50].

Event Categorization

The final stage in the selection procedure is to classify the events according to lepton flavour (either $e\nu q\bar{q}$, $\mu\nu q\bar{q}$ or $\tau\nu q\bar{q}$). Many events pass more than one relative likelihood selection, and there is considerable cross talk between the channels. In order to reduce this migration and unambiguously determine the event class, additional relative likelihood discriminants are constructed in the same way as before, according to the event categorization.

As an example, consider an event that passes both the WW → e$\nu q\bar{q}$ and WW → $\mu\nu q\bar{q}$ selections. In this case, two relative likelihoods are constructed (corresponding to the two selections) from six kinematic variables: lepton energy deposited in the electromagnetic calorimeters, electron and muon identification probabilities, invariant masses of the neutrino and electron (and neutrino and muon) candidates (where the neutrino momentum is considered to be the missing momentum), and the muon momentum in the $\mu\nu q\bar{q}$ selection. The three variables associated with the $e\nu q\bar{q}$ selection are used to construct a categorization weight defined as:

$$C^{\mu\bar{\nu}_\mu}_{e\bar{\nu}_e q\bar{q}} \;=\; \frac{L^{e\bar{\nu}_e}_{e\bar{\nu}_e q\bar{q}}}{L^{e\bar{\nu}_e}_{e\bar{\nu}_e q\bar{q}} + L^{\mu\bar{\nu}_\mu}_{e\bar{\nu}_e q\bar{q}}} \tag{5.5}$$

where the subscripts refer to the event selection and the superscripts refer to the alternative hypothesis being tested. This is the relative likelihood that an event which is selected by the WW → e$\nu q\bar{q}$ selection is genuinely a WW → e$\nu q\bar{q}$ event as opposed to being a WW → $\mu\nu q\bar{q}$ event. The likelihood terms in the denominator ($L^{e\bar{\nu}_e}_{e\bar{\nu}_e q\bar{q}}$ and $L^{\mu\bar{\nu}_\mu}_{e\bar{\nu}_e q\bar{q}}$) are evaluated from the reference MC distributions of WW → e$\nu q\bar{q}$ and WW → $\mu\nu q\bar{q}$ events passing the WW → e$\nu q\bar{q}$ likelihood cut. Categorization weights $C^{\mu\bar{\nu}_\mu}_{e\bar{\nu}_e q\bar{q}}$ and $C^{e\bar{\nu}_e}_{\mu\bar{\nu}_\mu q\bar{q}}$ are constructed for both hypotheses. The difference between these two quantities (ie the discriminant) is used to determine the event class.

Other categorization weights, likelihoods and discriminants are constructed for the other W decay chains in a similar manner and are described in [50]. Additional algorithms are applied to selected WW → $\tau\nu q\bar{q}$ events when the τ decays hadronically, to improve the identification of the τ decay products [83]. All these quantities significantly reduce the number of events incorrectly classified. The selection efficiencies and purities vary slightly for each E_{cm} event sample (due to statistical fluctuations). The 200 GeV data set, for example, has an overall selection efficiency of 86.3 ± 1.7 % and purity 89.8 % [84].

5.4.3 Additional Criteria for TGC Analyses

The selection of $\mathrm{W^+W^-} \rightarrow l\nu q\bar{q}$ events for the TGC analyses (based on the angular distribution methods, described in chapter 7) is slightly different to the selections used in the W mass, W pair cross section and TGC event rate analysis (which depends only on the number of events selected). For the TGC analysis described in this thesis, it is important to have fully reconstructed events with well defined tracks. In OPAL a complementary selection of trackless $\mathrm{WW} \rightarrow l\nu q\bar{q}$ events exist (which considers events with forward leptons outside the OPAL detector acceptance and events with energy clusters but not well reconstructed tracks). These events are not used for the TGC analysis in this thesis.

The 'standard' WW selections try to avoid using cuts which are correlated with the mass of the reconstructed W particles as this might introduce biases to the W mass measurement. The TGC analyses are not sensitive to these biases and so additional 'hard' cuts can be imposed to further improve the quality of the signal events and reject more background. These cuts are described in the kinematic fit section at the end of this chapter. An evaluation of the $\mathrm{WW} \rightarrow l\nu q\bar{q}$ likelihood selections for TGC studies has been made [85].

5.4.4 Selection of $\mathrm{W^+W^-} \rightarrow q\bar{q}q\bar{q}$ Events

Although high in statistics, fully hadronic events are not used in any of the analyses described in this thesis and so no details of the event selection are given here. They can be found in [86]. Essentially the four quark selection is similar to that for semi-leptonic events: preselection cuts followed by relative likelihood selections. Like the semi-leptonic channel the main background is from $\mathrm{Z^0}/\gamma \rightarrow q\bar{q}$ events where the quarks fragment into four jets, and similarly it is impossible to separate this background using conventional cut-based algorithms. For comparison with the other channels, the selection efficiency for the 200 GeV sample is 86.9 ± 1.7% and purity 76.9 % [84].

5.5 Kinematic Fitting

In order to improve the resolution of the reconstructed angles used in the TGC analysis (and discussed in section 7.3), the selected WW $\to l\nu q\bar{q}$ events undergo a series of constrained kinematic fits[6] [87]. These fits are based on energy and momentum conservation (in fact this corresponds to four separate constraints: the three momenta p_x, p_y, p_z and energy). It is assumed that any ISR photons radiated along the beam direction can be neglected so that the incident e^+e^- interact at the full beam energy, and overall there is zero net momentum in the laboratory frame. Constraints are also imposed on the W masses (this is acceptable for the TGC analyses). The three separate kinematic fits performed on the semi-leptonic events are:

1C Momentum and energy conservation. There are four constraints, but the three neutrino momentum components are unknown. This leaves one net constraint and hence this fit is called a 1C fit.

2C Equal mass constraint. An additional constraint is imposed by insisting that the invariant mass of both W bosons be equal.

3C Both W boson masses are constrained to the value used in the MC event generator, 80.33 GeV, in addition to the requirements of the 2C fit. Actually this is an over simplification, because it does not take into account the finite W width. This is explained further in [49].

The first kinematic fit is applied to all selected WW $\to$ e$\nu q\bar{q}$ and WW $\to \mu\nu q\bar{q}$ events. The fit is required to converge with fit probability greater than 0.001 for the event to be accepted. WW $\to$ e$\nu q\bar{q}$ and WW $\to \mu\nu q\bar{q}$ events which pass the 1C fit are also tested for the 3C fit (with the same fit probability cut) to improve the measurement of the kinematic variables. The 3C fit rejects significant background, but at the expense of the signal. Consequently events that pass the 1C fit (but not the 3C fit) are not rejected, and the 1C fit values of the kinematic quantities are used to reconstruct the angles.

---

[6] A constrained kinematic fit requires varying a set of measured parameters until a solution satisfying the specified set of constraints is found which minimizes the χ^2 difference between the measured and fitted values.

The equal mass constraint is only applied to WW $\rightarrow \tau\nu q\bar{q}$ events. This extra constraint is required because of the extra (unobserved) neutrino from τ decay. The τ direction is taken from its visible decay products, but the τ energy is unknown. This means that for WW $\rightarrow \tau\nu q\bar{q}$ events, this is in fact a 1C rather than a 2C fit.

The selected data and MC predicted number of events in each of the three semi-leptonic decay channels at each $\mathrm{E_{cm}}$ are listed in table 5.4, after the kinematic fit constraints have been applied. There is acceptable agreement between the data and MC expectations. An example of a WW $\rightarrow \mu\nu q\bar{q}$ event selected for the TGC analysis is shown on the title page of this thesis and in figure 3.5.

Channel	192 GeV		196 GeV		200 GeV		202	
	Data	Expected	Data	Expected	Data	Expected	Data	Expected
$e\nu q\bar{q}$	56	64.5 ± 0.6	186	173.6 ± 1.2	156	168.9 ± 1.2	94	84.3 ± 0.6
$\mu\nu q\bar{q}$	59	64.5 ± 0.6	168	172.7 ± 1.2	148	166.5 ± 1.1	71	81.6 ± 0.6
$\tau\nu q\bar{q}$	53	53.7 ± 0.6	139	140.6 ± 1.1	135	135.2 ± 1.0	65	66.7 ± 0.5
Total	168	182.6 ± 1.1	493	486.9 ± 2.0	439	470.7 ± 1.9	230	232.7 ± 1.0

Table 5.4: *Number of data events selected as WW$\rightarrow l\nu q\bar{q}$ compared with Monte Carlo predictions (SM signal + background) after the general TGC selections and kinematic cuts have been applied.*

Blind belief in authority is the greatest enemy of truth.

ALBERT EINSTEIN

Chapter 6

$W^+W^- \to l^+\nu l^-\bar{\nu}$ Classification

This chapter describes improvements made to the leptonically[1] decaying W pair classification used by certain physics analyses of 183 GeV data (for example [42, 88]). It is divided into three main sections: the first section describes the cuts used for 183 GeV data, the second describes the introduction of acollinearity dependent momentum cuts and finally the resulting improvements to the leptonic W branching ratio measurements are discussed.

It is important to be able to separate the processes: WW → $l\nu l\bar{\nu}$ from WW → $l\nu\tau\nu$ and WW → $l\nu\tau\bar{\nu}$ in a variety of physics analyses (for example measurements of the leptonic branching ratios, TGCs and searches). Particular problems arise when taus decay to electrons or muons. For example if a track is identified as an electron, it is very difficult to ascertain whether the electron was 'prompt' from the decay of a W boson or came via tau decay.

6.1 Existing Cuts used for 183 GeV Data

For the 183 GeV analysis of the W leptonic branching ratios [88], lepton classification was based primarily on lepton identification and a set of momentum cuts. Electron identification was based mainly on electromagnetic cluster energy/track momentum cuts and muons were identified by hits in the muon chambers and hadron calorimeters. Track multiplicity cuts were also applied to separate hadronically decaying taus. There were two momentum cuts: a high momentum cut which converted tracks identified as τ into l if they failed this cut, and a low momentum cut which converted identified l tracks into τ's if they failed this cut.

---

[1] In this chapter lepton (or leptonic) referes to e, μ or τ and $l \equiv e$ or μ.

For any given set of cuts an efficiency matrix can be obtained. Table 6.1 is an example of an efficiency matrix obtained using the momentum cuts at 183 GeV for 2 jet[2] events. Each matrix element[3] represents the percentage number of events selected and classified in a particular channel divided by the total number of MC tree level events for that channel. The (weighted) sum of each horizontal rows provides a measure of the classification purity:

$$\text{Purity}_i \;=\; \frac{w_i\;\varepsilon_{i=j}}{\displaystyle\sum_{j}^{j=1,4,6}\varepsilon_{ij}\;+\;\sum_{j}^{j=2,3,5} 2\times\varepsilon_{ij}} \tag{6.1}$$

A weight factor (w_i) of 2 is applied to $e\mu$, $e\tau$ and $\mu\tau$ events since there are two possibilities to obtain each combination. w_i=1 for ee, $\mu\mu$ and $\tau\tau$ events. If each event were perfectly classified then the matrix would be diagonal. The sum of each vertical column is the percentage selection efficiency for that class.

		MC Truth						
		ee	$e\mu$	$e\tau$	$\mu\mu$	$\mu\tau$	$\tau\tau$	Purity
S								
E	ee	62.8	0.1	5.2	0.0	0.0	0.5	85.0
L	$e\mu$	1.2	62.4	4.5	0.3	5.3	0.7	85.1
E	$e\tau$	15.3	9.2	56.8	0.0	1.2	9.9	71.2
C	$\mu\mu$	0.0	0.6	0.0	61.9	4.2	0.4	86.1
T	$\mu\tau$	0.2	4.7	0.5	12.8	54.3	5.8	78.8
E	$\tau\tau$	1.8	1.3	7.1	1.8	7.0	44.9	56.6
D	Total	81.3	78.3	74.1	76.8	72.0	62.2	

Table 6.1: *Efficiency Matrix for 189 GeV data (2 jet events) using already existing cuts determined for 183 GeV data. The figures are in percentages.*

In order to determine the relative performance of a given set of classification cuts, the

---

[2] The CONE jet-algorithm [76] is used with a cone half-opening angle of 20^o and a jet energy threshold of 2.5 GeV [77, 78].

[3] The individual matrix elements were calculated using an occupancy correction for the normalized transverse momentum (x_T) of the two jet system. See [78] for further details.

efficiency matrix can be parameterized in terms of the sum of the diagonal elements divided by the total sum of all the elements [89]:

$$D = \frac{\mathrm{Tr}\left(\varepsilon_{ij}\right)}{\sum_{ij} \varepsilon_{ij}} \tag{6.2}$$

The matrix in table 6.1 has a D value of 77.1 ± 0.4 %. If each selected event were correctly classified, D would equal 100%.

6.2 Acollinearity Dependent Momentum Cuts

One of the main changes to the 189 GeV lepton classification was the introduction of acollinearity dependent momentum cuts to replace the straight forward high and low momentum cuts used at 183 GeV. This section explains why lepton momenta are expected to vary with acollinearity and then describes how the actual cut values were determined.

6.2.1 Momentum Variation with Acollinearity

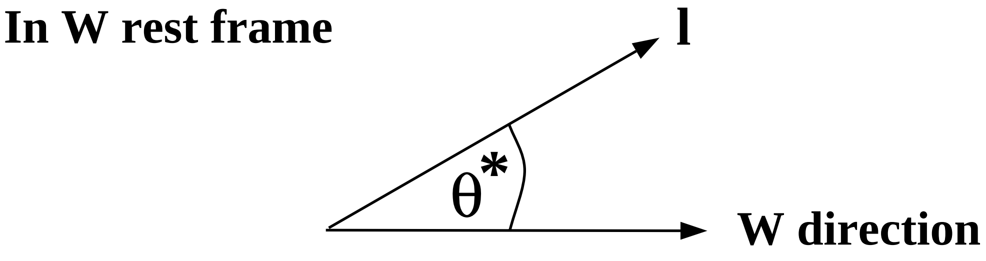

Figure 6.1: *W boson decaying leptonically. The angle between the initial W direction and the lepton is* θ^*.

Consider a W boson decaying into a lepton and a neutrino. The energy and momentum of the decay lepton can be determined from energy and momentum conservation in the W rest frame (as illustrated by figure 6.1). The maximum and minimum momentum can be determined from the decay angle of the lepton with respect to the W flight direction:

$$E_l \;=\; \frac{E_{\mathrm{W}}}{2}\,(1+\beta\cos\theta^*) \qquad\qquad \text{where } \beta = \frac{P_{\mathrm{W}}}{E_{\mathrm{W}}} \tag{6.3}$$

When the lepton is produced in the forward direction with respect to its parent W, its energy will tend to be greater ($E_l > E_{\mathrm{W}}/2$) than when the lepton is emitted in the opposite direction to the initial W direction.

In an event, the two W bosons from the e^+e^- interaction will be produced back-to-back. If both W bosons in the event decay leptonically at *low acollinearity*[4] (as illustrated by figure 6.2) then on average both leptons will be emitted in the forward direction and correspondingly tend to have high momenta [90]. (It is of course possible that both leptons could be emitted at the same angle with respect to their parent W's with correspondingly lower momenta and still have low acollinearity, but this is less likely to occur.)

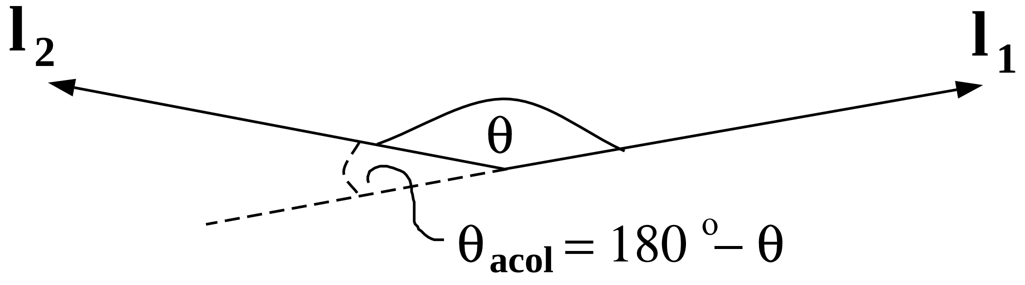

Figure 6.2: *When two leptons are emitted almost back-to-back at low acollinearity, there will be a tendency for them both to have higher momenta than when the leptons are emitted at smaller angles.*

Figure 6.3 illustrates the (measured) distribution of the highest momentum particle (X_1) versus the lowest momentum particle (X_2) for ll 2 jet events (left hand plot) and $l\tau$ 2 jet events (right hand plot) with low acollinearity angles ($< 15^o$) using Monte Carlo tree level information to determine the event class.

The ll plot is characterized by a cluster of events at high X_1 and X_2 values. The tail sloping down at 45^o corresponds to events where the electrons or muons are not produced in the forward direction with respect to their parent W bosons and so there is some smearing of the distribution. Generally the visible particles[5] produced from the decaying tau in $l\tau$

---

[4] The acollinearity angle is defined as the supplement of the angle between the two charged leptons.

[5] The plots show the momentum distribution of both hadronically and leptonically tau decay particles.

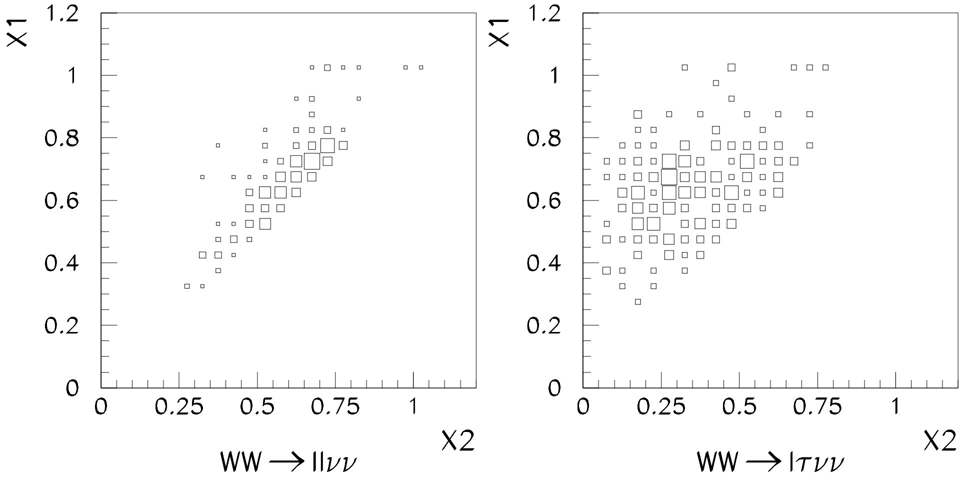

Figure 6.3: *2 jet events. The measured momentum (scaled by the beam energy) distributions of the highest momentum particle (X_1) versus the second highest momentum particle (X_2) for events with* $0^o <$ *acollinearity* $< 15^o$ *for* ll *(left hand plot) and* $l\tau$ *(right hand plot) events. Monte Carlo tree level information was used to determine the event class.*

events will have less energy than the electrons or muons produced promptly from the W boson because of the extra neutrino(s). The observable tau decay products (which are always boosted along the flight direction of the tau) generally follow closely the original tau direction. Hence X_1 will tend to correspond to the prompt electron (or muon) momentum and X_2 the visible tau decay particle momentum. Clearly the distribution along the horizontal axis is shifted downwards towards lower momentum compared with the ll events. The high momentum X_2 particles correspond to the case when the visible decay particles take most of the parent tau energy. Since there is a clear distinction between ll and $l\tau$ X_1 versus X_2 distributions for low acollinearity events, it is possible to determine appropriate cuts to separate these two classes of events.

Conversely, if the two leptons are emitted in almost the same direction (ie at *high acollinearity*), then it is likely that one of the leptons was emitted in the same direction as the parent W (with high momentum), and the other lepton from a W which decayed emitting its decay lepton backwards (as illustrated by figure 6.4).

Figure 6.5 illustrates the X_1 versus X_2 distribution for ll (left hand plot) and $l\tau$ events (right hand plot) for events with high acollinearities ($> 105^o$). Monte Carlo tree level information was used to determine the event class. Both distributions have shifted downwards towards lower momenta along the horizontal X_2 axis compared with figure 6.3. This agrees with

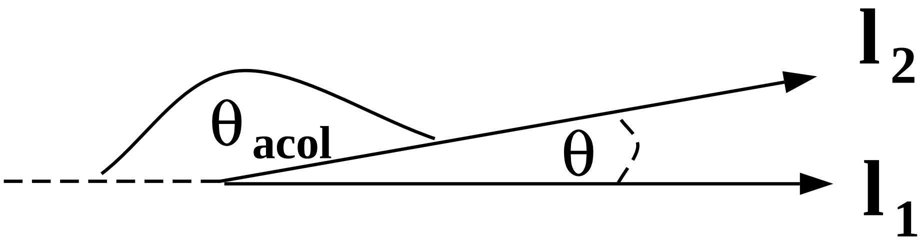

Figure 6.4: *Two leptons emitted at high acollinearity. If one of the leptons is emitted at a large angle with respect to its original parent W direction, it will tend to have lower momenta than a lepton emitted in the forward direction.*

the hypothesis that one particle is emitted forwards with respect to its parent W (X_1), and the other particle (X_2) is emitted backwards. Again the X_2 distribution for the $l\tau$ events is shifted towards lower values than the distribution for the ll events. Since the X_1 versus X_2 distributions vary with acollinearity, then it is sensible to apply acollinearity dependent momentum cuts to separate the different classes of events.

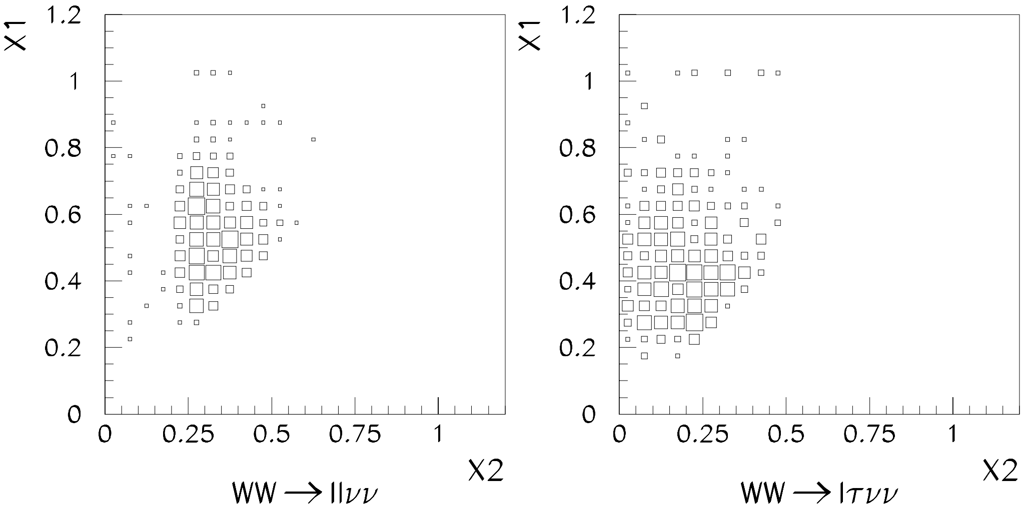

Figure 6.5: *ll and $l\tau$ events. The (measured) momentum (scaled by the beam energy) distributions of the highest momentum particle (X_1) versus the second highest momentum particle (X_2) for events with 105^o < acollinearity < 180^o. Monte Carlo tree level information was used to determine the event class.*

6.2.2 Cut determination for 2 Jet Events

Selected events were initially classified as either ll, $l\tau$ or $\tau\tau$ using basic lepton identification algorithms (as mentioned in section 6.1). Figure 6.6 illustrates the X_1 versus X_2 distributions for events that were initially classified as ll events (based on lepton identification). Events in the top left hand plot were correctly classified as ll events (using Monte Carlo tree level information). Events in the top right and lower left plots were in fact $\tau\tau$ and $l\tau$ events respectively. Each of the three different event classes have slightly different X_1 versus X_2 distributions (for reasons discussed in section 6.2.1). This suggests that a diagonal line cut and a horizontal line cut (on X_1) could be used to separate them as indicated by the thick lines which divide the X_1 versus X_2 phasespace into three regions. Most of the ll events populate the region to the right of the diagonal line, the $\tau\tau$ events tend to occupy the lower left trapezoidal region and the $l\tau$ events tend to occupy the remaining upper left region.

The plots in figure 6.7 show the same distributions for events with $105^o <$ acollinearity $< 180^o$. The X_2 distributions for all three classes of events have shifted downwards implying that the cuts should also shift with the distribution.

The plots in figure 6.8 illustrate the scaled momentum distributions of the electron/muon X_l versus the visible tau decay particles X_τ for initially classified $l\tau$ events at low acollinearities. Here the phase space can be divided into four regions by applying two cuts: one for X_l and the other on X_τ as indicated by the thick lines. Initially classified $l\tau$ events (which have been correctly classified using MC tree level information) tend to occupy the upper left hand side of the plot, whereas incorrectly classified ll events lie more to the right hand side, although there is some over-lap. Meanwhile lower momentum $\tau\tau$ events tend to populate the lower left hand side of the plot.

Figure 6.9 illustrates the X_l versus X_τ distributions for initially classified $l\tau$ events with acollinearities between 105^o and 180^o. All three distributions in this figure have shifted down towards lower momenta and consequently the optimum cut positions for this acollinearity region have also shifted downwards as illustrated by the thick lines.

In order to determine the actual cut values, the ll and $l\tau$ event samples were each divided into 7 and 6 regions of acollinearity respectively, with approximately the same number of events in each region. The values of the momentum cuts were then determined so that ‘D’ was maximized in each region. A function in terms of the acollinearity angle or its cosine was then fitted to each set of these optimized cut values (as illustrated in figure 6.10 for the

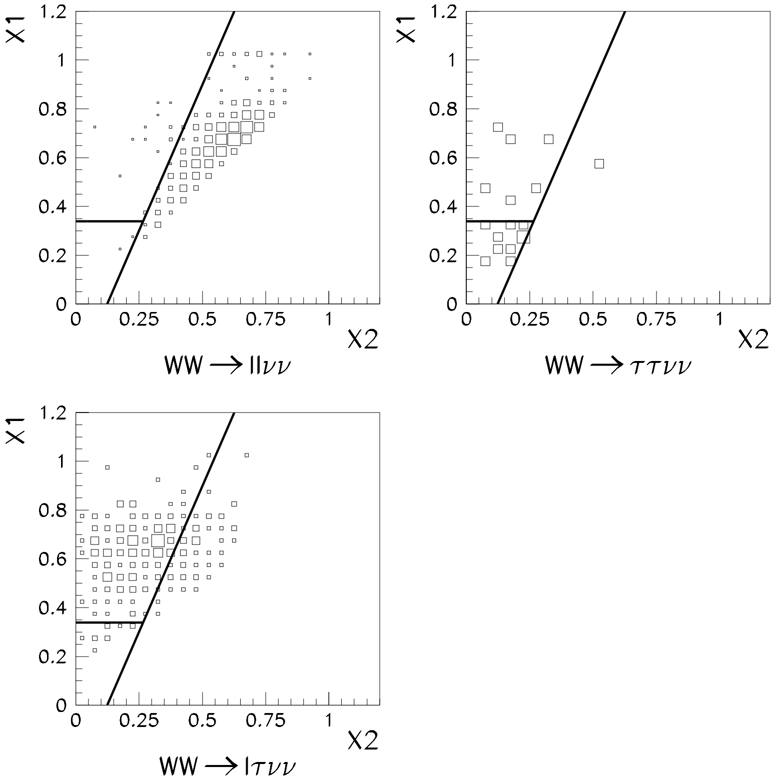

Figure 6.6: *X_1 versus X_2 distributions for initially classified ll events with 15^o < acollinearity < 30^o. MC tree level information was used to separate the 3 types of events in these plots.*

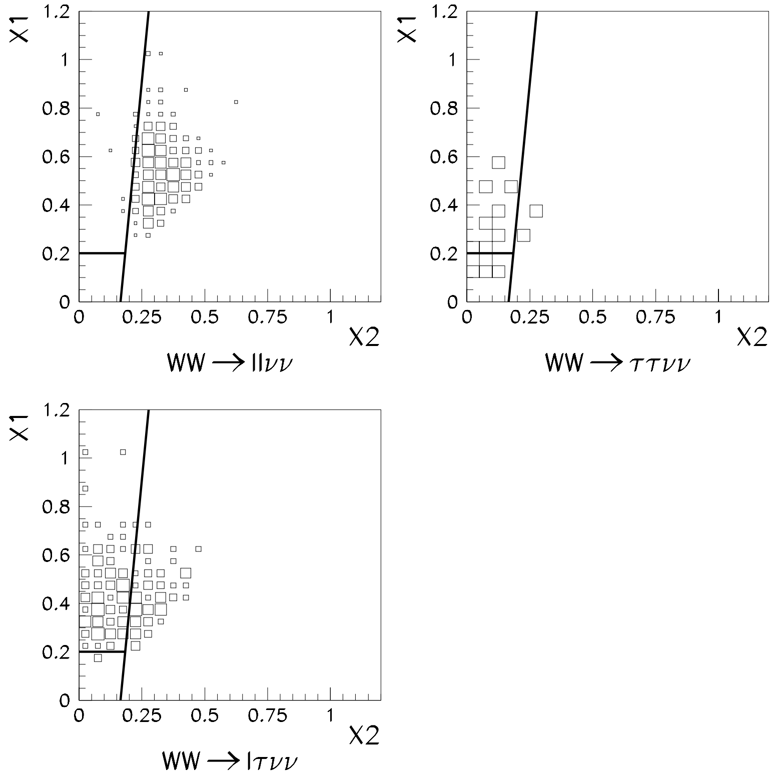

Figure 6.7: *X_1 versus X_2 distributions for initially classified ll events with 105^o < acollinearity < 180^o. MC tree level information was used to separate the 3 types of events in these plots.*

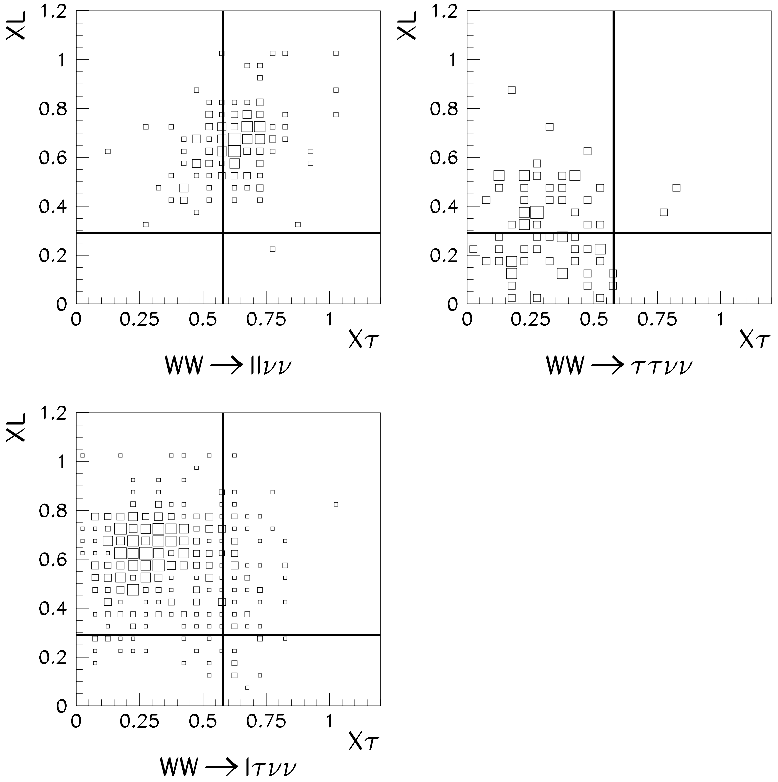

Figure 6.8: *X_l versus X_τ distributions for initially classified $l\tau$ events with 15^o < acollinearity < 30^o. MC tree level information was used to separate the 3 types of events in these plots.*

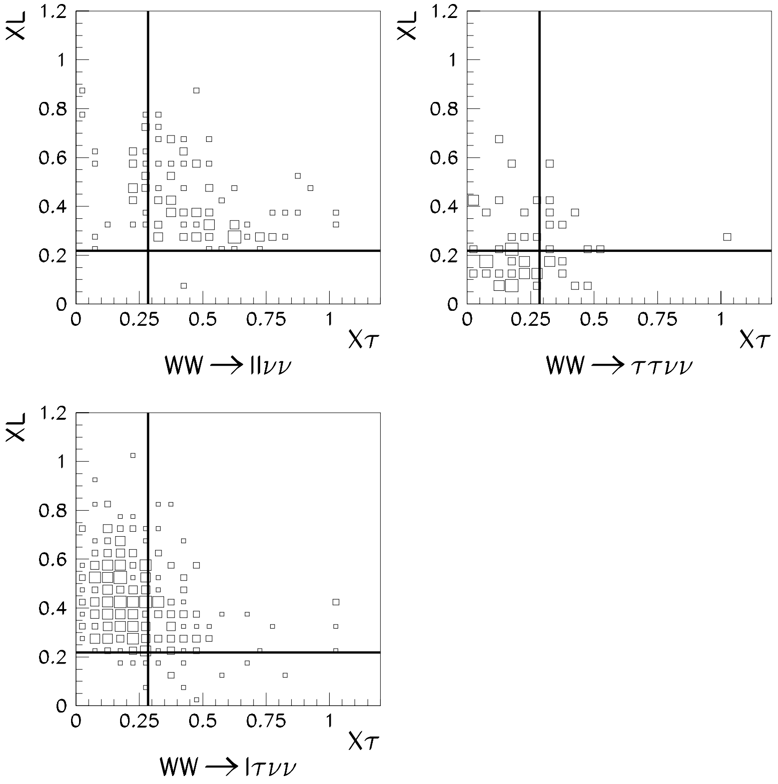

Figure 6.9: *X_l versus X_τ distributions for initially classified $l\tau$ events with 105^o < acollinearity < 180^o. MC tree level information was used to separate the 3 types of events in these plots.*

ll events diagonal line cut). The parameterized cuts were then applied to all the Monte Carlo events and the efficiency matrix and corresponding ‘D’ parameter determined. Finally, each of the parameterized cuts was re-optimized using all the events in a particular class across the entire acollinearity range of selected events.

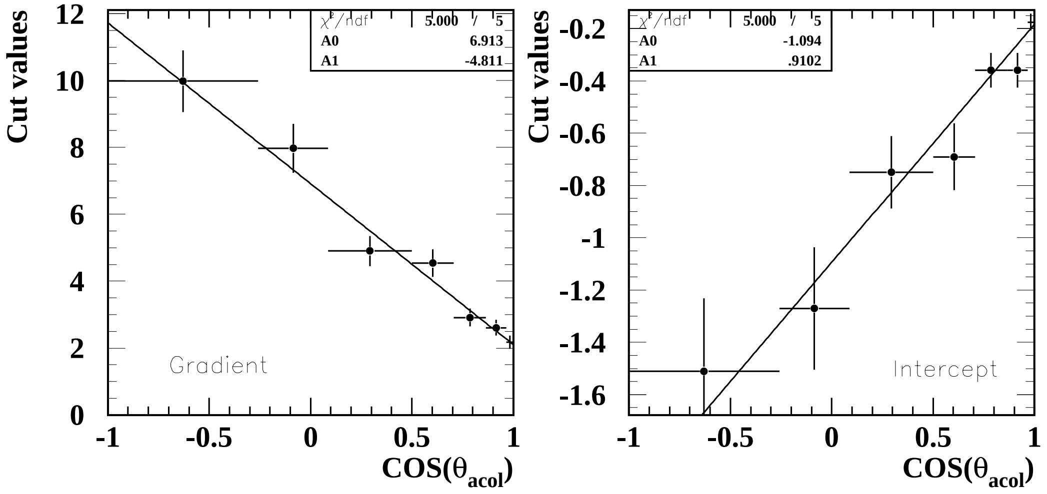

Figure 6.10: *Example for ll events illustrating how the diagonal line cut values were obtained. A function was fitted through each of the seven acollinearity region optimum cut values for the gradient (left plot) and intercept (right plot). The errors were scaled so that the straight line fit had a χ^2 per d.o.f=1. The fit parameters, A0 and A1, were then re-optimized for each of the individual cuts.*

Initially mis-classified ll events in figures 6.6 and 6.7 will be re-classified according to which region of the X_1 versus X_2 phasespace they lie in. Similarly incorrectly classified $l\tau$ events in figures 6.8 and 6.9 may be re-classified according to their X_l versus X_τ distributions[6].

$\tau\tau$ events

Acollinearity dependent momentum cuts were initially applied to identified $\tau\tau$ events but due the lack of statistics it was later decided to apply straight-forward momentum cuts, analogous to the already existing high and low momentum cuts (described in section 6.1) but optimized for 189 GeV data. Figure 6.11 illustrates the X_1 versus X_2 distribution for all events initially classified as $\tau\tau$ events across the entire acollinearity range after lepton

---

[6] Note: jets initially classified as τ will not be re-classified as l if there are several tracks associated with the jet (as discussed in section 6.1).

identification algorithms had been applied. The events in the top right hand plot were correctly classified as $\tau\tau$ and tend to occupy the lower left hand corner of this plot (since visible particles from tau decays will tend to have lower momenta than prompt leptons from W's). Events in the plots on the left hand side of this figure have been mis-classified as ll (upper plot) and $l\tau$ (lower plot) and will now be re-classified as a result of these cuts (subject to the tracks also satisfying track multiplicity criteria).

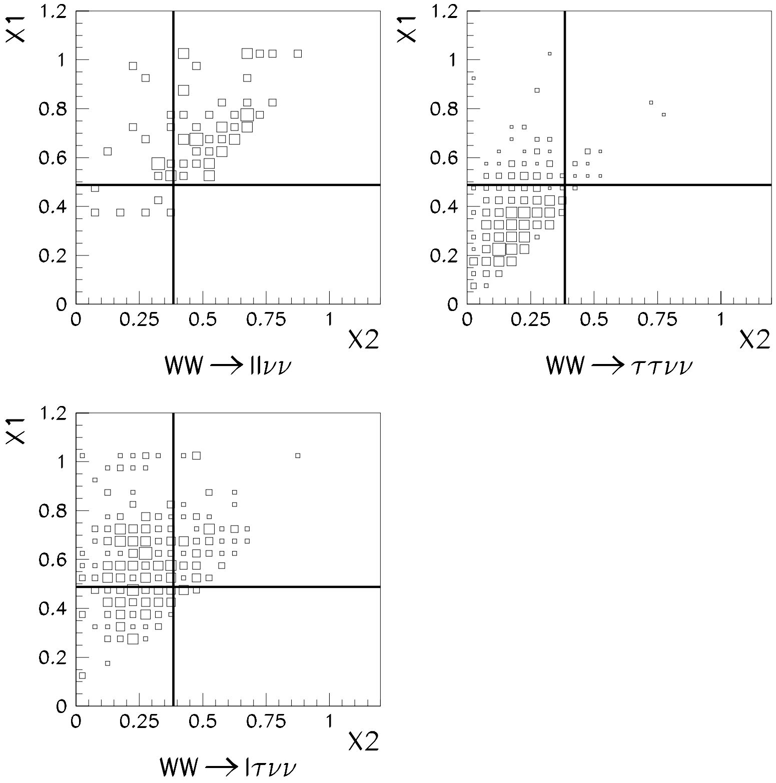

Figure 6.11: X_1 *versus* X_2 *distributions for initially classified* $\tau\tau$ *events (all acollinearities). MC tree level information was used to separate the 3 types of events in these plots.*

The parameterized cut values applied to ll, $l\tau$ and $\tau\tau$ two jet events are listed in table 6.3. The efficiency matrix for all 2 jet events after these new acollinearity dependent momentum cuts have been applied is shown in table 6.2. D = 83.2 ± 0.3 % for this matrix.

		MC Truth						
		ee	$e\mu$	$e\tau$	$\mu\mu$	$\mu\tau$	$\tau\tau$	Purity
S								
E	ee	72.4	0.3	6.6	0.0	0.0	1.0	83.0
L	$e\mu$	1.3	71.1	5.4	0.6	7.2	1.6	83.2
E	$e\tau$	7.1	3.5	58.3	0.0	1.1	10.7	81.2
C	$\mu\mu$	0.0	0.7	0.0	70.7	4.5	0.2	87.0
T	$\mu\tau$	0.0	2.7	0.3	5.2	56.0	6.9	86.1
E	$\tau\tau$	0.4	0.3	3.5	0.2	3.2	41.8	74.1
D								

Table 6.2: *Efficiency Matrix for two jet events after acollinearity dependent momentum cuts have been applied. D = 83.2 ± 0.3 %.*

ll Events

1) Diagonal line cut:

Gradient = $-4.866 \times \cos(\theta_{\text{acol}}) + 6.880$

Intercept = $0.863 \times \cos(\theta_{\text{acol}}) - 1.092$

Line = Gradient × X_2 + Intercept

2) X_1 cut = $-1.143 \times 10^{-3} \times \theta_{\text{acol}} + 0.364$

$l\tau$ Events

1) X_l cut = $-4.388 \times 10^{-4} \times \theta_{\text{acol}} + 0.281$

2) X_τ cut = $-1.782 \times 10^{-3} \times \theta_{\text{acol}} + 0.539$

$\tau\tau$ Events

1) X_1 cut = 0.488

2) X_2 cut = 0.385

Table 6.3: *2 jet events: Summary of parameterized cut values applied to initially classified ll, $l\tau$ and $\tau\tau$ events. The acollinearity angle (θ_{acol}) is measured in radians.*

6.2.3 1 and 3 Jet Events

In order to improve the classification of one and three jet events,high and low energy jet cuts were introduced[7] which convert τ's to l's and l's to τ's respectively for identified tracks which fail these cuts. The actual values of these cuts are: X_{high} cut = 0.46 and X_{low} cut = 0.24. In the three jet events these cuts are only applied to the two charged jets and not the neutral jet. Additional cuts (analogous to those already applied to 2 jet events) on the track multiplicity and number of electromagnetic clusters associated with a particular jet were introduced to further improve tau classification. D was improved from 63.5 $\pm$ 1.5% to 74.7 $\pm$ 1.4% after these cuts had been implemented.

6.2.4 Separating Electrons and Muons

If an initially classified τ jet in an $l\tau$ or $\tau\tau$ event fails one of the relevant cuts described sections 6.2.2 or 6.2.3, then in order to re-classify[6] it as either an electron or muon a cut is applied to the electromagnetic calorimeter energy associated with the track. If the energy is greater than this cut value the particle will be classified as an electron, or a muon if it is less. This cut was also re-optimized for the 189 GeV data and its scaled fractional value is 0.35.

6.3 Resulting Improvements to the $W \rightarrow$ leptons Branching Ratios

Table 6.4 is the resulting efficiency matrix for one, two and three jet events after all the new cuts described in this section have been applied. This matrix has a 'D' value of 82.5% (an improvement from 76.0% with the cuts used at 183 GeV). (This matrix was obtained using re-optimized cut values for the selection used in [80] but unfortunately these latest cut values were not used for the analysis described in [80]).

The fractional reduction in the statistical errors in the measurements of the leptonic branch-

---

[7] Graham Wilson should be credited with the introduction of these cuts which were later checked by the author.

		MC Truth						
		ee	$e\mu$	$e\tau$	$\mu\mu$	$\mu\tau$	$\tau\tau$	Purity
S								
E	ee	75.9	0.3	7.1	0.0	0.0	1.0	82.8
L	$e\mu$	2.6	77.8	6.6	0.7	7.8	1.8	82.1
E	$e\tau$	7.7	3.7	62.2	0.1	1.2	11.2	81.2
C	$\mu\mu$	0.0	1.2	0.1	80.2	6.1	0.3	84.2
T	$\mu\tau$	0.2	3.3	0.6	5.8	60.2	7.7	84.8
E	$\tau\tau$	0.4	0.3	3.7	0.2	3.4	44.3	74.2
D	Total	86.8	86.6	80.3	87.0	78.7	66.3	

Table 6.4: *Efficiency Matrix for all events after the new cuts have been applied. D = 82.5 ± 0.3 %.*

ing ratios and $\sigma_{\mathrm{WW}\to l\nu l\bar{\nu}}$ were determined from toy Monte Carlo experiments. The background contribution in each channel $\langle \mathrm{N_{bkg}} \rangle_i$ was estimated from Monte Carlo (see table 5.1). The expected number of signal events $\langle \mathrm{N_{sig}} \rangle_i$ was calculated from the data luminosity (L), the theoretically predicted WW cross section at 189 GeV ($\sigma_{\mathrm{WW}} = 16.65$pb) and the theoretical W leptonic branching ratio squared ($\mathrm{BR}^2_{\mathrm{lepton}} = 0.10556$, see table 2.2.4) :

$$\langle \mathrm{N_{sig}} \rangle_i = \sum_j \varepsilon_{i,j}\, L\, \sigma_{\mathrm{WW}}\, \mathrm{BR}^2_{\mathrm{lepton}} \tag{6.4}$$

where $\varepsilon_{i,j}$ is the appropriate 6×6 efficiency matrix and $i, j = 1$-6. The branching fractions for ee, $\mu\mu$ and $\tau\tau$ channels were assumed to be 1/9, and 2/9 for the $e\mu$, $e\tau$, and $\mu\tau$ channels. For each experiment, the total number of expected events (signal plus background) in each of the six channels was simulated using a Poisson random number generator with mean $\langle \mathrm{N_{Tot}} \rangle_i = \langle \mathrm{N_{sig}} \rangle_i + \langle N_{\mathrm{bkg}} \rangle_i$.

Fits were then made for the branching fractions: W $\to e\nu_e$ and W $\to \mu\nu_\mu$ and for the cross section: $\sigma_{\mathrm{WW}\to l\nu l\bar{\nu}}$. The branching fraction W $\to \tau\nu_\tau$ was obtained using the condition that the three leptonic branching fractions sum to unity. Figure 6.12 shows the distribution of branching fractions and cross section from 4000 toy Monte Carlo experiments. The fractional reductions in the statistical uncertainties for the leptonic branching ratios and cross section (table 6.5) were determined by comparing the rms values of these distributions, generated with the old efficiency matrix (ie before the acollinearity dependent momentum cuts

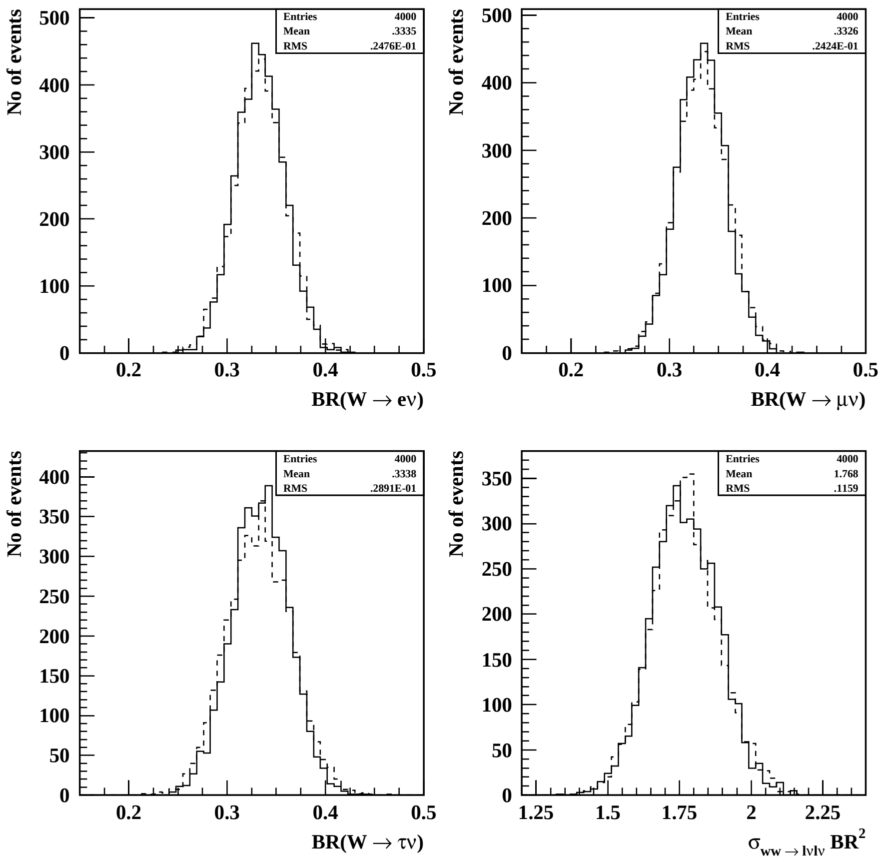

Figure 6.12: *Distributions of $W \to e\nu_e$, $W \to \mu\nu_\mu$ and $W \to \tau\nu_\tau$ branching fractions and $\sigma_{WW \to l\nu l\bar{\nu}}$ cross section obtained from 4000 toy Monte Carlo experiments. The solid histograms were produced with the new efficiency matrix (ie with acollinearity dependent momentum cuts), the dashed histograms show the distributions before these cuts were introduced.*

were introduced) and with the new efficiency matrix in table 6.4. The pull distributions for the three fitted quantities are shown in figure 6.13.

	% Improvement
BR(W → $e\nu_e$)	5.1
BR(W → $\mu\nu_\mu$)	7.0
BR(W → $\tau\nu_\tau$)	11.7
$\sigma_{WW \to l\nu l\bar{\nu}}$	1.5

Table 6.5: *Fractional reduction in the statistical errors in the measurements of the leptonic branching fractions and $\sigma_{WW \to lepton}$ (in percent) after the introduction of acollinearity dependent momentum cuts to 2 jet events and high and low momentum cuts to 1 and 3 jet events.*

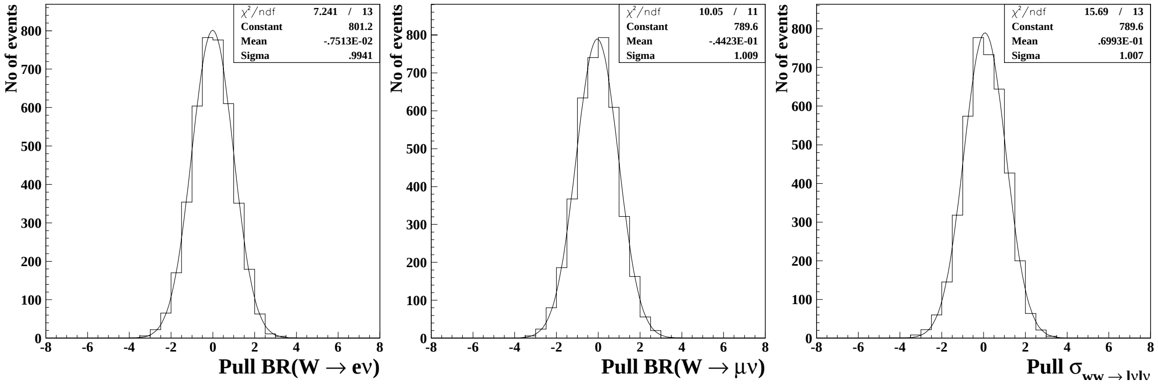

Figure 6.13: *Pull distributions for* $W \rightarrow e\nu_e$ *and* $W \rightarrow \mu\nu_\mu$ *branching fractions and* $\sigma_{WW\rightarrow l\nu l\bar{\nu}}$ *cross section obtained from 4000 toy Monte Carlo experiments generated with the efficiency matrix from table 6.4.*

6.4 Summary and Conclusion

The WW→lepton classification has been improved for the analyses of 189 GeV data. The straight-forward momentum cuts used to classify 2 jet events at 183 GeV have been replaced by acollinearity dependent momentum cuts. Separate cuts have also been introduced for 1 and 3 jet events to improve their classification. These new cuts have lead to a sizeable improvement in the classification efficiency matrix and reduction in the statistical errors for the individual W leptonic branching ratios.

It is a capital mistake to theorise before one has data. Insensibly one begins to twist the facts to suit theories, instead of theories to suit facts.

SIR ARTHUR CONAN DOYLE

Chapter 7

Introduction to Triple Gauge Boson Couplings

Measurement the triple gauge boson vertex not only provides an important test of electroweak gauge theory, but is also one of the main ways to probe for new physics if the new particles are too massive to be produced with currently available centre of mass collision energies at LEP. As discussed in chapter 2, anomalous[1] triple gauge boson couplings affect the total W pair cross section, modify the contributions of each of the W helicity states which in turn affects the angular distribution of the W bosons and their decay products.

Following on from chapter 2, this chapter explains some of the basic ideas behind triple gauge bosons couplings (TGCs) and how they arise in the Standard Model (SM). In addition to the WWZ and WWγ vertices studied in this thesis, there are other boson-boson couplings in other interactions (both SM and non-SM) and some of these are briefly summarized. There then follows a discussion on angular distributions and how they relate to the couplings. There are several methods employed by the LEP collaborations to extract the TGCs and the main approaches are briefly summarized. One of the most common techniques, and the analysis method employed in this thesis is the optimal observable method. The basic principles behind this technique are reviewed at the end of this chapter which serves as an introduction to the following analysis chapter.

---

[1] Anomalous means any deviation from Standard Model predictions.

7.1 Gauge Boson Couplings in W^+W^- events

As discussed in chapter 2, there are three main processes which can produce a pair of W bosons from e^+e^- interactions at LEP 2 (see figure 7.1). Only the s-channel processes contain couplings between three gauge bosons (TGCs). The t-channel process acts as interference and experimentally cannot be separated from the s-channel final state.

The couplings arise from the non-Abelian gauge structure of electroweak theory. Since the couplings are uniquely determined by the $SU(2)_L \otimes U(1)$ gauge invariance in the SM, precise measurements of the coupling vertices provide stringent tests of the theory. Any small deviations of the couplings from their SM predictions would violate the subtle cancellations among the three processes in figure 7.1 and lead to observable effects [91]. The couplings could also be sensitive to new physics beyond the SM, for example heavy 'new' particles could contribute loop effects to the TGC vertices. Small deviations to the SM predictions of the TGC parameters could be introduced by any theory that describes new physics whilst incorporating the electroweak theory as an effective low energy limit.

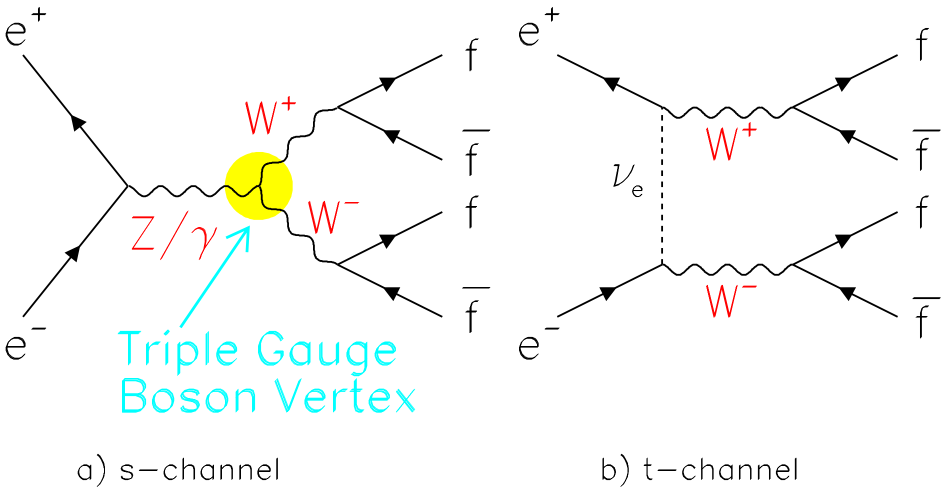

Figure 7.1: *Tree level Feynman diagrams for $e^+e^- \rightarrow W^+W^- \rightarrow 4f$. Only the s-channel processes in figure a) involve coupling between a neutral gauge boson and the two charged gauge bosons.*

The term (equation 2.4) in the electroweak Lagrangian (equation 2.3) that gives rise to the boson self-interactions can be re-written in terms of the physically observable gauge boson fields:

$$\begin{aligned}
\mathcal{L}_{YM} &= -\frac{1}{4}W^i_{\mu\nu}W^{\mu\nu}_i - \frac{1}{4}B_{\mu\nu}B^{\mu\nu} = \qquad (7.1)\\
&- \frac{1}{4}A_{\mu\nu}A^{\mu\nu} - \frac{1}{2}W^+_{\mu\nu}W^{-\mu\nu} - \frac{1}{4}Z_{\mu\nu}Z^{\mu\nu}\\
&- ig(W^{-\mu\nu}W^+_\nu - W^{+\mu\nu}W^-_\nu)(\cos\theta_W Z_\mu + \sin\theta_W A_\mu)\\
&- ig(\cos\theta_W Z^{\mu\nu} + \sin\theta_W A^{\mu\nu})W^+_\mu W^-_\nu\\
&- g^2\cos^2\theta_W\left[(Z_\mu Z^\mu)(W^+_\nu W^{-\nu}) - (Z_\mu W^{+\mu})(Z_\nu W^{-\nu})\right]\\
&- g^2\sin^2\theta_W\left[(A_\mu A^\mu)(W^+_\nu W^{-\nu}) - (A_\mu W^{+\mu})(A_\nu W^{-\nu})\right]\\
&+ g^2\sin^2\theta_W\cos^2\theta_W\\
&\quad\left[(A_\mu W^{+\mu})(Z_\nu W^{-\nu}) + (Z_\mu W^{+\mu})(A_\nu W^{-\nu}) - 2(Z_\mu A^\mu)(W^+_\nu W^{-\nu})\right]\\
&- \frac{g^2}{2}\left[(W^+_\mu W^{-\mu})(W^+_\nu W^{-\nu}) - (W^+_\mu W^{+\mu})(W^-_\nu W^{-\nu})\right]
\end{aligned}$$

where $G_{\mu\nu} = \partial_\mu G_\nu - \partial_\nu G_\mu$ ($G \equiv A, Z, \mathrm{W}^\pm$) and θ_W is the weak mixing angle. Equation 7.1 shows that there are two triple (WWγ and WWZ) and four quartic (WWZZ, $\gamma\gamma$WW, ZγWW and WWWW) gauge boson couplings predicted by the SM. Since the coupling constants (g) appear at second order in the quartic gauge coupling (QCG) terms, the strength of these interactions will be smaller than the TGCs.

In this thesis we are interested in TGCs, and in order to study them we need a parameterization of the vector gauge boson interactions that goes beyond the SM. The most general Lorentz and U(1)$_{\mathrm{EM}}$ gauge invariant effective Lagrangian used to describe the coupling vertices between WWγ and WWZ gauge bosons is given by [8]:

$$\begin{aligned}
i\mathcal{L}^{\mathrm{WWV}}_{\mathrm{eff}} &= g_{\mathrm{WWV}}\Bigg[g^{\mathrm{V}}_1 V^\mu\left(W^-_{\mu\nu}W^{+\nu} - W^+_{\mu\nu}W^{-\nu}\right) \qquad (7.2)\\
&+ \kappa_{\mathrm{V}}\, W^+_\mu W^-_\nu V^{\mu\nu} + \frac{\lambda_{\mathrm{V}}}{m^2_{\mathrm{W}}}\, V^{\mu\nu}W^{+\rho}_\nu W^-_{\rho\nu}\\
&+ ig^{\mathrm{V}}_4\, W^-_\mu W^+_\nu\, (\partial^\mu V^\nu + \partial^\nu V^\mu)\\
&+ ig^{\mathrm{V}}_5\, \epsilon_{\mu\nu\rho\sigma}\left((\partial^\rho W^\mu)W^{+\nu} - W^\mu(\partial^\rho W^{+\nu})\right) V^\sigma\\
&- \frac{\tilde{\kappa}_{\mathrm{V}}}{2}\, W^-_\mu W^+_\nu\, \epsilon^{\mu\nu\rho\sigma}\, V_{\rho\sigma} - \frac{\tilde{\lambda}_{\mathrm{V}}}{2m^2_{\mathrm{W}}}\, W^-_{\rho\mu}W^{+\mu}\, \epsilon^{\nu\rho\alpha\beta}\, V_{\alpha\beta}\Bigg]
\end{aligned}$$

where $V_{\mu\nu} = \partial_\mu V_\nu - \partial_\nu V_\mu$, V $\equiv \gamma$ or Z^0, and $\epsilon^{0123} = 1$. The overall coupling strengths are: $g_{\mathrm{WW}\gamma} = -e$ and $g_{\mathrm{WWZ}^0} = -e\cot\theta_W$, where e is the electric charge. Equation 7.2 consists of

14 free parameters (7 each for the WWγ and WWZ vertices) which are the coupling terms: $g_1^{\mathrm{V}}, \kappa_{\mathrm{V}}, \lambda_{\mathrm{V}}, g_4^{\mathrm{V}}, g_5^{\mathrm{V}}, \tilde{\kappa}_{\mathrm{V}}$ and $\tilde{\lambda}_{\mathrm{V}}$. The couplings g_1^{V}, κ_{V} and λ_{V} conserve charge (C) and parity (P) conjugation separately. g_4^{V} conserves only P while g_5^{V} violates C and P but conserves CP. The other two couplings, $\tilde{\kappa}_{\mathrm{V}}$ and $\tilde{\lambda}_{\mathrm{V}}$, only conserve C. If either g_4^{γ} or g_5^{γ} are non-vanishing at $q^2 = 0$, then the photon part of the Lagrangian will not be electromagnetically gauge invariant.

The static electromagnetic properties of the W boson [92] can be determined from the couplings associated with the WWγ vertex. The value of g_1^{Z} determines the charge (q_{W}) of the W$^+$ boson:

$$q_{\mathrm{W}} = e g_1^{\gamma} \tag{7.3}$$

The magnetic dipole (μ_{W}) and electric quadrupole (Q_{W}) moments are related to the κ_{γ} and g_1^{γ} couplings by:

$$\mu_{\mathrm{W}} = \frac{e}{2\,M_{\mathrm{W}}}\,(1 + \kappa_{\gamma} + \lambda_{\gamma}) \tag{7.4}$$

$$Q_{\mathrm{W}} \;=\; -\frac{e}{M_{\mathrm{W}}^2}\,(\kappa_{\gamma} - \lambda_{\gamma}) \tag{7.5}$$

The P and CP violating terms are related to the electric dipole (d_{W}) and magnetic quadrupole ($\tilde{q}_{\mathrm{W}}$) moments by:

$$d_{\mathrm{W}} = \frac{e}{2M_{\mathrm{W}}}\,(\tilde{\kappa}_{\gamma} + \tilde{\lambda}_{\gamma}) \tag{7.6}$$

$$\tilde{q}_{\mathrm{W}} = -\frac{e}{M_{\mathrm{W}}^2}\,(\tilde{\kappa}_{\gamma} - \tilde{\lambda}_{\gamma}) \tag{7.7}$$

In the SM at tree level the TGC parameters $g_1^{\mathrm{V}} = \kappa_{\mathrm{V}} = 1$, and all the other couplings are zero. The couplings are often stated in terms of their change in value from SM predictions, so for example: $\Delta g_1^{\mathrm{Z}} \equiv g_1^{\mathrm{Z}} - 1$ and $\Delta\kappa_{\gamma} \equiv \kappa_{\gamma} - 1$. This is the notation used in the following chapters.

With the limited statistics available at LEP 2, it is impossible to constrain the 14 parameters simultaneously. Therefore certain assumptions are normally made to reduce the number of measured parameters. If we assume that the Lagrangian in equation 7.2 respects both charge and parity conservation [93] as well as satisfying electromagnetic gauge invariance [8], then the number of free parameters is reduced to five (g_1^{Z}, κ_{Z}, κ_γ, λ_{Z} and λ_γ). Further relationships between these parameters can be obtained by requiring $\mathrm{SU(2)_L \otimes U(1)_Y}$ gauge invariance, ignoring operators with dimension greater than 6, and from previous high precision measurements at the Z^0 resonance (which have shown that the gauge boson propagators are not affected at tree level by anomalous TGCs). These new relationships:

$$\begin{aligned} \Delta\kappa_{\mathrm{Z}} &= \Delta g_1^{\mathrm{Z}} - \Delta\kappa_\gamma \tan^2\theta_W \\ \lambda_{\mathrm{Z}} &= \lambda_\gamma \end{aligned} \tag{7.8}$$

further reduce the number of coupling parameters to just three ($\Delta\kappa_\gamma$, $\Delta g_1^{\mathrm{Z}}$and λ_γ). These are the couplings investigated in this thesis. Experimentally it should be remembered that the coupling values or limits measured with a particular set of constraints cannot be converted into or compared with results obtained with different sets of constraints [94]. This means that some information is lost by assuming these relationships, which are the 'standard' set applied to most of the LEP results. However, the CP violating coupling have been measured by the OPAL [95], ALEPH [96, 97] and DELPHI [98] collaborations (prior to LEP 2 they were constrained by measurements of the neutron electric dipole moment [99]). The L3 [100] and ALEPH collaborations have also presented limits on some of the other couplings (including g_5^{Z}, λ_{Z} and κ_{Z}). Triple gauge boson couplings have been studied extensively in the literature. Further details of some of the theoretical aspects of TGCs can be found in, for example [8, 91, 101, 102].

7.2 Other Gauge Boson Coupling Processes

Although $\mathrm{W^+W^-}$ events have the highest statistics at LEP 2, due to the non-Abelian nature of electroweak gauge theory, there are many other processes which involve self-interactions between the gauge bosons. These include the single W and W fusion processes illustrated in figure 7.2. In both these diagrams, the photon could be replaced by a Z^0 to give a WWZ vertex (and in the case of the W fusion process, the Z^0 would subsequently decay into a fermion/anti-fermion pair), but these processes are heavily suppressed due to the large Z^0 mass. Therefore, single W and W fusion processes primarily probe the $\mathrm{WW}\gamma$ vertex.

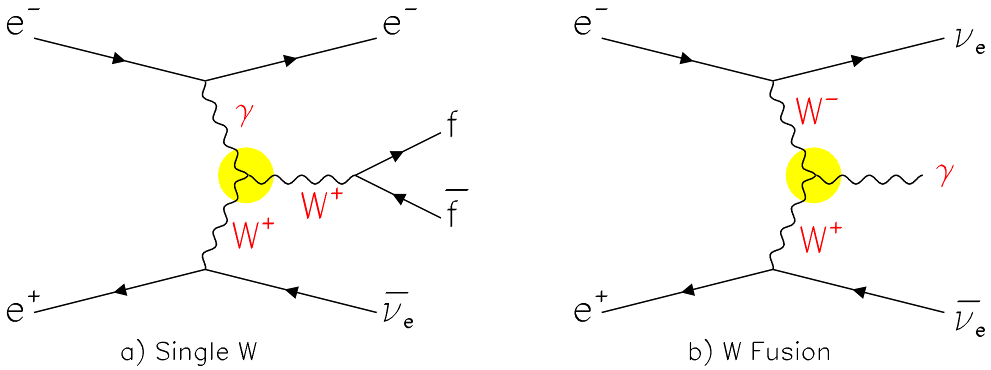

Figure 7.2: *The single W and W fusion processes also involve interactions with a WWγ vertex.*

Although the single W processes result in the same final states as W pair production, they can still be separated by event kinematics. Single W production is characterized by either a pair of acoplanar jets or a single (high energy) lepton from the W decay plus large missing transverse energy. In addition to the process with a WWγ vertex shown in figure 7.2a, there are other non-TGC single W diagrams (see for example 5.2f). The single photon channel offers a clean signature, with only a single high energy γ observed in the detector. The main background to the γX final state comes from the reaction: $e^+e^- \rightarrow$ Z$^o/\gamma$, where the photon is produced by initial state radiation and the Z^0 decays to $\nu\bar{\nu}$. Results from these two channels are complementary to the main W pair results since they allow independent measurements of the κ_γ and λ_γ couplings without the WWZ vertex. Often single W and γ results are combined with those from W pair production for publication by the LEP experiments [96, 100, 103, 104].

As discussed in the previous section, the non-Abelian gauge symmetry of the electroweak Lagrangian (equation 2.4) predicts four quartic gauge couplings: WWZγ, WW$\gamma\gamma$, ZγWW and WWWW in the SM. Examples of these processes are shown in figure 7.3 where each vertex involves at least two charged bosons. (An extra s-channel diagram involving a ZZ$\gamma\gamma$ coupling has also been searched for at LEP 2, but this coupling is predicted to be zero in the SM.) Searches at LEP 2 [105] have so far concentrated on the WWγ, $\nu\bar{\nu}\gamma\gamma$ and $Z\gamma\gamma$ final states but the sensitivity to quartic gauge boson couplings is poor compared with the TGCs (it will improve with the increased energies available at a future linear collider). Furthermore, there are several SM backgrounds, in particular W, initial and final state radiation diagrams, that completely dwarf the signal. A complete and general analysis of photonic quartic couplings has been performed by Belanger *et al.* [106], but essentially new terms are added to the Lagrangian in order to parameterize the effects of anomalous couplings.

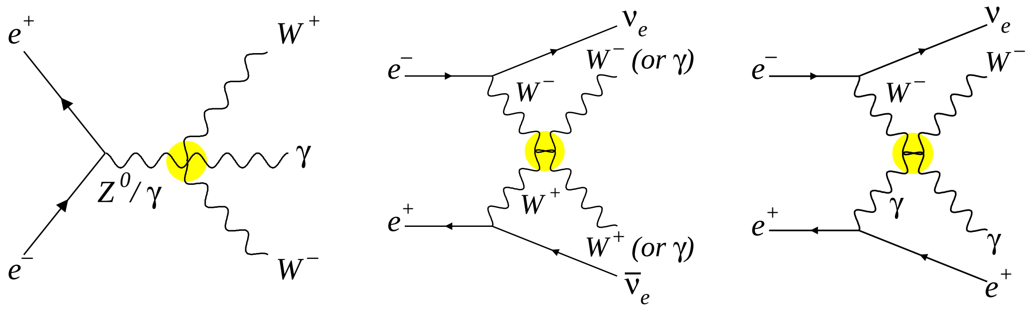

Figure 7.3: *Examples of quartic gauge couplings at LEP 2.*

Non Standard Model couplings

In addition to the charged TGC vertices, neutral gauge boson couplings with vertices ZZZ, Z$\gamma\gamma$ and ZZγ, have been searched for by the LEP collaborations [107]. All these couplings are expected to be zero in the SM so observation of these couplings would signal physics beyond the SM. There are two classes of neutral gauge boson couplings. The first involves anomalous Z$\gamma\gamma^*$ and ZγZ* couplings in the process $e^+e^- \to$ Zγ. The couplings are parameterized by eight independent form factors: h_i^V (where i=1,2,3,4 and $V \equiv \gamma,$ Z). The second class refers to the ZZγ^* and ZZZ* couplings in the process $e^+e^- \to$ ZZ. These are parameterized in terms of four couplings: f_i^V (where i=4,5) and are independent of the h_i^V couplings. Further details of the theoretical aspects concerning the neutral gauge boson couplings may be found in [108].

7.3 Angular Distributions

In the limit of small W widths, each W$^+$W$^-$ $\to f\bar{f}f\bar{f}$ event is characterized by five kinematic angles: $\cos\theta_{\mathrm{W}}$, $\cos\theta_l^*$, ϕ_l^*, $\cos\theta_j^*$ and ϕ_j^* as illustrated in figure 7.4 and defined by the convention in [93]. The angular distributions of the final state fermions reflect the underlying W helicities and V-A nature of W decay, and consequently they will be affected by the presence of anomalous couplings between the gauge bosons and a departure from Yang Mills behaviour. The differential cross section dσ may be expressed as a function of these five angles: d$\sigma\left(\cos\theta_{\mathrm{W}}, \cos\theta_l^*, \phi_l^*, \cos\theta_j^*, \phi_j^*\right)$.

The production angle ($\cos\theta_{\mathrm{W}}$) is defined to be the angle between the directions of flight

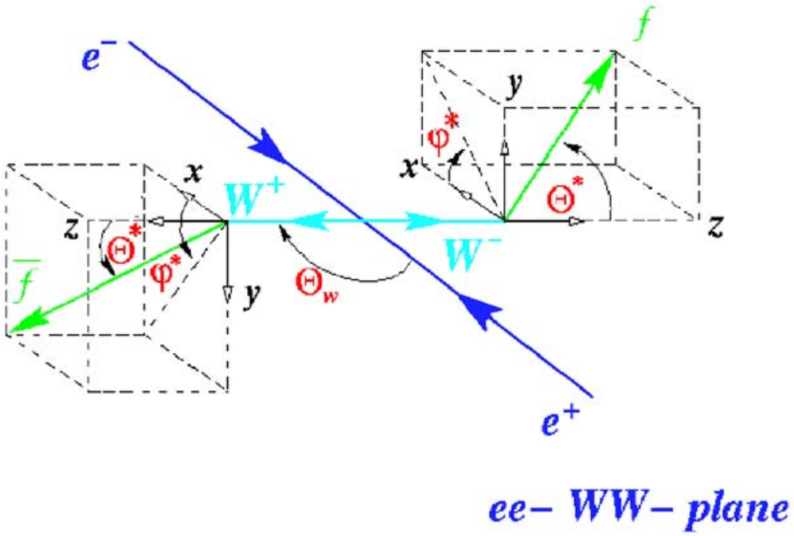

Figure 7.4: *The five kinematic angles* ($\cos\theta_{\rm W}, \cos\theta^*_l, \phi^*_l, \cos\theta^*_j$ *and* ϕ^*_j) *that characterize a WW*$\rightarrow$ $l\nu q\bar{q}$ *event. The information from these kinematically reconstructed angles is used in the TGC measurement.*

of the incoming electron and the outgoing $\rm W^-$ in the overall centre of mass frame. Since the beams were unpolarized in the transverse plane at LEP, the azimuthal angle ($\phi_{\rm W}$) is not used. The $\cos\theta_{\rm W}$ distribution is forward peaked along the initial charge direction and has the most sensitivity to anomalous couplings: the more positive the couplings, the steeper the distribution.

The polar (θ^*) and azimuthal (ϕ^*) angles are defined for the outgoing fermion from the $\rm W^-$ decay and for the antifermion from the $\rm W^+$ decay, within the framework of two right handed sets of orthogonal axes in the rest frames of the parent W boson (as shown in figure 7.4). Since the quark flavours cannot be determined from the jets, the decay angles (θ^*_j and ϕ^*_j) of the hadronically decaying W can only be determined with a twofold ambiguity. Hence, we average over both possibilities. The contribution of $\cos\theta^*_l$, ϕ^*_l, $\cos\theta^*_{jet}$, ϕ^*_{jet} to the overall sensitivity enters mainly through their correlations with $\cos\theta_{\rm W}$.

WW$\rightarrow l\nu q\bar{q}$ is the most powerful channel with which to study TGCs at LEP 2, since this is the only channel where it is possible to unambiguously reconstruct the $\cos\theta_{\rm W}$ distribution. In $\tau\nu q\bar{q}$ events, the $\cos\theta_{\rm W}$ distribution is determined by adding together the measured four-momenta of the two reconstructed jets. In order to reconstruct the decay angles, the flight direction of the τ is approximated by the direction of its charged decay products. The four unknown quantities (τ energy, ν_τ three momentum) can then be calculated using energy and momentum conservation.

The angular distributions for selected $\mathrm{WW} \rightarrow l\nu q\bar{q}$ events in the combined 1999 OPAL data set are shown in figure 7.5. The angular distributions for EXCALIBUR MC generated with SM and $\lambda = \pm 1$ couplings are also shown. In general there is good agreement between the data and the SM expectation. The background is essentially flat, which has the effect of slightly decreasing the slope of the $\cos\theta_{\mathrm{W}}$ distribution resulting in (slightly) more negative couplings. Since there is an increase in the cross section for the samples generated with anomalous couplings, these plots have been normalized to the number of events in the sample and not the luminosity with which the samples were generated. Effects such as radiative corrections will distort the angular distributions, and hence the importance of correctly modelling these effects in the MC in order to not bias the results.

7.4 Methods to measure TGCs

Several methods have been used to extract the TGCs from W pair events at LEP 2. One of the simplest methods exploits the total cross section sensitivity to anomalous couplings. The total number of observed events is compared with the expected number, which is parametrized as a second order polynomial for a given TGC value. Since the events do not need to be fully reconstructed, a looser set of selection cuts can be applied than in the main TGC analyses. In OPAL the total cross section analysis is done separately and the results combined at the end [49].

The angular information in $\mathrm{W}^+\mathrm{W}^-$ events has more sensitivity to the TGCs than the cross section measurement, and hence it is advantageous to incorporate as much of the angular information in each event as possible. Three different statistical techniques have been proposed [8] which exploit the angular distributions to measure the TGCs: the spin density matrix method, the maximum likelihood and the technique of optimal observables.

The spin density matrix (SDM) [93] is a traditional approach for studying the W decay angular distributions. SDM elements are observables which relate directly to the W polarization and the relative production of the various helicity states can be determined from their measurement. The TGCs are extracted by determining the SDM elements (and their

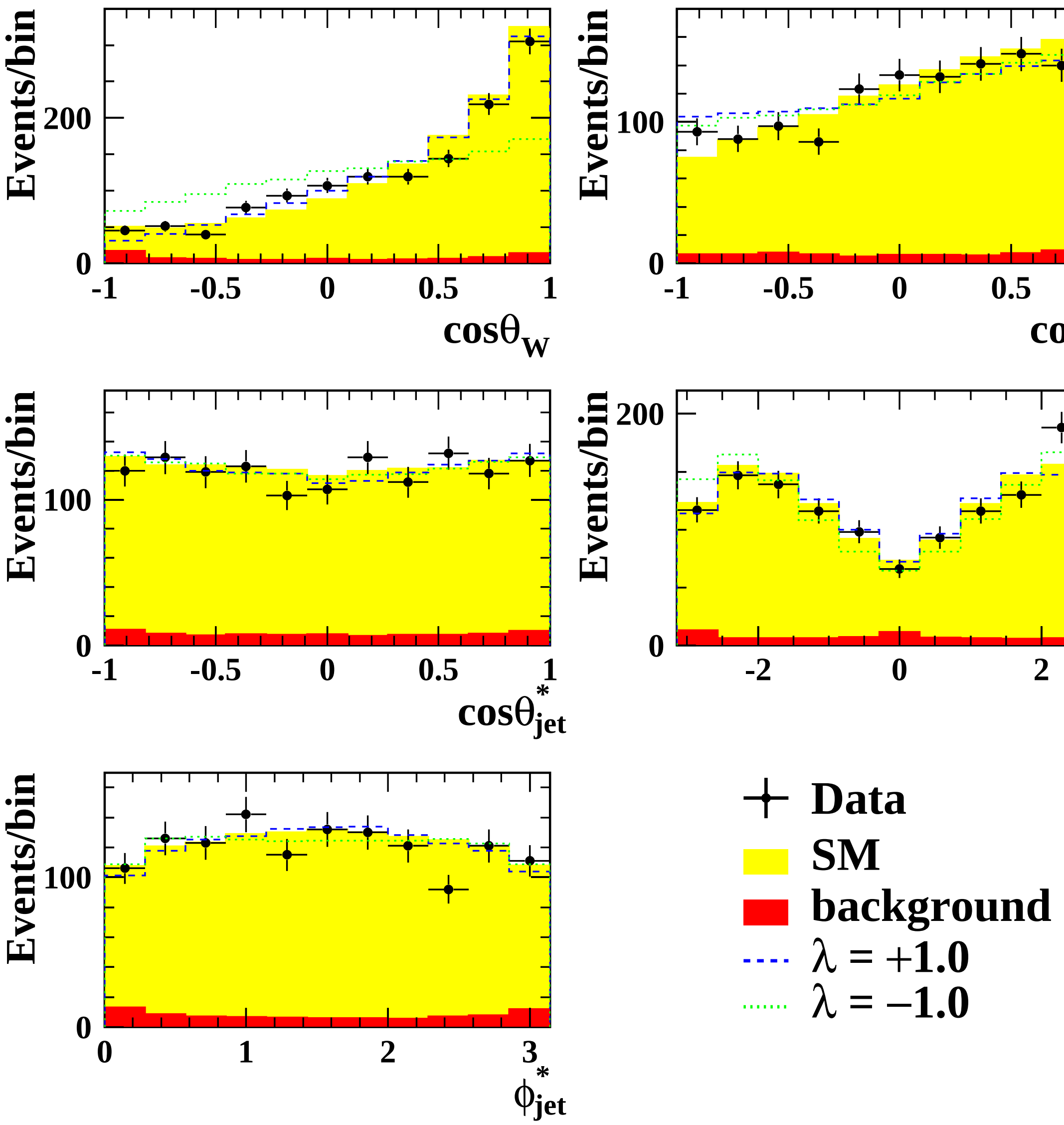

Figure 7.5: *The angular distributions for the combined 1999 data, for selected $WW \rightarrow l\nu q\bar{q}$ events. The expected distributions from MC for SM and anomalous coupling $\lambda = \pm 1$ are shown. The MC plots have been normalized to the number of data events. The value of ϕ_l^* has been shifted by π for $W^+ \rightarrow \bar{l}\nu_l$ decays in order to overlay the W^+ and W^- distributions on the same plot. The jet with $0 \leq \phi_j^* \leq \pi$ was chosen as the quark (anti-quark) jet from the decay of the W^- (W^+).*

statistical uncertainties) in bins of $\cos\theta$ from the angular distributions. These are then compared with different theoretical predictions in a χ^2 fit. The SDM functions exhibit different behaviour with respect to each of the TGC parameters. The main advantage of this approach is that it allows a model independent test of the TGCs and is particularly suited to the measurement of the CP-violating couplings [95]. One drawback arises from potential binning problems in the case of low statistics.

The maximum likelihood technique (ML) is one of the main methods to measure TGCs at LEP 2. The main advantage of this approach is that it exploits the full angular information directly in the fit [109]. In the *unbinned* maximum likelihood fit, the couplings are extracted by maximizing the likelihood function: $\mathcal{L} = \sum_{i=1}^{N} P\left(\Omega_k, \vec{\alpha}\right)$, where N is the observed number of events, $P(\Omega_k, \vec{\alpha})$ is the probability density for an event (with kinematic angle set represented by Ω_k and as a function of the coupling parameters $\vec{\alpha}$[2]). The probability density function is constructed from the differential cross section and normalized to unity by an integral over the phase space. The total cross section information can be included to increase sensitivity to the TGCs by using an *extended* maximum likelihood fit. However, in both these methods it is difficult to incorporate complications such as detector resolution, acceptance, ISR/FSR, finite W width, fragmentation and background contributions analytically in the differential cross section (dσ/dΩ). Effects not modelled in the fit could potentially give rise to biases and TGC dependent systematic fit errors.

These physical effects can be simulated in the MC, and a *binned* maximum likelihood (BML) fit performed to compare the observed data and MC distributions. This procedure requires a very large number of MC events because of the large number of bins in the five dimensional phase space corresponding to the five kinematic angles[3]. (Another problem associated with maximum likelihood methods is that they do not provide any criterion to check the quality of the fit as is the case for χ^2 fits.)

A popular approach at LEP 2 to circumvent the binning problems of low MC statistics whilst incorporating all the physical effects, is to use optimal observables ($\mathcal{OO}$) [94, 111]. This is the method used to exact the couplings in this thesis, and is discussed in the following section. The $\mathcal{OO}$ method is currently used by three of the four LEP collaborations for their main analyses. For the single parameter fits, it has been shown in [8] that the three methods should give similar precision when the same angular information is used.

---

[2] $\vec{\alpha}$ is a generic term used to denote the set of couplings $\{\Delta\kappa_\gamma, \Delta g_1^{\mathrm{Z}}, \lambda\}$ in this thesis and not the set of α parameters used in [8].

[3] Because of the problem of insufficient MC statistics, normally only a restricted set of the kinematic variables are used with fairly coarse binning. See for example [110].

7.5 Introduction to Optimal Observables

Optimal observables ($\mathcal{OO}$s) are quantities with maximal sensitivity to unknown parameters and give minimal statistical uncertainty. Their use was first suggested for the measurement of the magnetic moment and electric dipole moment form factors in top quarks [112] and for τ polarization [113]. In the TGC analyses, the basic idea behind the $\mathcal{OO}$ method is to project the information contained in the five-fold angular distributions onto a set of suitably defined observables without loss of sensitivity. The couplings are extracted either by fitting to the distributions or by using the mean $\mathcal{OO}$ values directly. The advantage of this technique is that it avoids the binning problems associated with the BML technique.

For simplicity we first consider the linear dependence of a single coupling parameter α. Ignoring higher order terms, the differential cross section can be written as:

$$\frac{\mathrm{d}\sigma}{\mathrm{d}\Omega}(\Omega,\alpha) = S^{(0)}(\Omega) + \alpha S^{(1)}(\Omega) \tag{7.9}$$

where Ω represents the set of five kinematic angles: $\{\cos\theta_{\mathrm{W}}, \cos\theta^*_l, \phi^*_l, \cos\theta^*_j, \phi^*_j\}$ and the S functions carry information describing the α dependence of $\mathrm{d}\sigma/\mathrm{d}\Omega$. For SM couplings (ie when $\vec{\alpha} = 0$), the differential cross section is simply $S^{(0)}(\Omega)$. The $\alpha S^{(1)}(\Omega)$ term corresponds to the contribution from an anomalous coupling. In [112] it was shown that for a linear function that parameterizes a physical parameter, there is an observable that minimizes the statistical uncertainty. In this case the observable is simply the ratio of these two co-efficients: $\mathcal{OO} = \mathcal{OO}(\Omega) = S^{(1)}(\Omega)/S^{(0)}(\Omega)$.

All the information from the five phase space variables is retained in this ‘first order’ optimal observable. Moreover, the mean ($\overline{\mathcal{OO}}$) of this one dimensional distribution for a linear function contains most of the sensitivity to α [94]. These ideas can be extended to several coupling parameters by replacing the second term in equation 7.9 by a summation over the couplings: $\sum_i \alpha_i S^{(1)}_i$, where α_i represents the set of coupling parameters $\{\Delta\kappa_\gamma, \Delta g^{\mathrm{Z}}_1, \lambda\}$. The $\mathcal{OO}$ distributions for these three couplings are shown in figure 7.6 for MC events that were generated with SM, and anomalous coupling values of $\alpha_i = \pm 0.5$.

The dependence of the angular distributions on the anomalous coupling parameters is non-linear and the sensitivity of the $\overline{\mathcal{OO}}$s is only maximal for coupling values close to the point about which the differential cross section was expanded (ie in this case the SM values when

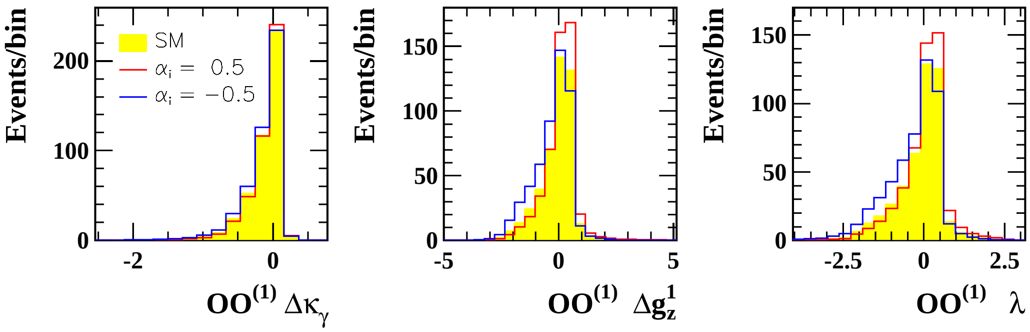

Figure 7.6: *The predicted first order $\mathcal{OO}_i^{(1)}$ distributions for SM MC compared with MC generated at $\alpha_i = \pm 0.5$, where $\alpha_i = \Delta\kappa_\gamma$, Δg_1^Z or λ.*

$\vec{\alpha} = 0$). For large anomalous coupling values, the sensitivity is no longer optimal. To improve this, the above formalism has been extended to include the quadratic dependence of the differential cross section.

Since the interaction Lagrangian (equation 7.2) is linear with respect to the TGCs, the differential cross section is a quadratic function which can be parameterized as:

$$\frac{\mathrm{d}\sigma(\Omega,\vec{\alpha})}{\mathrm{d}\Omega} = S^{(0)}(\Omega) + \sum_i \alpha_i \cdot S_i^{(1)}(\Omega) + \sum_{i,j} \alpha_i\alpha_j \cdot S_{ij}^{(2)}(\Omega) \tag{7.10}$$

From this equation, the full set of $\mathcal{OO}$s can be constructed for each event using the measured kinematic variables (Ω) [94]:

$$\mathcal{OO}_i^{(1)} = \frac{S_i^{(1)}(\Omega)}{S^{(0)}(\Omega)}, \qquad \mathcal{OO}_{ii}^{(2)} = \frac{S_{ii}^{(2)}(\Omega)}{S^{(0)}(\Omega)}, \qquad \mathcal{OO}_{ij}^{(2)} = \frac{S_{ij}^{(2)}(\Omega)}{S^{(0)}(\Omega)} \tag{7.11}$$

where $\mathcal{OO}_i^{(1)}$, $\mathcal{OO}_{ii}^{(2)}$ and $\mathcal{OO}_{ij}^{(2)}$ denote the first order, second order and second order cross terms respectively and are functions of Ω. For single or one parameter fits only the first and second order observables $\mathcal{OO}_i^{(1)}$ & $\mathcal{OO}_{ii}^{(2)}$ are used. In two parameter fits, the two first and second order $\mathcal{OO}$s are used together with the corresponding cross term $\mathcal{OO}_{ij}^{(2)}$, ie five $\mathcal{OO}$s in total. Only in the three parameter fits, where each coupling is allowed to vary simultaneously, are all nine $\mathcal{OO}$s used. Although most of the sensitivity is contained in the first order $\mathcal{OO}$s, the quadratic dependence of the differential cross section often results in a two fold ambiguity for the solution (and a double minimum structure for the log likelihood curves which are discussed in the next chapter). Using the second order $\mathcal{OO}$s helps to pick out the right minimum.

The couplings can be extracted from a likelihood fit to the $\mathcal{OO}$ distributions (this is sometimes referred to as the ‘shape’ analysis and is the method used by the DELPHI Collaboration [103]). Alternatively the $\overline{\mathcal{O}\mathcal{O}}$s can be compared with the expectations (obtained from fully simulated MC) for different values of the coupling parameters. This is the method preferred by the OPAL [104] and ALEPH [96] Collaborations. For the first order $\mathcal{O}\mathcal{O}$s it has the same sensitivity as the shape analysis and is less complicated. This method is explained in detail in the next chapter.

Although the $\overline{\mathcal{O}\mathcal{O}}$s are calculated analytically from a differential cross section which assumes zero W width and does not include ISR, this approximation does not introduce any bias since these effects are modelled in the MC to which the data is fitted. It does, however, lead to potential loss of optimality and a slightly increased statistical uncertainty.

Intellect has a keen eye for method and technique but is blind to value and aim.

ALBERT EINSTEIN

POLONIUS: *"Though this be madness, yet there is method in't."*

WILLIAM SHAKESPEARE, *Hamlet, II.2*

Chapter 8

Measurement of Triple Gauge Boson Couplings using Optimal Observables

This chapter describes the details of the TGC analysis used to measure the three coupling parameters ($\Delta\kappa_\gamma$, Δg_1^{Z} and λ) from WW$\rightarrow l\nu q\bar{q}$ events using the optimal observable ($\mathcal{OO}$) technique. The data were collected during the 1999 run around four separate centre of mass energies. Since the $\mathcal{OO}$s are energy dependent (although the actual couplings are not) and also to simplify matters, the analysis was performed separately on each data set, and the results combined at the end. Table 1.1 lists the luminosities collected at each of the four energies and table 5.4 lists the number of events selected after the general WW $\rightarrow l\nu q\bar{q}$ and kinematic fit selections (discussed in chapter 5). In general electrons and muons are measured with higher resolution than taus, and hence $e\nu q\bar{q}$ and $\mu\nu q\bar{q}$ events were analyzed separately from $\tau\nu q\bar{q}$ events, and the results combined in log likelihood (log-L) plots. In OPAL, the analyses of WW$\rightarrow l\nu l\bar{\nu}$ and WW$\rightarrow q\bar{q}q\bar{q}$ events are performed separately (by other people) and are described in [49, 114]. The results from all three W$^+$W$^-$ channels are combined with those from single W events, and previous results from data sets collected at with lower energies, to give the final OPAL results [49].

We begin this chapter with a discussion of the fit and reweighting procedures, including construction of the calibration curves from which the couplings were extracted using the log-L curves. We then go on to discuss two separate tests of the method: one to check for possible biases and the other to check the reliability of the statistical error estimates returned by the fitting method. The different systematic checks are then summarized, and it is explained how they were incorporated into the fit. Finally, we describe how the results from each energy were combined.

8.1 Extracting the Triple Gauge Boson Couplings

This section describes how the couplings were extracted from the data using the mean optimal observables ($\overline{\mathcal{OO}}$s). For each event in both the data and Monte Carlo (MC) samples, the nine $\mathcal{OO}$s were constructed using the Bilenky [93] calculator package (to determine the differential cross section) and the formulae given by equation 7.11. The calculator was initialized at the nominal average centre of mass energy for each data set. There was a small energy spread in the data, and the MC samples were generated at the nearest integer value (the effect of this is small and included as a systematic described in section 8.3.10). Figure 8.1 compares the $\mathcal{OO}$ distributions for the data and Standard Model (SM) MC. There is generally good agreement between the data and the predicted SM distributions and only a small background contribution. In order to reduce the effects of events with large $\mathcal{OO}$ values in the tails of these distributions when the mean is taken, loose window cuts were applied to both the data and MC samples. The effect of these cuts was primarily to reduce the background still further. The numbers of events surviving this final round of cuts are given in table 8.1.

Energy (GeV)	No. of Data events after TGC cuts	Predicted No. of events after TGC cuts	No. of Data events after $\mathcal{OO}$ cuts	Predicted No. of events after $\mathcal{OO}$ cuts
192	168	182.6 ± 1.1	165	180.8 ± 1.0
196	493	486.9 ± 2.0	489	481.0 ± 2.0
200	439	470.7 ± 1.9	436	463.2 ± 1.9
202	230	232.7 ± 1.0	226	228.3 ± 0.9

Table 8.1: *Comparing the number of data events selected and Monte Carlo predictions (SM signal + background) before and after the $\mathcal{OO}$ cuts. The events have already passed the general TGC selections and kinematic fit cuts described in chapter 5.*

Single Parameter fits

We first consider the extraction of a single parameter (denoted by the generic term α). Only α was allowed to vary and the other two couplings were fixed at their SM values of zero. In the one parameter fits only the first and second order observables ($\mathcal{OO}^{(1)}$ & $\mathcal{OO}^{(2)}$) were used. The basic idea is to compare the data mean $\mathcal{OO}$ values with the expected $\overline{\mathcal{OO}}$ values determined from MC samples as a function of α. These MC samples were generated using the EXCALIBUR generator with different TGC values. A full list of these samples for each E_{cm} may be found in Appendix B, tables B.3, B.5, B.7, B.9. In the following

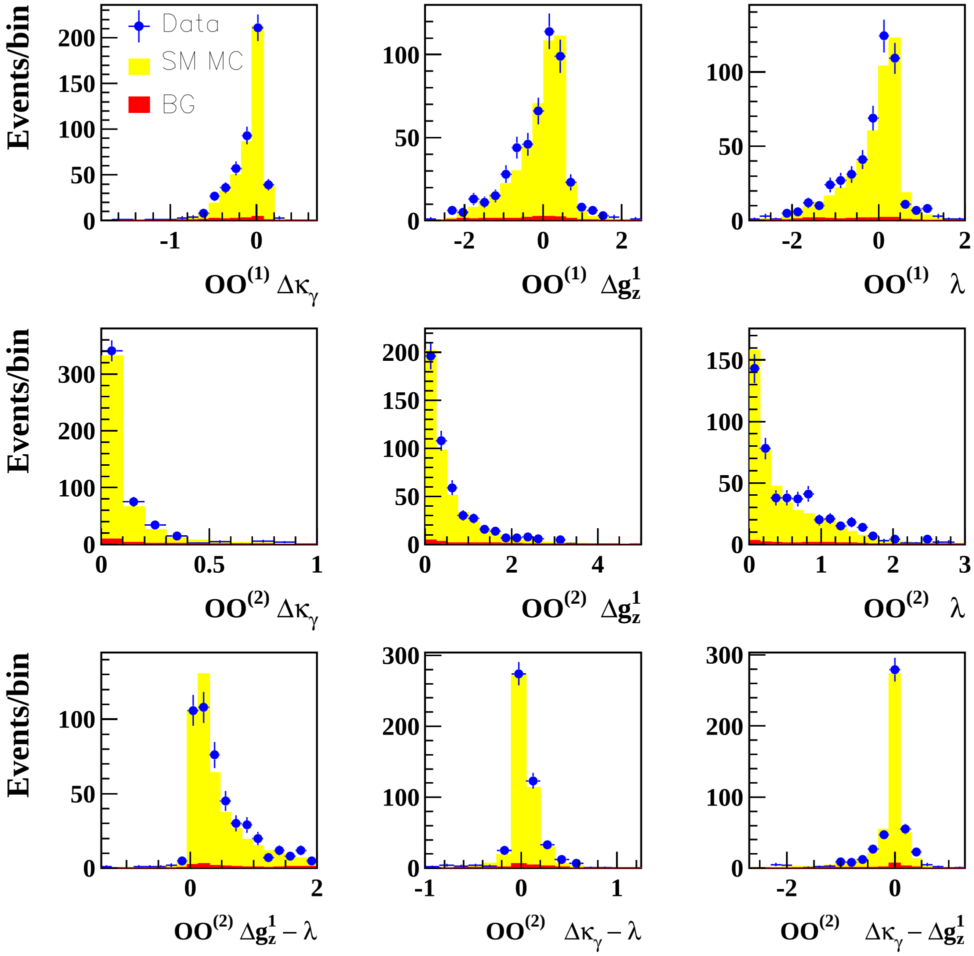

Figure 8.1: *$\mathcal{OO}$ Distributions for 196 GeV data compared with SM MC. The expected backgrounds are shown in red.*

discussions, these MC samples are referred to as the *'signal'* or *'reference'* set. Background contributions were estimated from other MC samples (also listed in tables B.3, B.5, B.7 and B.9) and added to the signal. These MC samples were used to construct *'calibration'* curves which describe the expectation values $\mathrm{E}[\mathcal{OO}](\alpha)$.

In the case of a single, first order observable $\mathcal{OO}^{(1)}$, the best estimate of the coupling ($\hat{\alpha}$) is obtained by solving:

$$\overline{\mathcal{OO}^{(1)}} - \mathrm{E}\left[\mathcal{OO}^{(1)}\right](\hat{\alpha}) = 0 \tag{8.1}$$

where $\overline{\mathcal{OO}^{(1)}}$ is measured from the data. In practice, α is extracted by minimizing a χ^2

curve given by:

$$\chi^2(\alpha) = \frac{\left(\overline{\mathcal{O}\mathcal{O}^{(1)}} - \mathrm{E}\left[\mathcal{O}\mathcal{O}^{(1)}\right](\alpha)\right)^2}{\sigma^2_{\overline{\mathcal{O}\mathcal{O}}}} \tag{8.2}$$

where $\sigma^2_{\overline{\mathcal{O}\mathcal{O}}}$ is the statistical error on $\overline{\mathcal{O}\mathcal{O}^{(1)}}$. This method can be extended to include the second order observable $\mathcal{O}\mathcal{O}^{(2)}$ in the χ^2, which can then be written out explicitly as:

$$\begin{aligned}
\chi^2(\alpha) \;=\; & \left(\overline{\mathcal{O}\mathcal{O}^{(1)}} - \mathrm{E}\left[\mathcal{O}\mathcal{O}^{(1)}\right](\alpha)\right) V^{-1}_{11} \left(\overline{\mathcal{O}\mathcal{O}^{(1)}} - \mathrm{E}\left[\mathcal{O}\mathcal{O}^{(1)}\right](\alpha)\right) \qquad (8.3)\\
+ & \left(\overline{\mathcal{O}\mathcal{O}^{(1)}} - \mathrm{E}\left[\mathcal{O}\mathcal{O}^{(1)}\right](\alpha)\right) V^{-1}_{12} \left(\overline{\mathcal{O}\mathcal{O}^{(2)}} - \mathrm{E}\left[\mathcal{O}\mathcal{O}^{(2)}\right](\alpha)\right)\\
+ & \left(\overline{\mathcal{O}\mathcal{O}^{(2)}} - \mathrm{E}\left[\mathcal{O}\mathcal{O}^{(2)}\right](\alpha)\right) V^{-1}_{21} \left(\overline{\mathcal{O}\mathcal{O}^{(1)}} - \mathrm{E}\left[\mathcal{O}\mathcal{O}^{(1)}\right](\alpha)\right)\\
+ & \left(\overline{\mathcal{O}\mathcal{O}^{(2)}} - \mathrm{E}\left[\mathcal{O}\mathcal{O}^{(2)}\right](\alpha)\right) V^{-1}_{22} \left(\overline{\mathcal{O}\mathcal{O}^{(2)}} - \mathrm{E}\left[\mathcal{O}\mathcal{O}^{(2)}\right](\alpha)\right)
\end{aligned}$$

where the expectations $\mathrm{E}[\mathcal{O}\mathcal{O}^{(1)}]$ and $\mathrm{E}[\mathcal{O}\mathcal{O}^{(2)}]$ were determined directly from the two calibration curves corresponding to the first and second order $\mathcal{O}\mathcal{O}$s. V_{ij} are the elements of the covariance matrix of the expected mean $\mathcal{O}\mathcal{O}$s: $V_{ij} = \mathrm{cov}(\mathcal{O}\mathcal{O}_i, \mathcal{O}\mathcal{O}_j) = \overline{\mathcal{O}\mathcal{O}_i\mathcal{O}\mathcal{O}_j} - \overline{\mathcal{O}\mathcal{O}}_i \cdot \overline{\mathcal{O}\mathcal{O}}_j$. The elements were calculated using the MC samples and then normalized to the number of data events. This provides a more accurate estimate of the covariance matrix than if it were constructed from the data, since the smaller data sample would lead to larger errors on V_{ij}. The covariance matrix was evaluated at the point where the couplings were set to their SM values.

The *statistical* covariance matrix has a block diagonal structure reflecting the fact that the $e\nu q\bar{q}/\mu\nu q\bar{q}$ and $\tau\nu q\bar{q}$ events are treated separately and are uncorrelated:

$$V_{\text{stat}} = \begin{pmatrix} V^{e,\mu}_{\text{stat}} & 0 \\ 0 & V^{\tau}_{\text{stat}} \end{pmatrix} \tag{8.4}$$

In single parameter fits (when only the first and second order $\overline{\mathcal{O}\mathcal{O}}$s are used), the covariance matrix is a 4×4 matrix. (Correlations between the $\mathcal{O}\mathcal{O}$s from different channels and energies were incorporated in the *full* covariance matrix, which has both statistical and systematic contributions. This is discussed further in sections 8.3 and 8.4.)

The statistical uncertainty σ for each TGC in the one parameter fits was determined directly from the χ^2 or maximum likelihood plots[1]. In the limit of a large number of data points,

---

[1] The χ^2 and log likelihood (log-L) functions are directly related by: log-L= -$\chi^2/2$ [115]. For historical reasons, the negative log-L curves are usually presented in TGC analyses.

σ is given by the difference in the TGC value at the minimum and where the curve has increased to ± 1.0 (for a χ^2) or ± 0.5 (for a log-L). For a smaller number of data points it is conventional to adopt the same procedure. An example of this is shown in figure 8.2 for the λ log-L at 200 GeV. In order to check the validity of this approach and the reliability of the error estimates, subsample tests were performed and these are described in section 8.2.2.

The negative log-L plots obtained from all the one parameter fits (as a function of the couplings) at each E_{cm} are presented in the next chapter (figure 9.1). The curves are asymmetric and quite non-Gaussian in some cases. Particularly for $\Delta\kappa_\gamma$, there is often a double minimum structure in the log-L curve, reflecting the quadratic dependence of the differential cross section. The deeper minimum is the preferred fit value, and for the 192 GeV data, the second minimum is deeper, which results in the wrong TGC value being picked out and a larger error estimate.

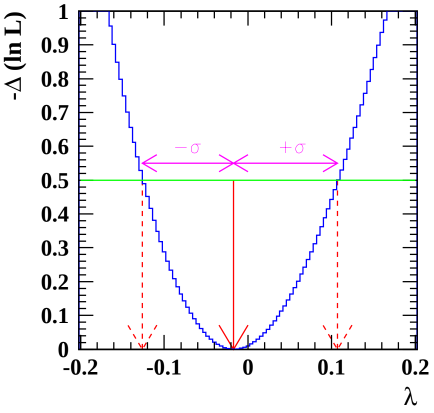

Figure 8.2: *The statistical uncertainty for 1 parameter fits may be estimated from the log-L curves by finding the change in the coupling between the minimum and when the curve equals 0.5. This curve shows the log-L distribution for λ at 200 GeV.*

Multi-Parameter fits

Fits were also performed in which two or all three of the couplings were allowed to vary simultaneously. In the two parameter fits, the coupling that was not being fitted was fixed to its SM value. Five $\overline{\mathcal{O}\mathcal{O}}$s were used in these fits, corresponding to the two first $\overline{\mathcal{O}\mathcal{O}_i^{(1)}}$ and two second $\overline{\mathcal{O}\mathcal{O}_i^{(2)}}$ order observables and the second order cross term $\overline{\mathcal{O}\mathcal{O}_{ij}^{(2)}}$ (with $i \neq j$), which have sensitivity to the couplings being fitted. In the three parameter fits, all nine $\overline{\mathcal{O}\mathcal{O}}$s were used. The χ^2 (equation 8.3) was replaced by a summation over the observables and the coupling set ($\vec{\alpha}$):

$$\chi^2(\vec{\alpha}) = \sum_i \sum_j \left(\overline{\mathcal{OO}_i} - \mathrm{E}[\mathcal{OO}_i](\vec{\alpha})\right) V_{ij}^{-1} \left(\overline{\mathcal{OO}_j} - \mathrm{E}[\mathcal{OO}_j](\vec{\alpha})\right) \tag{8.5}$$

where i, j run from 1-9 in the case of the three parameter fits. The couplings were extracted using the MINUIT [116] minimization package which also returned the fit errors. The statistical covariance matrix V_{ij} (equation 8.4) retained the same block structure and was still normalized to the number of events in the data, but was extended to an 18×18 matrix in the case of the three parameter fits.

8.1.1 The Reweighting Method

The calibration curves describe how the expected mean observables $\mathrm{E}[\mathcal{OO}_i]$ vary as a function of the couplings. They can be constructed either by generating lots of MC samples with different anomalous coupling values or by reweighting the existing MC samples. Since it is not practical to generate large samples of fully simulated MC events with a wide range of anomalous couplings to scan the whole parameter space, a reweighting technique was applied to the MC reference samples to simulate different anomalous couplings.

Essentially the reweighting technique changes the probability of a certain region of phase space to be populated with events. Consider a sample of events generated with coupling set $\vec{\alpha}_1$. In a certain region of phase space $[\Omega, \Omega + \mathrm{d}\Omega]$ there might be n_1 events. Another sample of events generated with the same luminosity but with a different set of anomalous couplings $\vec{\alpha}_2$, might have n_2 events in this same region of phase space. The $\mathcal{OO}$ distributions of the second sample can be simulated from the first by weighting this region of the $\mathcal{OO}$ spectrum by a factor n_2/n_1 [117].

The probability for an event to occur is given by its normalized cross-section. So the weights for an event (generated with TGC parameters $\vec{\alpha}_{\mathrm{gen}}$ and angular set Ω) were determined from the ratio of the differential cross sections (or equivalently from the ratio of matrix elements squared since the phase space part cancels in the quotient):

$$w(\vec{\alpha}_{\mathrm{new}}) = \frac{\mathrm{d}\sigma(\Omega, \vec{\alpha}_{\mathrm{new}})}{\mathrm{d}\sigma(\Omega, \vec{\alpha}_{\mathrm{gen}})} \equiv \frac{|\,\mathcal{M}(\Omega, \vec{\alpha}_{\mathrm{new}})\,|^2}{|\,\mathcal{M}(\Omega, \vec{\alpha}_{\mathrm{gen}})\,|^2} \tag{8.6}$$

where $\vec{\alpha}_{\mathrm{new}}$ are the coupling values to which the event is being reweighted.

To see how these weights were applied, it is first necessary to parameterize the expectations $\mathrm{E}[\mathcal{OO}_i]$ as a function of the couplings:

$$\mathrm{E}[\mathcal{OO}_i](\alpha) \;=\; \frac{\displaystyle\int \mathcal{OO}_i(\Omega)\,\frac{\mathrm{d}\sigma(\Omega)}{\mathrm{d}\Omega}\,\mathrm{d}\Omega}{\displaystyle\int \frac{\mathrm{d}\sigma(\Omega)}{\mathrm{d}\Omega}\,\mathrm{d}\Omega} \;\equiv\; \frac{1}{\sigma_{\text{Tot}}}\int \mathcal{OO}_i(\Omega)\,\mathrm{d}\sigma(\Omega) \tag{8.7}$$

where the normalization factor σ_{Tot} represents the total cross section[2]: $\sigma_{\text{Tot}} = \int \mathrm{d}\sigma(\Omega) = \int \frac{\mathrm{d}\sigma(\Omega)}{\mathrm{d}\Omega}\,\mathrm{d}\Omega$. This equation is the ratio of two parabolic functions (although it is not itself parabolic) since the differential cross section (equation 7.10) is a paraboloid of the form:

$$\text{paraboloid}(\vec{\alpha}) \;=\; C^{(0)} + \sum_i \alpha_i \cdot C_i^{(1)} + \sum_{i,j} \alpha_i\alpha_j \cdot C_{ij}^{(2)} \tag{8.8}$$

where C represents a set of co-efficients that uniquely define the paraboloid. For a single coupling parameter, equation 8.8 simplifies to a simple parabola: $C^{(0)} + \alpha\, C^{(1)} + \alpha^2\, C^{(2)}$ with three co-efficients which can be determined from three *'basis points'*. For two parameter fits a minimum of six basis points were needed and ten points[3] when all three couplings were fitted simultaneously. Using equation 8.6 to reweight the $\mathcal{OO}$s for each event n in any MC sample (generated with arbitrary coupling parameters) at these basis points, the expected mean $\mathcal{OO}$ values can be written as:

$$\mathrm{E}[\mathcal{OO}](\alpha_{\text{new}}) \;=\; \frac{\sum_{n=1}^{\text{Events}} w_n(\alpha_{\text{new}})\mathcal{OO}(\Omega_n, \alpha_{\text{gen}})}{\sum_{n=1}^{\text{Events}} w_n(\alpha_{\text{new}})} \tag{8.9}$$

Since the two parabolic functions are uniquely defined by these basis points, the expectation values for other anomalous couplings can be found by interpolation/extrapolation. The advantage of this technique (as opposed to the analytical calculation of $\mathrm{E}[\mathcal{OO}]$), is that all the physical effects (for example detector resolution, ISR/FSR, finite W width etc) can be simulated in the MC reference samples and hence automatically taken care of in the fit.

In theory it is possible to obtain the entire expected $\mathcal{OO}$ spectrum by reweighting just one sample of MC events. (Although a MC sample generated with, for example, TGCs $\vec{\alpha} = (1, 0, 0)$ would require very large weights if it were made to mimic a sample with couplings $\vec{\alpha} = (-1, 0, 0)$ and hence this would lead to statistical fluctuations). In practice,

---

[2] The total cross section can be modified to include an acceptance function.

[3] The 10 basis points chosen were: (0,0,0), (±1,0,0), (0,±1,0), (0,0,±1), (1,1,0), (1,0,1) and (0,1,1).

it is better to use all available MC samples for the reference to avoid certain regions of the phase space being insufficiently populated.

8.1.2 Calibration Curves

The couplings were estimated by comparing the $\mathrm{E}[\mathcal{O}\mathcal{O}](\alpha)$ from the calibration curves, to the experimental measurements of the $\overline{\mathcal{O}\mathcal{O}}$s. Examples of calibration curves from MC generated at 200 GeV are shown in figure 8.3. Although the curves for the $e\nu q\bar{q}/\mu\nu q\bar{q}$ and $\tau\nu q\bar{q}$ channels are similar in shape, there is a clear difference in their expectation values because of the poorer resolutions for taus.

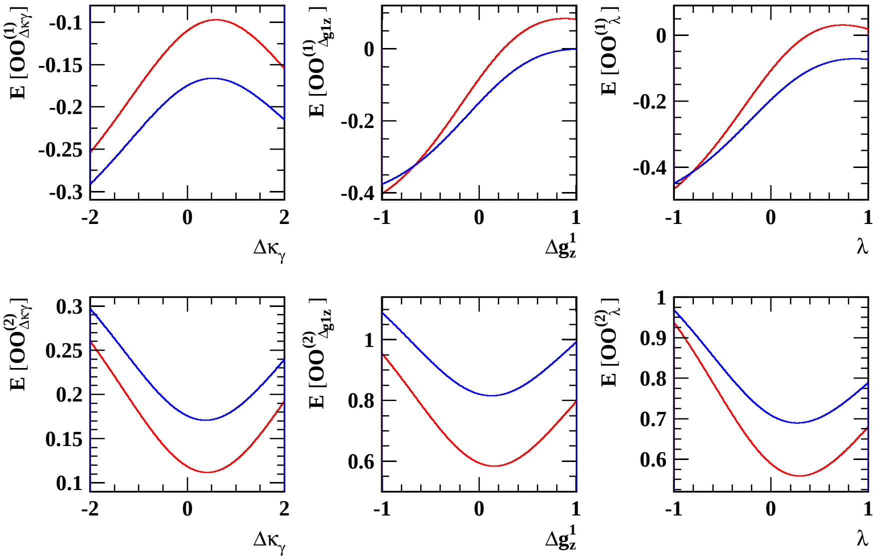

Figure 8.3: *Calibration curves determined from the MC reference samples generated at 200 GeV. The first order expectation values* $E[\mathcal{O}\mathcal{O}^{(1)}_{\alpha_i}]$ *are shown in the top row of plots and the second order* $E[\mathcal{O}\mathcal{O}^{(2)}_{\alpha_i}]$ *in the lower row. The curves for the* $e\nu q\bar{q}$ *and* $\mu\nu q\bar{q}$ *events (red) were made separately from from the* $\tau\nu q\bar{q}$ *events (blue) since the latter have poorer resolution.*

For single parameter fits, when only the first order $\mathcal{O}\mathcal{O}^{(1)}$ is used (and only one channel), the TGC value can be read off directly from the corresponding calibration curve. However, in some of the distributions in figure 8.3, two solutions are possible for certain $\mathrm{E}[\mathcal{O}\mathcal{O}]$ values. Hence the desirability of using both first and second order observables. This was achieved in both single and multi-parameter fits by summing the χ^2 curves (equations 8.3 and 8.5) to form a log-L.

8.2 Monte Carlo Tests

In most physics analyses, it is important to check for possible biases in the method which could affect the final results. If a significant bias is found, then it is necessary to either evaluate its effect and determine appropriate correction factors, or else to modify the experimental techniques to eliminate biases as far as possible. It is also important to check whether the statistical errors obtained from the fits agree with expectations. If not, appropriate scaling factors can be applied to the log-L curves. For both these types of test, MC samples were used as pseudo or 'test' data and the fit performed at each E_{cm} using these test samples. The advantage of using simulated events as test samples is that they have high statistics, so that the behaviour of the fit procedure can be tested in the high statistics limit as well as with the same statistics as the data. For the bias tests, MC samples generated with different TGC values were used so that the sensitivity to anomalous couplings could also be tested.

8.2.1 Bias Testing

In order to check for any bias (arising from, for example the fit procedure or reconstruction methods) high statistics four fermion EXCALIBUR MC samples generated with different TGC couplings were used as test data (these are listed in tables B.3, B.5, B.7 and B.9). For each test sample, the TGCs were extracted from the fits in the normal way. If the fit procedure is unbiased, then the fitted couplings should agree with the generated values (within statistical precision). For each test, the MC sample used as the pseudo test sample was removed from the reference MC set to avoid correlations when evaluating the $\overline{\mathcal{O}\mathcal{O}}$s and the covariance matrix elements.

The tests were performed both with and without MC background samples (normalised to the test sample). Unfortunately for some processes the available background MC is not really sufficient to create two independent sets (one set to make up the test sample and the other for the reweighting set). However, in order to test the actual fit procedure, it is not necessary to include background providing the reference and test data samples have the same diagrams. Hence all the bias test results presented here are without background.

Previous studies [117][4] and the current tests all indicate that there are no additional biases when background samples are included.

The results for the 196 GeV single parameter fits are shown in figure 8.4. The plots for the other three E_{cm} are similar. (For the 196 and 200 GeV tests, MC samples generated with one anomalous coupling $\alpha_i = \pm 0.5$ and ± 1.0 were available whereas only samples with $\alpha_i = \pm 1.0$ were available for 192 and 202 GeV). The top row of plots represent the measured couplings extracted from the fits (with their statistical error) versus the generated couplings. A straight line fit (red line) through the data points indicate good agreement between the fitted and generated couplings. The black dotted line represents the line at 45^0, along which all the points would lie if the fit procedure returned exactly the generated coupling values.

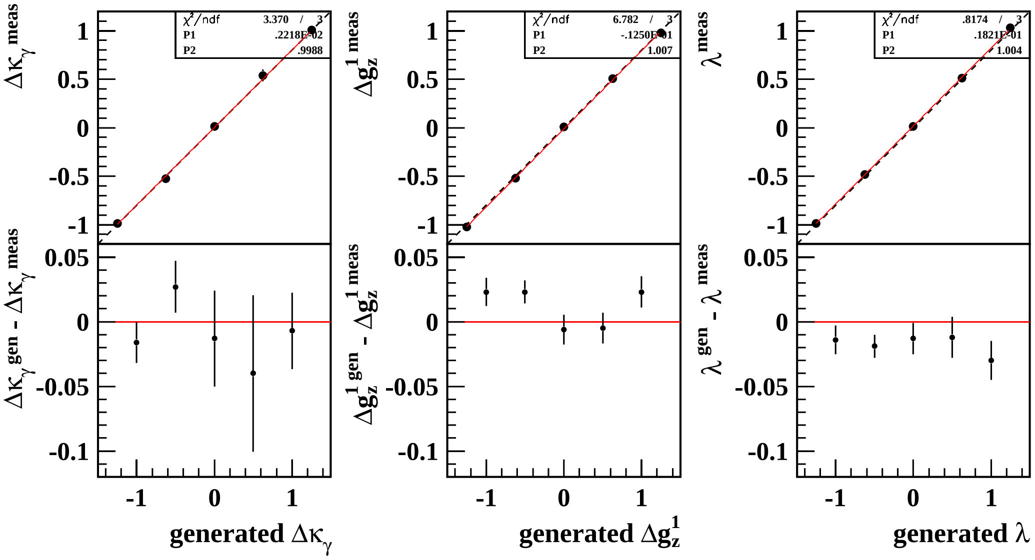

Figure 8.4: *Single parameter fit bias results for 196 GeV. The top row of plots indicate the fitted versus generated coupling values. Straight line fit results are shown by the red solid line. The black dotted lines indicate where the points should lie if the fit results are unbiased. The lower row of plots show the $\alpha^{gen} - \alpha^{meas}$ distributions. The horizontal line at y=0 indicates where the points would lie if the fit procedure returned exactly the same coupling values as the input generated ones.*

The difference between the generated and extracted coupling values are shown in the lower row of plots. For $\Delta\kappa_\gamma$ all the deviations of the measured TGCs from the true TGCs are compatible with zero and there is no evidence of any bias. For Δg_1^Z a few of the points at

---

[4] The bias tests at 189 GeV were performed slightly differently, using the subsampling technique (described in the next subsection) since historically the statistical covariance matrix was TGC dependent. Now that the statistical covariance matrix is determined only at the SM coupling values, this extra complication is no longer necessary.

large(ish) values of anomalous coupling are a few sigma away from the line y=0. However, for the region of interest around the SM expected value of zero, where the fit is most sensitive, the points are very close to this line and there is no problem. Although the points for λ are all within one or two sigma of zero, they lie slightly below the line. This indicates that there might be a small bias ($\sim 3\sigma$ effect). However, the other energies show no evidence of any bias in the single parameter fits for λ, and it would be assumed that any bias in the fitting methods would also be apparent at other energies (and maybe even energy dependent). Therefore no bias correction was assumed. In order to assign a possible systematic to this, straight line fits (y=constant) were made to the lower row of plots in figure 8.4. The results of these fits are shown in the left hand side of table 8.2. The majority of fit parameters (except Δg_1^{Z} at 196 and 200 GeV, and λ at 196 GeV) are within two sigma of zero. The errors from the horizontal line fits were taken to be the systematic uncertainties assigned to the bias. They vary from parameter to parameter and are listed in table 8.5.

Coupling	Energy	**One parameter fits**			**Three parameter fits**		
		Constant	χ^2	χ^2prob %	Constant	χ^2	χ^2prob %
$\Delta\kappa_\gamma$	192	0.004 ± 0.021	0.67	72	0.019 ± 0.024	0.49	78
	196	-0.003 ± 0.011	3.38	50	0.012 ± 0.012	3.42	49
	200	-0.013 ± 0.011	2.33	68	-0.014 ± 0.011	16.33	0.1
	202	0.031 ± 0.017	2.05	36	0.000 ± 0.020	0.83	66
Δg_1^{Z}	192	0.004 ± 0.010	6.27	4	0.017 ± 0.014	1.22	54
	196	0.013 ± 0.005	7.73	10	0.004 ± 0.007	2.75	60
	200	0.013 ± 0.005	5.26	26	0.011 ± 0.007	3.92	42
	202	0.006 ± 0.008	0.86	65	0.020 ± 0.012	2.30	32
λ	192	-0.001 ± 0.011	3.01	22	-0.018 ± 0.014	2.25	32
	196	-0.017 ± 0.005	1.08	90	-0.018 ± 0.007	1.30	86
	200	0.003 ± 0.005	12.26	2	0.006 ± 0.007	8.00	9
	202	0.016 ± 0.008	8.72	2	0.030 ± 0.010	10.26	0.5

Table 8.2: *χ^2, χ^2 probabilities (%) and horizontal straight line fit results for the one and three parameter bias tests. The systematic uncertainties are taken directly from the straight line fits.*

Examples of TGC couplings extracted from the three parameter fits using test samples generated with either SM couplings or one anomalous coupling parameter $\alpha_i = \pm 0.5$ are given in table 8.3. For these fits, all nine optimal observables were used. Except for 200 GeV $\Delta\kappa_\gamma = +0.5$ (where there is evidence of a second minimum), the fitted values are in good agreement with the generated couplings. In particular, all the SM couplings are within one sigma of expectation. An example of the three parameter fit bias plots for 200 GeV are shown in figure 8.5. The horizontal line fit results for all E_{cm} are shown in the right hand side of table 8.2. There is no evidence for any constant bias at all E_{cm}. Analogous to the one parameter fits, the systematic uncertainties for the bias are taken directly from the horizontal line fit errors.

Generated Coupling	E_{cm} (GeV)	**Fitted Coupling Values**		
		$\Delta\kappa_\gamma$	Δg_1^Z	λ
SM	192	0.023 ± 0.066	0.006 ± 0.026	-0.005 ± 0.025
SM	196	-0.006 ± 0.042	-0.005 ± 0.018	0.016 ± 0.017
SM	200	-0.003 ± 0.040	-0.019 ± 0.017	0.006 ± 0.016
SM	202	0.033 ± 0.050	-0.006 ± 0.019	0.004 ± 0.016
$\alpha = +0.5$	196	0.540 ± 0.073	0.522 ± 0.017	0.516 ± 0.019
$\alpha = -0.5$	196	-0.536 ± 0.021	-0.512 ± 0.012	-0.482 ± 0.013
$\alpha = +0.5$	200	0.252 ± 0.092	0.507 ± 0.016	0.530 ± 0.017
$\alpha = -0.5$	200	-0.486 ± 0.020	-0.506 ± 0.012	-0.520 ± 0.012

Table 8.3: *Three parameter fit results for SM and anomalous coupling values generated at* $\alpha = \pm 0.5$.

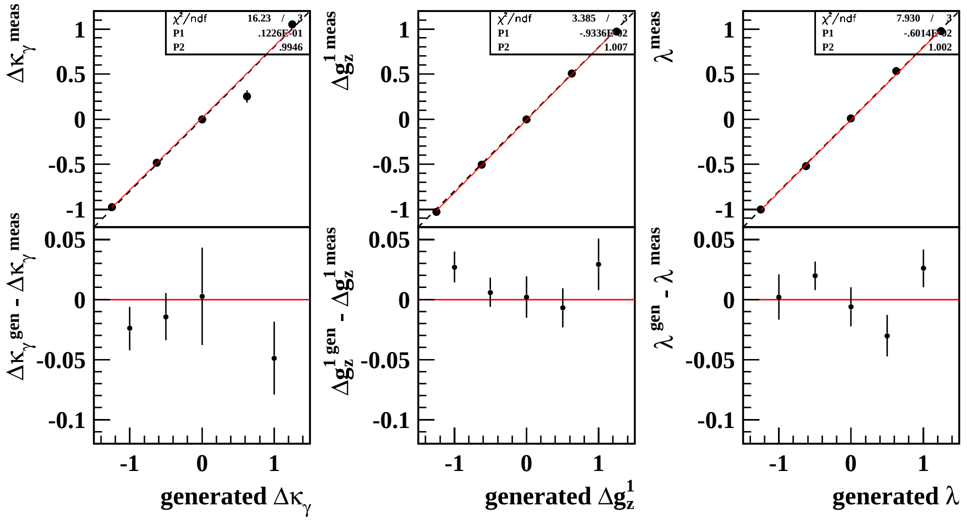

Figure 8.5: *Three parameter fit bias tests for 200 GeV.*

To further check the multi-parameter fits (both two and three parameter) at 196 and 200 GeV, MC samples generated with two anomalous couplings were used as test data. The 95% confidence level plots for these tests are shown in figure 8.6. Again there is good agreement with the generated couplings and no evidence of any bias. Additional bias tests were also made to show that greater sensitivity is achieved by using all anomalous coupling MC samples in the reference set, as opposed to simply reweighting samples generated with SM couplings.

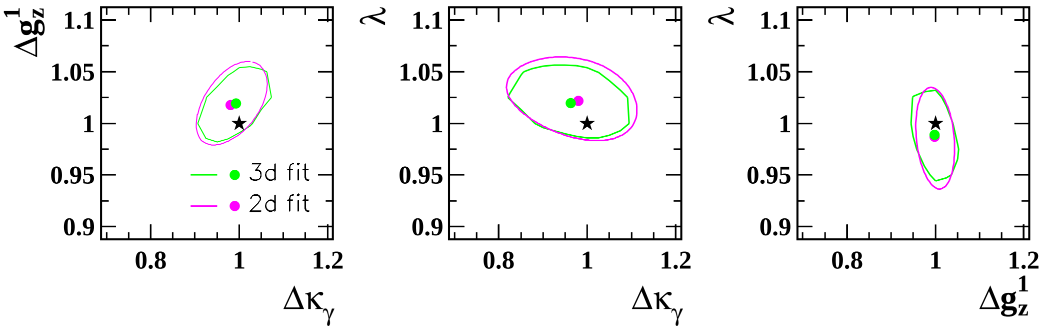

Figure 8.6: *Two and three parameter fit bias test results at 95% confidence level for 200 GeV. The plots show the projection onto the 2d plane. The black star indicates the position of the test sample generated coupling values.*

These tests demonstrate that the fit procedure is reliable in accurately predicting the couplings for events generated with values around the SM. They also demonstrate that within the uncertainties on the fit results, the fits can successfully extract the correct coupling values from the OPAL data. Systematic uncertainties have been assigned to cover any small residual biases.

8.2.2 Subsample Tests

In order to provide a consistency check on the statistical uncertainty, the so-called ‘bootstrap’ resampling technique [118–120] or subsampling with replacement was used. For each of the four energies, 999×9 subsamples were created from the SM and background MC samples, such that the size of each subsample corresponded to the luminosity of the data collected at that energy. The events were chosen randomly from the MC samples with replacement, which means that any event could occur more than once in a subsample or in several subsamples. Replacement was used because there is insufficient generated Monte Carlo to make a large number of independent subsamples. The actual number of subsamples (8991) was chosen for consistency with the 189 GeV analysis [117]. For these purposes it is thought [118] that this number of subsamples is adequate. The number of events in each subsample is Poisson distributed around the expected number for SM couplings.

The full fit procedure was performed on each subsample to extract all three couplings for both the single and three parameter fits. The one parameter fitted TGC values from the subsample log-Ls at 200 GeV are shown in figure 8.7. Although these distributions are centred around the SM expectation value of zero, they have non Gaussian tails and their errors are not symmetric. In particular the presence of the second minima can clearly be seen for $\Delta\kappa_\gamma$. This is reflected in the pull distributions (figure 8.8) where the tail for $\Delta\kappa_\gamma$ corresponds to the second minimum. For this reason, the pull distributions cannot be used directly to determine the expected statistical uncertainty. Instead the average of the statistical uncertainties obtained from the subsample fits was used. The corresponding statistical uncertainty distributions are shown in figure 8.9. The long tail for $\Delta\kappa_\gamma$ corresponds to subsample tests where the second minimum was chosen, since in general the log-L functions are broader for the second minimum (and consequently have larger statistical errors).

The pull distributions are given by: $\frac{\alpha_{\text{fit}}-\alpha_{\text{gen}}}{\sigma_{\text{fit}}}$, where the generated coupling (α_{gen}) equals the SM value of zero. Hence these distributions correspond to the error weighted coupling values (and could be used to test the sensitivity of the different methods [117]). If the pull distributions were completely Gaussian, then they should be centred at zero (generated value) and have widths equal to unity. This would mean that the statistical uncertainties were correctly modelled. If the widths were less than one then this would indicate that the statistical uncertainties are under estimated (and conversely over estimated for RMS values greater than one).

The reliability of the statistical error can be tested by calculating the fraction of subsamples which contain the true coupling value (ie $\alpha_i = 0$) within their error interval. Consider figure 8.10. The plot on the left shows a single parameter fit log-L function from one of the subsample tests for $\alpha_i = \Delta g_1^{\text{Z}}$. The positions of the magenta arrows indicate the 1σ error interval, defined as the distance between the minimum and the point where the log-L curve equals ±0.5 (see section 8.1). The red arrow represents the value of the log-L curve at the SM expectation (ie the true, generated value when $\alpha_i = 0$). The plot on the right shows the number of subsamples with a particular value of $-\Delta(\ln L)$ at the SM expectation. If the statistical error for a given coupling is reliable, then 68.3% of the subsamples should contain the true value within their error interval. Or equivalently, the value of the log-L at the SM expectation, will be less than or equal to 0.5 for 68.3% of the subsamples (indicated by the

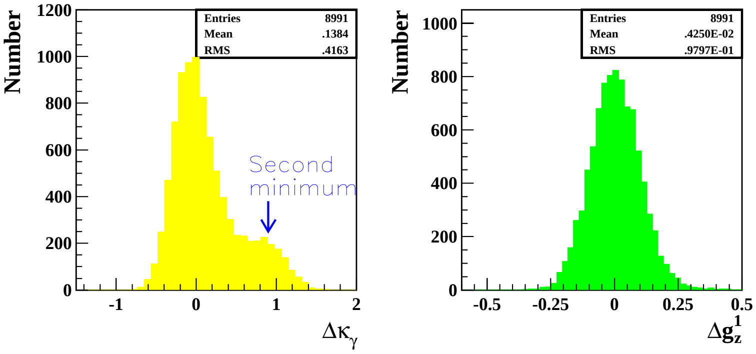

Figure 8.7: *Distribution of the single parameter fit couplings obtained from subsample tests at 200 GeV. The presence of a second minimum for $\Delta\kappa_\gamma$ is clearly seen and implies that this distribution is non Gaussian.*

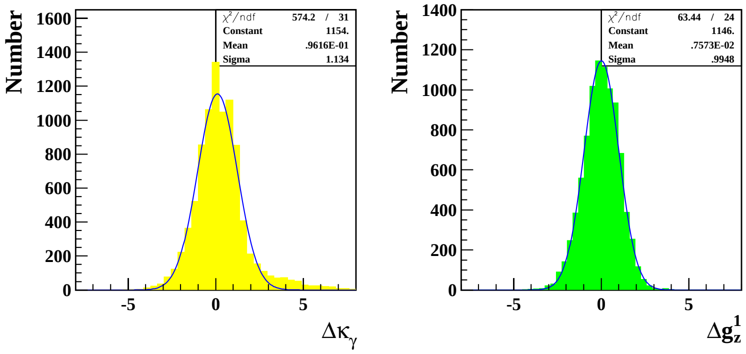

Figure 8.8: *One parameter fit pull distributions from subsample tests at 200 GeV. Because of the non Gaussian tails, its not possible to use the width of these distributions to determine the expected statistical uncertainty.*

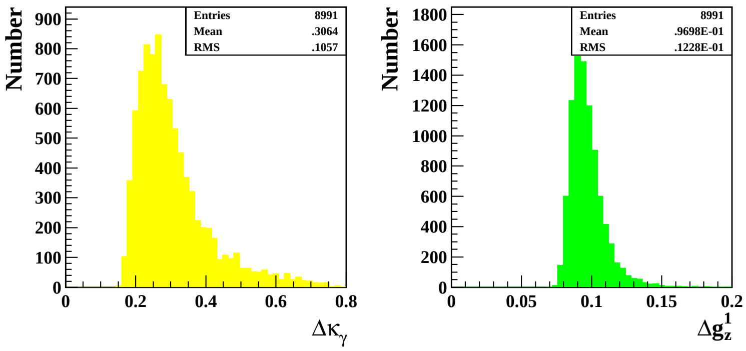

Figure 8.9: *One parameter fit statistical error distributions from the 200 GeV subsample tests. The expected uncertainty for each coupling is taken to be the average uncertainty.*

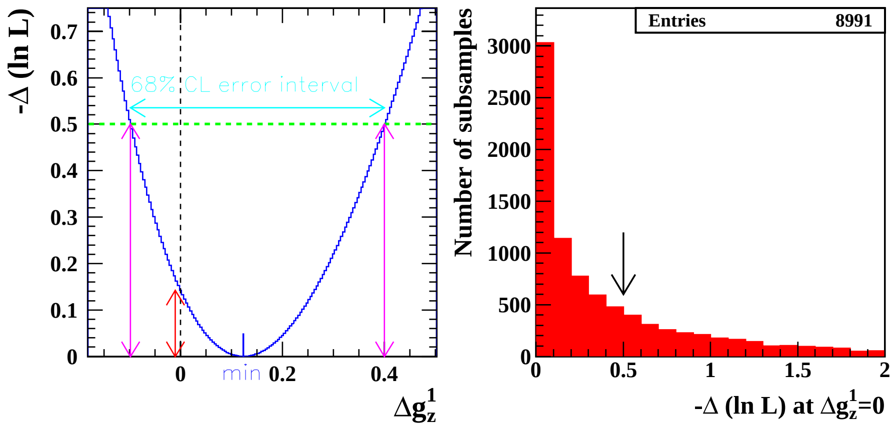

Figure 8.10: *The plot on the left is a log-L function from a Δg_1^Z subsample test illustrating the 1σ error interval (magenta arrows). The value of the log-L at SM expectation is shown by the red arrow. The distribution of $-\Delta(\ln L)$ evaluated at $\Delta g_1^Z = 0$ from all the subsample tests is shown in the right hand plot. If the statistical uncertainty were reliable, then exactly 68.3% of the subsamples would lie to the left of the black arrow. (See text for further explanation.)*

black arrow on the right hand plot). If more than 68.3% of the subsamples are within $\pm 1\sigma$, then the statistical error is over estimated. Conversely if less than 68.3% of the subsamples have values of $-\Delta(\ln L)$ less than 0.5 at $\alpha_i = 0$ (ie lying to the left of the black arrow in the right hand plot), then the statistical uncertainty would be under estimated. An appropriate scale factor would therefore need to be applied to the data log-Ls, so that 68.3% of the subsamples were within the 1σ error interval.

Scale factors can be determined by considering the value of $-\Delta(\ln L)$ at $\alpha_i = 0$ (right hand plot in figure 8.10) which corresponds to 68.3% of the subsamples having less than this value. The scale factor is simply the ratio of this number divided by 0.5 (ie the value of $-\Delta(\ln L)$ which normally defines the 68% confidence interval on a log-L plot. Scale factors were determined separately for each coupling at each $\mathrm{E_{cm}}$. It should be noted that scale factors were only applied conservatively, when the statistical uncertainties were under estimated by at least two sigma. Scale factors change the width of the data log-L curves. They do not change the central value of the coupling at the minimum, only the error interval. This is equivalent to changing the height at which the $\pm 1\sigma$ errors are read off the $-\Delta(\ln L)$ curves (ie the green dotted line in the left hand plot of figure 8.10 would be shifted upwards if a scale factor greater than one were applied). It should also be noted these these subsample tests assume SM couplings.

The results from the one parameter fit subsample tests are list in table 8.4. For both the

Δg_1^Z and λ couplings, all the scale factors are within 10% of unity. This implies that the there are no major problems with the 1σ statistical uncertainties. Larger scale factors were determined for $\Delta\kappa_\gamma$ because there is a greater tendency to pick out the second minimum for this coupling which increases the errors obtained from the log-Ls. The expected number of subsamples which should contain the SM expectation within the error interval is 6140.85 ± 44.12 subsamples, or 68.3% of the total. The errors on the observed percentage of subsamples within the 68.3% error interval are described by the binomial distribution, since a particular subsample either will or will not, contain the SM expectation within its error interval.

Coupling	Energy (GeV)	Observed No. of Subsamples at 68% CL	Percentage of total subsamples	Expected Error	Scale Factor
$\Delta\kappa_\gamma$	192	5769	64.16 ± 0.25	0.509	$1.166\,^{+0.020}_{-0.017}$
	196	5404	60.10 ± 0.26	0.325	$1.391\,^{+0.024}_{-0.023}$
	200	5572	61.97 ± 0.26	0.306	$1.282\,^{+0.022}_{-0.023}$
	202	5714	63.55 ± 0.25	0.382	$1.178\,^{+0.026}_{-0.020}$
Δg_1^Z	192	6014	66.89 ± 0.25	0.176	$1.055\,^{+0.027}_{-0.021}$
	196	5995	66.68 ± 0.25	0.097	$1.063\,^{+0.021}_{-0.018}$
	200	6168	68.60 ± 0.24	0.097	$0.991\,^{+0.018}_{-0.022}$
	202	6054	67.33 ± 0.25	0.134	$1.037\,^{+0.017}_{-0.020}$
λ	192	5978	66.49 ± 0.25	0.196	$1.073\,^{+0.024}_{-0.021}$
	196	6082	67.65 ± 0.25	0.103	$1.024\,^{+0.017}_{-0.019}$
	200	6223	69.21 ± 0.24	0.102	$0.971\,^{+0.013}_{-0.018}$
	202	6049	67.28 ± 0.25	0.142	$1.036\,^{+0.016}_{-0.018}$

Table 8.4: *Results from the one parameter fit subsampling tests. The observed number of subsamples are the number of subsamples which contain the true or SM expectation value within their error interval. The expected number of subsamples satisfying this requirement for each coupling was 6140.85 ± 44.12. Only scale factors > 1.0 are applied to the log-L results quoted in table 9.2.*

Subsample tests were also made for the three parameter fits. An example of the couplings extracted from these fits, and projected onto a 2d plane are shown in figure 8.11 for 202 GeV. Again, the presence of the second minimum can be seen for $\Delta\kappa_\gamma$. For the three parameter fits, the intrinsic correlations between the couplings give rise to overall larger statistical

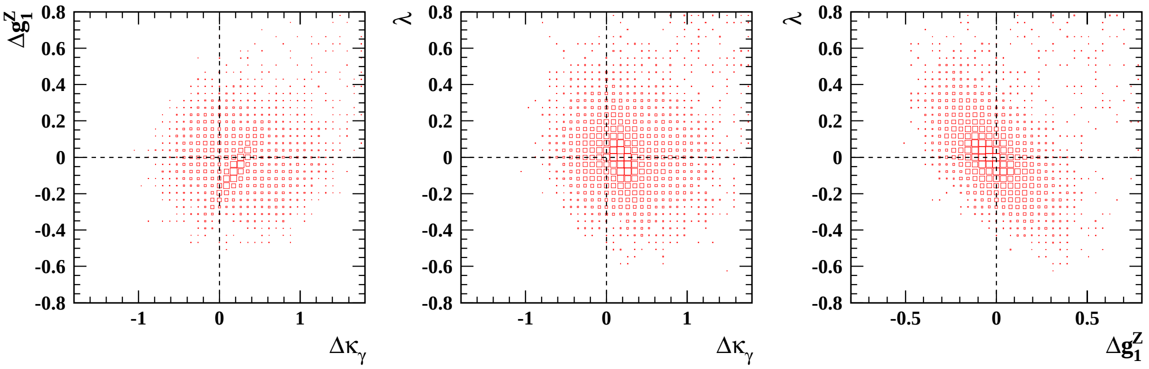

Figure 8.11: *Distribution of the three parameter fit couplings projected onto 2d planes for 202 GeV subsample tests.*

uncertainties than the single parameter fits. It was found that none of the three parameter fit tests under estimated their statistical uncertainties. For each E_{cm}, the observed number of subsamples in the 1σ error interval (corresponding to $\Delta(\ln L) = 1.77$), was greater than the expected number. Hence no scale factors were applied to the three parameter data log-Ls.

8.3 Systematics

In any physics analysis it is important to investigate sources of systematic uncertainties which could affect the final result. This is particularly true if the size of the systematic uncertainties approach or are larger than that of the statistical error. Fortunately this is not the case for the four data samples analysed in this thesis, but it could be an issue when the whole of LEP2 data is combined.

With the exception of the lepton charge mis-assignment systematic (section 8.3.4), all of the systematic sources described in this section were investigated for the previous 183 and 189 GeV TGC analyses and are described further in [117]. Most of the systematic sources are also common to other W^+W^- analyses with the same final state.

In order to determine the size of the individual systematic uncertainties for each parameter, the systematic variations from each source were applied in turn to the signal MC reference samples (from which the calibration curves were constructed), and the analysis repeated for each of the single parameter fits at each E_{cm}. The coupling values obtained (with the systematic variations applied) were then subtracted from the original reference values quoted in table 9.1.

In total 27 systematic checks were made for each coupling at each E_{cm} in addition to the bias uncertainties described in the previous section. Where several systematic sources constitute a particular category (for example there were seven sources of selection efficiency systematic) then these were added in quadrature. These results and the total combined systematic uncertainty for each coupling at each E_{cm} are listed in table 8.5.

The individual values in table 8.5 were not used further in the analysis because the dependence is nonlinear. Instead a systematic covariance matrix was constructed for each systematic effect (at each E_{cm}) using the difference ($\Delta\overline{\mathcal{O}\mathcal{O}}$) between the mean optimal observables ($\overline{\mathcal{O}\mathcal{O}}$s) in the reference MC and those obtained with the systematic variations applied by taking the Cartesian vector product of $\Delta\overline{\mathcal{O}\mathcal{O}}$ with itself. These individual systematic covariance matrices were then summed together to form a combined systematic covariance matrix (V_{sys}). Unlike the statistical covariance matrix (equation 8.4), the off-diagonal elements in the block structure were no longer equal to zero because of correlations between the e/μ and τ channels. Most of the systematic variations affect both e/μ and τ channels and cannot be separated from the statistical components. For some sources of systematic, it is clear that there can be no correlation between the two channels and for these cases the off-diagonal elements must have arisen from statistical fluctuations. These were then set to zero and are mentioned in the appropriate following sections. Essentially the same correlations between the e/μ and τ channels were assumed as for the 183 and 189 GeV analyses. A similar procedure was adopted for the combined fit described in section 8.4. The combined systematic covariance matrices were then added to the statistical covariance matrices ($V = V_{stat} + V_{sys}$), in equation 8.5. The χ^2 or log-L curves were re-determined with the combined covariance matrix and hence new coupling values were extracted from the data for both the one and three parameter fits at each E_{cm}. These new results for the one parameter fits are presented in table 8.6 (without subsample scaling factors). The results for the three parameter fits are shown in table 9.4.

From these two tables it can be seen that some of the combined (statistical + systematic) errors are slightly smaller than only the statistical errors in tables 9.1 and 9.3 (for example Δg_1^Z at 200 and 202 GeV in the one parameter fits). This is because inclusion of the systematic covariance not only alters the total uncertainties, but also shifts the actual coupling

Source	192 GeV			196 GeV			200 GeV			202 GeV		
	$\Delta\kappa_\gamma$	Δg_1^Z	λ	$\Delta\kappa_\gamma$	Δg_1^Z	λ	$\Delta\kappa_\gamma$	Δg_1^Z	λ	$\Delta\kappa_\gamma$	Δg_1^Z	λ
MC Statitics		N	E	G	L	I	G	I	B	L	E	
Reconstruction	0.015	0.010	0.008	0.010	0.003	0.008	0.007	0.005	0.007	0.017	0.007	0.007
Charge mis-assignment	0.058	0.005	0.006	-0.031	0.001	0.011	-0.010	0.003	0.012	-0.026	0.005	0.007
Selection Efficiency	0.077	0.028	0.020	0.065	0.025	0.027	0.078	0.024	0.024	0.095	0.020	0.024
Fragmentation	0.002	-0.003	-0.009	0.001	-0.001	-0.001	-0.020	-0.010	0.001	-0.015	-0.009	0.005
MC Generator	-0.050	-0.010	0.007	0.019	0.009	0.024	0.020	-0.002	-0.030	-0.004	0.008	0.007
Background	0.024	0.004	0.009	0.020	0.016	0.009	0.028	0.008	0.009	0.050	0.007	0.010
W mass	0.000	0.003	0.001	0.005	0.003	0.002	0.004	0.003	0.001	0.004	0.003	0.002
Beam Energy	0.000	-0.003	-0.001	-0.005	-0.003	-0.002	-0.006	-0.003	-0.002	-0.006	-0.002	-0.001
Bias	0.021	0.010	0.011	0.011	0.005	0.005	0.010	0.005	0.005	0.017	0.008	0.008
Total	0.114	0.034	0.029	0.079	0.032	0.041	0.090	0.029	0.042	0.114	0.027	0.030

Table 8.5: *Summary of changes in the measured values of couplings (extracted from single parameter fits) when systematic effects are applied individually. (See text for further details).*

Energy (GeV)	$\Delta\kappa_\gamma$	Δg_1^Z	λ
192	$1.413\,^{+0.372}_{-0.504}$	$0.121\,^{+0.272}_{-0.218}$	$-0.126\,^{+0.179}_{-0.166}$
196	$-0.301\,^{+0.256}_{-0.208}$	$-0.100\,^{+0.105}_{-0.099}$	$-0.091\,^{+0.113}_{-0.105}$
200	$-0.338\,^{+0.251}_{-0.204}$	$-0.047\,^{+0.113}_{-0.104}$	$-0.019\,^{+0.121}_{-0.108}$
202	$-0.242\,^{+0.513}_{-0.289}$	$-0.007\,^{+0.160}_{-0.140}$	$-0.125\,^{+0.130}_{-0.120}$

Table 8.6: *Single parameter fit results obtained with combined statistical and systematic covariance matrices.*

values. It just so happens that the shapes of the log-L curves at these new 'shifted' positions give slightly smaller errors at ±0.5 than previously. A check was made by forcing the couplings to their SM predicted values (ie zero) and comparing the shapes of the log-L curves with and without systematics. In all cases the combined (statistical + systematic) errors were larger than the statistical only ones when the log-L curves were forced to have their minimum at zero.

The various sources of systematic uncertainty studied in this analysis are discussed in the following subsections.

8.3.1 Monte Carlo Statistics

The uncertainties in the MC predictions due to limited MC statistics were taken into account by adding these errors to the errors on the measured mean $\mathcal{OO}$ values in the χ^2 (ie in equation 8.2 replace the denominator by $\sigma^2_{\overline{\mathcal{OO}}_{\rm data}} + \sigma^2_{\overline{\mathcal{OO}}_{\rm MC}}$). This is equivalent to scaling the statistical covariance matrix by $1 + \frac{\rm N_{data}}{\rm N^{SM}_{MC}}$ [121], where $\rm N_{data}$ is the number of selected data events and $\rm N^{SM}_{MC}$ is the number of selected signal MC events weighted at the SM coupling values. The whole fit procedure was repeated for each $\rm E_{cm}$. The effects were found to be negligible because the ratios: $\rm N_{data}/N^{SM}_{MC}$ were very small.

8.3.2 Jet Reconstruction

Accurate jet reconstruction is important because it affects the TGC sensitive angles. Uncertainties arise from data-MC mis-modelling. Extensive studies [122] of back-to-back jets in Z^o calibration data collected at the start of each year's data taking have suggested the following systematic checks should be made:

- **Jet energy resolution** This was varied by 3% in the barrel region and 20% in the endcap.
- **Jet energy scale** The overall jet energy was scaled by the following $\cos\theta$ dependent factors:

$0.0 < \cos\theta < 0.4$	0.985
$0.4 < \cos\theta < 0.7$	0.995
$0.7 < \cos\theta < 0.82$	1.000
$0.82 < \cos\theta < 0.92$	1.020
$0.92 < \cos\theta < 1.00$	1.050

- **Jet $\cos\theta$ resolution** The angular resolution in $\cos\theta$ (measured in the lab frame) was degraded by 5%.
- **Jet $\cos\theta$ shift** This was offset by 0.0003 (absolute value).
- **Jet ϕ angle resolution** This was smeared by 3%.

The signal EXCALIBUR MC samples were scaled, shifted or smeared on an event by event basis for each test. The kinematic fits were then remade and the analysis repeated. The differences between the normal reference values and the coupling values obtained with the systematic variations applied are listed in table 8.7.

8.3.3 Lepton Reconstruction

Analogous to the jet reconstruction systematics, the τ reconstruction systematics in $\tau\nu q\bar{q}$ events were investigated by smearing the resolution in $\cos\theta$ and ϕ by 5% and 3% respectively, and shifting $\cos\theta_\tau$ by 0.0003. The lepton energy (in $e\nu q\bar{q}$, $\mu\nu q\bar{q}$ and $\tau\nu q\bar{q}$ events) was scaled by 0.5%. These scale factors were used in the 189 GeV analysis [117]. The systematic effects were determined in the usual way by taking the difference between the reference and the systematically varied coupling values (these results are shown in table 8.8),

Source	192 GeV			196 GeV			200 GeV			202 GeV		
	$\Delta\kappa_\gamma$	Δg_1^Z	λ	$\Delta\kappa_\gamma$	Δg_1^Z	λ	$\Delta\kappa_\gamma$	Δg_1^Z	λ	$\Delta\kappa_\gamma$	Δg_1^Z	λ
E_{jet} Resolution	0.007	0.003	-0.006	0.006	0.002	-0.006	0.005	0.004	-0.005	0.015	0.005	-0.003
E_{jet} Scale	-0.012	-0.008	0.005	0.000	-0.001	0.005	0.002	-0.003	0.003	0.002	-0.002	0.006
$\cos\theta_{\text{jet}}$ Resolution	0.002	-0.002	-0.001	0.001	-0.001	-0.001	0.000	0.001	0.000	0.001	0.002	0.002
$\cos\theta_{\text{jet}}$ Shift	0.003	-0.001	0.000	0.000	0.000	0.000	0.000	0.000	-0.001	0.001	0.002	0.001
ϕ_{jet} Resolution	0.002	-0.001	0.000	0.001	0.001	0.000	-0.001	0.000	-0.001	0.002	0.002	0.002
Total	0.014	0.009	0.008	0.006	0.003	0.008	0.005	0.005	0.006	0.015	0.006	0.007

Table 8.7: *Jet reconstruction systematics for single parameter fits.*

Source	192 GeV			196 GeV			200 GeV			202 GeV		
	$\Delta\kappa_\gamma$	Δg_1^Z	λ	$\Delta\kappa_\gamma$	Δg_1^Z	λ	$\Delta\kappa_\gamma$	Δg_1^Z	λ	$\Delta\kappa_\gamma$	Δg_1^Z	λ
$\cos\theta_\tau$ Resolution	0.001	-0.002	0.001	-0.008	-0.001	0.002	-0.004	0.000	0.002	-0.005	0.001	0.001
$\cos\theta_\tau$ Shift	-0.001	-0.001	0.000	0.001	0.000	0.000	0.000	0.000	-0.001	0.001	0.001	0.000
ϕ_τ Resolution	-0.001	-0.003	-0.001	0.001	0.000	0.000	0.001	0.000	-0.001	0.004	0.001	0.000
E_{lept} Scale	-0.003	-0.003	-0.001	0.001	0.001	0.000	0.001	0.000	-0.002	0.003	0.001	0.001
Total	0.003	0.005	0.002	0.008	0.001	0.002	0.004	0.000	0.003	0.007	0.002	0.001

Table 8.8: *Lepton reconstruction systematics for single parameter fits.*

and constructing a systematic covariance matrix for later combination. The contribution of all the lepton reconstruction systematics to the total systematic uncertainty is small. The combined reconstruction systematics (lepton and jet) are shown in table 8.5.

8.3.4 Charge mis-assignment

Lepton charge was determined from the direction of track curvature the particle made as it traversed the central tracking detectors. High momentum particles' trajectories were less curved (equation A.4) than lower momentum ones. High momentum particles therefore have a greater probability of mis-assigned charge as per equation A.2.

The standard OPAL $W^+W^- \rightarrow l\nu q\bar{q}$ selection and fitting routines use the momentum measured by the electromagnetic calorimeters for electrons not in the overlap[5] region, and the combined central tracking detectors for muons, taus and remaining electrons.

From MC studies, it was observed that $\sim$4% of all $WW \rightarrow l\nu q\bar{q}$ events had mis-measured charge. Of these, only $\sim$1% of all $e\nu q\bar{q}$ and $\mu\nu q\bar{q}$ events had mis-assigned charge compared with $\sim$12% for $\tau\nu q\bar{q}$ events. The reason for this difference is because it was very easy to mis-assign one (or more) of the tracks in the quark jets as originating from the hadronically decaying τ jet or mistake the τ jet as coming from a quark jet.

There were two aspects to consider in this investigation: firstly the effects of mis-measuring the charge (which can be estimated from MC) and secondly, the effects of data-MC mis-modelling. In order to address these problems, a number of things were investigated including:

1. Randomly flipping the sign of W_{lept} in a small fraction of MC events.
2. Removing events with electron or muon tracks in the anode region of CJ.
3. Smearing the quantity:

$$\Delta = \left(\frac{q}{p_t}\right)_{\text{Tree}} - \left(\frac{q}{p_t}\right)_{\text{Meas}} \tag{8.10}$$

---

[5] The overlap region is defined to be the region $0.72 < |\cos\theta| < 0.82$ where the barrel and endcaps overlap (figure 3.3b). Energy measurements from the electromagnetic calorimeters were degraded in this region and hence a better resolution could be obtained from the tracking detectors.

by 10%, where q is the particle charge and p_t is the transverse momentum.

The first point directly addresses the subject of data-MC mis-modelling. The question then arose as to what fraction of events should have their $\mathrm{W_{lept}}$ charge flipped. To get a rough estimate for this, we took the same fractions determined for $\mathrm{Z}^0 \rightarrow l^+l^-$ events [123] and subtracted the percentage of charge mis-assignment predicted directly from the MC. The kinematic fits were remade and the analysis repeated with these changes in place. The effect was found to be significant. Aside from the fact that $\mathrm{Z}^0 \rightarrow l^+l^-$ events are topologically very different to $\mathrm{WW} \rightarrow l\nu q\bar{q}$ events, one of the main problems with this approach was that there was no consideration of event kinematics or detector geometry. In practice one would expect events with tracks in certain detector regions (for example close to the beam pipe, in the overlap or in CJ anode plain) and very high momentum tracks to have worse charge mis-assignment. The random flipping was applied across all selected events.

The second criteria removed approximately 5-7% of events with lepton tracks within 0.5^o of each of the CJ anode planes, making a total dead area of about 24^o. $\tau\nu q\bar{q}$ events were not removed in this study since (correctly identified) lower momentum τ's will generally have better track curvature measurement. The reduction in size of the data sample lead to a large increase in the statistical error which was difficult to separate from the effect under investigation. Therefore this approach was not pursued further.

The third technique, and the one finally adopted in [49] was to smear the MC track curvature (κ) or equivalently the charge/transverse momentum distribution (equation 8.10) by 10%. The figure of 10% was derived from LEP I studies at the Z^0 peak [124]. Figure 8.12 shows this distribution fitted with a Breit Wigner. After smearing, the individual lepton momentum components (p_x and p_y) were re-calculated, the events kinematically refitted and the analysis repeated. The results of these tests are shown in table 8.5. The advantage of this method is that it simultaneously considers both the effects of charge mis-assignment (TGC sensitive) and poor momentum measurements (not so TGC sensitive). The disadvantage of this approach, is that it does not consider the effects of data-MC mis-modelling, but the conservative estimate of 10% is an attempt to do just that.

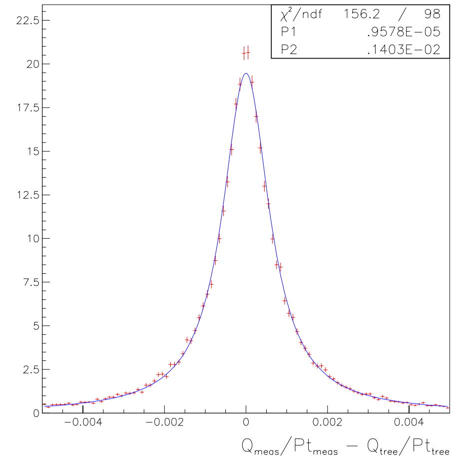

Figure 8.12: *The* $(q/p_t)_{Tree} - (q/p_t)_{Meas}$ *distribution for 200 GeV data fitted with a Breit Wigner.*

8.3.5 Selection Efficiencies

The comparative selection efficiencies for data and MC may not be equal over the full angular range or energy spectrum. In order to check for any effects from selection cuts on event kinematics, five independent tests were made of the jet and lepton energies, jet and lepton polar angles, and the angle between the highest energy jet and the charged lepton. Except for 192 GeV data (see below), good agreement was found between the data and MC distributions. The MC referred to in this subsection consisted of SM four fermion EXCALIBUR samples plus background, all normalized to the data.

In order to quantify each uncertainty, the ratio of data to MC was parameterised as a straight line fit (see figure 8.13). Originally this was done separately for each E_{cm} but for the final result all energies were combined in order to reduce statistical fluctuations. This assumed that jet and lepton energy distributions do not change with E_{cm}. Over the 10 GeV range that the data were collected, this was found to be a valid approximation. However, for the final combination of all LEP 2 data (>40 GeV spread), it may be necessary to review this procedure and normalize these quantities to the beam energy.

The intercept and slope ($A0$ and $A1$) obtained from the fit were then used as a linear correction factor to weight the MC events:

$$w_{\text{corr}} = A1 \times X + A0 \tag{8.11}$$

where X is the kinematic variable under study. Ideally, the slope should be ≈ 0 and the

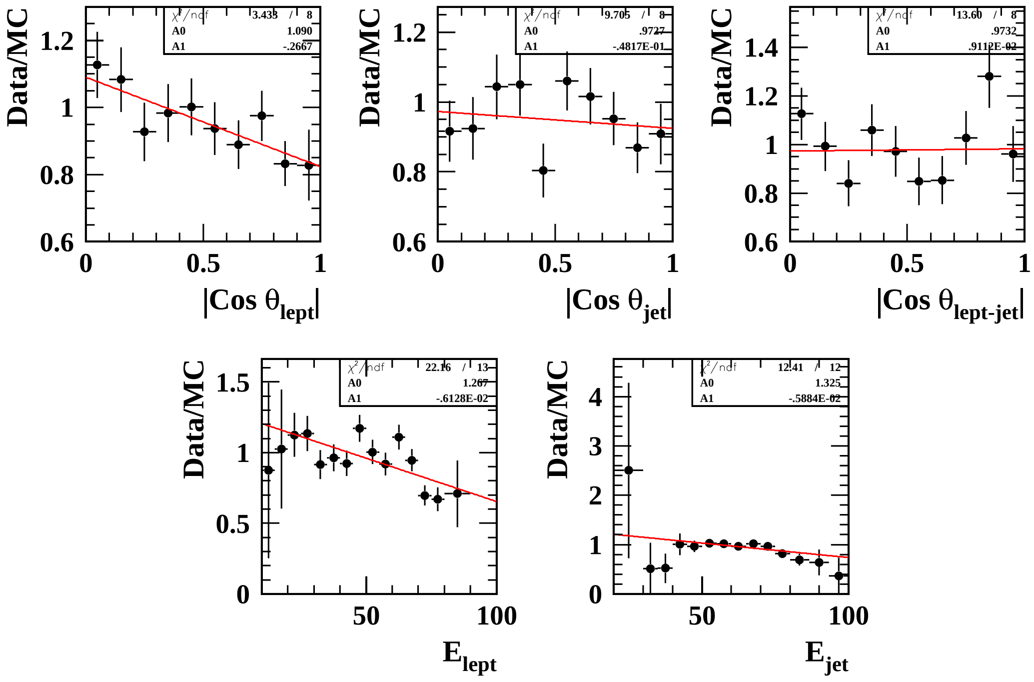

Figure 8.13: *Ratio of data/MC$_{TOT}$ as a function of lepton and jet energies,* $|\cos\theta|$ *and cosine of the angle between the leptons and jets for the combined 1999 data.*

intercept ≈ 1. The analysis was then repeated (for each quantity under investigation) with the weighted MC events. The revised coupling values, and hence the systematic uncertainties were extracted in the usual way. The individual results from each test are shown in table 8.9. As can be seen from table 8.5, the combined selection efficiency systematics are the dominant error for most of the couplings.

Additional systematic checks were made on the relative selection efficiency of $\mu\nu q\bar{q}$ and $\tau\nu q\bar{q}$ events compared with $e\nu q\bar{q}$ events by applying a weighting factor of 1% to misclassified $\mu\nu q\bar{q}$ and $\tau\nu q\bar{q}$ MC signal events. This is a conservative estimate to cover the effects of tracking losses described in [50]. The estimated uncertainties (listed in table 8.9) are small compared with the other sources in this category.

192 GeV anomaly

For the 192 GeV data, a discrepancy between data and MC was observed in the lepton energy spectrum for $E_{\text{lept}} > 70$ GeV (and correspondingly in the $\cos\theta_l^*$ distribution) as shown in figure 8.14. The deficit in the data was observed in all three lepton channels and in other analyses using the WW $\rightarrow l\nu q\bar{q}$ event selection [125]. The deficit was intensively investigated by checking the lepton energy distribution for Bhabha and μ pair events, comparing the MC spectra at different energies, checking for any known detector effects and com-

Source	192 GeV			196 GeV			200 GeV			202 GeV		
	$\Delta\kappa_\gamma$	Δg_1^Z	λ	$\Delta\kappa_\gamma$	Δg_1^Z	λ	$\Delta\kappa_\gamma$	Δg_1^Z	λ	$\Delta\kappa_\gamma$	Δg_1^Z	λ
E_{lept}	0.061	0.024	-0.005	-0.046	-0.005	-0.007	-0.058	-0.002	-0.001	-0.069	0.003	-0.013
$\cos\theta_{\text{lept}}$	-0.001	-0.014	-0.018	-0.012	-0.019	-0.024	-0.022	-0.018	-0.020	-0.034	-0.015	-0.018
E_{jet}	0.045	-0.004	-0.005	-0.043	-0.015	-0.007	-0.046	-0.015	-0.010	-0.054	-0.012	-0.005
$\cos\theta_{\text{jet}}$	0.011	-0.002	-0.006	-0.008	-0.004	-0.008	-0.010	-0.005	-0.009	-0.010	-0.004	-0.006
$\cos\theta_{\text{jet-lept}}$	0.003	0.001	-0.001	-0.001	0.000	-0.001	-0.001	0.000	-0.002	-0.001	0.000	-0.001
$\mu\nu q\bar{q}$ rel. sel. eff.	0.000	-0.001	0.000	0.001	0.000	0.000	0.001	0.000	0.000	0.000	0.001	0.000
$\tau\nu q\bar{q}$ rel. sel. eff.	0.000	-0.001	-0.001	-0.001	0.000	0.000	0.000	0.000	-0.001	-0.001	0.000	0.000
Combined	0.077	0.028	0.020	0.065	0.025	0.027	0.078	0.024	0.024	0.095	0.020	0.024

Table 8.9: *Selection efficiency systematics for single parameter fits.*

Source	192 GeV			196 GeV			200 GeV			202 GeV		
	$\Delta\kappa_\gamma$	Δg_1^Z	λ	$\Delta\kappa_\gamma$	Δg_1^Z	λ	$\Delta\kappa_\gamma$	Δg_1^Z	λ	$\Delta\kappa_\gamma$	Δg_1^Z	λ
$q\bar{q}$ fragmentation	0.020	0.002	-0.004	0.018	-0.012	-0.002	-0.026	0.006	-0.008	-0.050	0.006	-0.009
$q\bar{q}$ I.S.R.	0.012	-0.002	0.007	-0.001	-0.010	-0.006	-0.007	0.005	-0.003	0.003	-0.002	-0.005
$q\bar{q}$ correction	0.004	0.001	-0.004	-0.009	-0.001	-0.006	-0.006	-0.002	-0.004	-0.005	-0.002	-0.002
remove $\gamma\gamma$	0.004	0.003	0.002	-0.001	0.002	0.002	-0.001	0.000	0.000	-0.001	0.001	0.000
Combined	0.024	0.004	0.009	0.020	0.016	0.009	0.028	0.008	0.009	0.050	0.007	0.010

Table 8.10: *Background systematics for single parameter fits.*

paring fitted versus reconstructed distributions. Variation with time was also searched for. Despite all these efforts, no explanation for this anomaly could be found except that of a statistical fluctuation. Only 29.3 pb^{-1} of data were collected at this E$_{\rm cm}$.

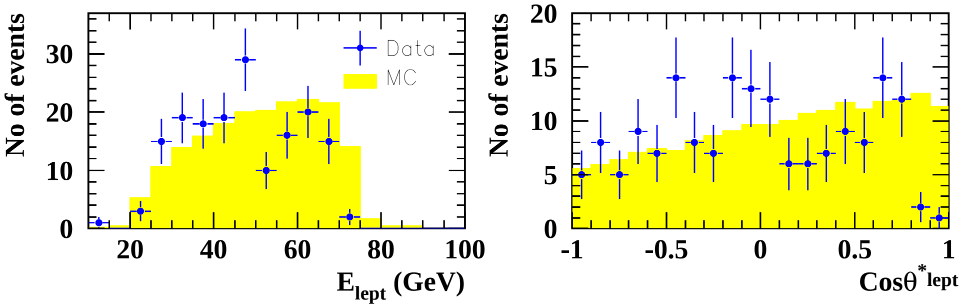

Figure 8.14: *The Lepton energy and* $\cos\theta^*_{lept}$ *distributions for 192 GeV data. In both plots there is a clear deficit of data events compared to MC prediction which is not present at other energies.*

8.3.6 Fragmentation

The EXCALIBUR reference MC employed the JETSET [54] fragmentation scheme. The uncertainty associated with hadronization modelling was estimated by comparing two large GRC4F [68] CC03 MC samples that had been generated with the same four vectors but using different hadronization models, either HERWIG [55] or JETSET. One of the samples was used as the test (or pseudo-data) set and the other was used for the reference (or reweighting) MC set. Since both the GRC4F samples were CC03, they could not be compared directly with EXCALIBUR. Instead, the differences in the mean optimal observables ($\Delta\overline{\mathcal{OO}}s$) between these two samples were added to the expected mean optimal observables E$[\mathcal{OO}](\alpha)$ in the EXCALIBUR reference sets to 'shift' the calibration curves. New coupling values were determined after the fits were repeated using these 'shifted' calibration curves. The expected uncertainty due fragmentation modelling was evaluated in the usual way from the differences between the shifted and the original reference coupling values. These are shown in table 8.5. The effects are seen to be small, and part of the uncertainty could also be due to statistical effects arising from the detector simulation of the MC. No correlation was assumed between the e/μ and τ channels because the observed shift in the $\Delta\overline{\mathcal{OO}}$ values arising from this systematic effect could not be separated from the statistical component.

8.3.7 Monte Carlo Generator

Different event generators have different specifications, limitations and associated uncertainties. In order to check the effect of different generator modelling of W-decay kinematics, four fermion samples generated with GRC4F [68] and KORALW [61] were used in turn as test data with the normal EXCALIBUR as the reference (reweighting) set. The differences in the mean optimal observables ($\Delta\overline{\mathcal{O}\mathcal{O}}$ values) were then added to the EXCALIBUR expected mean optimal observables E$[\mathcal{O}\mathcal{O}](\alpha)$, and the analysis repeated with the adjusted calibration curves. The systematic uncertainties were evaluated in the same way as for the fragmentation error. The results are listed in table 8.11.

Energy (GeV)	192	196	200	202
KORALW				
$\Delta\kappa_\gamma$	-0.050	0.019	0.020	-0.004
Δg_1^Z	-0.010	0.009	-0.002	0.008
λ	0.007	0.024	-0.030	0.007
GRC4F				
$\Delta\kappa_\gamma$	-0.034	0.034	0.015	0.030
Δg_1^Z	0.007	-0.018	0.015	0.021
λ	0.003	-0.014	0.010	0.002

Table 8.11: *Single parameter fit Monte Carlo generator systematics with* KORALW *and* GRC4F.

Since both GRC4F and KORALW use the GRC4F matrix elements in their calculations and have the same fragmentation with JETSET, it is not possible to combine these systematics in quadrature. Instead, the event generator systematic is taken to be the one from the KORALW sample, since this gives on balance slightly larger errors, and KORALW is reported to have a better treatment of ISR and τ polarization.

8.3.8 Backgrounds

Four potential sources of systematic effects were studied in this category, the most important of which concern the modelling of the two fermion $\mathrm{Z}^0/\gamma \rightarrow q\bar{q}$ background. This is the main source of background in the selection of $\mathrm{W^+W^-} \rightarrow l\nu q\bar{q}$ events with a cross section 13 times larger than the signal. There are two aspects to this uncertainty: modelling of the underlying physics processes and modelling of the detector response.

The shape of the $\mathrm{Z}^0/\gamma \rightarrow q\bar{q}$ background was varied by replacing the KK2F MC used in the main analysis, with samples generated with PYTHIA (which has a different treatment of ISR) and HERWIG (which uses a different hadronization model). Its normalization was checked by applying event correction factors of ±15% [50]. This same factor was applied to the cross section analysis [126]. For each of these checks, the uncertainty was determined in the usual way from the shift in the central coupling values before/after the systematic variation was applied. The e/μ and τ channels were assumed to be independent and uncorrelated.

Although the expected number of two photon events surviving the selection cuts is small (∼0.1%), these events occupy regions of phase space which are poorly modelled. A conservative estimate of the systematic uncertainty from this source was obtained by completely removing the 2γ background sample and repeating the analysis.

The results from these tests are presented in table 8.10. The quadrature sum of all these effects represent the total systematic uncertainty due to background variations and are the figures quoted in table 8.5.

8.3.9 W Mass

The majority of MC samples used in this analysis were generated with W boson mass equal to 80.33 GeV/c^2. This same value was also used in the kinematic fits described in section 5.5. However, the latest results from LEP [5] and the Tevatron collider at Fermilab [127] quote somewhat higher values of $\mathrm{M_W} = 80.450 \pm 0.039$ and 80.448 ± 0.062 GeV/c^2 respectively. For this systematic, the uncertainty on the W mass ($\Delta\mathrm{M_W}$) was taken to be the linear difference between the statistically independent Tevatron result and the MC generated value, plus the uncertainty on the Tevatron result (0.18 GeV/c^2).

The effect of the W mass uncertainty was assessed by performing the analysis (at each $\mathrm{E_{cm}}$) with CC03 MC test samples generated with values of $\mathrm{M_W}$ ±0.5 and ±1.0 GeV/c^2 away from the normal generated/fit value. The usual four fermion EXCALIBUR MC used for the reweighing was replaced by a SM CC03 KORALW sample. The difference in the SM $\overline{\mathcal{O}\mathcal{O}}$s between the KORALW reference and $\mathrm{W_{mass}}$ samples, were plotted as a function of M_W and parameterised as a linear fit. The $e\nu q\bar{q}/\mu\nu q\bar{q}$ and $\tau\nu q\bar{q}$ events were combined to reduce statistical fluctuations. An example for the 196 GeV MC, is shown in figure 8.15. For each $\overline{\mathcal{O}\mathcal{O}}$, a weighted average of the four slopes from each $\mathrm{E_{cm}}$ was made and combined with $\Delta\mathrm{M_W}$ to give the $\Delta\overline{\mathcal{O}\mathcal{O}}$ values. These were then added to the EXCALIBUR reference $\overline{\mathcal{O}\mathcal{O}}$, and the analysis repeated in the usual way (for each $\mathrm{E_{cm}}$) to extract the new coupling values with the systematic applied. The systematic uncertainties were evaluated from the change in coupling values in the usual way and the results are presented in table 8.5. As can be seen, there is little TGC dependence on the W mass.

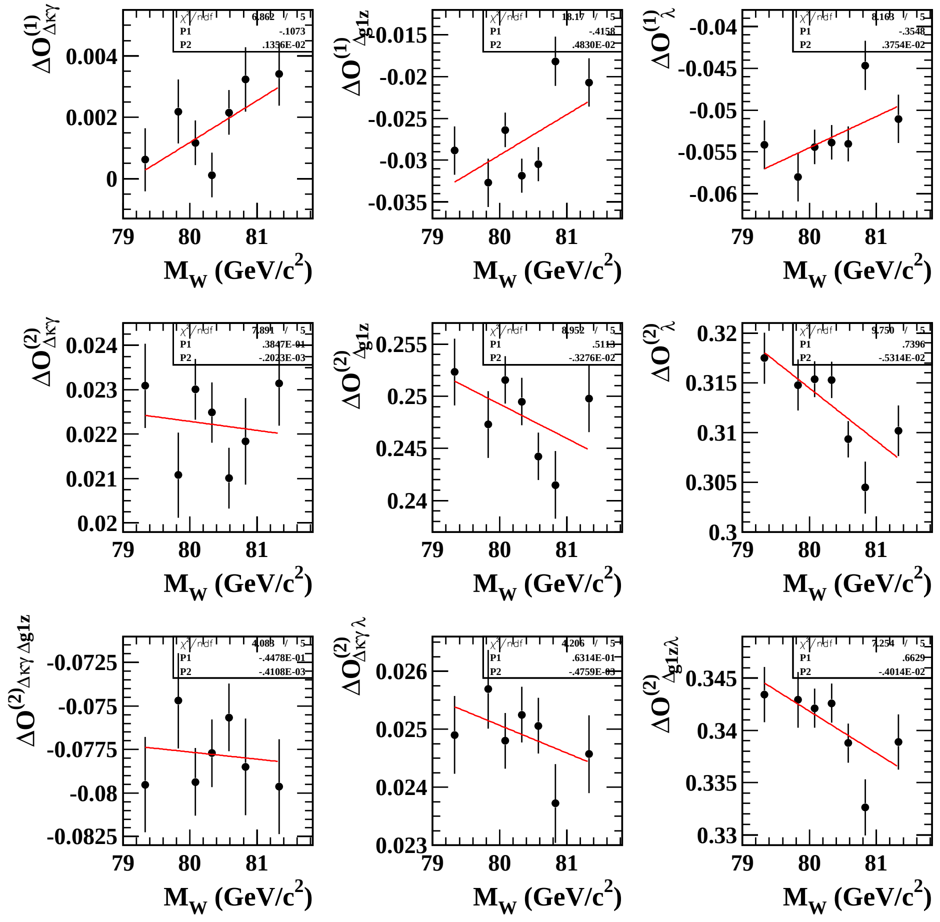

Figure 8.15: *Expected change in mean optimal observable ($\Delta\overline{\mathcal{O}\mathcal{O}}$) values with W mass for 202 GeV data. The $e\nu q\bar{q}/\mu\nu q\bar{q}$ and $\tau\nu q\bar{q}$ events were combined to increase statistics.*

8.3.10 Beam Energy

The LEP Energy working group has estimated the uncertainty on the beam energy to be ±20 MeV [128]. The EXCALIBUR and background MC samples were generated at centre of mass energies of 192, 196, 200 and 202 GeV, but the data were recorded at average centre of mass energies: 191.588, 195.528, 199.522 and 201.658 GeV [129]. These values were the ones used in the $\mathcal{OO}$ calculations. The systematic effects due the beam energy uncertainty were evaluated in a similar manner to that of the $\mathrm{W_{mass}}$ systematic by performing the analysis with test samples generated at different $\mathrm{E_{cm}}$ and parameterizing the $\overline{\mathcal{OO}}$s as a linear function of $\mathrm{E_{cm}}$. An example for the 202 GeV data is shown in figure 8.16.

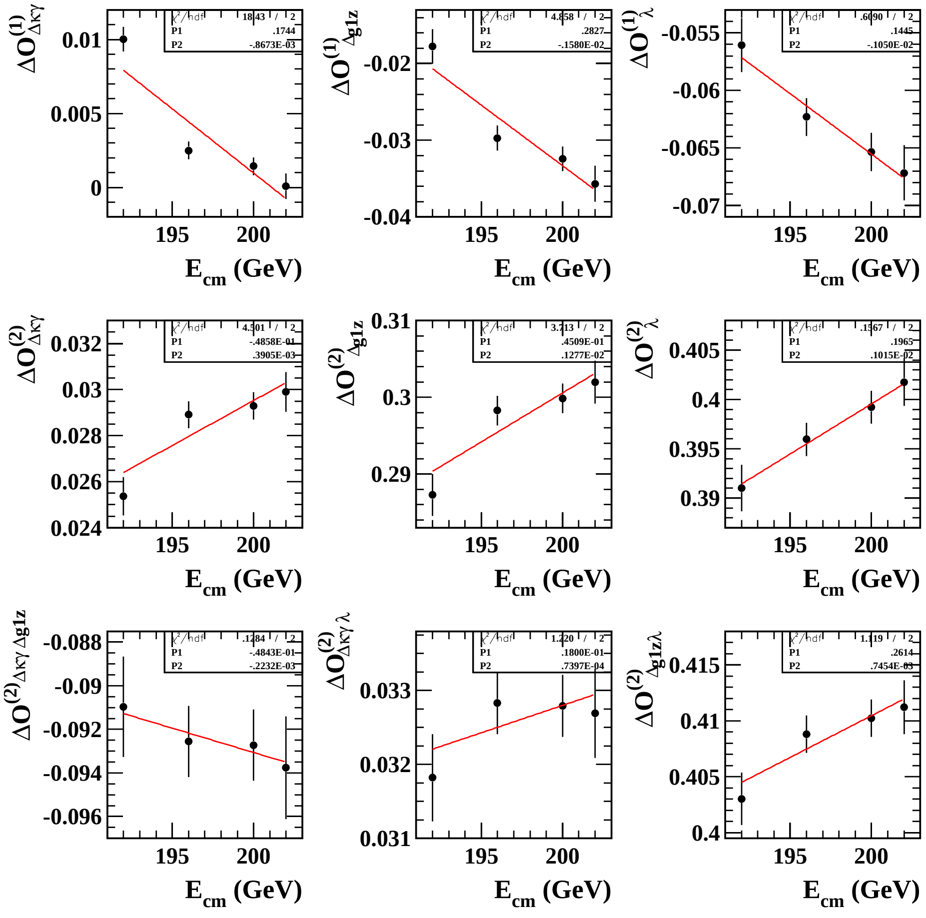

Figure 8.16: *Expected change in optimal observable ($\Delta\overline{\mathcal{OO}}$) values with centre of mass energy. The $e\nu q\bar{q}$/$\mu\nu q\bar{q}$ and $\tau\nu q\bar{q}$ events are combined.*

The uncertainty in the energy ($\Delta\mathrm{E_{cm}}$) was taken to be the difference between the value at which the MC were generated and the average E_{cm} of the data plus the uncertainty on the beam energy (of 20 MeV) from the LEP working group. Unlike the W_{mass} systematic, the same test samples were used for all four centre of mass energies and hence simple weighted averages of the slopes could not be made. Instead, the systematics were evaluated independently for each E_{cm} by adding the change in the optimal observables ($\Delta\overline{\mathcal{O}\mathcal{O}}s$) to the original EXCALIBUR reference $\overline{\mathcal{O}\mathcal{O}}$s and repeating the analysis. The uncertainties are listed in table 8.5 and are seen to be small. Although the $\mathcal{O}\mathcal{O}$s are energy dependent, as expected the actual coupling values are not.

8.4 Combining the different energies

In order to combine the results from the four different energies, various approaches can be applied. The simplest is to add up the log-L curves (as shown by the solid black line in figure 9.1). This is fine when the uncertainties are only statistical. However, when systematic uncertainties are involved, correlations between the different energies cannot be considered properly.

An alternative approach, and the one used in this thesis, is to construct a covariance matrix from the $\mathcal{O}\mathcal{O}$s and perform the fit for all the energies and channels simultaneously. For example, if there are nine $\mathcal{O}\mathcal{O}$s, two channels (e/μ and τ) and four energies in a 3 parameter fit, then a 72×72 covariance matrix is needed. This approach is equivalent to adding up the log-Ls, but now systematic correlations can also be included. For the one and three parameter fit results (shown in tables 9.2 and 9.4), the systematics from the different energies were assumed to be fully correlated. Correlations between the e/μ and τ channels were discussed in section 8.3.

It may be so, there is no arguing against facts and experiment

ISAAC NEWTON, *Sir Isaac Newton, E. N. da C. Andrade, Fontana Books (1961)*

Chapter 9

TGC Results

The couplings were extracted from four sets of data recorded by the OPAL experiment at LEP during 1999 with centre of mass energies: 192, 196, 200 and 202 GeV and total integrated luminosity of 212 pb^{-1}. All the results presented in this section incorporate the assumptions and relationships outlined in section 7.1.

The TGC values extracted from the single parameter fits (when one coupling was allowed to vary from its Standard Model (SM) value and the other two were fixed at zero), together with their statistical uncertainties are shown in table 9.1. These results correspond to the minimum of the log likelihood (log-L) curves shown in figure 9.1. The coloured dotted lines show the results from each centre of mass energy ($\mathrm{E_{cm}}$) and the black solid curve shows the combined result obtained from adding up the log-L curves. The second minimum in $\Delta\kappa_\gamma$ is picked out for the 192 GeV data. This data set has the lowest statistics and has only a small effect on the combined result. Apart from the results for $\Delta\kappa_\gamma$ and Δg_1^{Z} at 192 GeV, all of the coupling parameters are negative. The statistical uncertainties were obtained from the log-L plots, at the points where the curves have increased to $\pm$0.5 their minimum value. All the results are within 2σ of SM expectation except for $\Delta\kappa_\gamma$ at 192 GeV and the combined result (which is affected by the 192 GeV result).

The results from the single parameter fits when systematics were included are shown in table 9.2. The systematic errors are assumed to be fully correlated between the different energy data sets. Scale factors obtained from the subsample tests (listed in table 8.4) were applied to these results. The corresponding log-L plots are shown in figure 9.2. As expected there is very little change in the central coupling values (well within 1σ). Most of the

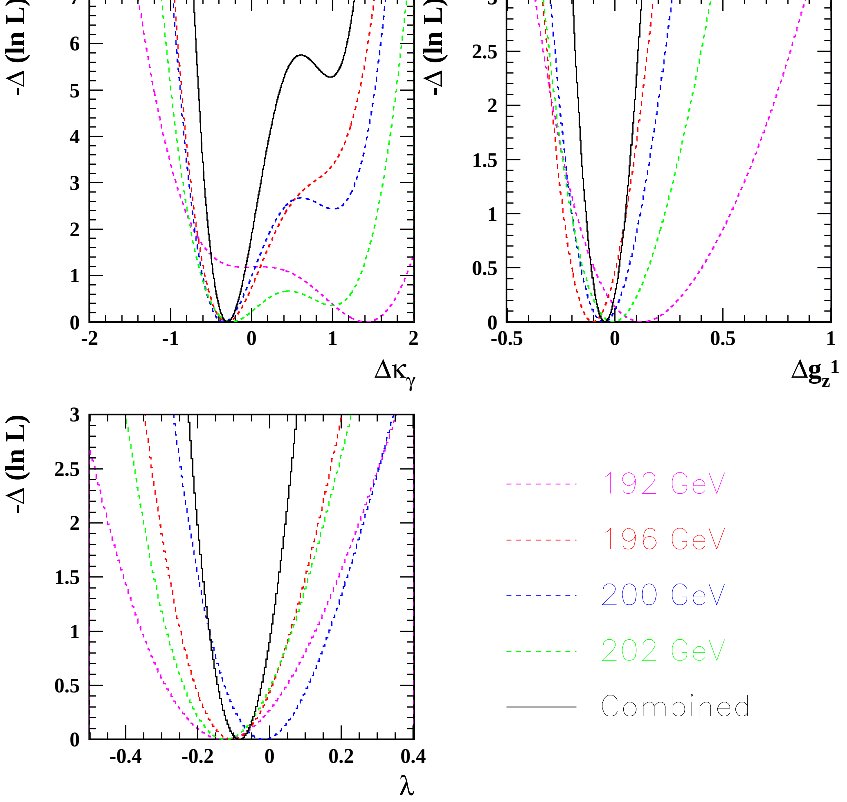

Figure 9.1: *The single parameter fit log-Ls. Errors are statistical only. No scale factors (from the subsample tests) were applied.*

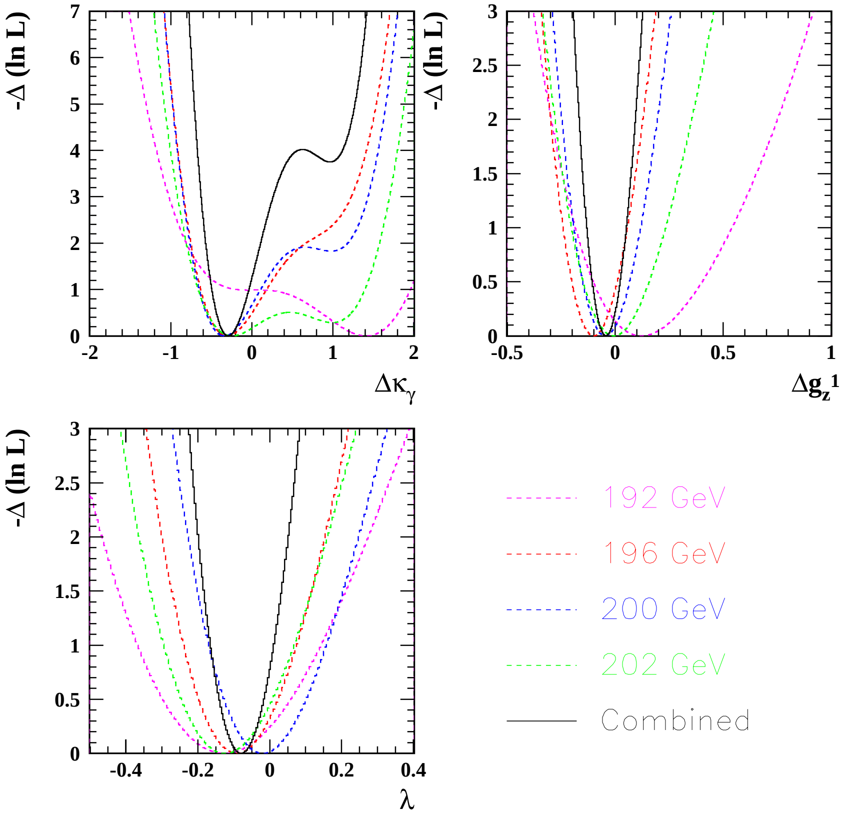

Figure 9.2: *The single parameter fit log-Ls. Errors are statistical and systematic. Scale factors (from the subsample tests listed in table 8.4) have been applied.*

Energy (GeV)	$\Delta\kappa_\gamma$	Δg_1^{Z}	λ
192	$1.410\,^{+0.363}_{-0.489}$	$0.123\,^{+0.277}_{-0.221}$	$-0.127\,^{+0.175}_{-0.163}$
196	$-0.303\,^{+0.242}_{-0.197}$	$-0.102\,^{+0.106}_{-0.098}$	$-0.104\,^{+0.112}_{-0.103}$
200	$-0.343\,^{+0.229}_{-0.189}$	$-0.053\,^{+0.117}_{-0.105}$	$-0.017\,^{+0.124}_{-0.109}$
202	$-0.249\,^{+0.450}_{-0.274}$	$-0.008\,^{+0.162}_{-0.140}$	$-0.123\,^{+0.127}_{-0.116}$
Combined	$-0.298\,^{+0.141}_{-0.123}$	$-0.047\,^{+0.066}_{-0.063}$	$-0.084\,^{+0.062}_{-0.059}$

Table 9.1: *Single parameter fit results obtained from the log-L curves. Errors are statistical only. No scale factors (from the subsampling tests) have been applied.*

Energy (GeV)	$\Delta\kappa_\gamma$	Δg_1^{Z}	λ
192	$1.412\,^{+0.398}_{-0.559}$	$0.121\,^{+0.281}_{-0.223}$	$-0.126\,^{+0.185}_{-0.172}$
196	$-0.301\,^{+0.307}_{-0.239}$	$-0.100\,^{+0.108}_{-0.101}$	$-0.091\,^{+0.115}_{-0.106}$
200	$-0.339\,^{+0.285}_{-0.226}$	$-0.047\,^{+0.113}_{-0.103}$	$-0.020\,^{+0.119}_{-0.106}$
202	$-0.243\,^{+0.655}_{-0.308}$	$-0.007\,^{+0.163}_{-0.142}$	$-0.125\,^{+0.132}_{-0.122}$
Combined	$-0.278\,^{+0.191}_{-0.160}$	$-0.038\,^{+0.066}_{-0.063}$	$-0.070\,^{+0.064}_{-0.062}$

Table 9.2: *Single parameter fit results obtained from the log-L curves scaled by the factors obtained from the subsample tests. Errors are both statistical and systematic combined.*

combined (statistical and systematic) uncertainties have increased (an explanation as to why the combined uncertainties can sometimes be (slightly) less than the statistical only case is given in section 8.3).

The multi-parameter fits provide an opportunity to study correlations between the parameters. The results for the three parameter fits were obtained from the MINUIT minimization package [116] and are listed in tables 9.3 (statistical only errors) and 9.4 (statistical plus systematic errors). Since none of the couplings were fixed but instead allowed to vary simultaneously, these fits are less model dependent. Consequently they are expected to have greater sensitivity to (potential) new physics which is expected to manifest itself as an anomaly in one or more of the couplings. The uncertainties for the multi-parameter fits are larger than those obtained from the single parameter fits because there was more freedom to vary the individual parameters and this worsens the overall χ^2. In the single parameters fits the χ^2 was minimized for just one parameter, and so the uncertainties on the other two (fixed at SM couplings) were zero. In the multi-parameter fits, the overall χ^2 was optimized for all three parameters simultaneously so that the uncertainties on the individual couplings are larger.

Energy (GeV)	$\Delta\kappa_\gamma$	Δg_1^Z	λ
192	$1.657^{+0.666}_{-1.774}$	$0.317^{+0.463}_{-0.319}$	$-0.371^{+0.258}_{-0.264}$
196	$0.473^{+0.307}_{-0.778}$	$-0.197^{+0.237}_{-0.106}$	$0.029^{+0.156}_{-0.150}$
200	$-0.422^{+0.215}_{-0.183}$	$-0.024^{+0.132}_{-0.141}$	$0.050^{+0.170}_{-0.158}$
202	$-0.202^{+0.313}_{-0.253}$	$0.190^{+0.149}_{-0.149}$	$-0.217^{+0.159}_{-0.147}$
Combined	$-0.251^{+0.138}_{-0.123}$	$0.071^{+0.075}_{-0.077}$	$-0.098^{+0.086}_{-0.083}$

Table 9.3: *Three parameter fit results obtained from* MINUIT *fit. Errors are statistical only.*

Energy (GeV)	$\Delta\kappa_\gamma$	Δg_1^Z	λ
192	$1.682^{+0.791}_{-1.796}$	$0.333^{+0.535}_{-0.332}$	$-0.380^{+0.265}_{-0.276}$
196	$0.344^{+0.362}_{-0.653}$	$-0.175^{+0.225}_{-0.114}$	$0.017^{+0.153}_{-0.168}$
200	$-0.338^{+0.266}_{-0.202}$	$-0.018^{+0.132}_{-0.145}$	$0.024^{+0.166}_{-0.156}$
202	$-0.190^{+0.328}_{-0.261}$	$0.190^{+0.152}_{-0.152}$	$-0.216^{+0.161}_{-0.151}$
Combined	$-0.154^{+0.180}_{-0.143}$	$0.052^{+0.076}_{-0.080}$	$-0.091^{+0.086}_{-0.084}$

Table 9.4: *Three parameter fit results. Errors include both statistical and systematic components. (There were no scale factors for the three parameter fits).*

The 95% CL contour plots obtained from the multi-parameter fits to the combined 1999 data are shown in figure 9.3. The uncertainties include both statistical and systematic errors. The two parameter fits (when the third parameter was fixed at its SM value) are shown in magenta. The projection of the three parameter fits onto the two dimensional plane are shown by the green lines. It can be seen that the allowed range for each parameter is extended when the constraints on the other parameters are removed. The central fit values and SM expectations are shown by the dots and stars respectively. All results agree with SM predictions at the 95% CL. In the (Δg_1^Z, $\Delta\kappa_\gamma$) fits two regions are indicated by the 95% CL contour, corresponding to the double minimum of the log-L plots. The minimum furthest away from the SM predictions was chosen in the two parameter fits. The non-elliptic shapes of these curves reflect the non-Gaussian behaviour of the log-L functions and the presence of local minima.

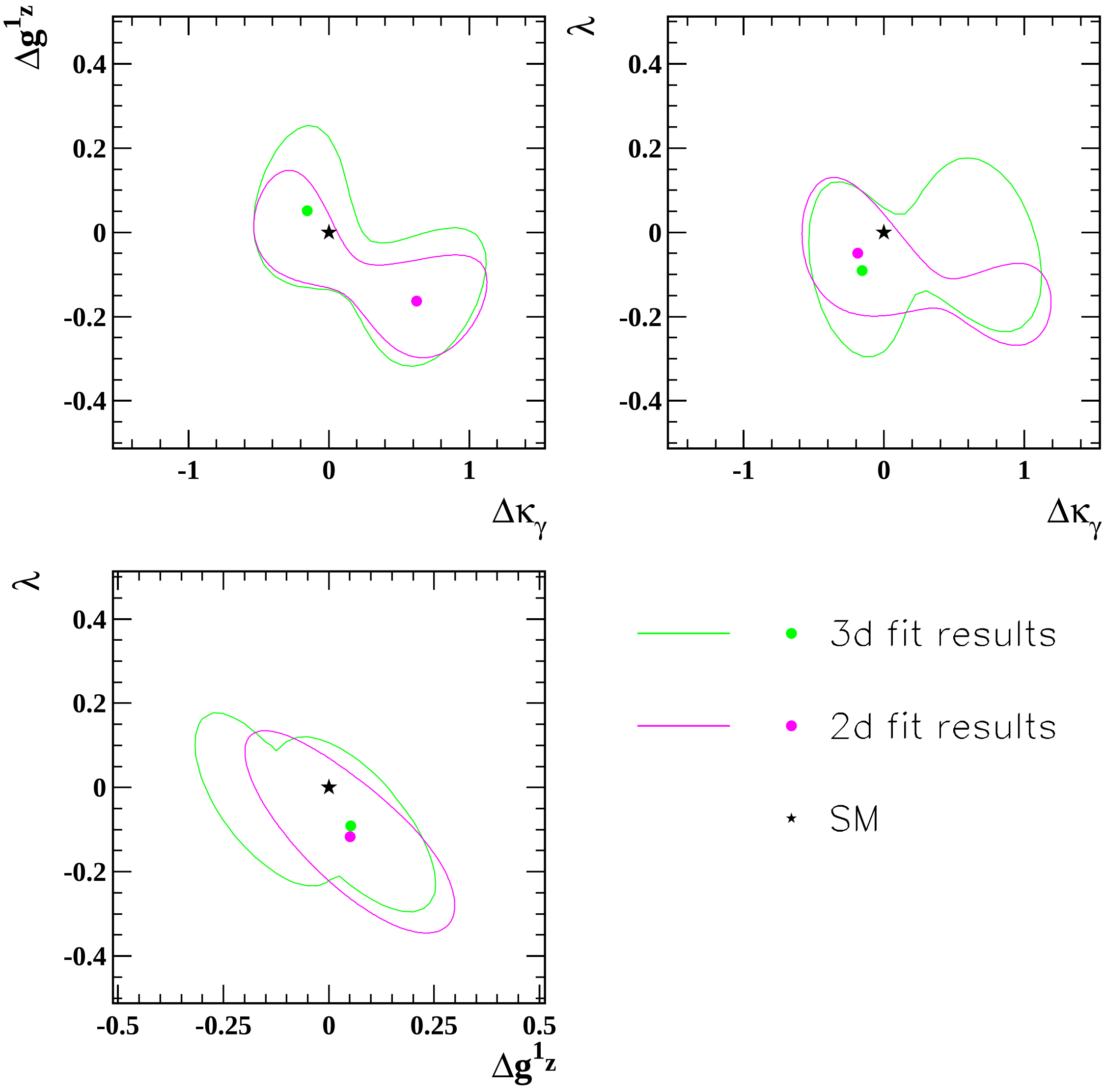

Figure 9.3: *The two and three parameter fit log-L contour plots corresponding to* $-\Delta(\ln L) = 2.995$ *(95% CL) for the combined 1999 data. For the three parameter fit, the green line represents a projection onto the two dimensional plane. The errors include both statistical and systematic contributions. The central fit values and SM expectations are indicated on the plots.*

Multi-parameter fits were also be used to extract the magnetic dipole (μ_W) and electric quadrupole moments (Q_W) defined by equations 7.4 and 7.5 respectively. The results for the combined 1999 data set (including systematics), in terms of the W mass (M_W) and electron charge (e) were found to be:

$$\mu_W = 1.75\,^{+\,0.19}_{-\,0.14}\left(\frac{e}{2\,M_W}\right) \qquad\qquad Q_W = -0.94\,^{+\,0.19}_{-\,0.21}\left(\frac{e}{M_W^2}\right)$$

These results are within the 95% CL of their SM predicted values of: 2 and -1.

9.1 Comparison with other results

The results from the OPAL total cross section analysis (single parameter fits) for the combined 192-202 GeV data set ($l\nu q\bar{q}$ channel) are [130]:

$$\Delta\kappa_\gamma = 0.00\,^{+\,0.89}_{-\,0.36} \qquad \Delta g_1^{\mathrm{Z}} = 0.00\,^{+\,0.31}_{-\,0.24} \qquad \lambda = -0.02\,^{+\,0.35}_{-\,0.22}$$

where the errors include both statistical and systematic contributions. These results are consistent with those in table 9.2, but they have much larger uncertainties since the total cross section measurements are less sensitive at LEP 2 energies. Consequently the inclusion of the total cross section results does not significantly improve the results obtained using the full angular information, although sometimes they can help determine the correct minimum for $\Delta\kappa_\gamma$.

The latest charged TGC results for the single parameter fits from the four LEP collaborations are shown in table 9.5. These results are for the combined $\mathrm{W^+W^-}$, single W and single photon channels and include both preliminary and published numbers. Errors include both statistical and systematic uncertainties. The ALEPH results include data collected during the year 2000 run, all the others are for 1999 and earlier years. These results are consistent at the 95% CL with the single parameter fit results presented in table 9.2. It should be noted that the OPAL results include an earlier, preliminary set of WW $\rightarrow l\nu q\bar{q}$ results obtained from the same analysis code used for the results in this thesis.

In addition to the LEP 2 results from e^+e^- interactions (at fixed $\mathrm{E_{cm}}$), direct measurements of TGCs have also been made at $\mathrm{p\bar{p}}$ colliders. The first such measurement was by the UA2 collaboration [133] and more recently limits have been set by the CDF and DØ experiments

Collaboration	$\Delta\kappa_\gamma$	Δg_1^{Z}	λ
ALEPH [97]	$-0.021\ ^{+0.079}_{-0.073}$	$0.015\ ^{+0.035}_{-0.032}$	$-0.001\ ^{+0.034}_{-0.031}$
DELPHI [131]	$0.06\ ^{+0.12}_{-0.11}$	-0.03 ± 0.04	0.06 ± 0.05
L3 [100]	-0.04 ± 0.12	$-0.07\ ^{+0.06}_{-0.05}$	-0.08 ± 0.06
OPAL [49]	$-0.09\ ^{+0.11}_{-0.10}$	$-0.046\ ^{+0.042}_{-0.041}$	$-0.103\ ^{+0.040}_{-0.039}$
LEP (combined) [132]	$-0.002\ ^{+0.067}_{-0.065}$	-0.025 ± 0.026	$-0.036\ ^{+0.028}_{-0.027}$

Table 9.5: *Combined $W^+W^- \to$ all, single W and single γ published and preliminary results for single parameter fits from the four LEP collaborations and the LEP Electroweak working group. The results included data collected in 1999 and earlier years (the ALEPH results also include data collected during 2000).*

at the Tevatron [134] with $\sqrt{s} = 1.8$ TeV. Unlike LEP which has a fixed centre of mass collision energy, the interacting quarks in the $\mathrm{p\bar{p}}$ collisions have variable fractions of the proton energy. Furthermore, much larger momentum transfers are involved at the Tevatron. Consequently a dipole form factor with cutoff scale Λ_{FF} is used to modify the TGC parameters in the Lagrangian:

$$\alpha \to \frac{\alpha_0}{(1 + \hat{s}/\Lambda_{\mathrm{FF}})}$$

where $\hat{s}$ represents the invariant mass of the vector boson pair. This avoids unitarity violations at tree level but it also means that the limits on the couplings are dependent on the choice of Λ_{FF}, the point at which the SM breaks down and new phenomenon (responsible for the anomalous couplings) would be directly observable. At the Tevatron Run I the following final states have been considered: W$\gamma \to l\nu\gamma$, WW$\to l\nu l\nu$, WW/WZ$\to l\nu q\bar{q}$ and WZ$\to q\bar{q}l^+l^-$, where $l \equiv e$ or μ. The latest Tevatron results at 95% CL are:

	$\underline{\lambda}$ $(\Delta\kappa = 0)$	$\underline{\Delta\kappa}$ $(\lambda = 0)$	$\underline{\Lambda_{\mathrm{FF}}\ (\mathrm{TeV})}$
DØ [135]	$-0.18 \leq \lambda \leq 0.19$	$-0.29 \leq \Delta\kappa \leq 0.53$	2
CDF [136]	$-0.81 \leq \lambda \leq 0.84$	$-1.11 \leq \Delta\kappa \leq 1.27$	1

In deriving these bounds, $\Delta\kappa_\gamma = \Delta\kappa_Z$ and $\lambda_\gamma = \lambda_Z$ were assumed. Details of these analyses and their assumptions can be found in the references. The CDF [136] and DELPHI [103] collaborations have also presented limits on the electric quadrupole and magnetic dipole moments.

Indirect limits on the TGC parameters have also been made from low energy precision measurements, including loop corrections to the W, Z, and γ propagators (oblique parameters) [137], atomic parity violation [138], $(g-2)_\mu$ [139], Z$\rightarrow b\bar{b}$ [140] and the $b \rightarrow s\gamma$ [141] decay rate. However, most of these estimates require additional assumptions and depend on specific models. Since the measurements are often sensitive to several vertices, interference effects could inhibit the detection of (potential) anomalous couplings. Hence these estimates cannot serve as a replacement for the direct measurements from W pair production.

The higher energies and luminosities available at the forthcoming Large Hadron Collider (LHC) [142] and e^+e^- linear collider (LC) [143] will allow more stringent direct tests of the TGC parameters. A comparison of the predicted bounds and sensitivities on anomalous trilinear couplings of the gauge bosons at the various experiments may be found in [144].

9.2 Future Outlook

The TGC analysis presented here built heavily upon the foundations of the 189 GeV analysis [117], with some updates and improvements. In OPAL and the LEP wide TGC and WW groups there are many ongoing studies for example, of systematics, MC modelling and detector effects etc. Although most of these improvements are expected to have only very small effects on any one data sample (because of the relatively low statistics), there could be a noticeable cumulative effect when all the LEP 2 data are combined. Eventually, all of the LEP 2 data recored by OPAL will be re-analysed (and the results combined for publication) with most of these improvements incorporated. A few suggestions for improvements are discussed here, the most important of which is the change of signal MC to incorporate additional order α radiative correction factors:

- **YFSWW3 vs. EXCALIBUR Monte Carlo** Studies presented at the Sesimbra Workshop [145] using YFSWW3 [146] MC have shown that higher order radiative corrections, not implemented in the current signal EXCALIBUR MC, are expected to shift the TGC parameters by approximately the following amounts[1]:

$$\begin{array}{rl} \Delta\kappa_\gamma & 0.170 \pm 0.050 \\ \Delta g_1^{\rm Z} & 0.044 \pm 0.012 \\ \lambda & 0.036 \pm 0.014 \end{array}$$

Examples of some of these $\mathcal{O}(\alpha)$ corrections for W pair events are shown in figure 9.4. Essentially, these new calculations decrease the $\mathrm{W^+W^-}$ production cross section by $\simeq$2.5% compared with the previous GENTLE predictions (figure 2.2) and also reduces the theoretical uncertainty from 2% to 0.5% [148]. This in turn influences the shape of the $\cos\theta_W$ distribution which is TGC sensitive. At the time of writing, investigations are still under way within OPAL and the LEP TGC working groups as to how best to incorporate these new developments. The most promising solution seems to be a new hybrid MC, KandY [149] which is a convolution of KORALW with YFSWW3.

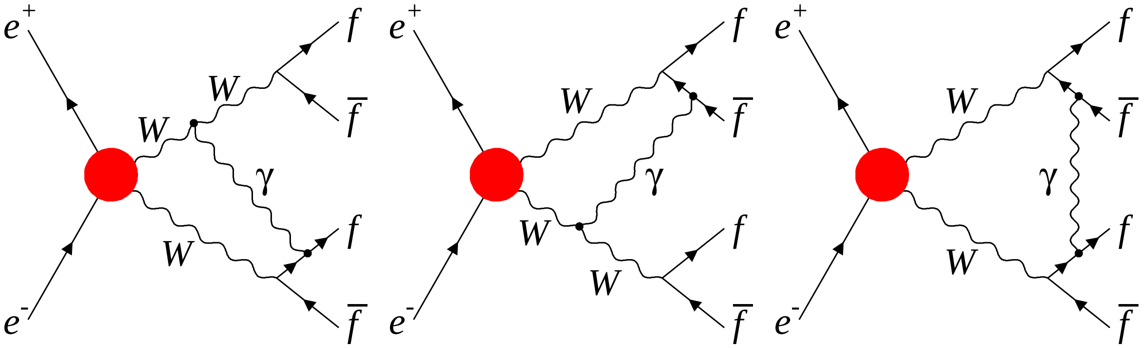

Figure 9.4: *Examples of virtual non-factorizable corrections to W pair production modelled by the new Monte Carlo.*

- **τ cuts** The kinematic fit cuts on $\tau\nu q\bar{q}$ events (described in section 5.5), are being updated [150] for $\mathrm{E_{cm}} \geq 192$ GeV data.

- **Charge mis-assignment** The amount (10%) of charge smearing that was applied to evaluate this systematic, was determined from studies at the $\mathrm{Z^0}$. Given the different event topologies of a $\mathrm{Z^0}$ and $\mathrm{W^+W^-}$, this figure could be looked at in more detail.

---

[1] These figures were obtained by comparing YFSWW3, KORALW and EXCALIBUR MC samples generated at 189 GeV with the OPAL detector simulation. Other LEP collaborations have different implementations of these corrections [147], but in general the results are broadly consistent.

- **MT vs. GCE jet reconstruction** For jet reconstruction, the GCE [82] clustering algorithm was used to combine information from the various subdetector components. An alternative package, MT [151] has more recently become compatible with the standard OPAL WW packages, and is thought to give slightly better jet energy resolution [152]. Further study needs to be done on this and the effects on the TGC coupling parameters ascertained.

- **τ identification** Another benefit of using the MT algorithm, is that a recent OPAL WW library routine can be called to more accurately identify the tau jet in WW → $\tau\nu q\bar{q}$ events [83].

- **g_5^Z coupling** It has been suggested that this additional coupling from the Lagrangian (equation 7.2) could also be determined from the fits.

- **GRC4F llqq background and systematic** Studies [153] of the GRC4F MC, have shown that this event generator does not fully represent the OPAL data for $llqq$ and $llll$ final states. In order to remedy this, an event weight calculator package has been produced to increase or decrease the event weights in certain areas of phase space. However, since the expected $e^+e^- \rightarrow eeqq$ and $e^+e^- \rightarrow ee\tau\tau$ backgrounds are small then the effect is thought to be small.

- **Jet parameter systematics** Recent and ongoing studies of jets in Z^0 calibration data, have resulted in minor updates to the numbers quoted in sections 8.3.2 and 8.3.3 for hadronic and tau jet reconstruction systematics.

- **Minor improvements and updates** Various minor improvements to this analysis could be made. For example further simplification of the analysis code and in particular the subsampling procedure. In February 2001 the OPCAL database was updated to include modifications for the EB calibrations. The effect on the TGCs is thought to be small however.

> *Upon a slight conjecture I have ventured on a dangerous journey, and I already behold the foothills of new lands. Those who have the courage to continue the search will set foot upon them.*
>
> IMMANUAL KANT, 1775

Chapter 10

Conclusions

Measurement of the triple gauge boson couplings (TGCs) provides an important test of the non-Abelian nature of Standard Model (SM) electroweak theory. In this thesis, the optimal observable technique was used to extract the couplings from samples of $W^+W^- \rightarrow l\nu q\bar{q}$ events. The data were recorded by the OPAL detector at centre of mass collision energies between 192 and 202 GeV and had a total integrated luminosity of 212 pb^{-1}. The basic idea behind the optimal observable method is to project the five kinematic phase space variables onto a set of suitably defined observables (without loss of sensitivity or information). Furthermore just the means of these observables are used in the fit. No significant biases were found in this method.

The TGCs were parameterized in terms of three couplings: κ_γ, g_1^Z and λ. The combined results for the single parameter fits (where one coupling was allowed to vary from its SM prediction) are:

$$\kappa_\gamma = 0.722\,^{+0.191}_{-0.160} \qquad g_1^Z = 0.962\,^{+0.066}_{-0.063} \qquad \lambda = -0.070\,^{+0.064}_{-0.062}$$

These errors include both statistical and systematic uncertainties. The three parameter fit results (where all three couplings were allowed to vary simultaneously) are:

$$\kappa_\gamma = 0.846\,^{+0.180}_{-0.143} \qquad g_1^Z = 1.052\,^{+0.076}_{-0.080} \qquad \lambda = -0.091\,^{+0.086}_{-0.084}$$

These results are in agreement with SM predictions ($\kappa_\gamma = g_1^Z = 1$ and $\lambda = 0$) at 95% confidence and also agree with the latest LEP combination results [132].

Using these results, limits have also been placed on the magnetic dipole and electric quadrupole moments:

$$\mu_W = 1.75\,^{+\,0.19}_{-\,0.14}\left(\frac{e}{2\,M_W}\right) \qquad\qquad Q_W = -0.94\,^{+\,0.19}_{-\,0.21}\left(\frac{e}{M_W^2}\right)$$

which also agree with SM predictions at the 95% CL.

Recent studies (for example [145, 148]) have highlighted a problem with order (α) corrections to the Monte Carlo, so this analysis needs to be repeated before the final results can be published.

Appendix A

OPAL Track Parameters

The five OPAL track parameters: $\boldsymbol{\kappa}$, $\mathbf{d_o}$, $\boldsymbol{\phi_o}$, $\boldsymbol{\tan\lambda}$ and $\boldsymbol{z_o}$ [75] define a helix. The first three quantities describe the r-ϕ trajectory and the last two describe the motion in the z direction. The parameters are defind as:

- **Curvature $\boldsymbol{\kappa}$**

  Track curvature is defined as:

  $$\mid \kappa \mid = \frac{1}{2\rho} \tag{A.1}$$

  where ρ is the radius of track curvature. κ is 'signed' so that negative κ corresponds to decreasing ϕ if one moves along the track trajectory from the point of closest approach to the origin in the r-ϕ plane. Using this quantity, a particle's electric charge can be determined from:

  $$\mathrm{q} = -\,\text{sign of}\left(\frac{\mathrm{B}_z}{\kappa}\right) \tag{A.2}$$

  where B_z is the axial magnetic field component along the positive z axis. Hence, a particle will have positive physical charge if κ is negative.

- **Impact Parameter $\mathbf{d_o}$**

  $|\,\mathrm{d}_o\,|$ is defined as the distance from the origin of the co-ordinate system (not the beam interaction point) to the point of closest approach. It may be also written as:

  $$\mathrm{d}_o = \hat{\phi} \wedge \vec{d} \cdot \hat{z} \tag{A.3}$$

where $\hat{\phi}$ is the unit track vector at the point of closest approach, $\vec{d}$ is the vector from the origin to the point of closest approach and $\hat{z}$ is the unit vector along z axis.

- **Azimuthal Angle ϕ_o**
  ϕ_o is defined as the azimuthal angle made by the track tangent at the point of closest approach to the origin.
- **Track Polar Angle $\tan\lambda$**
  $\tan\lambda = \cot\theta$ where θ is the track polar angle measured from the positive z axis.
- **z co-ordinate of closest approach z_o**
  z_o is defined as the z co-ordinate when the track is at the point of closest approach.

Physical Quantities

The above definitions of track parameters may be used to determine physical quantities. They are related to the physical track variables by:

$$p_{xy} = a\left|\frac{\mathrm{B}_z}{\kappa}\right| \tag{A.4}$$

where p_{xy} is the transverse or x-y component of momentum and a is a constant given by:

$$a = \frac{c}{2} \times 10^{-14} \simeq 1.5 \times 10^{-4}$$

when p_{xy} is measured in GeV/c, B_z in kG and κ in cm^{-1}.

The components of particle momentum may be written in terms of:

$$\begin{aligned} p_x &= p_{xy}\cos\phi_o \\ p_y &= p_{xy}\sin\phi_o \\ p_z &= p_{xy}\tan\lambda \\ p &= p_{xy}\sqrt{1+\tan^2\lambda} \end{aligned} \tag{A.5}$$

The physical charge is given by equation A.2.

Appendix B

List of Monte Carlo Samples

B.1 WW Classification

The main Monte Carlo sample used to determine the acollinearity dependent momentum cut values (described in chapter 6) for the 189 GeV data was the KORALW CC03 sample run 8058[1]. Later, other high statistics KORALW CC03 samples became available (including a dedicated WW$\rightarrow l\nu l\bar{\nu}$ sample) which were used to verify the cut positions. These are listed in table B.1.

Run	Generated events	Selected events	Lumi (fb^{-1})	Process
8058	150000	12891	9.01	$W^+W^- \rightarrow$ all
8626	200000	17668	12.02	$W^+W^- \rightarrow$ all
8627	60000	49870	12.02	WW$\rightarrow l\nu l\bar{\nu}$
8628	60000	50297	36.06	WW$\rightarrow l\nu l\bar{\nu}$ (E_{cm}= 183 GeV)

Table B.1: *CC03* KORALW *Monte Carlo samples used to determine and verify the acollinearity dependent momentum cut positions. All samples were generated at 189 GeV unless otherwise stated.*

The non-four fermion background (for the improvements to the W leptonic branching ratio measurements) was estimated from 16 different samples of MC (listed in table B.2). The contribution from four fermion sources was more complicated, reflecting the fact that exper-

---

[1] In OPAL, the different MC samples are refered to by the internal run numbers with which they were generated.

imentally it is extremely difficult if not impossible to separate the CC03 contribution from other four fermion processes. A TGC dependent EXCALIBUR four fermion sample run 8100 (including only $ee\nu_e\nu_e$, $\mu\mu\nu_\mu\nu_\mu$, $\tau\tau\nu_\tau\nu_\tau$, $e\nu_e\mu\nu_\mu$, $e\nu_e\tau\nu_\tau$ and $\mu\nu_\mu\tau\nu_\tau$ final states) was added to a four fermion (non-WW) GRC4F sample run 7844 (with only $ee\nu_\mu\nu_\mu$, $ee\nu_\tau\nu_\tau$, $\mu\mu\nu_e\nu_e$, $\mu\mu\nu_\tau\nu_\tau$, $\tau\tau\nu_e\nu_e$ and $\tau\tau\nu_\mu\nu_\mu$ final states included). Then a CC03 EXCALIBUR sample run 8263 (using only $ee\nu_e\nu_e$, $\mu\mu\nu_\mu\nu_\mu$, $\tau\tau\nu_\tau\nu_\tau$, $e\nu_e\mu\nu_\mu$, $e\nu_e\tau\nu_\tau$ and $\mu\nu_\mu\tau\nu_\tau$ final states) was subtracted from the combination to determine the overall background contribution from non-CC03 diagrams including interference terms.

Run	Generator	Generated events	Contribution to x-section (pb)	Lumi (fb^{-1})	Process
Non $l\nu l\bar{\nu}$ background					
1545	KORALZ	80000	19.08 ± 1.38	10.00	$e^+e^- \to \tau\tau$ (tau pairs)
1032	VERMASEREN	430000	7.86 ± 2.83	0.98	$e^+e^- \to ee\tau\tau$ (2 photon)
8055	GRC4F	43396	4.94 ± 0.99	5.00	$e^+e^- \to llqq$ (4f)
7848	GRC4F	9168	3.50 ± 0.84	5.00	$e^+e^- \to ee\tau\tau$ (4f)
1031	VERMASEREN	800000	2.91 ± 1.71	0.99	$e^+e^- \to eeee$ (2 photon)
1436	KORALZ	35000	2.81 ± 0.22	58.46	$e^+e^- \to \nu\nu\gamma(\gamma)$ (photon(s) + E_{miss})
1614	KORALZ	80000	2.45 ± 0.50	10.00	$e^+e^- \to \mu\mu$ (muon pairs)
1344	BHWIDE	600000	1.93 ± 1.39	1.01	$e^+e^- \to ee$ (electron pairs)
1346	TEEGG	700000	1.00 ± 1.01	0.99	$e^+e^- \to e^+e^-\gamma(\gamma)$ (radiative Bhabhas)
7847	GRC4F	63685	0.99 ± 0.44	5.00	$e^+e^- \to ee\mu\mu$ (4f)
7849	GRC4F	127583	0.58 ± 0.34	5.00	$e^+e^- \to eeqq$ (4f)
7862	GRC4F	91810	0.19 ± 0.20	5.00	$e^+e^- \to eeee$ (4f)
Total non $l\nu l\bar{\nu}$ contribution to x-section:			48.25 ± 4.26		
$l\nu l\bar{\nu}$ background					
8100	EXCALIBUR	460000	1523.81 ± 7.77	25.26	$e^+e^- \to 4f$ (not eell/eeqq final states)
7844	GRC4F	15855	47.88 ± 3.09	5.00	$e^+e^- \to llll$ (4f)
8263	EXCALIBUR	200000	-1461.17 ± 11.01	12.06	$W^+W^- \to$ all (CC03)
Corrected $l\nu l\bar{\nu}$ background contribution:			48.27 ± 3.11		

Table B.2: *Background contributions to the improved branching ratio measurements (section 6.3).*

B.2 TGC Analysis

Monte Carlo samples used in the TGC analysis for each E_{cm} are listed below. The signal MC EXCALIBUR samples include all (interfering) TGC dependent Feynmann diagrams (except eell/eeqq final states). The remaining non-tgc dependent four fermion diagrams were included in the samples labelled non-tgc (except eell/eeqq final states). A complete four fermion sample was made up by adding these two SM EXCALIBUR samples to GRC4F samples with eell/eeqq final states. Similarly for the MC generator systematic studies, three samples of either KORALW or GRC4F ($l\nu l\bar{\nu}$, $l\nu q\bar{q}$ and $q\bar{q}q\bar{q}$ final states) made up a complete four fermion sample. For the signal excalibur samples (both SM and AC), the generated coupling values are listed in the order: $\Delta\kappa_\gamma$, Δg_1^Z and λ.

Run	Type	Generator	Generated events	Selected events	Lumi (fb^{-1})	Comments/Process
Signal samples						
9484	4f	EXCALIBUR	93000	30041	5.05	SM (0,0,0)
10012	4f	EXCALIBUR	49999	15526	2.51	AC (1,0,0)
10013	4f	EXCALIBUR	50000	16564	2.43	AC (-1,0,0)
10014	4f	EXCALIBUR	50000	16345	2.06	AC (0,0,1)
10015	4f	EXCALIBUR	50000	16550	1.96	AC (0,0,-1)
10016	4f	EXCALIBUR	50000	16233	1.96	AC (0,1,0)
10017	4f	EXCALIBUR	50000	16801	1.90	AC (0,-1,0)
Background samples						
9585	4f	EXCALIBUR	10000	343	5.06	non-tgc
9276	4f	GRC4F	9113	5	5.00	$e^+e^- \rightarrow ee\tau\tau$
9277	4f	GRC4F	207129	227	5.00	$e^+e^- \rightarrow eeqq$
5195	2f	KK2F	250000	328	2.64	$Z^0/\gamma \rightarrow q\bar{q}$
1049	2γ	HERWIG	150000	6	0.50	2γ (generated at 189 GeV)

Table B.3: *Monte Carlo samples used in the main 192 GeV analysis.*

Run	Type	Generator	Generated events	Selected events	Lumi (fb^{-1})	Comments/Process
8755	CC03	GRC4F	83974	29262	5.00	Jetset fragmentation
8793	CC03	GRC4F	83974	29135	5.00	Herwig fragmentation
9205	4f	KORALW	44986	30142	5.00	$e^+e^- \rightarrow llqq$ final state
9206	4f	KORALW	16055	11	5.00	$e^+e^- \rightarrow llll$ final state
9204	4f	KORALW	43704	125	5.00	$e^+e^- \rightarrow qqqq$ final state
8750	4f	GRC4F	44735	30051	5.00	$e^+e^- \rightarrow llqq$ final state
9542	4f	GRC4F	16173	9	5.00	$e^+e^- \rightarrow llll$ final state
8751	4f	GRC4F	43286	131	5.00	$e^+e^- \rightarrow qqqq$ final state
5105	2f	PYTHIA	100000	145	1.11	$\mathrm{Z}^0/\gamma \rightarrow q\bar{q}$ background
5102	2f	HERWIG	100000	125	1.10	$\mathrm{Z}^0/\gamma \rightarrow q\bar{q}$ background
8700	CC03	KORALW	100000	34720	5.91	$\mathrm{W}^+\mathrm{W}^- \rightarrow$ all (signal)
10082	CC03	KORALW	50000	16121	2.71	$\mathrm{M_W}$=79.33 GeV, $\mathrm{E_{cm}}$=191.588 GeV
9902	CC03	KORALW	50000	15938	2.69	$\mathrm{M_W}$=79.83 GeV, $\mathrm{E_{cm}}$=191.588 GeV
9901	CC03	KORALW	100000	31774	5.37	$\mathrm{M_W}$=80.08 GeV, $\mathrm{E_{cm}}$=191.588 GeV
9900	CC03	KORALW	100000	32186	5.36	$\mathrm{M_W}$=80.33 GeV, $\mathrm{E_{cm}}$=191.588 GeV
9903	CC03	KORALW	100000	32107	5.35	$\mathrm{M_W}$=80.58 GeV, $\mathrm{E_{cm}}$=191.588 GeV
9904	CC03	KORALW	50000	16089	2.68	$\mathrm{M_W}$=80.83 GeV, $\mathrm{E_{cm}}$=191.588 GeV
10083	CC03	KORALW	50000	16077	2.67	$\mathrm{M_W}$=81.33 GeV, $\mathrm{E_{cm}}$=191.588 GeV

Table B.4: *Monte Carlo samples used for systematic studies in the 192 GeV analysis.*

Run	Type	Generator	Generated events	Selected events	Lumi (fb^{-1})	Comments/Process
Signal samples						
9486	4f	EXCALIBUR	190000	60152	10.10	SM (0,0,0)
9746	4f	EXCALIBUR	100000	30163	4.89	AC (1,0,0)
9747	4f	EXCALIBUR	100000	31140	5.24	AC (0.5,0,0)
9748	4f	EXCALIBUR	100000	32356	5.11	AC (-0.5,0,0)
9749	4f	EXCALIBUR	100000	32775	4.68	AC (-1,0,0)
9750	4f	EXCALIBUR	100000	32485	3.89	AC (0,0,1)
9751	4f	EXCALIBUR	100000	31844	4.91	AC (0,0,0.5)
9752	4f	EXCALIBUR	100000	32058	4.74	AC (0,0,-0.5)
9753	4f	EXCALIBUR	100000	32807	3.68	AC (0,0,-1)
9754	4f	EXCALIBUR	100000	32108	3.74	AC (0,1,0)
9755	4f	EXCALIBUR	100000	31736	4.84	AC (0,0.5,0)
9756	4f	EXCALIBUR	100000	32463	4.72	AC (0,-0.5,0)
9757	4f	EXCALIBUR	100000	33119	3.60	AC (0,-1,0)
9758	4f	EXCALIBUR	100000	30674	3.82	AC (1,1,0)
9759	4f	EXCALIBUR	100000	31305	3.58	AC (1,0,1)
9760	4f	EXCALIBUR	100000	33022	2.44	AC (0,1,1)
Background samples						
9487	4f	EXCALIBUR	21000	766	10.34	non-tgc
9279	4f	GRC4F	8984	2	5.00	$e^+e^- \rightarrow ee\tau\tau$
9280	4f	GRC4F	202483	275	5.00	$e^+e^- \rightarrow eeqq$
5196	2f	KK2F	250000	327	2.78	$\text{Z}^0/\gamma \rightarrow q\bar{q}$
1085	2γ	HERWIG	310000	10	1.00	2γ

Table B.5: *Monte Carlo samples used in the main 196 GeV analysis.*

Run	Type	Generator	Generated events	Selected events	Lumi (fb^{-1})	Comments/Process
9101	CC03	GRC4F	85365	29627	5.00	Jetset fragmentation
9124	CC03	GRC4F	85365	29445	5.00	Herwig fragmentation
9202	4f	KORALW	91802	60622	10.00	$e^+e^- \rightarrow llqq$ final state
9203	4f	KORALW	32751	21	10.00	$e^+e^- \rightarrow llll$ final state
9201	4f	KORALW	89210	292	10.00	$e^+e^- \rightarrow qqqq$ final state
9096	4f	GRC4F	45700	30209	5.00	$e^+e^- \rightarrow llqq$ final state
9543	4f	GRC4F	16474	10	5.00	$e^+e^- \rightarrow llll$ final state
9097	4f	GRC4F	44082	130	5.00	$e^+e^- \rightarrow qqqq$ final state
5106	2f	PYTHIA	250000	352	1.97	$\text{Z}^0/\gamma \rightarrow q\bar{q}$ background
5103	2f	HERWIG	100000	115	1.17	$\text{Z}^0/\gamma \rightarrow q\bar{q}$ background
8704	CC03	KORALW	200000	68871	5.81	$\text{W}^+\text{W}^- \rightarrow$ all (signal)
10084	CC03	KORALW	50000	15757	2.66	M_W=79.33 GeV, E_cm=195.528 GeV
9907	CC03	KORALW	50000	15766	2.65	M_W=79.83 GeV, E_cm=195.528 GeV
9906	CC03	KORALW	100000	31387	5.27	M_W=80.08 GeV, E_cm=195.528 GeV
9905	CC03	KORALW	100000	31586	5.26	M_W=80.33 GeV, E_cm=195.528 GeV
9908	CC03	KORALW	100000	31733	5.24	M_W=80.58 GeV, E_cm=195.528 GeV
9909	CC03	KORALW	50000	15791	2.61	M_W=80.83 GeV, E_cm=195.528 GeV
10085	CC03	KORALW	50000	15861	2.59	M_W=81.33 GeV, E_cm=195.528 GeV

Table B.6: *Monte Carlo samples used for systematic studies in the 196 GeV analysis.*

Run	Type	Generator	Generated events	Selected events	Lumi (fb^{-1})	Comments/Process
Signal samples						
9488	4f	EXCALIBUR	192000	59973	10.07	SM (0,0,0)
9761	4f	EXCALIBUR	100000	29589	4.78	AC (1,0,0)
9762	4f	EXCALIBUR	100000	30719	5.15	AC (0.5,0,0)
9763	4f	EXCALIBUR	100000	32102	5.02	AC (-0.5,0,0)
9764	4f	EXCALIBUR	100000	32437	4.55	AC (-1,0,0)
9765	4f	EXCALIBUR	100000	32149	3.70	AC (0,0,1)
9766	4f	EXCALIBUR	100000	31705	4.79	AC (0,0,0.5)
9767	4f	EXCALIBUR	100000	31785	4.62	AC (0,0,-0.5)
9768	4f	EXCALIBUR	100000	32763	3.49	AC (0,0,-1)
9769	4f	EXCALIBUR	100000	31932	3.59	AC (0,1,0)
9770	4f	EXCALIBUR	100000	31569	4.74	AC (0,0.5,0)
9771	4f	EXCALIBUR	100000	32088	4.60	AC (0,-0.5,0)
9772	4f	EXCALIBUR	100000	32827	3.44	AC (0,-1,0)
9773	4f	EXCALIBUR	100000	30615	3.68	AC (1,1,0)
9774	4f	EXCALIBUR	100000	31257	3.39	AC (1,0,1)
9775	4f	EXCALIBUR	100000	32634	2.27	AC (0,1,1)
Background samples						
9590	4f	EXCALIBUR	21000	755	10.21	non-tgc
9317	4f	GRC4F	8898	0	5.00	$e^+e^- \to ee\tau\tau$
9318	4f	GRC4F	197391	238	5.00	$e^+e^- \to eeqq$
5119	2f	KK2F	300000	366	3.51	$Z^0/\gamma \to q\bar{q}$
1086	2γ	HERWIG	314000	4	1.00	2γ

Table B.7: *Monte Carlo samples used in the main 200 GeV analysis.*

Run	Type	Generator	Generated events	Selected events	Lumi (fb^{-1})	Comments/Process
9540	CC03	GRC4F	86290	29134	5.00	Jetset fragmentation
9541	CC03	GRC4F	86290	29116	5.00	Herwig fragmentation
9208	4f	KORALW	93245	60631	10.00	$e^+e^- \to llqq$ final state
9209	4f	KORALW	33272	18	10.00	$e^+e^- \to llll$ final state
9207	4f	KORALW	90198	270	10.00	$e^+e^- \to qqqq$ final state
9313	4f	GRC4F	46385	30067	5.00	$e^+e^- \to llqq$ final state
9312	4f	GRC4F	16727	8	5.00	$e^+e^- \to llll$ final state
9314	4f	GRC4F	44545	152	5.00	$e^+e^- \to qqqq$ final state
5121	2f	PYTHIA	250000	343	2.07	$Z^0/\gamma \to q\bar{q}$ background
5118	2f	HERWIG	100000	143	1.11	$Z^0/\gamma \to q\bar{q}$ background
9210	CC03	KORALW	200000	68111	11.50	$W^+W^- \to$ all (signal)
10086	CC03	KORALW	50000	15405	2.63	M_W=79.33 GeV, E_{cm}=199.520 GeV
9912	CC03	KORALW	50000	15574	2.61	M_W=79.83 GeV, E_{cm}=199.520 GeV
9911	CC03	KORALW	100000	31195	5.21	M_W=80.08 GeV, E_{cm}=199.520 GeV
9910	CC03	KORALW	100000	31299	5.18	M_W=80.33 GeV, E_{cm}=199.520 GeV
9913	CC03	KORALW	100000	31063	5.16	M_W=80.58 GeV, E_{cm}=199.520 GeV
9914	CC03	KORALW	50000	15620	2.57	M_W=80.83 GeV, E_{cm}=199.520 GeV
10087	CC03	KORALW	50000	15563	2.54	M_W=81.33 GeV, E_{cm}=199.520 GeV

Table B.8: *Monte Carlo samples used for systematic studies in the 200 GeV analysis.*

Run	Type	Generator	Generated events	Selected events	Lumi (fb^{-1})	Comments/Process
Signal samples						
9850	4f	EXCALIBUR	192000	59519	10.01	SM (0,0,0)
10018	4f	EXCALIBUR	49999	14638	2.37	AC (1,0,0)
10019	4f	EXCALIBUR	50000	15860	2.25	AC (-1,0,0)
10020	4f	EXCALIBUR	50000	15833	1.81	AC (0,0,1)
10021	4f	EXCALIBUR	50000	15987	1.70	AC (0,0,-1)
10022	4f	EXCALIBUR	50000	15780	1.76	AC (0,1,0)
10023	4f	EXCALIBUR	50000	16223	1.68	AC (0,-1,0)
Background samples						
9851	4f	EXCALIBUR	20500	749	9.90	non-tgc
9808	4f	GRC4F	8763	1	5.00	$e^+e^- \to ee\tau\tau$
9713	4f	GRC4F	195239	245	5.00	$e^+e^- \to eeqq$
5199	2f	KK2F	250000	272	3.00	$Z^0/\gamma \to q\bar{q}$
1086	2γ	HERWIG	314000	4	1.00	2γ (generated at 200 GeV)

Table B.9: *Monte Carlo samples used in the main 202 GeV analysis.*

Run	Type	Generator	Generated events	Selected events	Lumi (fb^{-1})	Comments/Process
9726	CC03	GRC4F	86572	29052	5.00	Jetset fragmentation
9727	CC03	GRC4F	86572	29084	5.00	Herwig fragmentation
9702	4f	KORALW	93969	60451	10.00	$e^+e^- \to llqq$ final state
9703	4f	KORALW	33497	17	10.00	$e^+e^- \to llll$ final state
9701	4f	KORALW	90342	261	10.00	$e^+e^- \to qqqq$ final state
9711	4f	GRC4F	46595	29815	5.00	$e^+e^- \to llqq$ final state
9829	4f	GRC4F	16817	5	5.00	$e^+e^- \to llll$ final state
9712	4f	GRC4F	44722	142	5.00	$e^+e^- \to qqqq$ final state
5126	2f	PYTHIA	150000	194	1.27	$Z^0/\gamma \to q\bar{q}$ background
5118	2f	HERWIG	100000	140	1.11	$Z^0/\gamma \to q\bar{q}$ background (generated at 200 GeV)
9809	CC03	KORALW	200000	66762	11.46	$W^+W^- \to$ all (signal)
10088	CC03	KORALW	50000	15277	2.62	M_W=79.33 GeV, E_{cm}=191.588 GeV
9917	CC03	KORALW	50000	15204	2.59	M_W=79.83 GeV, E_{cm}=191.588 GeV
9916	CC03	KORALW	100000	30720	5.18	M_W=80.08 GeV, E_{cm}=191.588 GeV
9915	CC03	KORALW	100000	31029	5.16	M_W=80.33 GeV, E_{cm}=191.588 GeV
9918	CC03	KORALW	100000	30873	5.12	M_W=80.58 GeV, E_{cm}=191.588 GeV
9919	CC03	KORALW	50000	15748	2.55	M_W=80.83 GeV, E_{cm}=191.588 GeV
10089	CC03	KORALW	50000	15573	2.52	M_W=81.33 GeV, E_{cm}=191.588 GeV

Table B.10: *Monte Carlo samples used for systematic studies in the 202 GeV analysis.*

Appendix C

Glossary

$\boldsymbol{\alpha_i}$ Generic term used to denote a set of coupling parameters (for example: $\Delta\kappa_\gamma$, Δg_1^{Z}, λ).

$\boldsymbol{\mathcal{OO}}$ Optimal Observables (defined by equation 7.11).

$\boldsymbol{\overline{\mathcal{OO}}}$ Mean Optimal Observable.

$\boldsymbol{\Delta\overline{\mathcal{OO}}}$ Change in $\mathcal{OO}$ from reference value (obtained with Excalibur).

E$[\boldsymbol{\mathcal{OO}}]$ Expectation value. Expected $\mathcal{OO}$ value determined from mean of probability distribution.

AC Anomalous Coupling (ie not SM predicted value).

CC Charged Current interaction, ie one mediated by a W boson propagator.

DST Data Summary Tape. After event reconstruction, the reprocessed OPAL data is stored in DST format for offline analysis (see section 3.2.11).

$\mathbf{E_{cm}}$ Centre of mass energy.

FSI Final State Interactions (eg Bose-Einstein or colour reconnection effects).

FSR Final State Radiation.

GCE Globally Corrected Energy [82]. Algorithm to sum over energy clusters and tracks in an event, to correct for double counting of jet energy.

ISR Initial State Radiation.

$\mathcal{L}$ Lagrangian or Lagrangian density.

log-L Log likelihood function.

MC Monte Carlo (simulated data).

NC Neutral Current interaction, ie one mediated by the exchange of a Z^0 or γ propagator.

QFT Quantum Field Theory.

SDM Spin Density Matrix. A statistical technique to extract the TGCs in a completely model independent way.

SM Standard Model of particle physics.

TGC Triple Gauge (boson) Coupling. The coupling parameters defined in the standard electroweak Lagrangian (equation 7.2).

YFS Yennie-Frautschi-Suura exponentiation [64] (treatment of ISR in MC).

> *A man should keep his little brain-attic stocked with all the furniture that he is likely to use, and the rest he can put away in the lumber-room of his library, where he can get it if he wants it.*
>
> SHERLOCK HOLMES, The Five Orange Pips

References

[1] F. Halzen and A. D. Martin, *"Quarks and Leptons: An Introductory Course in Modern Particle Physics"*, John Wiley & Sons, (1994).
D. H. Perkins *"Introduction to High Energy Physics"* (3rd edition), Addison-Wesley Publishing Company, Inc. (1987).
I. J. R. Aitchison & A. J. G. Hey, *"Gauge Theories in Particle Physics"* (2nd Edition), Instititute of Physics Publishing, 1989.

[2] S. L. Glashow, *"Partial Symmetries of Weak Interactions"*, Nucl. Phys. **B22**, (1961) 579.
S. Weinberg, *"A Model of Leptons"*, Phys. Rev. Lett. **19** (1967).
A. Salam, *"Weak and Electromagnetic Interactions"*, originally printed in "Svartholm: Elementary Particle Theory, Proceedings Of The Nobel Symposium Held 1968 at Lerum, Sweden", Stockholm (1968).

[3] C. N. Yang and R. L. Mills, *"Conservation Of Isotopic Spin And Isotopic Gauge Invariance"*, Phys. Rev. **96** (1954) 191.

[4] P. W. Higgs, *"Broken Symmetries And The Masses Of Gauge Bosons"*, Phys. Rev. Lett. **13** (1964) 508.

[5] The LEP Collaborations: ALEPH, DELPHI, L3, OPAL and the LEP W Working Group, E. Barberio *et al.*, *"Combined Preliminary Results on the Mass and Width of the W Boson Measured by the LEP Experiments"*, LEPEWWG/MASS/2000-01 (July 2001).

[6] OPAL Standard Model, WW and QCD Working Groups, *"Measurements of Standard Model Processes in e^+e^- Collisions at $\sqrt{s}$ 203 - 209 GeV"*, OPAL Physics Note PN469, (February 2001).

[7] D. Bardin, J. Biebel, D. Lehner, A. Leike, A. Olchevski and T. Riemann, "GENTLE, *A program for the Semi-Analytic Calculation of Predictions for the Process $e^+e^- \rightarrow 4$ fermions"*, hep-ph/9612409, December 1996.

[8] G. Altarelli, T. Sjöstrand and F. Zwirner *et al.*, *Physics at LEP2*, CERN yellow report, CERN 96-01 (February 1996).

[9] W. Beenakker and A. Denner, *"Standard Model Predictions for W-Pair Production in Electron-Positron Collisions"*, Int. J. Mod. Phys. **A9** (1994) 4837.

[10] T. Muta, R. Najima and S. Wakaizumi, *“Effects Of The W Boson Width In $e^+e^- \to W^+W^-$ Reactions”*, Mod. Phys. Lett. **A1** (1986) 203.

[11] *“Large Electron Positron Storage Ring Technical Notebook”*, CERN publication, (November 1989).
S. Myers and E. Picasso, *“The design, construction and commisioning of the CERN Large Electron Positron Collider”*, Contemp. Phys. **31** (1990) 387.

[12] OPAL Collaboration, K. Ahmet *et al.*, *“The OPAL detector at LEP”*, Nucl. Instr. Meth. **A305** (1991) 275.

[13] ALEPH Collaboration, D. Decamp *et al.*, *“ALEPH: a detector for electron-positron annihilations at LEP”*, Nucl. Instr. Meth. **A294** (1990) 121.

[14] DELPHI Collaboration, P. Aarnio *et al.*, *“The DELPHI detector at LEP”*, Nucl. Instr. Meth. **A303** (1991) 233.

[15] L3 Collaboration, B. Adeva *et al.*, *“The construction of the L3 experiment”*, Nucl. Instr. Meth. **A289** (1990) 35.

[16] P. P. Allport *et al.*, *“The OPAL Silicon Microvertex Detector”*, Nucl. Inst. Meth. **A324** (1993) 34.

[17] P. P. Allport *et al.*, *“The OPAL Silicon Strip Microvertex Detector with Two Coordinate Readout”*, Nucl. Instr. Meth. **A346** (1994) 476.

[18] S. de Jong, *“The OPAL Phase III Microvertex Detector”*, Nucl. Instr. Meth. **A386** (1997) 23.
S. Anderson *et al.*, *“The extended OPAL Silicon Strip Microvertex Detector”*, Nucl. Instr. Meth. **A403** (1998) 326.

[19] J. R. Carter *et al.*, *“The OPAL Vertex Drift Chamber”*, Nucl. Instr. Meth. **A286** (1990) 99.

[20] H. M. Fischer *et al.*, *“The OPAL Jet Chamber”*, Nucl. Instr. Meth. **A283** (1989) 492.

[21] M. Hauschild *et al.*, *“Particle identification with the OPAL jet chamber”*, Nucl.Instr. Meth. **A314** (1992) 74.

[22] H. Mes *et al.*, *“Design and Tests of the Z Coordinate Drift Chamber System for the OPAL Detector at LEP”*, Nucl. Inst. Meth. **A265** (1988) 445.

[23] A. Ji-Gang *et al.*, *“Influence of Gas Mixture and Primary Ionization on the Performance of Limited Streamer Mode Tubes”*, Nucl. Instr. Meth. **A267** (1988) 386.

[24] C. Beard *et al.*, *“Thin, High Gain Wire Chambers for Electromagnetic Presampling in OPAL”*, Nucl. Instr. Meth. **A286** (1990) 117.

[25] T. Kobayashi, *“Realization of OPAL Electromagnetic Barrel Calorimeter”*, Prepared for the 2$^{\text{nd}}$ International Conference on Calorimetry in High-Energy Physics, Capri, Italy (1991).

[26] William B. Rolnick, *"The Fundamental Particles and their Interactions"*, Addison-Wesley Publishing Company, (1994).

[27] M. Akrawy *et al.*, *"Development Studies for the OPAL Endcap Electromagnetic Calorimeter using Vacuum Photo Triode Instrumented Lead Glass"*, Nucl. Inst. Meth. **A290** (1990) 76.

[28] G. Artusi *et al.*, *"Limited Streamer Tubes for the OPAL Hadron Calorimeter"*, Nucl. Inst. Meth. **A279** (1989) 523.

[29] G. Mikenberg, *"Thin Gap Gas Chambers for Hadronic Calorimetry"*, Nucl. Inst. Meth. **A265** (1988) 223.
S. Dado *et al.*, *"A New High Gain Thin Gap Detector for the OPAL Hadronic Calorimetry"*, Nucl. Inst. Meth. **A252** (1986) 511.

[30] R. J. Akers *et al.*, *"The OPAL Muon Barrel Detector"*, Nucl. Inst. Meth. **A357** (1995) 253.

[31] G. T. J. Arnison *et al.*, *"Production and Testing of Limited Streamer Tubes for the Endcap Muon Subdetector of OPAL"*, Nucl. Inst. Meth. **A294** (1990) 431.

[32] D. C. Imrie *et al.*, *"An Array Of Proportional Tubes For The Location Of Electromagnetic Showers In The Opal Forward Detectors"*, Nucl. Instrum. Meth. **A283** (1989) 515.
B.E. Anderson *et al.*, *"Compact Drift Chambers For The Opal Forward Detectors"*, Nucl. Inst. Meth. **A283** (1989) 650.

[33] B.E. Anderson *et al.*, *"The OPAL Silicon-Tungsten Calorimeter Front End Electronics"*, IEEE Trans. Nucl. Sci. **41** (1994) 845.

[34] OPAL Collaboration, G. Aguillion *et al.*, *"Thin Scintillating Tiles with High Light Yield for the OPAL Endcaps"*, Nucl. Inst. Meth. **A417** (1998) 266.

[35] M. Arignon *et al.*, *"The Trigger System of the OPAL Experiment at LEP"*, Nucl. Instr. Meth. **A313** (1992) 103.

[36] D. Charlton *et al.*, *"The Online Event Filter of the OPAL Experiment at LEP"*, Nucl. Inst. Meth. **A325** (1993) 129.

[37] J. T. M. Baines *et al.*, *"The Data Acquisition System of the OPAL Detector at LEP"*, Nucl. Inst. Meth. **A325** (1993) 271.

[38] C. Hawkes *et al.*, *"ROPE 410 User Guide"*, OPAL Offline Note 16/OFFL-0487, (February 1996).

[39] R. Cranfield *et al.*, *"OPCAL 506 User Guide"*, OPAL Offline Note OFFL-0036 (February 1992).

[40] D. Ward and J. Banks, *"A Grope Primer"*, internal OPAL manual (March 1995).

[41] OPAL Collaboration, K. Ackerstaff *et al.*, *"Search for Anomolous Production of Di-lepton Events with Missing Transverse Momentum in e^+e^- Collisions at $\sqrt{s}$ = 161 and 172 GeV"*, Eur. Phys. J. **C4**, 47 (1998).

[42] OPAL Collaboration, G. Abbiendi *et al.*, *"Search for Acoplanar Lepton Pair Events in e^+e^- Annihilation at $\sqrt{s}$ = 161, 172 and 183 GeV"*, Eur. Phys. J. **C12** 551 (2000).

[43] OPAL Collaboration, G. Abbiendi *et al.*, *"Search for Anomalous Production of Acoplanar Di-lepton Events in e^+e^- collisions at $\sqrt{s}$ = 183 and 189 GeV"*, Eur. Phys. J. **C14** 51 (2000).

[44] S. Bentvelsen, *"Physics Analyis I: Finished LEP1 Analyses and Detector Upgrade Plans*, OPAL Plenary talk, detector session (December 1997).

[45] UA1 Collaboration, G. Arnison *et al.*, *"Experimental Observation of Isolated Large Transverse Energy Electrons with associated missing energy at $\sqrt{s}$ = 540 GeV"*, Phys. Lett. **B122** 103 (1983).

[46] UA2 Collaboration, M. Banner *et al.*, *"Observation of Single Isolated Electrons of high transverse momentum in events with missing transverse energy at the CERN $p\bar{p}$ Collider"*, Phys. Lett. **B122** 476 (1983).

[47] CDF Collaboration, F. Abe *et al.*, *"Observation of W^+W^- Production in $p\bar{p}$ Collisions at $\sqrt{s} = 1.8$ TeV"*, Phys. Rev. Lett. **78** 4536 (1997).

[48] DØ Collaboration, S. Abachi *et al.*, *"W and Z Boson Production in $p\bar{p}$ Collisions at $\sqrt{s}$ = 1.8 TeV"*, Phys. Rev. Lett. **75** 1456 (1995).

[49] The TGC Working group, *"Triple gauge boson couplings in W^+W^- production at LEP energies up to 202 GeV"*, OPAL Physics Note PN441 (July 2000).

[50] M. A. Thomson, *"The OPAL $W^+W^- \rightarrow l\nu q\bar{q}$ Event Selection"*, OPAL Technical Note TN 635 (2000).

[51] I. Trigger and S. von Dobschuetz, *"A Likelihood Jet Pairing Method and a Jetcharge Technique for Reconstruction and determining the W charges in WW$\rightarrow q\bar{q}q\bar{q}$ Events*, OPAL Technical Note TN476 (1997).

[52] OPAL Collaboration, G. Abbiendi *et al.*, *"W^+W^- Production Cross Section and W Branching Fractions in e^+e^- Collisions at 189 GeV"*, Phys. Lett. **B493**, 249 (2000).

[53] T. Sjostrand, "Jet Fragmentation Of Nearby Partons", Nucl. Phys. **B248** (1984) 469.

[54] T. Sjostrand, *"High-energy physics event generation with PYTHIA 5.7 and JETSET 7.4"*, Comput. Phys. Commun. **82** (1994) 74.

[55] G. Abbiendi *et al.*, *"HERWIG Version 5.9"*, hep-ph/9607393 (Jul 1996).

[56] Pat and David Ward, *"A GOPAL Primer (latest revisions for GOPAL133) "*, (January 1995).
J. Allison *et al.*, *"The Detector simulation program for the OPAL experiment at LEP"*, Nucl. Instr. Meth. **A317** (1992) 47.

[57] R. Brun *et al.*, *"GEANT Users Guide (Version 3)"*, CERN EE EE 84/1, (1984). Available at http://consult.cern.ch/writeup/geant.
CERN Application Software Group, *"GEANT Detector Description and Simulation Tool"*, Software Manual CERN Program Library Long Writeup W5013, CERN (1993).

[58] S. Jadach, G. Passarino and R. Pittau *et al.*, *"Reports of the Working Groups on Precision Calculations for LEP 2 Physics"*, CERN yellow report, CERN 2000-009 (September 2000).

[59] F. A. Berends, R. Pittau and R. Kleiss *"EXCALIBUR: A Monte Carlo program to evaluate all four fermion processes at LEP-200 and beyond"*, Comput. Phys. Commun. **85**, 437 (1995)

[60] H. Voss, *Private Communique*, (May 2001).

[61] S. Jadach *et al.*, *"Monte Carlo program* KORALW *1.42 for all four-fermion final states in e^+e^- Collisions"* Comput. Phys. Commun. **119** (1999) 272.

[62] S. Jadach, B. F. L. Ward, and Z. Was, *"The Monte Carlo Program* KORALZ *for the Lepton or Quark Pair Production at LEP/SLC Energies"*, Comput. Phys. Commun. **124** 233 (2000).

[63] Minami-Tateya collaboration, T. Ishikawa *et al.*, *"GRACE manual: Automatic Generation of Tree Amplitudes in Standard Models: Version 1.0"*, KEK Report **92-19** (1993).

[64] M. Skrzypek *et al.*, *"Initial state QED corrections to W pair production at LEP 2/NLC: Monte Carlo versus semianalytical approach"*, Phys. Lett. **B372** (1996) 289.

[65] E. Barberio and Z. Was, *"PHOTOS: A Universal Monte Carlo for QED radiative corrections. Version 2.0"*, Comput. Phys. Commun. **79** (1994) 291.

[66] V. S. Fadin *et al.*, "Coulomb effects in $\mathrm{W}^+\mathrm{W}^-$ production, Phys. Rev. **D52** (1995) 1377.

[67] S. Jadach, Z. Was, R. Decker and J. H. Kuhn, *"The tau decay library TAUOLA: Version 2.4"*, Comput. Phys. Commun. **76** (1993) 361.

[68] J. Fujimot *et al.*, *"grc4f version1.1: a Four-fermion Event Generator for e^+e^- Collisions"*, Comput. Phys. Commun. **100** (1997) 128.

[69] J. A. M. Vermaseren, *"Two Photon Processes at Very High Energies"*, Nucl. Phys. **B229** 347 (1983).

[70] S. Jadach, B. F. L. Ward and Z. Was *'The precision Monte Carlo event generator KK for two-fermion final states in e^+e^- collisions,"*, Comput. Phys. Commun. **130** (2000) 260.

[71] T. Sjostrand, *"High-energy physics event generation with PYTHIA 5.7 and JETSET 7.4"*, Comput. Phys. Commun. **82** (1994) 74.

[72] S. Jadach, W. Placzek and B. F. Ward, *"BHWIDE 1.00: O(α) YFS exponentiated Monte Carlo for Bhabha scattering at wide angles for LEP1/SLC and LEP2"*, Phys. Lett. **B390** (1997) 298.

[73] D. Karlen, *"Radiative Bhabha Scattering For Singly Tagged And Untagged Configurations"*, Nucl. Phys. **B289** (1987) 23.

[74] C. P. Ward *et al.* *"WW111 manual"*, OPAL internal document (May 1998).

[75] S. L. Lloyd, *"The OPAL Primer"*, internal OPAL manual, version 98a (July 1998).

[76] OPAL Collaboration, R. Akers *et al.*, *"QCD Studies Using a Cone-based Jet Finding Algorithm for e^+e^- Collisions at LEP"*, Zeit. fur Physik **C63** 197 (1994).

[77] G. Wilson, *"Towards an Event Selection of Acoplanar Di-Lepton Events Optimized for the WW$\rightarrow l\nu l\bar{\nu}$ channel at $\sqrt{s} \approx 2\ M_W$"*, OPAL Technical Note TN382 (1996).
G. Wilson, *"An Improved Selection of Acoplanar Dilepton Events with High Visible Energy at $\sqrt{s}$ = 172 GeV"*, OPAL Technical Note TN446 (1996).

[78] G. Wilson, *"Further Improvements to an Event Selection for Events with Two Charged Leptons and Missing Energy"*, OPAL Technical Note (in preparation).

[79] K. Roscoe, *"Improvements to the Classification of Leptonically Decaying W pair Events at $\sqrt{s}$ = 189 GeV"*, OPAL Technical Note TN617 (1999).

[80] OPAL Collaboration *W^+W^- production in e^+e^- collisions at 189 GeV*, OPAL Physics Note PN378 (1999).

[81] S. Catani *et al.*, *"New clustering algorithm for multi - jet cross-sections in e^+e^- annihilation"*, Phys. Lett. **B269** (1991) 432.
S. Bethke *et al.*, *"New jet cluster algorithms: Next-to-leading order QCD and hadronization corrections"*, Nucl. Phys. **B370** (1992) 310 [Erratum-ibid. **B523** (1992) 681.]
N. Brown and W. J. Stirling, *"Finding jets and summing soft gluons: A New algorithm"*, Z. Phys. **C53** (1992) 629.

[82] E. Duchovini *et al.*, *"GCE++ An Algorithm for Event Energy Measurement"*, OPAL Technical Note TN306 (1995).

[83] Robin Coxe, *"Measurement of the Mass and Width of the W Boson with the OPAL Detector at LEP"*, University of Chicago, Ph.D. Thesis (June 2000).

[84] OPAL Collaboration, G. Abbiendi *et al.*, *"Measurements of Standard Model Processes in e^+e^- Collisions at $\sqrt{s} > 202$ GeV*, OPAL Physics Note, PN467 (November 2000).

[85] S. Betts, *"An evaluation of the WW$\rightarrow l\nu q\bar{q}$ likelihood selection in the WW110 package for use by the TGC group"*, OPAL Technical Note (in preparation).

[86] Eric Torrence, *"$W^+W^- \rightarrow q\bar{q}q\bar{q}$ Event Selection at 189 GeV"*, OPAL Technical Note TN650 (2000).

[87] OPAL TGC working group, *"Embrionic users manual for the WV package, Version: WV110-26"*, Informal TGC Note / Version-3, (April 1997).

[88] OPAL Collaboration, G. Abbiendi *et al.*, *W^+W^- production and triple gauge boson couplings at LEP energies up to 183 GeV*, Eur. Phys. J. **C8**, 191 (1999).

[89] G. Wilson, *Private Communique*, (October 1998).

[90] T. Wyatt, *Private Communique*, (July 1998).

[91] K. Hagiwara, R. D. Peccei, D. Zeppenfeld and K. Hikasa *"Probing the Weak Boson Sector in $e^+e^- \rightarrow W^+W^-$"*, Nucl. Phys. **B282**, 253 (1987).

[92] H. Aronson, *"Spin-1 Electrodynamics with an Electric Quadrupole Moment"*, Phys. Rev. **186** (1969) 1434.
J. Schwinger, *"On Quantum Electrodynamics and the Magnetic Moment of the Electron"*, Phys. Rev. **73** (1948) 416.
A. B. Lahanas, *"Static Quantities of the W boson in the MSSM"*, Phys. Lett. **B334** 378 (1994).

[93] M. Bilenky *et al.*, *"Trilinear Couplings amoung the Electroweak Vector Bosons and their determination at LEP200"*, Nucl. Phys. **B409** (1993) 22.

[94] M. Diehl and O. Nachtmann, *"Optimal Observables for the measurement of three gauge boson couplings in $e^+e^- \rightarrow W^+W^-$"*, Z. Phys. **C62**, 397 (1994).
M. Diehl and O. Nachtmann, *"Anomalous three gauge boson couplings in $e^+e^- \rightarrow W^+W^-$ and "optimal" strategies for their measurement"*, Eur. Phys. J. **C1** 177 (1998).

[95] OPAL Collaboration, G. Abbiendi *et al.*, *"Measurement of W boson polarisations and CP-violating triple gauge couplings from W^+W^- Production at LEP"*, Eur. Phys. J. **C19** 229 (2001).

[96] ALEPH Collaboration, *"Measurement of Triple Gauge-Boson Couplings at LEP energies up to 189 GeV"*, CERN EP/2001-022.

[97] ALEPH Collaboration, *"Measurement of Triple Gauge Boson Couplings in e^+e^- collisions up to 208 GeV"*, CONF 2000-021 (March 2001).

[98] DELPHI Collaboration, P. Abreu *et al.*, *" Measurement of Trilinear Gauge Couplings in* e^+e^- *Collisions at 161 GeV and 172 GeV"*, Phys. Lett. **B423** 194 (1998).

[99] C. Hamzaoui *et al.*, *"CP violating but P preserving Electromagnetic Couplings of the* $W^\pm$ *and* Z^0*"*, Phys. Rev. **D43** 3683 (1991).

[100] L3 Collaboration, *"Preliminary Results on the Measurement of Triple-Gauge-Boson Couplings of the W Boson at LEP"*, L3 Note 2567 (June 2000).

[101] K. J. F. Gaemers and G. J. Gounaris, *"Polarization Amplitudes for* $e^+e^- \rightarrow W^+W^-$ *and* $e^+e^- \rightarrow ZZ$, Z. Phys. **C1** (1979) 259.

[102] A. De Rújula *et al.*, *"The self-couplings of vector bosons: does LEP 1 obviate LEP 2 ?"*, Nucl. Phys. **B384**, (1992) 3.

[103] DELPHI Collaboration, *"Measurement of Trilinear Gauge Boson Couplings* WWV*, (*$V \equiv Z, \gamma$*) in* e^+e^- *Collisions at 189 GeV"*, Phys. Lett. **B502** 9 (2001).

[104] OPAL Collaboration, G. Abbiendi *et al.*,*"Measurement of triple gauge boson couplings from* W^+W^- *production at LEP energies up to 189-GeV,"*, Eur. Phys. J. **C19** 1 (2001).

[105] OPAL Collaboration, G. Abbiendi *et al.*, *"Measurement of the* $W^+W^-\gamma$ *Cross Section and first direct limits on Anomalous Electroweak Quartic Gauge Couplings*, Phys. Lett. **B471** 307 (1999).
ALEPH Collaboration, *"Constraints on Anomalous Quartic Gauge Boson Couplings from photon pair events from 189 to 200 GeV"*, CONF 2001-049
L3 Collaboration, M. Acciarri *et al.*, *"Measurement of the* $W^+W^-\gamma$ *Cross Section and Direct Limits on Anomalous Quartic Gauge Boson Couplings at LEP"*, Phys. Lett. **B490** (2000) 187.
L3 Collaboration, M. Acciarri *et al.*, *"Measurement of the* $e^+e^- \rightarrow Z\gamma\gamma$ *Cross Section and Determination of Quartic Gauge Boson Couplings at LEP "*, Phys. Lett. **B478** (2000) 39.

[106] G. Bélanger *et al.*, *"Bosonic Quartic Couplings at LEP 2"*, Eur. Phys. J. **C13** 283 (2000).

[107] ALEPH Collaboration, *"Limits on anomalous neutral gauge couplings using data from ZZ and* $Z\gamma$ *production between 183-208 GeV"*, CONF 2000/041 (July, 2001).
DELPHI Collaboration, *"Study of Trilinear Neutral Gauge Boson Couplings ZZZ,* $ZZ\gamma$ *and* $Z\gamma\gamma$*"*, CONF 525, (July 2001).
L3 Collaboration, *"Search for Anomalous* $ZZ\gamma$ *and* $Z\gamma\gamma$ *Couplings using the process* $e^+e^- \rightarrow Z\gamma$ *at LEP*, L3 Note 2672 (July 2001).
OPAL Collaboration, G. Abbiendi *et al.*, *"Search for Trilinear Neutral gauge Boson Couplings in* $Z\gamma$ *production at* $\sqrt{s} = 189$ *GeV at LEP"*, Eur. Phys. J. **C17** (May 2000) 553.
OPAL Collaboration, *"Study of Z Pair Production and Anomalous Couplings in* e^+e^- *Collisions at* $\sqrt{s}$ *between 190 and 209 GeV"*, OPAL PN482 (July 2001).

[108] G. J. Gounaris, J. Layssac and F. M. Renard, *"Signatures of the anomalous Zγ and ZZ production at the lepton and hadron colliders"*, Phys. Rev. **D61** (2000) 073013.

[109] R. L. Sekulin, *"Ambiguities in the determination of the vector boson couplings at LEP200"*, Phys. Lett. **B338** 369 (1994).

[110] OPAL Collaboration, K. Ackerstaff *et al.*, *"Measurement of the Triple Gauge Boson Coupling $\alpha_{W\phi}$ from W$^+$W$^-$ Production in e^+e^- Collisions at $\sqrt{s} = 161$ GeV"*, Phys. Lett. **B397** 147 (1997).
OPAL Collaboration, K. Ackerstaff *et al.*, *"Measurement of the Triple Gauge Boson Couplings from W$^+$W$^-$ Production at $\sqrt{s} = 172$ GeV"*, Eur. Phys. J. **C2** 597 (1998).

[111] C. G. Papadopoulos, *"Studying trilinear gauge couplings at LEP 2 using Optimal Observables"*, Phys. Lett. **B386** 442 (1996).

[112] D. Atwood and A. Soni, *"Analysis for magnetic moment and electric dipole moment form factors of the top quark via $e^+e^- \to t\bar{t}$"*, Phys. Rev. **D45** (1992) 2405.

[113] M. Davier, L. Duflot, F. Le Diberder and A. Rouge, *"The Optimal Method for the Measurement of tau Polarization"*, Phys. Lett. **B306**, 411 (1993).

[114] D. Charlton and A. Lloyd, *"Measurement of Triple Gauge Coupling Parameters with Optimal Observables for W$^+$W$^-$ $\to$ $l^+\nu l^-\bar{\nu}$ Events at $\sqrt{s} = 189$ GeV"*, OPAL Technical Note TN633, (revised March 2000).

[115] R. J. Barlow, *"Statistics"*, The Manchester Physics Series, John Wiley & Sons, (1989).

[116] F. James, "MINUIT *Function Minimisation and Error Analysis"*, CERN Program Library Long Writeup, D506.

[117] Helge Voss, *"Messung der Drei-Eichboson-Kopplungen in W$^+$W$^-$ $\to q\bar{q}l\bar{\nu}_l$ Ergnissen mit optimalen Observablem bei OPAL"*, thesis submitted to University of Bonn (2000).
Helge Voss, *"TGC Measurement at 189 GeV in the W$^+$W$^-$ $\to q\bar{q}l\bar{\nu}_l$ Channel Using Optimal Observables"*, OPAL Technical note (in preparation).

[118] Bradley Efron and Robert J. Tibshirani, *"An Introduction to the Bootstrap" (Monographs on Statistics and Applied Probability, No 57)*, Chapman and Hall 1993.

[119] R. J. Barlow, *"Application of the Bootstrap Resampling Technique to Particle Physics Experiments"*, Preprint MAN-HEP-99-4 (April 2000)
(available under: http://www.hep.man.ac.uk/hep/preprints.html).

[120] R. J. Barlow, *Lecture 6: "Resampling and the Bootstrap"*, SLUO Lectures on Statistics and Numerical Methods in HEP (August 2000)
(available under: http://hepwww.ph.man.ac.uk/ roger/home.html).

[121] G. Bella, *Private Communique*, (June 2000).

[122] C. P. Ward and D. R. Ward, *"Measurement of the Mass of the Mass of the W boson at 183 GeV using an analytic Breit-Wigner fit"*, OPAL Technical Note TN564 (September 1998).

[123] P. G. Bright-Thomas, *"Systematic studies of* $A_{FB}^{\mu\mu}$*"*, OPAL Technical Note TN662 (August 2000).

[124] M. Hauschild, *Private Communique*, (July 2000).

[125] G. Bella, *"First View of the 1999* $l\nu q\bar{q}$ *Data"*, OPAL Plenary talk, TGC session (December 1999).
Eric Torrence, *Private Communique*, (December 1999).

[126] OPAL Standard Model, WW and QCD Working Groups, *"Measurements of Standard Model Processes in* e^+e^- *Collisions at* $\sqrt{s} >$ *190 GeV"*, OPAL Physics Note PN420 (November 1999).

[127] DØ Collaboration, B. Abbott *et al.*, *"A Measurement of the W Boson Mass using Electrons at Large Rapidities"*, Phys. Rev. Lett. **84** 222 (2000).
CDF Collaboration, F. Abe *et al.*, *"Measurement of the W Boson Mass"*, Phys. Rev. Lett. **75** (1995) 11.

[128] LEP Energy Working Group, A. Blondel *et al.*, *"Evaluation of the LEP Centre-of-Mass Energy above the W Pair Production Threshold"*, Eur. Phys. J. **C11** 573 (1999).

[129] M. A. Thomson, *Private Communique*, (December 1999).

[130] G. Bella, *Private Communique*, (November 2001).

[131] T. J. V. Bowcock *et al.*, *"Measurement of Trilinear Gauge Boson Couplings in* e^+e^- *Collisions at 192-202 GeV"*, DELPHI 2000-146 CONF 445 (June 2000).

[132] The LEP Collaborations ALEPH, DELPHI, L3, OPAL and the LEP TGC Working Group, *"Combined Preliminary Results on Electroweak Gauge Boson Couplings Measured by the LEP Experiments"*, LEPEWWG/TGC/2000-02 (September 2000).

[133] UA2 Collaboration, J. Alitti *al.*, *"Direct Measurement of the W*γ *coupling at the CERN $\bar{p}p$ Collider"*, Phys. Lett. **B277** (1992) 194.

[134] J. Ellison and J. Wudka, *"Study of Trilinear Gauge Boson Couplings at the Tevatron Collider"*, hep-ph/9804322.

[135] B. Abbott *al.*, *"Studies of WW and WZ Production and Limits on Anomalous WW*γ *and WWZ Couplings"*, Phys. Rev. **D60**, (1999) 072002.

[136] F. Abe *al.*,*"Limits on WWZ and WW*γ *couplings from WW and WZ production in p$\bar{p}$ collisions at* $\sqrt{s} = 1.8$ *TeV"*, Phys. Rev. Lett. **75** (1995) 1017.

[137] S. Alam, S. Dawson and R. Szalapski, *"Low-energy constraints on new physics reexamined"*, Phys. Rev. **D57** (1998) 1577.

[138] S. Godfrey and H. König, *“Atomic parity violation as a probe of anomalous gauge-boson couplings”*, Phys. Rev. **D45** (1992) 3196.

[139] A. Grau and J. A. Grifols, *“Effects Of Anomalous Magnetic Dipole And Electric Quadrupole Moments Of The Charged Weak Boson On (g-2)$_\mu$”*, Phys. Lett. **B154** (1985) 283.
F. Herzog, *“Constraints on the Anomalous Magnetic Moment of the W Boson from the magnetic moment of the muon”*, Phys. Lett. **B148** (1984) 355.

[140] O. Eboli *et al.*, *“Indirect constraints on the triple gauge boson couplings from Z $\rightarrow b\bar{b}$ Partial width: An update”*, Mod. Phys. Lett. **A15** (2000) 1

[141] S. Playfer and S. Stone, *“Rare b Decays”*, Int. J. Mod. Phys. **A10** (1995) 4107.
X. He and B. McKellar, “Constraints on the anomalous WWγ couplings from $b \rightarrow s\gamma$”, Phys. Lett. **B320** (1994) 165.
T. Rizzo, “Constraints on the Anomalous Gauge Boson Couplings from $b \rightarrow s\gamma$”, Phys. Lett. **B315** (1993) 471.

[142] J. Womersley, *“The LHC Physics Program”*, To be published in the proceedings of 20th International Workshop on Fundamental Problems of High-Energy Physics and Field Theory, Protvino, Russia, 24-26 Jun 1997.
Z. Parsa (ed.), *“Future High Energy Colliders”*, Prepared for ITP Conference on Future High-energy Colliders, Santa Barbara, CA, 21-25 October 1996. AIP (1997) (AIP conference proceedings 397).
ATLAS Collaboration, *“ATLAS: Detector and Physics Performance Technical Design Report”*, Vol. II, (May 1999) CERN-LHCC-99-15, ATLAS-TDR-15.

[143] ECFA/DESY Linear Collider Physics Working Group, E. Accomando *et al.*, *“Physics with e^+e^- Linear Colliders”*, hep-ph/9705442 (May 1997), DESY-100.

[144] DPF Study, *“Electroweak Symmmetry Breaking and Beyond the Standard Model”*, T. L. Barklow *et al.*, (World Scientific 1996); DPF/DBP Summer Study on New Directions for High Energy Physics, Snowmass 1996.

[145] E. Torrence, *“YFSWW-KORALW Comparisions by OPAL”*, talk presented at WWMM Workshop, Sesimbra, Portugal (November 2000).

[146] S. Jadach *et al.*, *“The Monte Carlo Event Generator YFSWW3 version 1.16 for W-Pair Production and Decay at LEP2/LC Energies”*, preprint CERN-TH/2001-017, UTHEP-01-0101, January 2001; hep-ph/0103163, submitted to Comput. Phys. Commun.

[147] J. Hansen, *“Review of $\mathcal{O}(\alpha)$ activities for charged TGC’s”*, talk presented at WWMMI Workshop, CERN (April 2001).
S. Villa, *“$\mathcal{O}(\alpha)$ Effects on TGC’s - the L3 status”*, talk presented at WWMMI Workshop, CERN (April 2001).

[148] S. Jadach, G. Passarino and R. Pittau *et al.*, *"Reports of the Working Groups on Precision Calculations for LEP 2 Physics"*, CERN yellow report, CERN 2000-009 (September 2000).

[149] S. Jadach *et al.*, *"The Monte Carlo Program KoralW version 1.51 and The Concurrent Monte Carlo KoralW & YFSWW3 with All Background Graphs and First Order Corrections to W-Pair Production"*, CERN-TH-2001-040, UTHEP-01-0102, April 20001; Submitted to Comput. Phys. Commun.

[150] Ian Bailey, *"Unpdate on Studies in the WW* $\rightarrow \tau\nu q\bar{q}$ *Channel"*, OPAL Plenary talk, TGC session (September 2000).

[151] T. Omori *et al.*, *"A Matching Algorithm: MT package"*, OPAL Technical Note TN381 (1996).

[152] K. Ishii *et al.*, *"Jet error parameterisation"*, OPAL Technical Note TN449 (1996).
G. Bella, Private Communique, January 2001.

[153] Oana Boeriu, *Private Communique*, (August 2001).